Petrogenesis and metallogenesis of the Panzhihua Fe-Ti oxide ore-bearing mafic layered intrusion, SW China

A thesis submitted in fulfilment of the requirements of the degree of

Doctor of Philosophy

at

Rhodes University

by

Geoffrey Hamilton Howarth

December 2012

Department of Geology, Rhodes University

South Africa

Abstract

The Panzhihua intrusion is one of several large Fe-Ti oxide ore bearing intrusions related to the major flood volcanism of the Emeishan Large Igneous Province (ELIP), SW China. The Panzhihua intrusion in particular has recently become the focus of numerous studies owing to the excellent exposure in large open pit mining operations. The formation of Fe-Ti oxide ore layers has been the focus of these studies and has become a somewhat controversial topic with three separate models currently proposed for ore formation.

The gabbroic Panzhihua intrusion extends for ± 19 km along strike, has a maximum thickness of 3000 m and hosts extensive (up to 60 m thick) Fe-Ti oxide ore layers in the lower portions of the intrusion. The intrusion has been divided into five zones: marginal zone (MGZ), lower zone (LZ), middle zone A (MZa), middle zone b (MZb) and the upper zone (UZ). The gabbroic rocks are comprised of plagioclase, clinopyroxene and interstitial Fe-Ti oxides with minor olivine. Apatite is present within the MZb only and shows no correlation with Fe-Ti oxide ore layers. Fe-Ti oxides are present throughout the stratigraphy of the intrusion. This is unlike typical layered intrusions where significant Fe-enrichment through fractionation of Fe-poor silicate phases (i.e. plagioclase) is required before Fe-Ti oxide saturation. There are no oxide-free cumulate rocks at the Panzhihua intrusion, implying either an evolved parent magma or very high Fe content of the source rocks.

I present here new mineral composition data, whole-rock major and trace element geochemistry along with whole-rock Sr-Nd isotopes and PGEs in order to constrain the evolution of the Panzhihua parent magma en route from source to chamber and the formation of Fe-Ti oxide ore layers. Furthermore an initial pilot study using O-isotope data is conducted on Ti-magnetite and plagioclase separates from gabbroic vs. ore rocks. Results are coupled with detailed thermodynamic modeling using the software PELE in order to further constrain Fe-Ti oxide ore layer formation.

The intrusion is characterised by extreme depletion of PGEs relative to the coeval flood basalts and picrites. High Cu/Pd and Pd/Pt imply two separate stages of S-saturated and S-undersaturated depletion of PGEs. Pd is highly compatible in sulphide and is quickly scavenged by sulphide liquids resulting in an increase in Cu/Pd of the residual liquid. Furthermore decoupling of Pd and Pt can be achieved by either late stage hydrothermal alteration or through S-undersaturated stage of PGE

depletion where Pt is scavenged by Pt-rich alloys or oxide minerals. I show that the latter is more likely. Fractionation modeling suggests that the Panzhihua parent magma formed at depth from original picritic magma. This is consistent with several other recent studies on other layered intrusions of the ELIP. Sr-Nd isotopic ratios indicate very little crustal contamination has occurred en route to the current chamber.

Sr and Nd concentrations of footwall rocks are too low to produce any significant change in initial Sr and Nd isotopic ratios of the intruding basaltic magmas, indicating that crustal contamination will not be indicated by Sr-Nd isotopic ratios. Gradational change in the Sr-Nd isotope ratios across the MGZ provides strong evidence for formation in an open system by multiple replenishments of progressively less contaminated magmas from depth. Contamination is difficult to constrain but must be occurring prior to emplacement at the current level (low Sr and Nd contents of footwall). A gradational upward decrease in highly incompatible element across the MGZ can then be explained by continuous magma flow, which effectively removes the evolved intercumulus liquids from the growing cumulate pile at the base of the chamber. The initial stages of formation of the Panzhihua intrusion are interpreted to result from prolonged low volume pulses of magma into a slowly opening chamber.

The timing of Fe-Ti oxide crystallisation is fundamental in the understanding of the petrogenesis of ore layers. Distinct geochemical variation in whole-rock Fe_2O_3/TiO_2 and Zr/Nb indicates that Ti-magnetite is the dominant oxide within the lower ± 270 m of the intrusion whereas above this level both Ti-magnetite and ilmenite are present as cumulus phases. This is interpreted to indicate a variation in the fO_2 where the lower intrusion crystallises at higher fO_2 relative to that above this level. Silicates within the ore layers, in particular plagioclase, are highly embayed and resorped where in contact with Fe-Ti oxides. This characteristic of the silicate grains implies early crystallisation prior to Fe-Ti oxides with subsequent disequilibrium conditions resulting in resorption. Furthermore distinct reaction rims of kaersutite amphibole, Fo-enriched olivine, An-enriched plagioclase and pleonaste are observed. The abundance of amphibole suggests H_2O involvement in this reaction and consumption of silicates. A model for parent magma crystallisation at various H_2O contents indicates that plagioclase crystallisation temperature is very sensitive to H_2O content of the parent magma. Plagioclase crystallises early for “dry” compositions but significantly later for “wet” compositions.

Fe-Ti oxide ore layers are generally well layered, contain gabbroic xenoliths and are observed traversing/cross-cutting the cumulate stratigraphy. I present here a new model for ore layer formation in order to account for these distinct features of the ore layers. A model invoking multiple replenishments of magma with variable oxide microphenocryst content, H_2O content and volume is proposed. Magma evolving in the plumbing system and fed to the Panzhihua chamber is variably enriched in H_2O, which results in significantly different crystallisation paths. High H_2O magmas (> 2 wt %) crystallise Fe-Ti oxides early whereas low H_2O magmas (< 1 wt %) crystallise oxides late. Early pulses of H_2O-poor magma crystallise a sequence of plag+cpx+Fe-Ti oxide (±ol). Later pulses of H_2O-rich magma subsequently intrude the partially crystallised cumulate sequence incorporating and consuming previously crystallised silicates with subsequent early crystallisation of Ti-magnetite and formation of ore layers. H_2O-rich magmas likely have suspended Ti-magnetite microphenocrysts as well, which crystallise at depth in the plumbing system. This model can account for the various characteristic features of the Fe-Ti oxide ore layers at the Panzhihua intrusion as well as other Fe-Ti oxide ore bearing intrusions in the region.

“The man who does things makes many mistakes, but he never makes the biggest mistake of all – doing nothing.”

Benjamin Franklin

Declaration

All material contained in this thesis represents the original work of the author except where specific acknowledgement is made to the work of others.

G.H. Howarth (MSc)

December 2012

Department of Geology

Rhodes University

Grahamstown

South Africa

Acknowledgements

Firstly, I would like to greatly thank my supervisor Dr. Steve Prevec without whom this project would not have been possible. Steve has allowed me to develop my own ideas but at the same time was always around for discussions and advice on numerous aspects of the project. I would also like to thank Steve for numerous hours put into proof reading and editing this thesis and for the preparation of papers submitted for review in international journals. Furthermore I would like to thank Steve for organising the logistics of field work and sample analyses at the various facilities used.

I would like to thank my co-supervisor, Prof. Mei-Fou Zhou who was our collaborator in China. In particular Mei-Fou is thanked for logistical issues of field work in China. Field work would not have been possible without his help and knowledge of the PANXI region and related layered intrusions. I would also like to thank Mei-Fou for very useful discussions on the Panzhihua intrusion. I would also like to thank Dr. Christina Wang for help with field work and in particular with packaging and shipping of the samples from SW China to South Africa.

This study would not have been possible without the technical assistance of numerous individuals. I would like to thank Dr. Gabi Costin for many hours of help with microprobe analyses and subsequent data analysis. I would also like to thank John Hepple and his technicians at Rhodes University for help with sample preparation and this section production. I would also like to thank Dr. Marc Poujol at the CNRS in Rennes, France, for running Sr-Nd isotope analysis. Dr. Dave Reid, University of Cape Town is thanked for aided in whole-rock major element XRF analysis and facilitating trace ICP-MS trace element analysis. PGE analyses were done at the University of Quebec at Chicoutimi, Canada and they are also thanked.

I would also like to thank the members of the Rhodes University Magmatic Ores Group (MORG) for useful discussions on igneous processes.

I would lastly like to thank those organisations which funded both the project and me over the last three years. Firstly, I would like to acknowledge the research funding given by the South African National Science Foundation (NRF) Grant SA/China Project 67220. Secondly, thanks are given to the NRF for supporting me with a Scarce Skills scholarship for 2011-2012.

Contents

Figure and Table Captions

Figures

Tables

1. Introduction

Layered intrusions are important igneous bodies, which provide evidence for differentiation and evolution of magmas prior to eruption at the surface. In general our understanding of magma chamber processes is based on detailed studies on these intrusions. Layered intrusions form through complex open and closed system processes. The Skaergaard intrusion (Greenland) is generally considered as an example of closed system evolution of basaltic magma. Early crystallising phases (e.g. olivine, orthopyroxene, chromite) settle to the base of the intrusion forming ultramafic cumulates. As the magma is depleted in Mg through the crystallisation of olivine and/or orthopyroxene, later cumulates evolve to more gabbroic compositions, characterised by the occurrence of plagioclase. Tholeiitic basaltic magmas commonly evolve to Fe-rich liquids, which culminates in the crystallisation of ferrogabbros at late stages in the upper parts of intrusions. Fe-enrichment trend, known as the Fenner trend (Fenner, 1929), is characteristic of tholeiitic basaltic magmas due to the crystallisation and fractionation of abundant olivine and more importantly plagioclase. Calc-alkaline basaltic magmas are characterised by early crystallisation of Fe-Ti oxides, which does not allow for Fe-enrichment. Ferrobasalts erupting at the surface are generally rare, which is interpreted to be due to the high density of these magmas (Sparks et al. 1980). However examples are known, such as the Columbia River Flood basalts (12-19 wt % total Fe; Lange, 2002) and the Emeishan Flood basalts (9-14 wt % total Fe; Xiao et al. 2004). The eruption potential of ferrobasalts is interpreted to be the result of high volatile content of the magmas; > 4 wt % H_2O+CO_2 (Lange, 2002), in the case of the Columbia River flood basalts. This implies that the magmas forming the ELIP may also be characterised by high volatile contents. High concentrations of H_2O in a basaltic magma has been shown to influence phase relations and shift the tholeiitic trend to a calc-alkaline trend (Grove et al. 2003; Berndt et al. 2005; Botcharnikov et al. 2008), which does not allow for Fe-enrichment of the magma.

Layered intrusions are hosts to major economic ore bodies of Ni-Cu-PGE, Cr and Fe-Ti-V. Generally Ni-Cu-PGE and Cr ore bodies are associated with ultramafic portions and Fe-Ti-V with the mafic portions of layered intrusions. Fe-Ti-V oxide ore bodies are associated with ferrogabbros crystallising at a late stage of evolution within layered intrusions. This is generally after a sustained period of Fe-enrichment and formation of ultramafic cumulates at the base of the intrusion (e. g. Bushveld Complex; Cawthorn and Ashwal, 2009).

The Emeishan Large Igneous Province (ELIP), located in SW China (Wignall, 2001), contains both ultramafic-mafic layered intrusions and mafic intrusions, which are spatially and temporally

associated with the Emeishan Flood basalts. The current study focuses on the Panzhihua mafic layered intrusion, which is comprised of ferrogabbros and major Fe-Ti oxide ore layers. No ultramafic cumulates are present at the base of the intrusion implying the parent magma was already enriched in Fe either through Fe-enrichment at depth or as a function of the source rocks. Numerous mechanisms for the formation of Fe-Ti-V oxide ore bodies have been proposed in the literature and are reviewed below as this will be one of the main themes for this study.

1.1 Ferrogabbro and Fe-Ti oxide ore layers

Ferrogabbros are common constituents of the upper part of layered ultramafic-mafic intrusions but may also occur within relatively small intrusions comprised of ferrogabbro alone. The occurrence of Fe-Ti oxide ore layers at the base of intrusions is less common. Examples of ultramafic-mafic intrusions with ferrogabbroic upper zones are given below and include the Fe-Ti oxide ore-bearing Bushveld Complex and the Skaergaard intrusion. The Fedorivka intrusion is also included as an example of a ferrogabbroic intrusion crystallising magnetite throughout the intrusion. Fe-Ti oxide ores are also associated with Proterozoic anorthosite complexes. These are dominated by ilmenite rather than magnetite and are generally associated with apatite. These deposits are significantly different from Fe-Ti oxide ores in layered mafic intrusions and are not reviewed here.

1.1.1 Occurrences

The Skaergaard intrusion is a classic example of magma differentiation in a closed system. The intrusion is comprised of several zones: the layered series (crystallising from the floor up), the Upper Border Series (crystallising from the roof down) and the marginal border series (crystallising form the walls inward). The layered series can be further sub-divided into the Lower, Middle and Upper zones based on the appearance/disappearance of primary cumulus phases (McBirney, 1996). These zones represent typical differentiation trends of a basaltic magma within a closed system. Mineral compositions evolve to Na- and Fe-rich compositions and the liquid becomes Fe-enriched in the middle/upper zones, resulting in the crystallisation of cumulus magnetite and the crystallisation of ferrogabbros with total Fe of 20-30 wt % (McBirney, 1996). Fe-enrichment is due to the crystallisation of the 800 m thick lower zone sequence, where magnetite is absent (Botcharnikov et al. 2008). The Skaergaard intrusion is an example of a tholeiitic basaltic magma crystallising along the typical Fe-enrichment Fenner trend (Hunter and Sparks, 1987).

The Fedorivka intrusion (Ukraine) is a relatively small layered intrusion comprised of melanocratic oxide-rich olivine gabbro and leucocratic gabbro (Duchesne et al. 2006). No ultramafic rocks are

observed at the base of the intrusion. The intrusion extends for 3.5 km along strike, is 450 m in width and has a maximum thickness of 320 m. The intrusion is divided into three zones: Lower Zone (LZ), Middle Zone (MZ) and the Upper Border Zone (UBZ). Magnetite and ilmenite occurs throughout the stratigraphy. TiO_2 content of the magnetite increases from the uppermost part of the LZ to the UBZ (Duchesne et al. 2006). V in magnetite is inversely correlated with TiO_2 and decreases from 1.5 wt % at the base of the intrusion to 0.5 wt % at the top. Plagioclase (An_{39}-An_{45}), olivine (Fo_{32}-Fo_{45}) and augite (Mg# - 50) compositions are highly evolved and evolve to lower An, Fo and Mg# upward in the sequence. No massive ore layers are present but whole-rock total Fe content reaches up to 50 wt %. The Fedorivka intrusion is interpreted to represent the crystallisation of at least two pulses of Fe-rich magma (Duchesne et al. 2006). The magma forming the MZ essentially behaves like a closed system with constant evolution of the cumulus minerals upward in the sequence.

The Bushveld Complex (South Africa) is one of the most famous ultramafic-mafic layered intrusions in the world and hosts extensive Fe-Ti oxide ore layers in the upper parts of the intrusion. The Bushveld Complex is comprised of several zones from the base upward: Marginal Zone, Lower Zone, Critical Zone, Main Zone and the Upper Zone. The Marginal Zone is comprised of fine-grained mafic rocks interpreted to represent a chilled margin. The Lower Zone (± 1200 m thick) consists of dunite cumulates alternating with orthopyroxenites and harzburgites. The Critical Zone (± 1000 m) is composed of norite, orthopyroxenite and anorthosite layers with subordinate dunite, harzburgite and chromitite. The zone hosts the famous Merensky Reef along with several other PGE ore horizons (e.g. UG 2 Chromitite). This zone is overlain by the Main Zone (± 3500 m) and is composed of a monotonous sequence of gabbro-norite and anorthosite. The base of the Upper Zone (UZ) (± 1500 m total thickness) is marked by the first occurrence of magnetite in the sequence and is comprised of a well layered sequence of gabbro, ferrogabbro, anorthosite and massive magnetite layers. Magnetite is a common constituent of all rock types and has an average abundance of 8-10 vol. % (Klemm et al. 1985). A total of 24 magnetite layers are observed with a maximum thickness of ± 2 m. Cumulus apatite is observed in the upper half of the Upper Zone stratigraphy only. Magnetite layers have sharp lower contacts but in general have gradational upper contacts with increasing abundance of silicate phases. Plagioclase laths are typically aligned parallel to the layering. Magnetite within the ore layers shows some variation in composition with stratigraphic height. The magnetite of the lower layers are characterised by the highest V and Cr contents, which decreases quickly upward in the sequence (Klemm et al. 1985). TiO_2 of ore layer magnetite increases upward in the sequence (Klemm et al. 1985). Plagioclase composition shows a general decrease in An content upward in the sequence with several reversal to more primitive compositions, although no trends are observed in

spatial relation to magnetite layers (Cawthorn and Ashwal, 2009). The composition evolves from the most primitive plagioclase (An_{62}) to more Na-rich plagioclase (An_{40}) toward the top of the sequence (Cawthorn and Ashwal, 2009).

Numerous recent studies on layered intrusions associated with the Emeishan Large Igneous Province (ELIP) have described massive Fe-Ti oxide layers up to 80 m in thickness (e. g. Pang et al. 2008a; Bai et al. 2012). This study presents new data on the Panzhihua intrusion (ELIP), which contains extensive Fe-Ti oxide ore layers. The geology of the Panzhihua intrusion and the ELIP is reviewed in section 2.

1.1.2 Formation of Fe-Ti oxide ore layers

The formation of Fe-Ti oxide ore layers has been the subject of numerous studies over the last several decades. In the 1980's numerous studies (e.g. Cawthorn and McCarthy, 1980; Klemm et al. 1985; von Gruenewaldt et al. 1985; Reynolds, 1985a; 1985b) were done on the Bushveld Complex (South Africa) and most subsequent studies have built on observations and interpretations from these studies. Numerous mechanisms have been proposed to explain the formation of Fe-Ti oxide ore layers including: early crystallisation of Fe-Ti oxides (Botcharnikov et al. 2008; Pang et al. 2008b), increases in fO_2 (Klemm et al. 1985; von Gruenewaldt et al. 1985), increases in pressure (Cawthorn and Ashwal, 2009) and liquid immiscibility (Reynolds, 1985a, 1985b; Zhou et al. 2005).

Early crystallisation of Fe-Ti oxides: Fe-Ti oxides in a basaltic magma generally crystallise late after a period of Fe-enrichment, as described above; e.g. Fenner trend (Fenner, 1929). Botcharnikov et al. (2008) showed experimentally that a high proportion of H_2O significantly reduces the crystallisation temperature of silicate phases, in particular plagioclase, resulting in the early crystallisation of Fe-Ti oxides from a basaltic magma. Pang et al. (2008b) modeled a ferrobasaltic magma using MELTS and showed that with approximately 1.5 wt % initial H_2O content that a Fe-Ti oxide will crystallise prior to plagioclase and clinopyroxene. The result of this is the early depletion of the magma in Fe and the magma follows a typical calc-alkaline evolution trend. In this way Fe-Ti oxides crystallise early and settling/sorting of these grains within the magma chamber may lead to the accumulation in a layer at the base of the chamber.

Increases in fO_2: Periodic fluctuation in fO_2 has been proposed by numerous studies as a potential mechanism for the formation of massive Fe-Ti oxide ore layers (e. g. Klemm et al. 1985; von Gruenewaldt et al. 1985; Ganino et al. 2008). von Gruenewaldt et al. (1985) showed that Ti-

magnetite within ore layers vs. those occurring in gabbroic rocks have different microtextures, which are interpreted to result from varying degrees of oxidation and exsolution. Klemm et al. (1985) showed compositional variations between magnetite in ore layers vs. those in gabbroic rocks, which were interpreted to result from an increase in fO_2 conditions. The most convincing compositional variation is that of V, which in general is higher in the gabbroic Ti-magnetite relative to the ore Ti-magnetite (Klemm et al. 1985). Toplis and Corgne (2002) showed that V concentration of magnetite is not only controlled by the distribution co-efficient but also by fO_2. V content of magnetite decreases with increasing fO_2 conditions. This mechanism requires no change in the composition of the magma, apart from the increase in Fe^{3+}/Fe^{2+} ratio. This would affect the composition of Fe-bearing silicates but not plagioclase. The composition of plagioclase should remain constant above and below magnetite layers. The main concern with this model raised by Cawthorn and Ashwal (2009) is the mechanism by which the fO_2 is increased so that the Fe-Ti oxide layers are consistent in terms of composition over large lateral distances.

Increases in pressure: An increase in pressure is proposed as a mechanism for the formation of Fe-Ti oxide layers as it presents a solution for the lateral consistency of many Fe-Ti oxide ore layers in the Bushveld Complex (Cawthorn and Ashwal, 2009). Increases in total pressure may shift phase boundaries so that the liquidus becomes isolated in the Ti-magnetite field (Cameron, 1980). An increase in pressure, similarly to an increase in fO_2, does not change magma compositions and An content of plagioclase should not change above Fe-Ti oxide layers. Cawthorn and Ashwal (2009) suggest that the magma may no longer be saturated in clinopyroxene as a result of the excessive Ti-magnetite formation, which explains the lack of clinopyroxene in the gradational upper contacts of Bushveld Fe-Ti oxide ore layers. However Hatton (1984) suggests that the pressure variations required to shift phase boundaries is not feasible. Therefore the applicability of this mechanism remains uncertain.

Liquid immiscibility: The separation of an evolving basaltic magma into Fe- and Si-rich immiscible liquids was proposed by Bateman (1951). Reynolds (1985a and 1985b) has applied this to the upper apatite-rich oxide ore layers of the Bushveld Complex. Cawthorn and Ashwal (2009) suggest that a Fe-rich liquid, which would have a high density and low viscosity, would percolate through the underlying crystal mush pile resulting in gradational lower contacts. Recent experimental work on immiscible Fe-rich liquids in basaltic systems suggest that most Fe-rich immiscible liquids produced have approximately 30-40 wt % total Fe (Phillpots, 1982; Jakobsen et al. 2011), which is significantly lower than Fe-Ti oxide ore layers, implying that Ti-magnetite crystallising from these liquids would

still need to be concentrated into layers. Furthermore Fe-rich immiscible liquids are characterised by high P_2O_5 wt %, which results in the association of Ti-magnetite and apatite in proportions of approximately 2:1 (Philpotts, 1967). This model is generally applied to Kiruna-type deposits containing nelsonite. The upper parts of the Upper Zone of the Bushveld contain Fe-Ti oxide ore layers, which has up to 30 vol. % apatite (Reynolds, 1985b). In this case a mechanism involving Fe-rich immiscible liquids is more likely to stand up to scrutiny.

1.2 Previous work on the Panzhihua intrusion

The Panzhihua intrusion has been the subject of numerous recent studies. It is generally accepted that the Panzhihua parent magma was similar to the Emeishan high-Ti basalt (Zhou et al. 2005; Pang et al. 2008b; Ganino et al. 2008; Pang et al. 2010). Zhou et al. (2005) presented whole-rock major and trace element geochemical data for the Panzhihua intrusion in order to constrain the petrogenesis of the parent magma and the formation of large scale Fe-Ti oxide ore layers present at the base of the intrusion. Zhou et al (2005) interpreted the formation of Fe-Ti oxide ore layers to result from the separation of a Fe-immiscible liquid based on intrusive contacts of the ore layers with surrounding gabbroic rocks, poikilitic masses of Ti-magnetite enclosing silicate and distinct reaction textures of silicate in contact with Fe-Ti oxides.

Pang et al. (2008a; 2008b; 2009) presented a detailed series of studies concentrating on mineral compositional variation through the entire stratigraphy of the intrusion. Pang et al. (2008b) interpreted the formation of the Fe-Ti oxide ore layers as the result of early crystallisation of Ti-magnetite from ferrobasaltic magma. This interpretation is based on the presence of fine-grained inclusions of Cr-rich magnetite in cumulus olivine in the marginal zone rocks of the Panzhihua intrusion. This argument is further supported by MELTS modeling of Emeishan high-Ti basalt at relatively high H_2O content (> 1.5 wt %). Ganino et al. (2008) presented a model for the formation of the Fe-Ti oxide ore layers through the interaction of the magma with footwall carbonates and the subsequent increase in fO_2 related to CO_2 degassing. This argument is also supported by PELE modeling of a high-Ti Emeishan basalt at low H_2O content (0.5 wt %).

1.3 Scope of study and objectives

The current study presents new data for an entire section through the Panzhihua intrusion. Samples were collected in late 2009 during an excursion to the Emeishan LIP. Several intrusions, including Taihe, Xinjie and Baima, were visited but the Panzhihua intrusion was selected for further detailed study due to the accessibility of good outcrop within current open pit mining operations and road-

cuttings in the area. Samples were collected at regular intervals for the entire stratigraphy of the intrusion for petrographic, geochemical and mineral composition studies.

The main objectives of this study are: 1) Constrain the evolution of the parent magma en route from source to chamber, 2) Evolution of the magma within the chamber, 3) Timing of Fe-Ti oxide ore mineral crystallisation, 4) Interpret the mechanism for major consumption of silicate phases in the Fe-Ti oxide ore layers and 5) Present a petrogenetic model for the formation of Fe-Ti oxide ore layers at the Panzhihua intrusion.

Petrography: Petrographic analysis of all the samples is presented in order to constrain the timing of crystallisation of Fe-Ti oxide ore minerals. In particular comparison of Fe-Ti oxides within ore layers vs. gabbroic layers is described in detail. Distinct microtextural variations are observed with implications for the formation of Fe-Ti oxide ore layers. Furthermore silicate disequilibrium textures within the ore layers are also observed and described, which have further implications for Fe-Ti oxide ore layer formation.

Mineral chemistry: Compositional data for silicates and Fe-Ti oxides are presented for the lower half of the intrusion only, as previous studies (Pang et al. 2008a; Pang et al. 2009) have presented full sequences for the intrusion and I do not intend to repeat previous work. I concentrate on the variation of the composition of silicates/oxides within ore layers vs. gabbroic rocks. Furthermore I present the first compositional data for a section of samples through the main ore layer. I also present detailed compositional data for distinct reaction rims observed surrounding silicates within the Fe-Ti oxide ore layers.

Whole-rock major and trace element geochemistry: Whole-rock major and trace element geochemistry is presented for a full sequence of the Panzhihua intrusion in order to constrain the evolution of the magma within the chamber and for general characterisation of the stratigraphy of the intrusion. REE data is presented for the lower half of the intrusion only and used to constrain the evolution of the parent magma from source to chamber.

Whole-rock Sr-Nd isotope geochemistry: Sr-Nd isotopes were analysed to evaluate the parent magma source and potential for crustal contamination of the parent magma due to significant interaction with the footwall rocks. Furthermore I present the first detailed isotope data for the main Fe-Ti oxide ore layer in order to further constrain the formation of Fe-Ti oxide layers.

PGE geochemistry: The Panzhihua intrusion does not contain PGE-enriched horizons and PGE data is presented here for the lower half on the intrusion as a petrogenetic tool. PGE data is used to further evaluate the evolution of the parent magma from source to chamber.

PELE modeling of ferrobasaltic parent magma: In order to constrain the crystallisation sequence, evolution of crystallising phases and the evolution of the magma during differentiation, I present data from PELE modeling of Emeishan ferrobasaltic compositions at various fO_2 and H_2O conditions. Significant variations are observed, which have significant implications for the H_2O content of the parent magma, the formation of Fe-Ti oxide ore layers and the evolution of the magma within the chamber.

2. Regional geology and the Panzhihua intrusion

2.1 Emeishan Large Igneous Province (ELIP)

The ELIP is located on the western margin of the Yangtze Craton, SW China (Figure 2.1). It is generally accepted that the ELIP was formed in a rift setting through mantle plume activity (e.g. Chung and Jahn, 1995; Dmitriev and Bogatikov, 1996). There has been a significant amount of work on the ELIP since the early 2000's covering a range of topics and rock types including: source characteristics, parent magma composition, metallogenesis, classification of basalts, geochronology and related mass extinction events to name a few. The ELIP can be divided into two components: a) flood basalts and 2) mafic-ultramafic layered intrusions.

2.1.1 Aerial extent and volume

Size estimation of the ELIP is difficult due to extensive erosion, significant buried portions and structural complexity. The main outcrop area is estimated at approximately $2.5x10^5$ km^2 – $3.3x10^5$ km^2 (Wignall, 2001 and Ali et al. 2005; Figure 2.1), although additional sub-surface basalts are know from drilling in the Sichuan Basin to the NE and the Red River Fault displaced fragments in southern China and northern Vietnam (Xiao et al. 2003). Xu et al. (2001) assumed an average thickness of 700 m for the flood basalts and estimated the volume of the province at $0.3x10^6$ km^3. This is a minimum estimate owing to an unknown amount of erosion and the layered intrusions have not been taken into account. The ELIP is relatively small compared with other Permian and younger LIPs such as the Siberian Traps ($2 x10^6$ km^3) and the Karoo flood basalts ($2.5x10^6$ km^3) (Wignall, 2001).

2.1.2 Stratigraphy

The ELIP flood basalts unconformably overly an extensive limestone unit of the late Middle Permian Maokou Formation. The volcanic sequences of the ELIP vary substantially in composition and thickness across the outcrop area. The northern and eastern regions are characterised by compositionally uniform tholeiitic to alkaline basalt (Xu et al. 2001). Sequences of basalt flows range in thickness from 170-600 m (Ali et al. 2005). The central and western regions of the ELIP are characterised by a variety of volcanic rocks including: basalt, basaltic andesite, picrite, rhyolite-trachyte and basaltic pyroclastics (Xu et al. 2001; Xu et al. 2003). The volcanic sequences in these areas are significantly thicker, 1-2 km thick, with a maximum thickness of 5336 m in the Binchuan

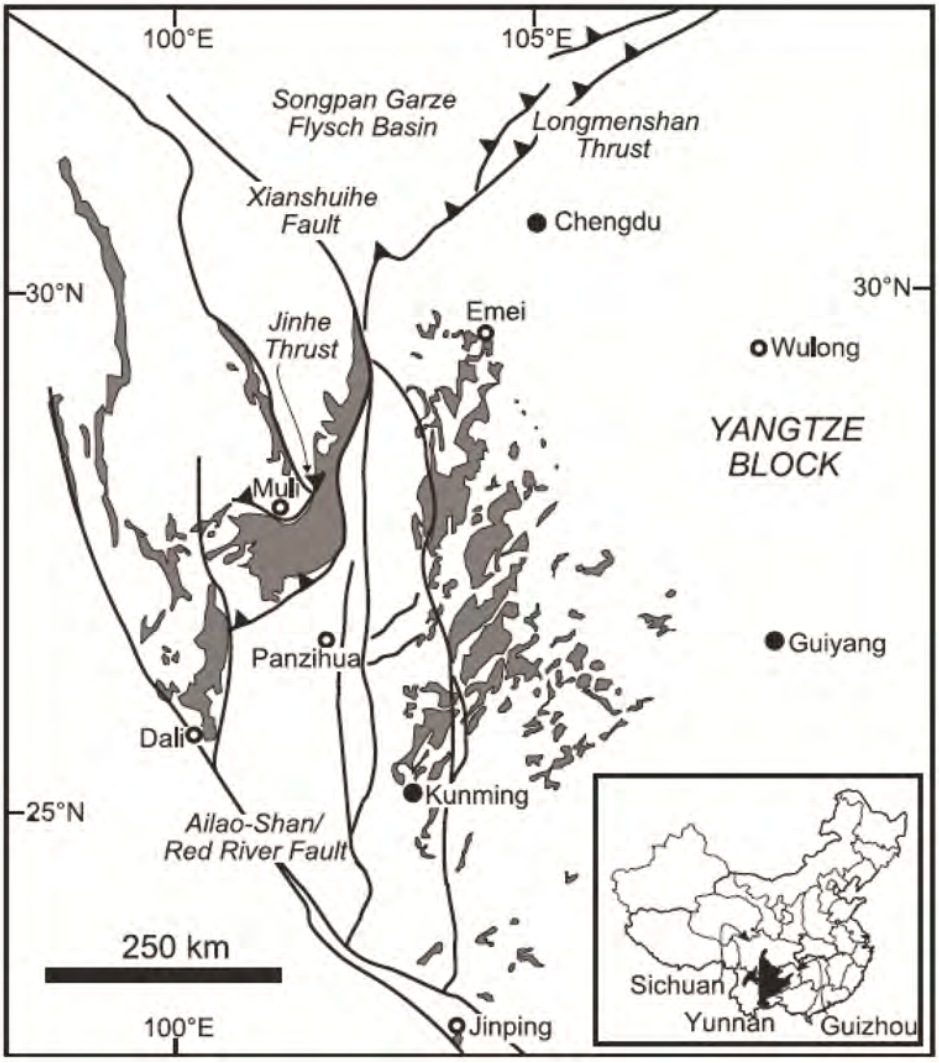

Figure 2.1 Overview of the aerial extent of the Emeishan Large Igneous Province (Figure after Ali et al. 2005).

section (Xu et al. 2004). The mafic volcanic and pyroclastic rocks are generally inter-layered throughout the sequences with the more evolved rhyolitic rocks at the top.

2.1.3 Age of province

The recent temporal link of the extrusion of flood basalts related to the ELIP and the end-Guadalupian mass extinction event (Zhou et al. 2002) has led to a series of studies reporting detailed geochronology for the ELIP. Wignall (2001) showed that extinction events linked to the extrusion of flood basalts are only observed where the underlying lithologies are carbonates, which is the case for the ELIP. Major release of greenhouse gases associated with metamorphism of the carbonates is linked to these mass extinction events. Zhou et al. (2002) first established a reliable age of 259 (+/-

3) Ma for the Xinjie intrusion, which is interpreted to represent the main stage of Emeishan volcanism and more recently other intrusions have been dated: olivine gabbroic dyke near Panzhihua intrusion – 262 (+/- 2) Ma (Guo et al. 2004), Hongge intrusion – 259 (+/- 1) Ma (Zhong and Zhu, 2006) and the Baimazhai intrusion – 259 (+/- 3) Ma (Wang et al. 2006). The Panzhihua intrusion is dated at 263 (+/- 3) Ma (Zhou et al. 2005). He et al. (2007) report an age of 263 (+/- 4) Ma for silicic ignimbrite in the upper part of the volcanic succession, implying an end to the volcanism at this time. Detrital zircons from the overlying clastic sedimentary Xuanwei Formation, which are interpreted to be sourced from Emeishan felsic extrusives, yield similar ages of 257 (+/- 3) Ma and 260 (+/- 5) Ma (He et al. 2007). These ages represent the termination of Emeishan volcanism and are indistinguishable from those of the intrusions (i. e. main stage of volcanism) and imply a very short duration of Emeishan volcanism.

2.2 Flood basalt chemistry

The Emeishan flood lavas vary in composition as described above. I present here a review of the mafic basaltic and picritic lavas. The Emeishan basaltic lavas can be divided into two groups: high-Ti and low-Ti basalts (Xu et al. 2001; Xiao et al. 2004). This discrimination is based on Ti/Y ratios where high-Ti > 500 and low-Ti < 500 (Xu et al. 2001). The high-Ti basalt generally has TiO_2 > 3.5 wt % whereas the low-Ti basalt generally has TiO_2 < 1.5 wt % (Xiao et al. 2004). There are some more subtle variations in trace element composition, PGE abundance and radiogenic isotope ratios, which are reviewed below. The picritic lavas are far less abundant but represent the most primitive lavas within the sequences and are including in reviews below.

2.2.1 Trace element and Sr-Nd isotope variation

Trace element and Sr-Nd isotopic variation is reviewed here with specific reference to elements and profiles used in later discussions on the Panzhihua intrusion. In particular V and Cr, which are highly compatible in spinel, are reviewed as they have implications for parent magma evolution and ore forming processes.

Elements compatible in Ti-magnetite of importance such as V and Cr show some notable variation. Low-Ti basalts have a range in concentration of 280-406 ppm V and 25-509 ppm Cr (average of 236 ppm) (Xiao et al. 2004). High-Ti basalt have ranges of 190-414 ppm V and significantly lower Cr; 18-

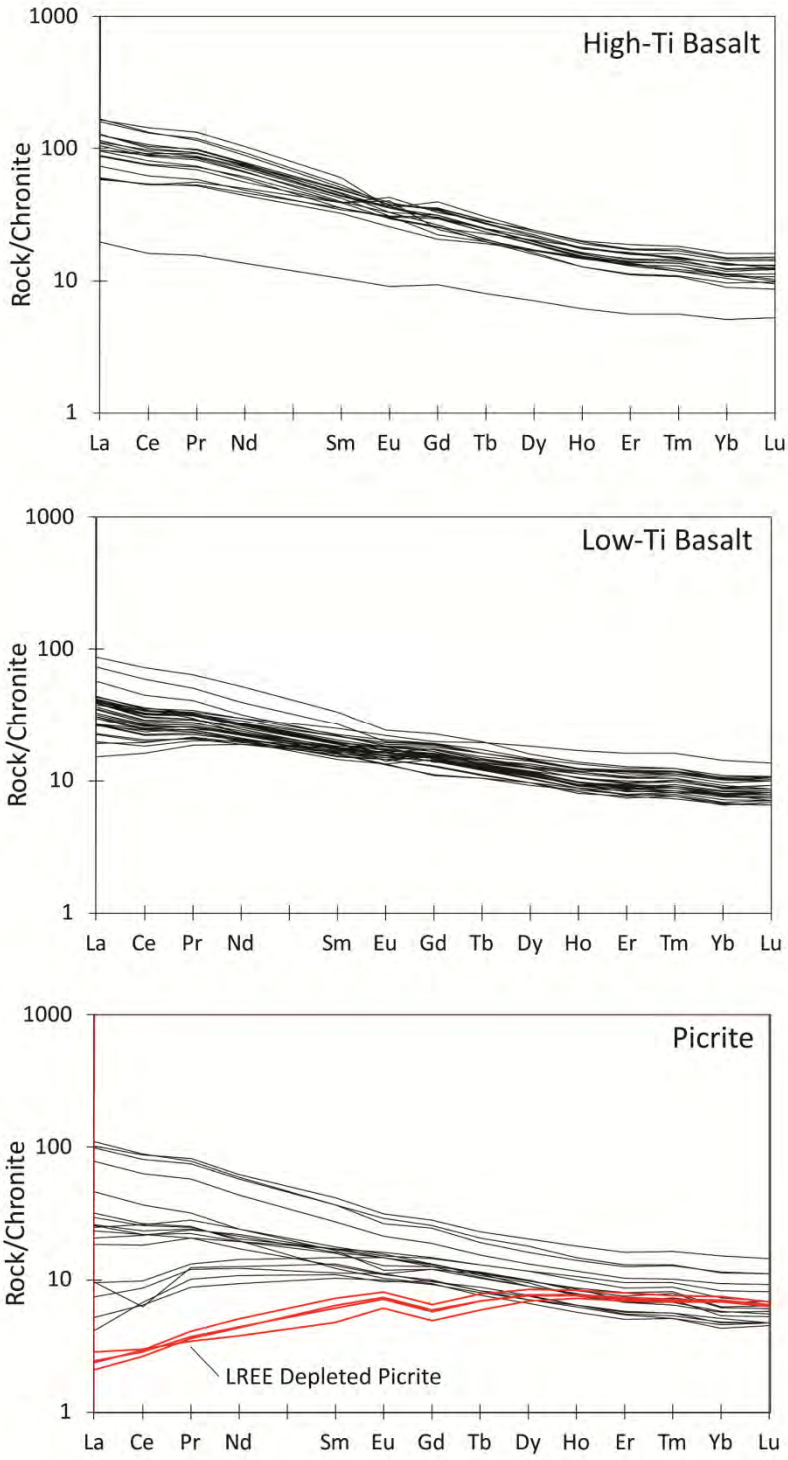

Figure 2.2 Chondrite-normalised REE profiles for the Emeishan high-Ti basalt, low-Ti basalt and picrite. LREE depleted picrite highlighted in blue. High-Ti and low-Ti basalt data from Xiao et al. (2004) and Wang et al. (2007). Picrite data from Li et al. (2010) and LREE depleted picrites data from Wang et al. (2007).

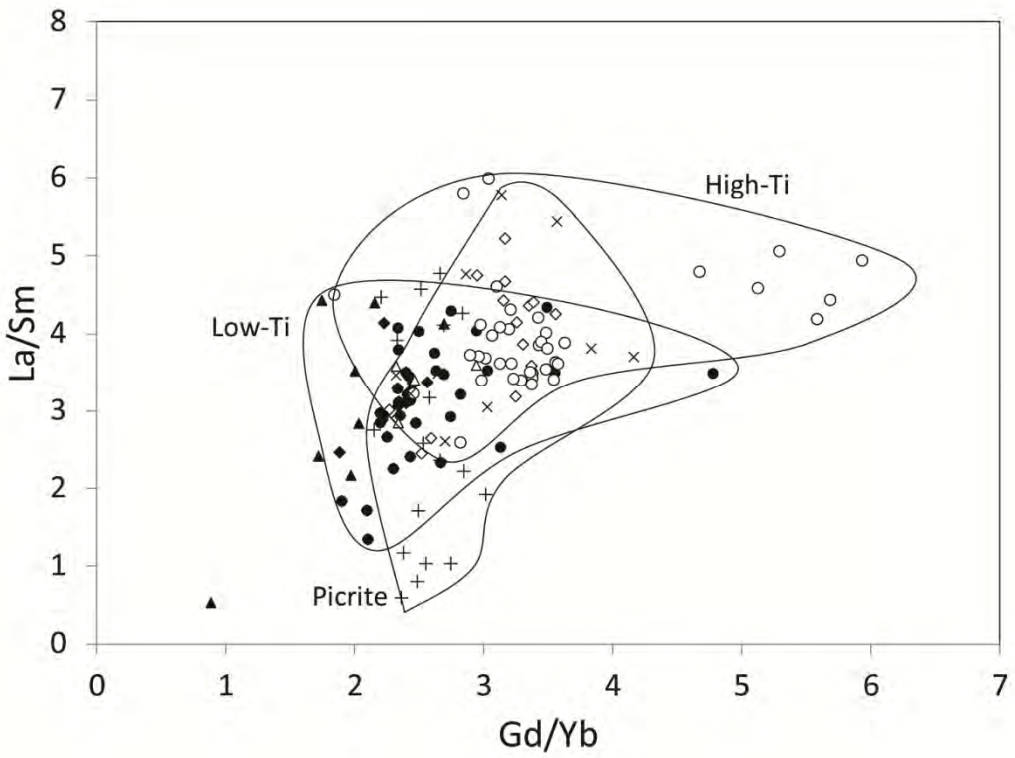

Figure 2.3 La/Sm vs. Gd/Yb for the Emeishan high-Ti basalt, low-Ti basalt and picrite. Data for high-Ti basalt (open symbols) and low-Ti basalt (solid symbols) from Xiao et al. (2004) and Wang et al. (2007. Picrite (plus symbols) data from Li et al. (2010) and X symbols are data from Zhang et al. (2006).

106 ppm (Xiao et al. 2004). Picrite have a similar concentration of V; 223-347 ppm but a significantly higher range in Cr concentration; average of 1260 ppm (Li et al. 2010). Chondrite-normalised REE profiles for the basalts and picrites clearly show variation (Figure 2.2). High-Ti basalts are more enriched in REEs relative to the low-Ti basalt. La/Sm and Gd/Yb ratios show some overlap (Figure 2.3) but high-Ti basalt show slightly higher ratios for both La/Sm and Gd/Yb. Wang et al. (2007) classified picrites from the Son Da region (Northern Vietnam) as LREE depleted (Figure 2.2). The variation of picrite La/Sm spans both the high-Ti and low-Ti range whereas the Gd/Yb ratio for the picrite lavas is more constrained ranging from 2-3 (Figure 2.3).

Primitive mantle-normalised trace element diagrams show that all samples, apart from several low-Ti basalts, have distinct negative Sr anomalies as well as negative K anomalies (Figure 2.4). Picrite samples how a large variation.

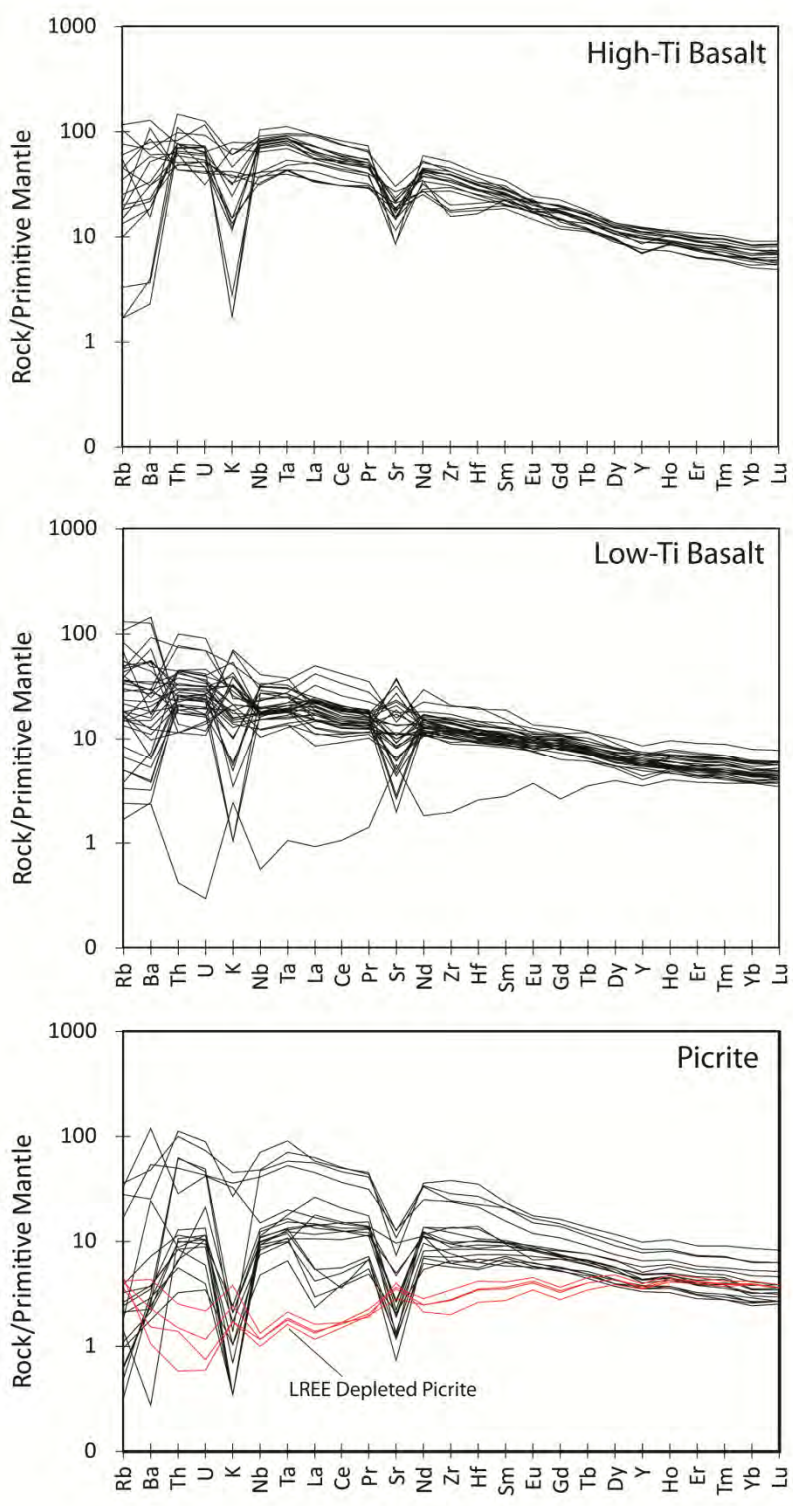

Figure 2.4 Primitive mantle-normalised extended trace element diagrams for the Emeishan basalts and picrites. LREE depleted picrites highlighted in blue. Data for basalts from Xiao et al. (2004) and Wang et al. (2007). Picrite data from Li et al. (2010) and LREE depleted picrites data from Wang et al. (2007).

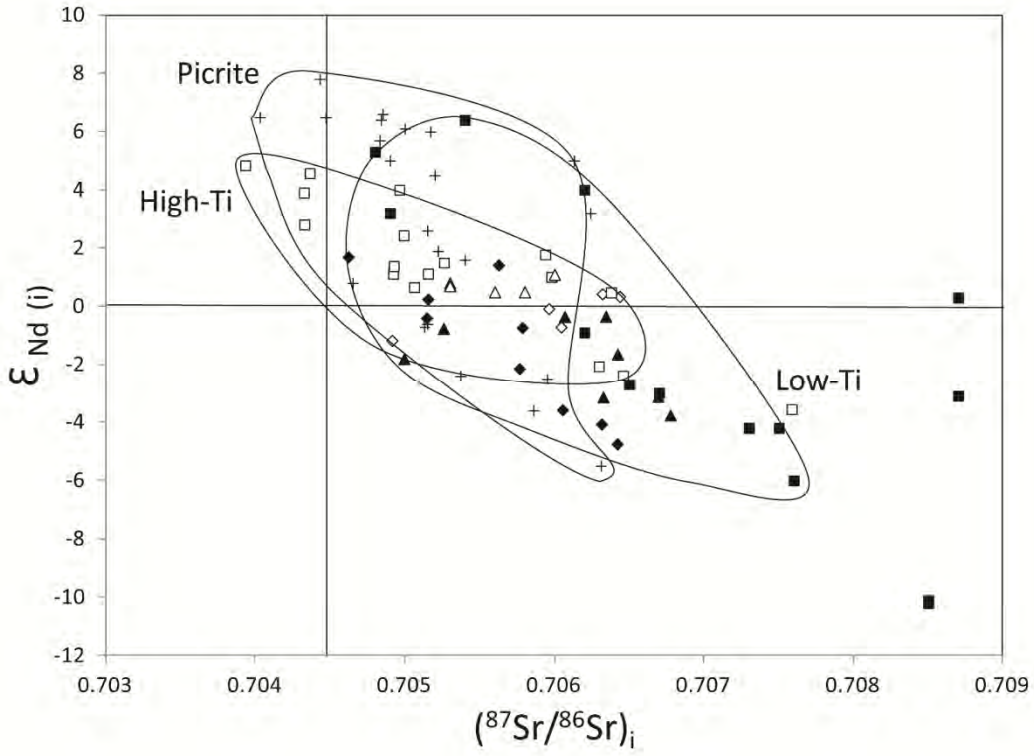

Figure 2.5 Sr-Nd isotopic variations for the Emeishan basalts and picrite. High-Ti basalt (open symbols) and Low-Ti basalt (solid symbols) data from Xu et al. (2001), Xiao et al. (2004) and Wang et al. (2007). Picrite (plus symbols) data from Zhang et al. (2006) and Li et al. (2010).

There is significant overlap in Sr-Nd isotopic ratios (Figure 2.5). Generally the high-Ti basalt and picrite have low $^{87}Sr/^{86}Sr$ and high εNd_i. The low-Ti basalts show high $^{87}Sr/^{86}Sr$ and low εNd_i. This has been interpreted to indicate up to 25 % contamination of the low-Ti basalt by middle to upper crustal material (Wang et al. 2007).

2.2.2 PGE abundance

The total PGE abundance of the low-Ti basalts varies substantially from PGE depleted low-Ti basalts with total PGE of < 5 ppb to PGE undepleted low-Ti basalts with total PGEs up to 23 ppb (Song et al. 2009). The high-Ti basalts are generally undepleted with total PGE abundance of > 20 ppb (Song et al. 2009). Picrites have total PGE abundance > 20 ppb (Wang et al. 2007; Li et al. 2012). Pt and Pd generally show positive correlation with MgO (wt %) and Cr (ppm). Cu/Pd ratios for PGE depleted basalts are high (> 10000) implying a sulphide control on PGE depletion (Song et al. 2009). Pd/Pt

ratios are generally within the mantle range of 0.6 but may be as high as 3.5 implying a mafic silicate control on Pt variation in certain cases (Song et al. 2009) (Discussed further in section 8).

2.3 Mafic-ultramafic layered intrusions

Layered intrusions within the ELIP have been divided into two end member types: a) Ni-Cu-PGE-bearing ultramafic-mafic intrusions and b) Fe-Ti oxide ore-bearing mafic intrusions (Zhou et al. 2008; Zhang et al. 2009). These are end members with several intrusions containing features intermediate between the two (e.g. Xinjie). The intrusions are generally exposed along north-south striking faults and form a 400 km long belt from Mianning in the north through Xichang and Miyi in the centre of the Sichuan Province and through Panzhihua to Mouding in the south in the Yunnan Province (Figure 2.6).

2.3.1 Ni-Cu-PGE-bearing ultramafic-mafic intrusions

Ultramafic-mafic intrusions are small relative to the Fe-Ti oxide mafic intrusions (Figure 2.6); for example the Jinbaoshan intrusion is approximately 150 m thick, 5 km wide and 1 km in width (Tao et al. 2007). The Limahe intrusion is one of the largest and is 1.2 km thick extends 7.5 km along strike and is 1.5 km in width (Zhang et al. 2009). Other important ultramafic-mafic intrusions include Yangliuping and Baimazhai (described in Song et al. 2003 and Wang et al. 2006 respectively). These intrusions are dominantly ultramafic composition and contain Ni-Cu-PGE sulphide ore bodies. They are characterised by enriched Sr-Nd isotopic ratios; e.g. Limahe intrusion: $(^{87}Sr/^{86}Sr)_i$ - > 0.708 and εNd_i - < 0.8 (Zhang et al. 2009). This is more similar to that of the low-Ti basalt and on this basis the parent magmas for the ultramafic-mafic intrusions has been interpreted to be low-Ti basalt (Zhou et al. 2008).

2.3.2 Fe-Ti oxide ore-bearing mafic intrusions

The Fe-Ti oxide ore-bearing intrusions range in composition and are general significantly larger in size relative to the ultramafic-mafic sills (Figure 2.6). Figure 2.7 presents the general stratigraphy for several of the important Fe-Ti oxide ore-bearing intrusions. The Panzhihua and Baima intrusions are the largest within the Emeishan and are mafic only with no ultramafic basal portion (Figure 2.7). The Hongge and Xinjie intrusions contain major Fe-Ti oxide ore layers but also contain significant

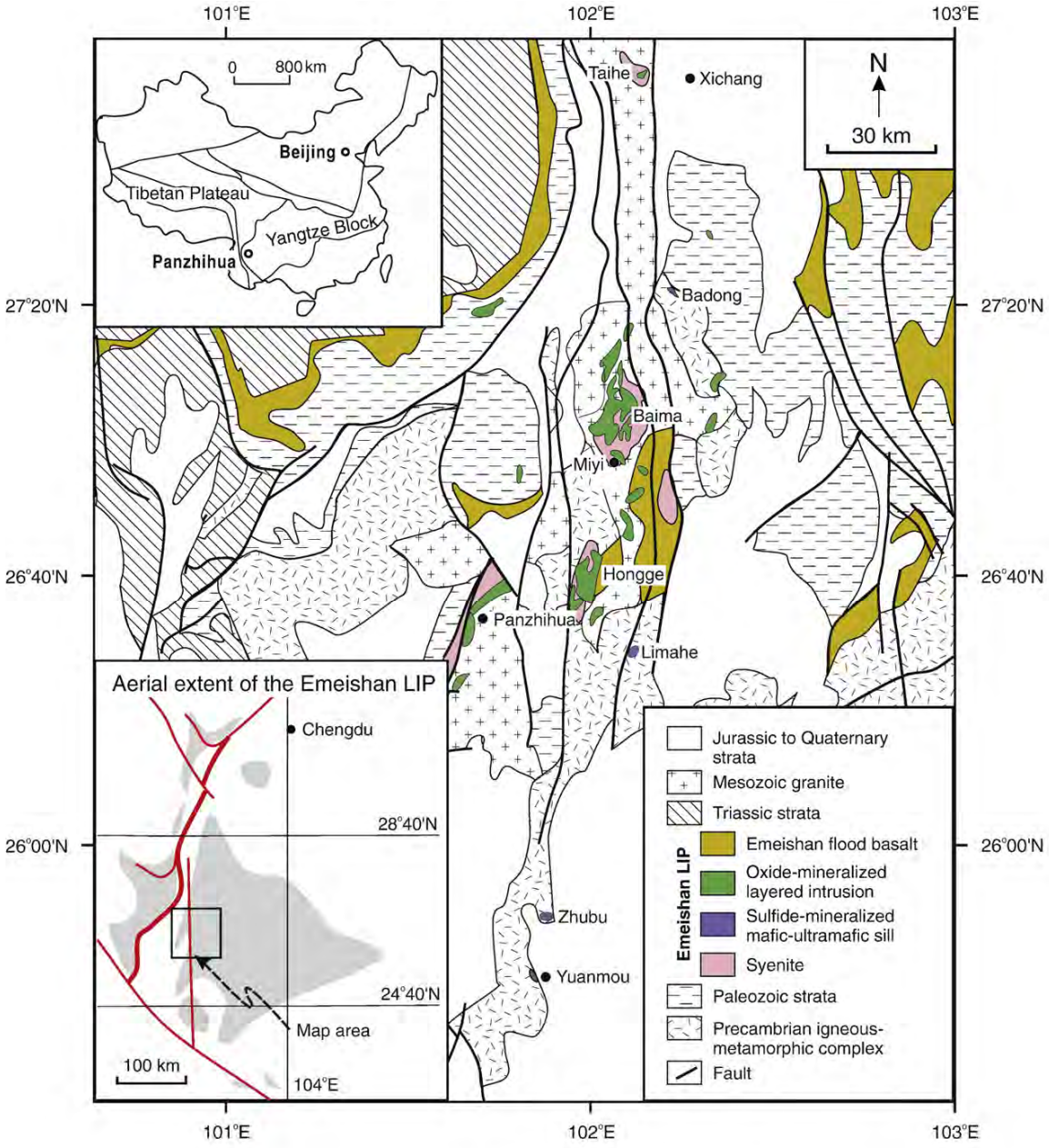

Figure 2.6 Geological map of the PANXI region, SW China, showing the distribution of the layered intrusion within the region. Figure from Pang et al. (2009).

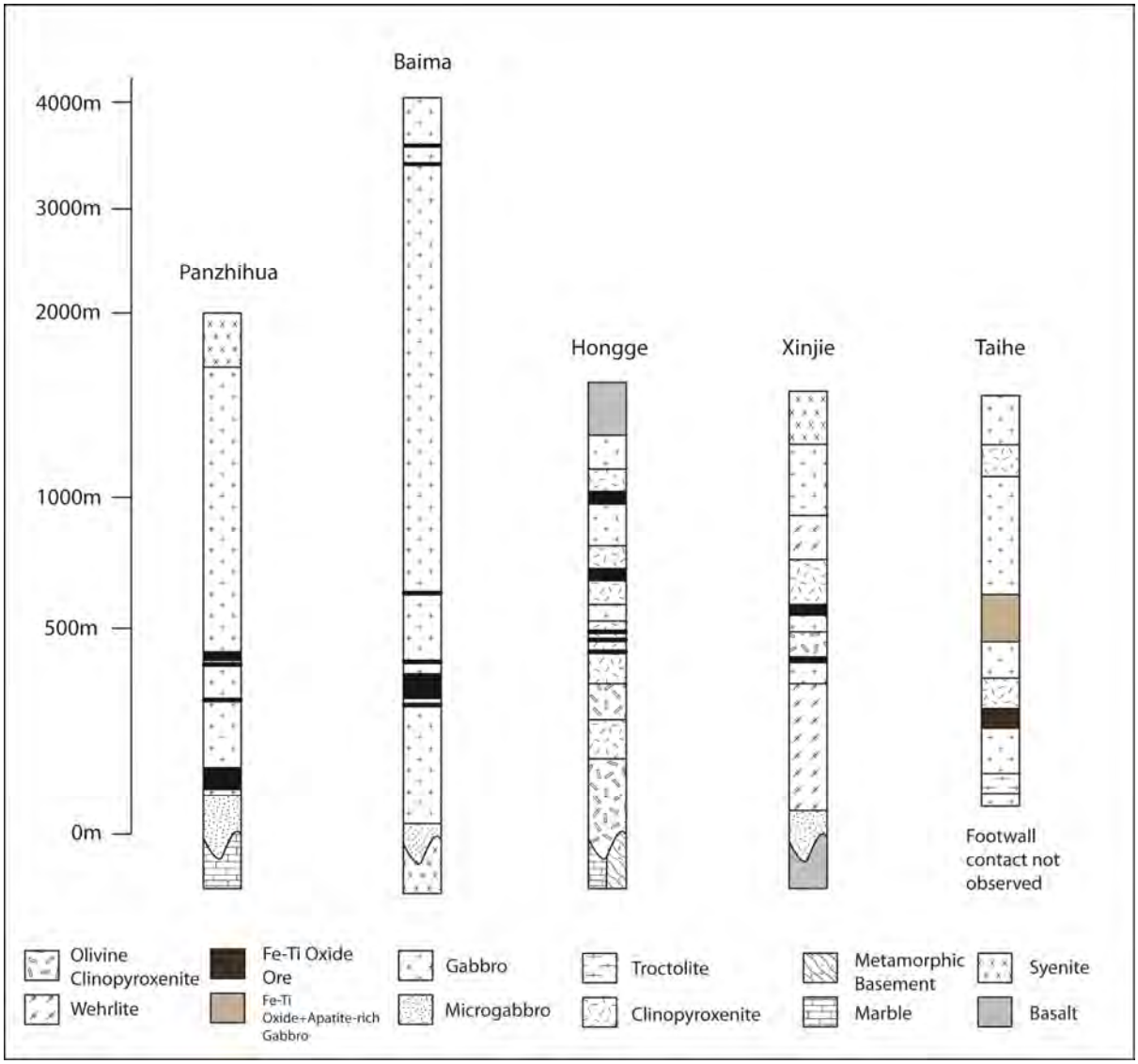

Figure 2.7 Stratigraphy of the Panzhihua, Baima, Hongge and Xinjie intrusions. Modified after Pang et al. (2010) and Hou et al. (2012).

portions of ultramafic rocks. In these latter cases the Fe-Ti oxide ores are hosted in the middle to upper parts of the intrusion (Figure 2.7). In the former case the Fe-Ti oxide ores are hosted toward the base of the intrusion and may be up to 60-80 m in thickness (Figure 2.7). The Taihe intrusion is dominated by gabbroic rocks with minor ultramafics, with Fe-Ti oxide ore layers in the lower half. The important feature of the Taihe intrusion is the association of Fe-Ti oxides and apatite within one distinct horizon (Figure 2.7), although apatite is not ubiquitous with ore layers of the Taihe intrusion (Hou et al 2012). The intrusions are hosted in a variety of local country rock settings with footwall rocks of limestone, syenite, coeval Emeishan basalt and metamorphic basement. Fe-Ti oxide ore-bearing intrusions are temporally and spatially generally associated with syenitic complexes

emplaced above the mafic intrusions. Shellnutt and Jahn (2010) present a model showing a plutonic-hypabyssal volcanic system linking the Panzhihua mafic intrusion with the spatially associated syenitic pluton.

The Panzhihua intrusion contains a massive Fe-Ti oxide ore layer at the base with a reserve of 1333 Mt, which has been mined for several decades at a grade of 43 wt % FeO, 12 wt % TiO_2 and 0.3 wt % V_2O_5 (Ma et al. 2003). The Hongge and Baima intrusions have only recently been exploited and contain ore reserves of 4272 Mt and 1497 Mt respectively (Ma et al. 2003).

2.4 Geology of the Panzhihua intrusion

The Panzhihua intrusion was first described by Zhou et al. (2005) and more recently by Pang et al. (2008a), Pang et al. (2008b), Ganino et al. (2008), Pang et al. (2009) and Pang et al. (2010). It is a sill-like body dipping at 35-65^{o} to the NW (Pang et al. 2009), ranging in thickness 1400-3000 m, extending for 19 km along strike (NE-SW) and has an outcrop area of approximately 30 km^2 (Zhou et al. 2005). The intrusion can be divided into six distinct fault controlled blocks, from north to south: Zujiabaobao, Lanjiahuoshan, Jianshan, Daomakan, Gongshan and Nalaqing (Figure 2.8). It intruded dolomitic limestone's of the Late Neoproterozoic Dengying Formation (up to 800 m thick in the Panzhihua region) and formed a contact metamorphic aureole more than 300 m thick (Ganino et al. 2008). Preservation textures within the limestone indicate relatively shallow burial equivalent to 2 kb (Ganino et al. 2008). The limestone has been metamorphosed to marbles and skarns. Near the intrusion the limestone has been metamorphosed to marbles containing brucite, forsterite, diopside and other silicates, the dominant rock type within the aureole is a homogenous white marble containing very low proportions (1 vol. %) of silicates but up to 40 vol. % brucite (Ganino et al. 2008). Rocks at the immediate contact of the footwall and intrusion are characterised by high hornblende content, which may be as much as 95 vol. % (Pang et al. 2009). The roof contact of the intrusion is not exposed but has been mapped as a thrust against coeval syenitic rocks (Pang et al. 2009). Both the mafic intrusion and associated syenitic pluton are unconformably overlain by Triassic clastic sediments.

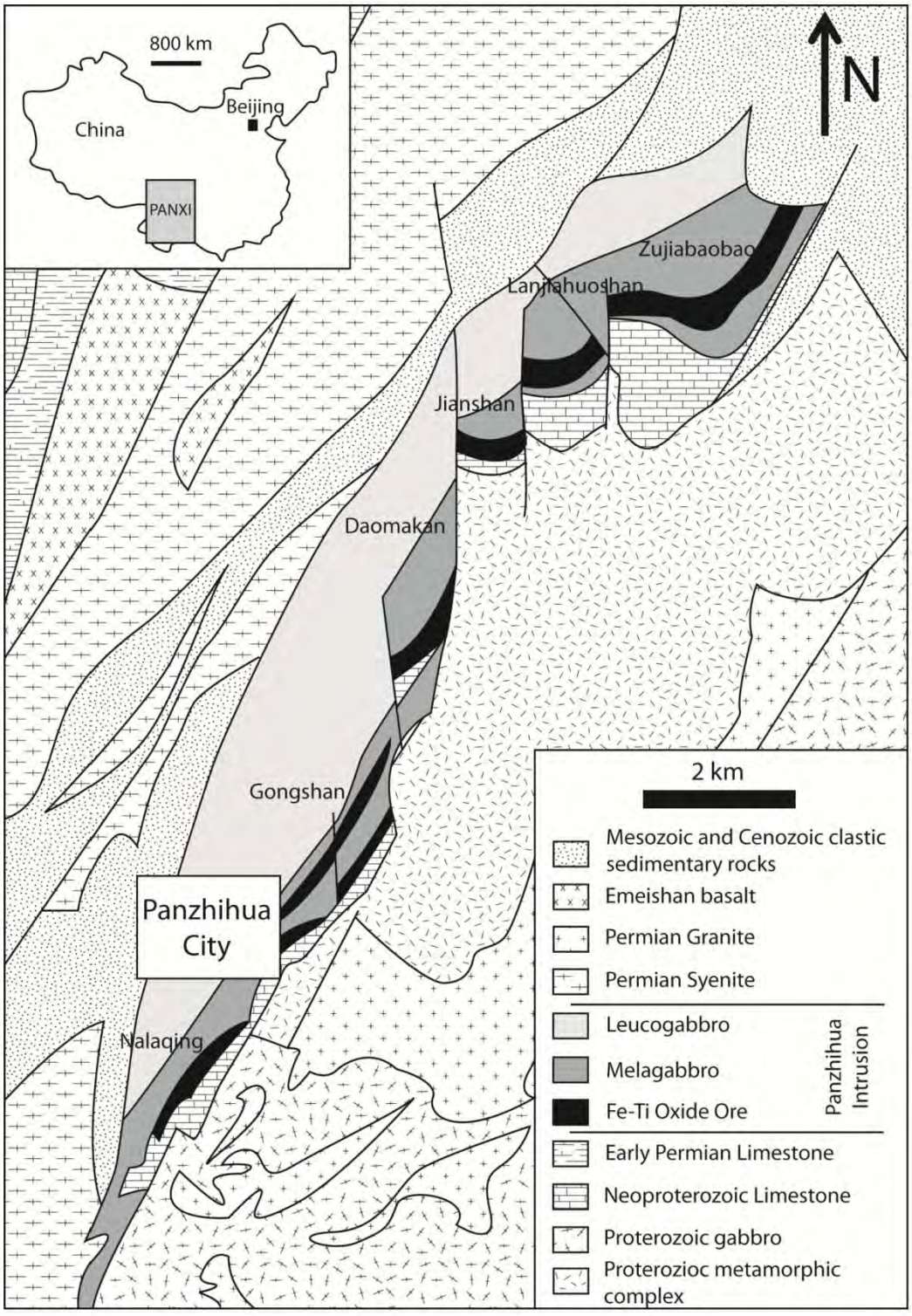

Figure 2.8 Geological map of the Panzhihua intrusion. Modified after Pang et al. (2009).

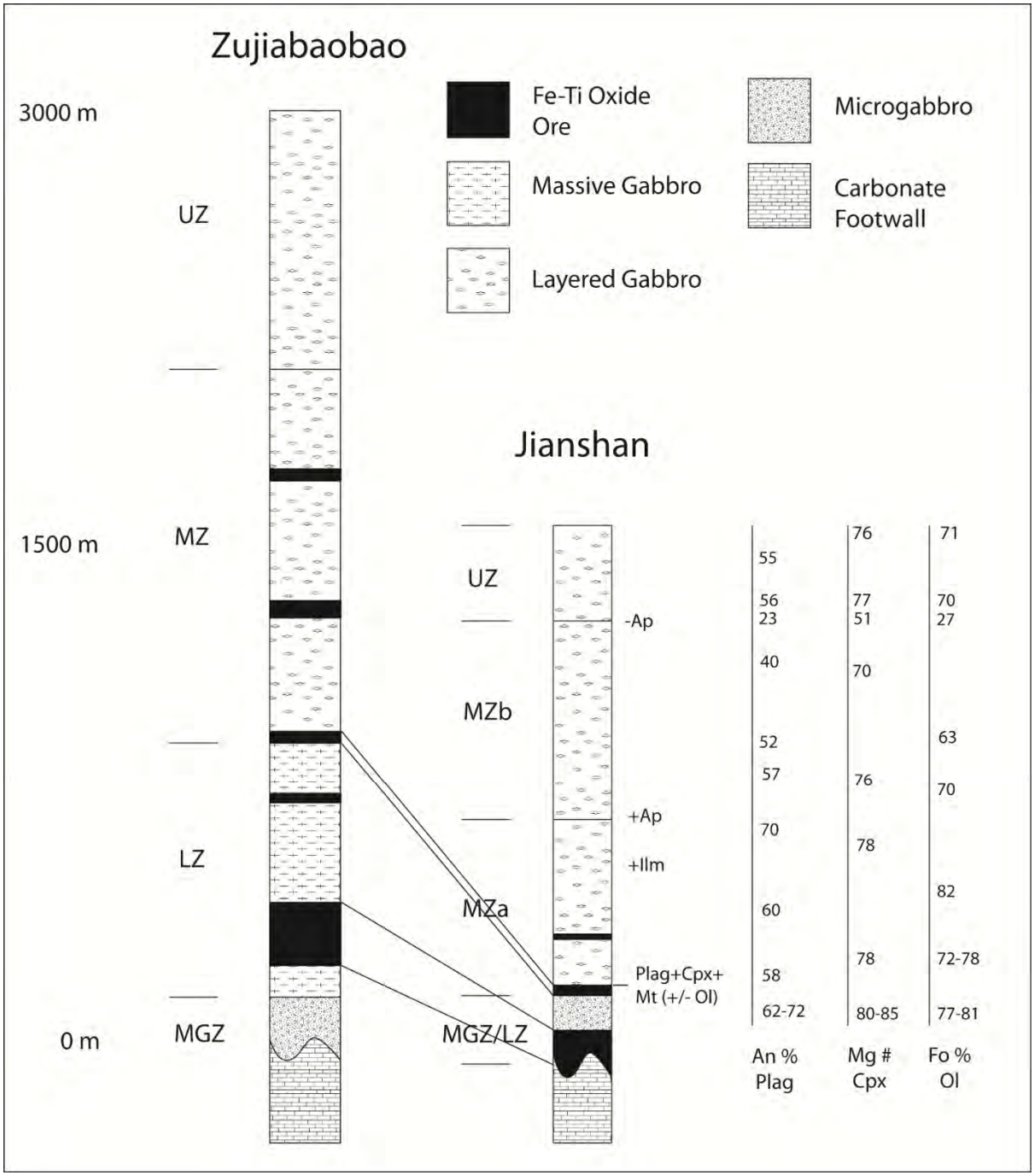

Figure 2.9 Stratigraphy of the Zujiabaobao and Jianshan Blocks, Panzhihua intrusion. Stratigraphy from Zhou et al. (2005), Pang et al. (2009) and this study. Mineral compositions summarised here are from Pang et al. (2009).

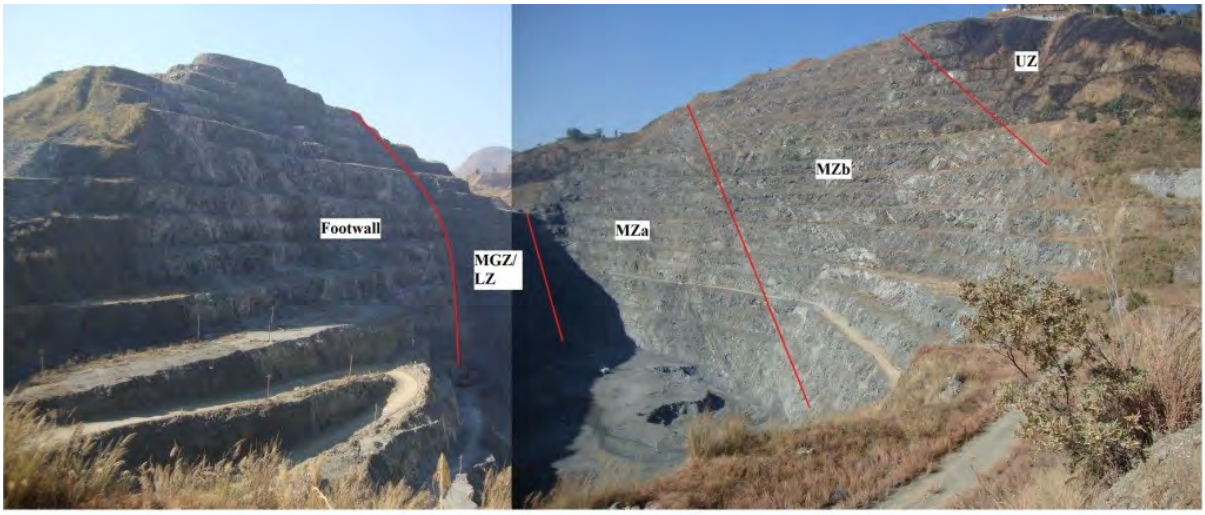

Figure 2.10 Photograph of the Jianshan Block open pit highlighting the different zones.

2.4.1 Stratigraphy

The Panzhihua intrusion has been divided from the base upward into five stratigraphic zones: Marginal Zone (MGZ), Lower Zone (LZ), Middle Zone A (MZa), Middle Zone B (MZb) and the Upper Zone (UZ) (Figure 2.9). The stratigraphy is also show in Figure 2.10 of the Jianshan block open pit sampling site.

The MGZ is the basal zone of the intrusion and is dominated by fine-grained hornblende-bearing gabbro. This zone has been interpreted as the chilled base of the intrusion (Pang et al. 2008a). The MGZ is typically heterogeneous and ranges in thickness from 0-40m. The LZ is characterised by coarse grained, massive gabbros, which are typically rich in Fe-Ti oxides. Local pegmatoidal facies are also common, which are typically absent from the MZ and UZ. The LZ ranges in thickness from 0-110 m and Fe-Ti oxide layers reach up to 60 m thickness. The MZ contains similar Fe-Ti oxide-rich gabbros but have a medium grain size. Furthermore this zone is characterised by the development of rhythmic layering. The layers form alternating melanocratic and leucocratic bands, which range in size from a few cm up to several m. Magmatic foliation is noted through the alignment of plagioclase grains along their long axis. The MZ reaches up to 800 m thickness and is divided into two sub-zones based on the presence of cumulus apatite. The UZ is characterised by the absence of apatite and leucogabbros with minor olivine gabbro, olivine clinopyroxenite and anorthosite. The UZ ranges in thickness from 500-1500m. The stratigraphy is somewhat compressed within the Jianshan Block

relative to the northern Zujiabaobao Block (Figure 2.8). In particular the MGZ and LZ are compressed into a single heterogeneous zone of mixed characteristics (MGZ/LZ) in the Jianshan Block.

3. Sampling

The Panzhihua intrusion outcrops over a horizontal distance of approximately 16 km. The Jianshan Block was chosen for detailed sampling due to availability of outcrop as well as to compliment the previous study of Pang (2008). Approximately 75% of the Panzhihua intrusion stratigraphy outcrops in the Jianshan open pit with the remainder outcropping in road-cuttings to the north of the open pit (Figure 3.1). The bulk of the sampling for this study has been done within the Jianshan open pit at three sample site transects. A further two sample transects were done to the north of the open pit along road-cuttings. The Nalaqing Block at the southern end of the intrusion was also visited during this study and very fresh outcrop of the main Fe-Ti oxide ore body was observed. The main ore body was sampled at Nalaqing for comparison with the Jianshan ore body. GPS data for the sample sites are given in Appendix A. Figure 3.1 and 3.2 show the locations of the main sample sites at the Jianshan block.

3.1 Jianshan Block open pit

Sampling transects were done at three sites within the Jianshan open pit: 1) At the base of the pit through the main Fe-Ti oxide ore body; 2) Bench transect and 3) Look-out road transect (Figure 3.2 and 3.3). Firstly, the main ore body was exposed at the base of the Jianshan pit and allowed for a detailed sample transect across the ore body. Ten samples (05-1 - 05-10) were taken across the main ore body at 1-8 m intervals (Figure 3.2; Mag. ore body transect).

The bench chosen for sampling was an active bench, where two addits are being developed for underground mining purposes. Sampling was started at the base of the intrusion and moved upward in stratigraphy. This bench transect (Figure 3.2 and 3.3) covers the stratigraphy from above the main Fe-Ti oxide ore layer in the MGZ/LZ to the top of the MZa zone. 60 samples were taken at 10 m intervals (BT-01 to BT-55; Appendix B). Detailed sampling was done over smaller intervals where Fe-Ti oxide ore layers were observed. The bench is oriented at 45^{o} to the strike of the intrusion and 10 m intervals for sampling does not equal 10m upward in stratigraphy. Recalculation of the stratigraphic heights was done for the samples and presented in Appendix B along with the geochemistry.

The third sample transect was done on an upper bench, which has been converted into an entrance road (look-out road; Figure 3.2 and 3.3). Sampling was done from the upper stratigraphy downward

Figure 3.1 Google Earth image showing the Zujiabaobao, Lanjiahuoshan and Jianshan Blocks, Panzhihua intrusion with the location of sample sites for this study.

Figure 3.2 Google Earth image of the Jianshan Open Pit with locations of sampling transect for the open pit.

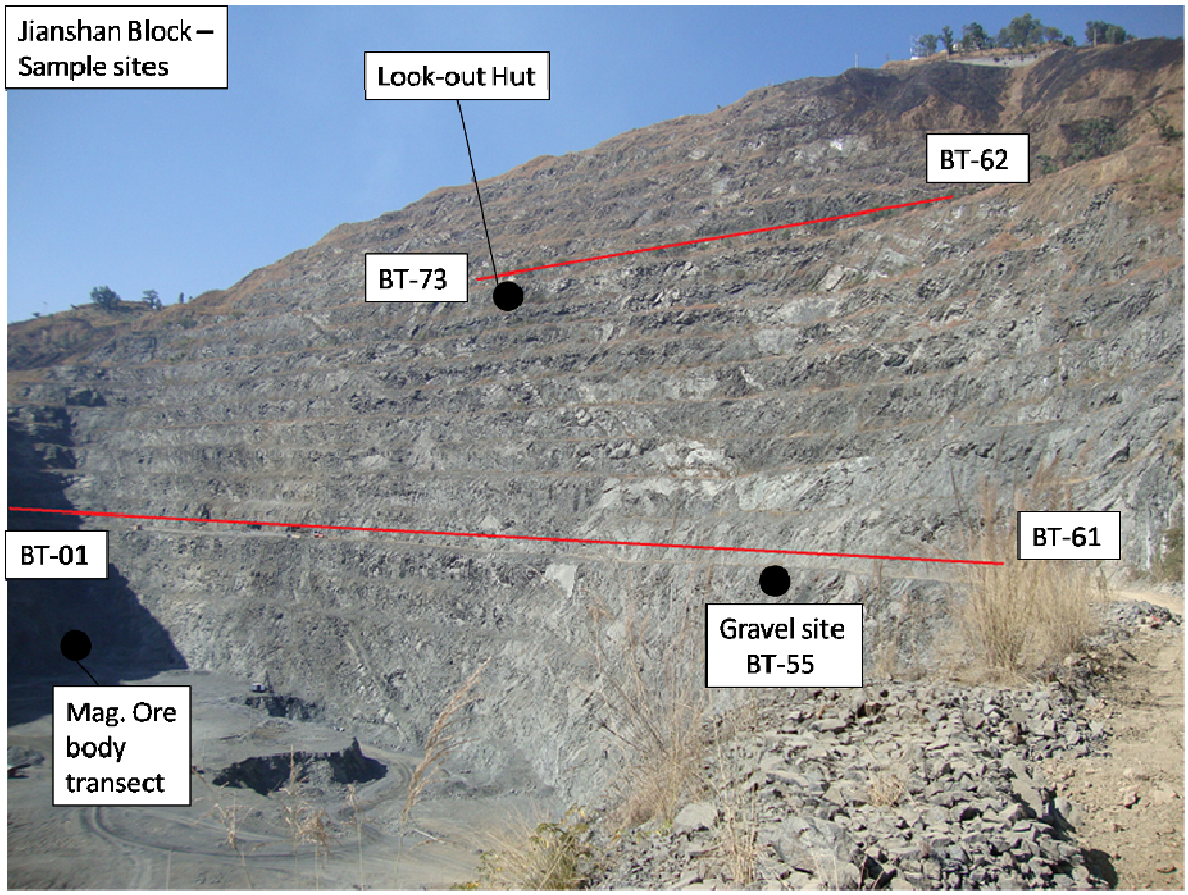

Figure 3.3 Photograph showing the location of sample transects and sample numbers for the Jianshan Open Pit. BT-01 represents the 'bench transect start' shown in Figure 3.2.

as indicated by the sample numbers in Figure 3.3. 11 samples were taken from this level. The look-out road transect is essentially the MZb zone of the intrusion.

3.2 Jianshan Block road cut sites

The upper zone of the intrusion was not exposed in the Jianshan open pit and was sampled along road cuttings to the north of the open pit (Figure 3.1 and 3.4; Road cut Sites 1-8). The main road cut transect extended from the top of the intrusion at road cut site 1 (Figure 3.4) southwards/downward in stratigraphy to road cut site 8. A second transect was done to the east of road cut site 8, labelled PH-RC-samples (Figure 3.4). 11 samples were collected between road cut sites 1-8 (UZ-01 – UZ-11) and a further 11 samples were collected from the PH-RC sample transect (Figure 3.4).

Figure 3.4 Google Earth Image showing the location of sample sites along road-cuttings for the UZ of the Jianshan Block, Panzhihua intrusion.

3.3 Nalaqing Block outcrops

The southern Nalaqing Block of the Panzhihua intrusion was also visited and excellent outcrop of the main Fe-Ti oxide ore layer was observed. Detailed sampling was conducted across this ore layer for comparison with ore layers in the Jianshan Block. 12 samples were taken below, through and above the ore layer at approximately 1-4m intervals.

4. Field observations and petrography

4.1 Jianshan block – Panzhihua intrusion

The Jianshan Block is located in the north eastern part of the intrusion (Figure 2.8; Figure 2.9; Figure 2.10). The block has a dip direction of 355^{o} at a dip angle ranging between 55-60^{o}. The Jianshan block has been the subject of several recent studies due to the excellent outcrop available for sampling (Pang et al. 2008a; Pang et al. 2008b; Pang et al. 2009). The lower contact is intrusive into carbonates (Figure 4.1 a). The stratigraphy is relatively similar to that of the intrusion as a whole, although the Jianshan block is only 1400m thick compared to the maximum thickness of 3000m (Figure 2.9). The UZ, in particular, in less extensive 250m thick relative to the typical variation of 500-1500m. This is likely due to a greater loss of the upper portion of the intrusion during later tectonic activity. The main Fe-Ti oxide ore layer in this case is in direct contact with the footwall unlike the Zujiabaobao Block where it occurs within the LZ (Figure 2.9). The MGZ and LZ in the Jianshan block are essentially one heterogeneous zone of mixed characteristics (Figure 2.9).

The main Fe-Ti oxide ore layer within the Jianshan Block is approximately 40 m in thickness. The lower and upper contacts are gradational with the massive ore in the centre. The MGZ proper consists dominantly of microgabbro with varying proportions of hornblende. The hornblende proportion increases toward the footwall contact and grade into rocks composed almost entirely of hornblende when in contact with the footwall. The microgabbro is well laminated, which consists dominantly of hornblende with lesser biotite and clinopyroxene (Pang, 2008). Abundant marble xenoliths are observed in spatial relation with the footwall contact. Away from the footwall the microgabbro has clinopyroxene and plagioclase as dominant components with minor olivine, hornblende, Fe-Ti oxides and apatite (Pang, 2008). Rare clinopyroxenite and olivine-rich wehrlite are also present within this zone. This zone is thought to represent a chilled margin, simply based on its fine grain size and proximity to the footwall (Pang et a. 2008a). The LZ portion of the zone is comprised of essentially massive gabbros and oxide gabbros, which do not show any distinct layering. The gabbros are coarse grained and local pegmatitic facies are observed. Typical grain size reaches up to 1 cm. The top of the zone is marked by a Fe-Ti oxide ore layer (MZa ore Layer) (Figure 4.1 b). The mineralogy of the MZ rocks is similar to the underlying LZ, although the gabbros are medium grained relative to the coarse grained LZ gabbros. The main difference from the underlying LZ is the well layered nature of the MZ rocks (Figure 4.1 c and d). The layering is in the form of modal layers with alternating felsic dominated and mafic dominated layers. Plagioclase grains show distinct

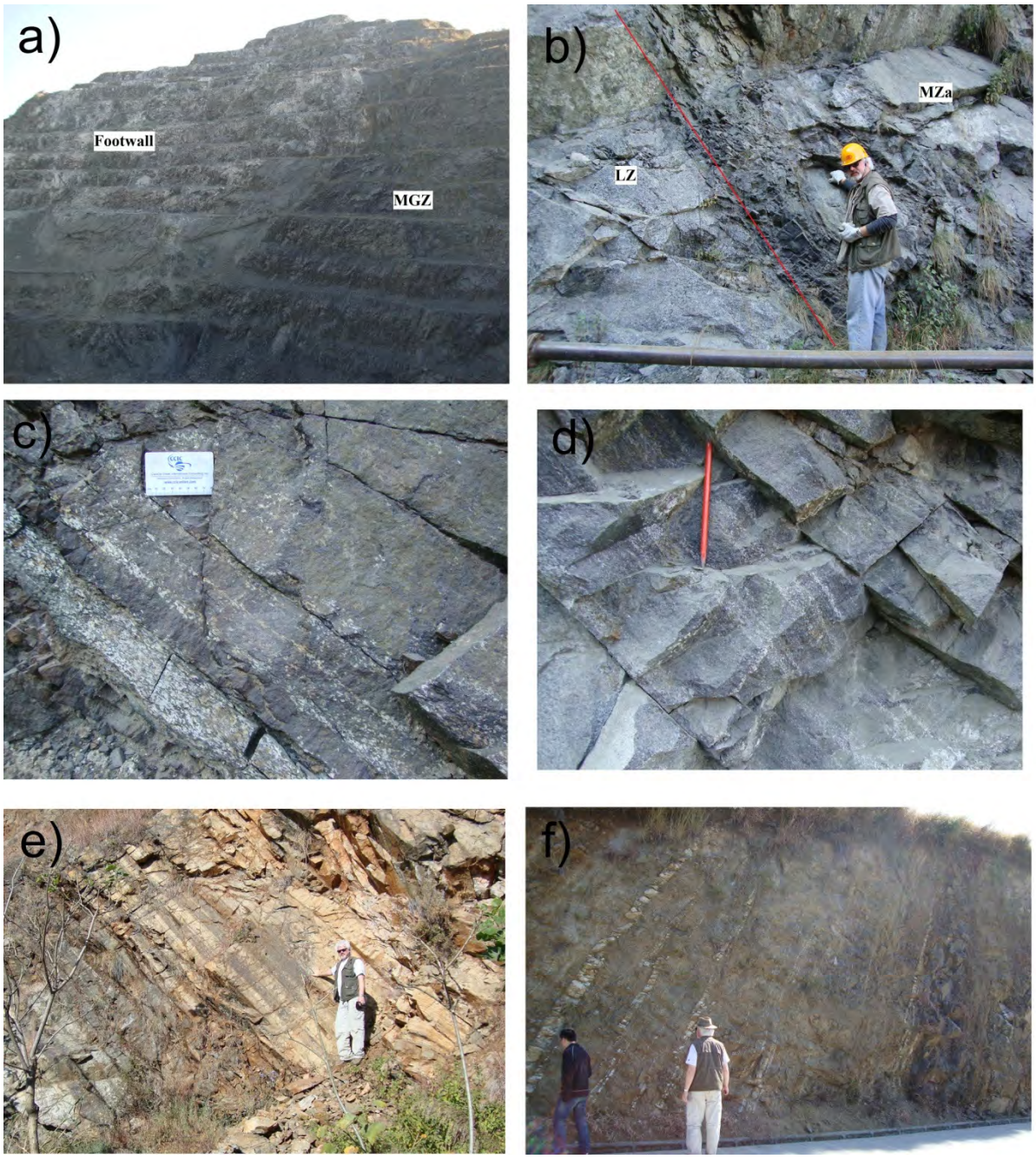

Figure 4.1 Photographs from the Jianshan Block Open pit and road cuttings, Panzhihua intrusion. a) Intrusive footwall contact with metamorphosed carbonates. b) Contact between the lower zone (LZ) and middle zone A (MZa). c) Layering at the base of the MZa. d) Layering in the MZa. e) Layering in the UZ. Mafic layers are clinopyroxenite. f) Layering in the UZ showing altered gabbro with anorthosite and clinopyroxenite.

alignment along the long axis parallel to the layering. Several oxide ore layers are present in the lower half of this zone although they are not nearly as extensive as the main ore body in the MGZ/LZ. Oxide ores are absent in the MZb. The MZb is characterised by the occurrence of apatite and the gabbros become more leucocratic.

The UZ is not exposed in the pit but is present in several road cuttings to the north of the Jianshan open pit. The UZ is characterised by the occurrence of leucogabbros with anorthosite and clinopyroxenite layers, which are absent from the MZ. The UZ is similarly well layered with alternating felsic and mafic dominated layers (Figure 4.1 e and f).

4.2 Nalaqing block – Panzhihua intrusion

The southern Nalaqing Block hosts several lens shaped Fe-Ti oxide ore bodies, which are < 30 m in thickness (Zhou et al. 2005). Small scale mining operations provide excellent accessible exposure in this region. The Fe-Ti oxide ore layer observed at the Nalaqing Block in this study is 9 m in thickness, occurs 15 m from the base of the intrusion and has a gradational lower and upper contact characterised by Fe-Ti oxide-rich gabbros. The ore layer contains variable proportions of silicates dominated by plagioclase and clinopyroxene, olivine is present but rare (< 3 vol. %). Plagioclase laths show distinct alignment parallel to the direction of layering (Figure 4.2 a). The ore layer itself is well layered with massive Fe-Ti oxide layers and silicate-rich layers.

4.3 Fe-Ti oxide ore layers

Fe-Ti oxide (Ti-magnetite and ilmenite) ore layers at the Panzhihua intrusion occur within the lower half of the intrusion (Figure 2.9). The main Fe-Ti oxide ore layer varies in thickness and stratigraphic occurrence. It occurs within the LZ of the Zujiabaobao block and is ± 60 m thick (maximum thickness). Within the Jianshan block the main ore layer is ± 40 m thick and occurs at or within several meters of the footwall carbonate. Within the Jianshan block it varies between 10-40 m in thickness but is generally closer to the upper limit. At the southern Nalaqing block the maximum thickness of the main ore layer is 30 m but is generally ± 20 m thick and it occurs within 15 m of the base of the intrusion. The maximum thickness of the main ore layer is within the northern

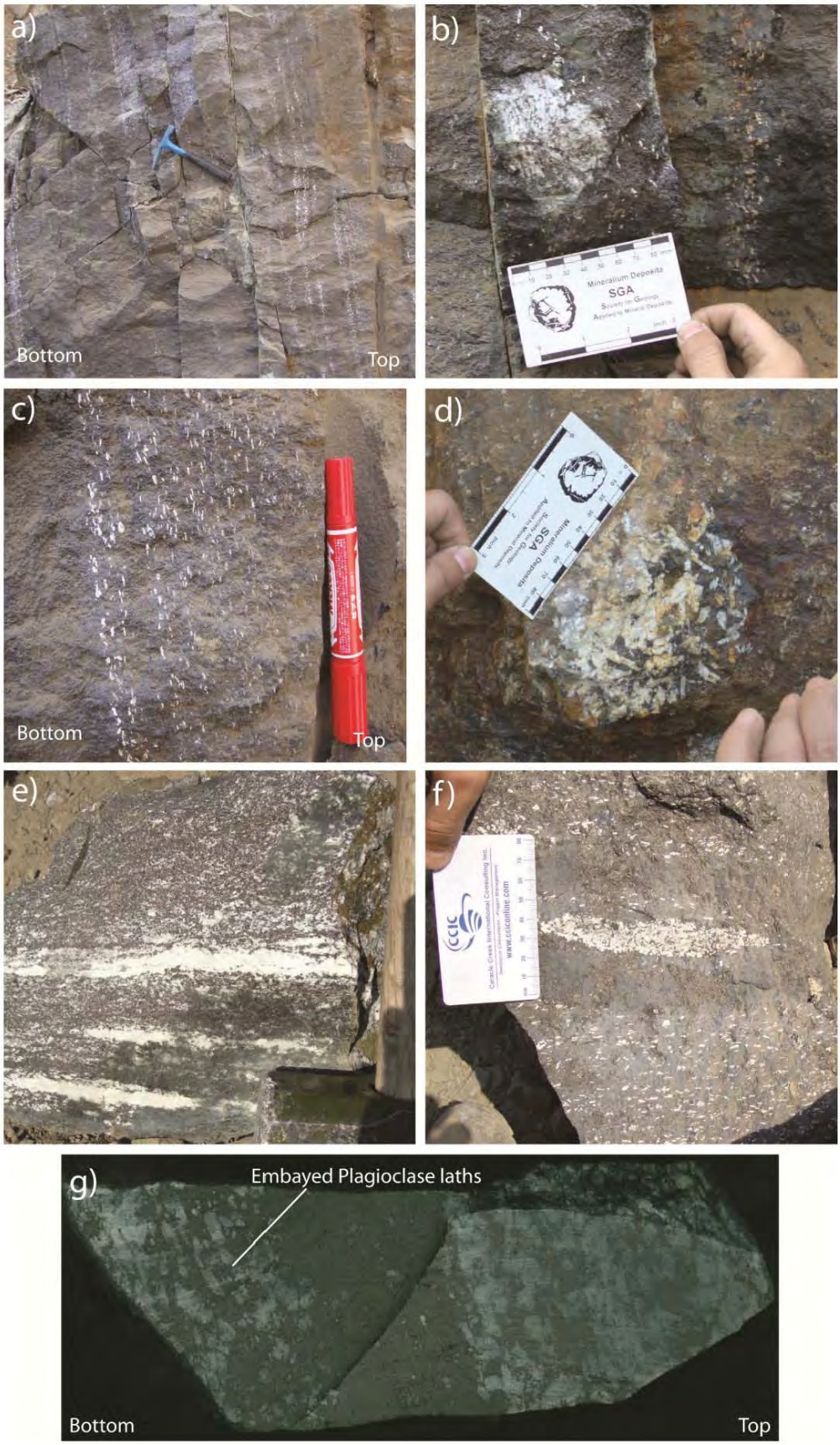

Figure 4.2 See caption overleaf

Figure 4.2 Photographs of the main Fe-Ti oxide ore layer at the Nalaqing Block, Panzhihua intrusion. a) main Fe-Ti oxide ore layer showing the distinct alignment of plagioclase laths with their long axis parallel to the magmatic layering. b) Leucocratic gabbroic inclusion within the main ore layer. c) Layering within the main ore layer; massive layer at the bottom overlain by a plagioclase-rich layer with distinct alignment of plagioclase laths. d) Pegmatoidal domain within the main ore layer. e) leucocratic layers with very low proportion of mafic phases. f) lenses shaped aggregation of plagioclase within a massive oxide layer. g) Thin ore layer (massive section is 6 cm thick) with a gradational lower contact where plagioclase is being incorporated from the gabbroic layer below.

Zujiabaobao block and becomes thinner into the south. No data is available for the thickness within the central zones of the intrusion due to the absence of good outcrop. The MZa contains numerous significantly thinner cm-1 m scale ore layers. No ore layers occur within the MZb and UZ.

Lower contacts of ore layers have been reported to be sharp (e.g. Zhou et al. 2005 and Pang et al. 2008a) and, in general, upper contacts are gradational into oxide-rich gabbro and gabbro. The main ore layer and MZa observed in this study have gradational upper and lower contacts as highlighted by the Fe_2O_3 wt % reported in section 6. Several thin ore layers within the MZa also have gradational lower contacts where it often appears that silicate minerals from the gabbroic layer beneath the ore layer are being incorporated into the ore layer (Figure 4.2 g). The more extensive ore layers show distinct layering with alternating massive ore layers and silicate-rich layers (Figure 4.2 a and c). Plagioclase laths show clear alignment along long axes parallel to the magmatic layering. Rare occurrences of lenses of extremely leucocratic material are observed within ore layers, which are essentially 100 % plagioclase (Figure 4.2 e). Rare pegmatoidal domains are also observed within the ore layers (Figure 4.2 d). A particularly important characteristic, which will be discussed later when interpreting the petrogenesis of the ore layers, is the occurrence of gabbroic xenoliths within the ore layers (Figure 4.2 b), which appear to be disaggregating around the margins. A further important observation is that some of the thinner ore layers within the MZa cross-cut the magmatic layering traversing the cumulate stratigraphy (Pang et al. 2008a).

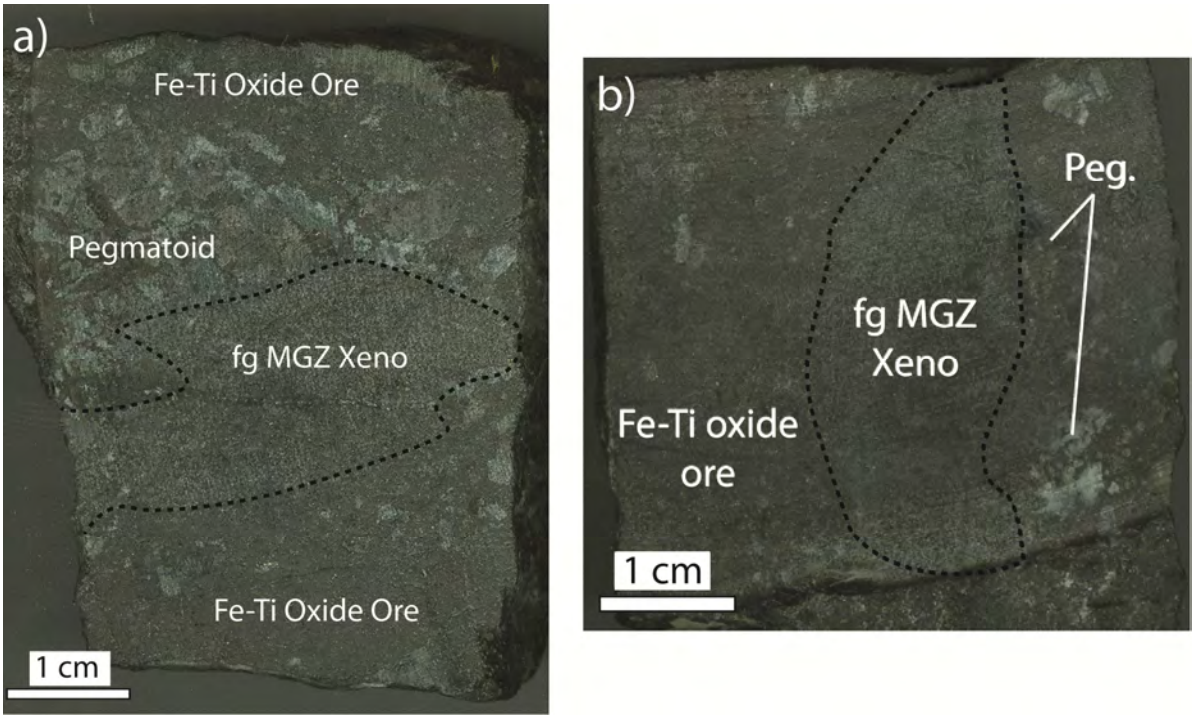

Figure 4.3 Photographs of sample slabs from the heterogeneous gradational lower contact between the MZa ore layer and footwall MGZ/LZ. a) Fine grained microgabbro xenolith (fg MGZ Xeno) within a massive Fe-Ti oxide ore zone within the heterogeneous zone. Xenoliths are commonly associated with pegmatoidal zone surrounding them. b) Fine grained microgabbro xenolith (fg MGZ Xeno) within massive Fe-Ti oxide zone, similarly associated with pegmatoidal zone.

The lower contact of the MZa ore layer has a distinct gradational contact, which is compositionally and texturally heterogeneous. This ± 1 m thick heterogeneous zone is comprised of a large range in grain size from 0.1-0.3 mm and up to 3-5 mm patches. Furthermore relatively thin (< 5 cm) thick Fe-Ti oxide ore layers are present within the zone, which contain xenoliths of MGZ fine grained gabbro (Figure 4.3). These xenoliths are generally associated with pegmatoidal grain sizes surrounding the margins of the xenoliths. This heterogeneous zone is of particular importance for later discussion of the formation of the marginal zone and for ore forming processes, which are discussed in section 9.

4.4 General petrography

The general petrography of the Panzhihua intrusion has been described by Zhou et al. (2005), Pang (2008) and Pang et al. (2009). Detailed descriptions for the gabbroic rocks are not repeated here but rather summarised. The following section provides detailed petrographic analysis into the silicate

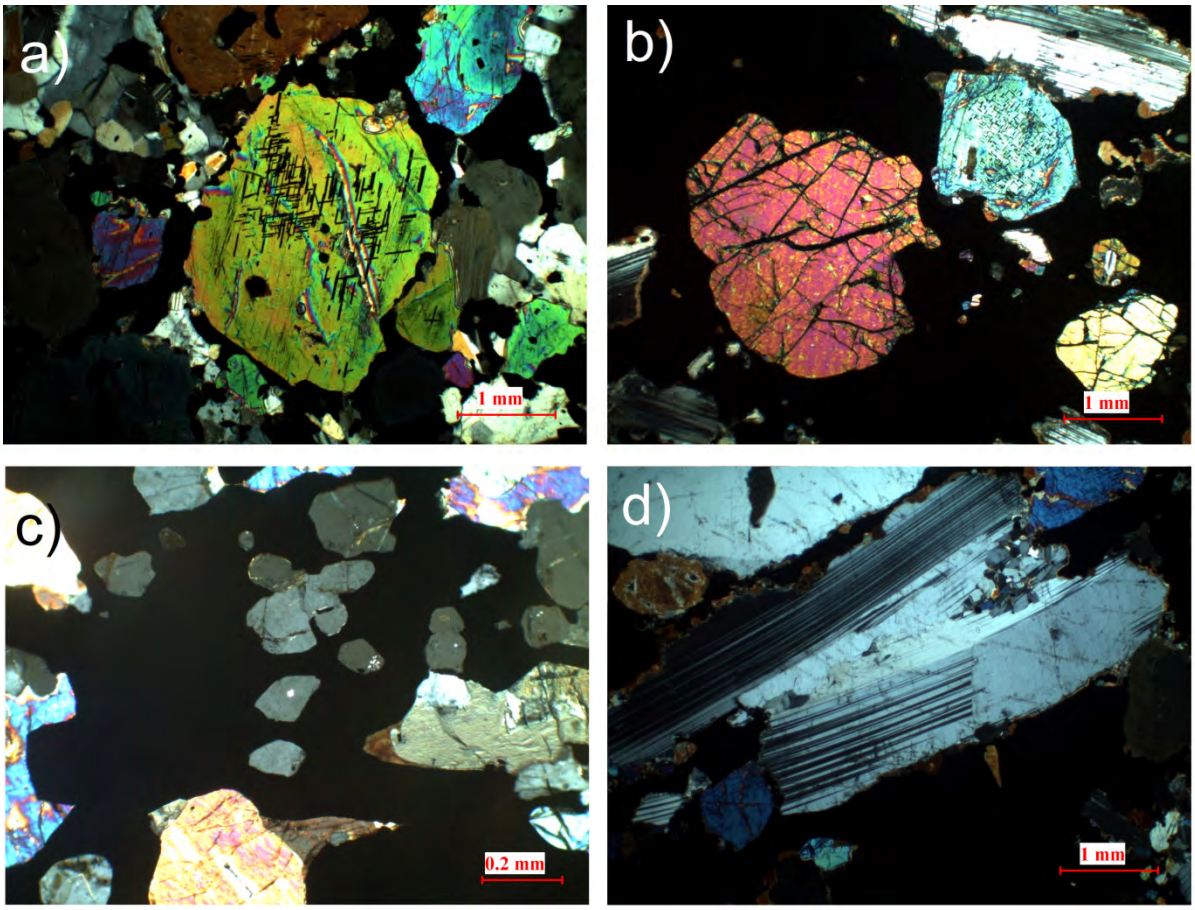

Figure 4.4 Photomicrographs of the minerals of the Panzhihua gabbroic rocks: a) Clinopyroxene grains with abundant exsolutions of ilmenite along cleavage planes (Sample BT-08). b) Olivine grain (centre left; Sample BT-06). c) Apatite grains (centre), present only in the MZb and generally < 0.5 mm in size (sample BT-64). d) Typical plagioclase laths (Sample BT-08).

rim textures observed for the Fe-Ti oxide ore rocks and the microscopic features of the ore minerals both within the massive ore rocks and the hosting gabbroic rocks.

The gabbroic rocks of the Panzhihua intrusion are comprised of silicates including: clinopyroxene, plagioclase, olivine and minor amphibole and apatite (Figure 2.8 and 4.4) as well as abundant Fe-Ti oxides. The MGZ/LZ is a heterogeneous zone comprised of dominantly microgabbro and lesser medium-coarse massive gabbro, along with the main Fe-Ti oxide ore layer at the base (described in detail below). Specific characteristics of the MGZ relevant to later discussion are described below in section 4.8 and illustrated in Figures 4.5 (c), (d) and Figure 4.6. The Middle Zone is comprised of two

subzones: the Middle Zone A (MZa) and Middle Zone B (MZb). The base of the MZa is marked by a distinct massive ore layer (MZa ore layer). The MZa is characterised by the presence of distinct layering (Pang, 2008), which is made obvious by plagioclase grains aligned with the long axis parallel to the layering. This layering is observed within the gabbros directly overlying the MZa ore layer. The gabbros of the MZa are distinguished from the underlying MGZ/LZ rocks by the distinct layering and medium to coarse grain size (Figure 4.5 d). The gabbros of the MZa are comprised of plagioclase, clinopyroxene, Ti-magnetite, ilmenite and minor proportions of olivine and amphibole. Green spinel is also present in the oxide-rich rocks of the MZa. The characteristics of the MZb are very similar to that of the MZa apart from the appearance of apatite (Figure 4.4 c). The MZb is clearly distinguished from the underlying MZa by the appearance of cumulus apatite. Furthermore the gabbros of the MZb are more leucocratic in character. Oxide-rich gabbro and massive ore layers are completely absent from the MZb.

Rocks of the UZ are comprised of clinopyroxene, plagioclase, olivine, Ti-magnetite, ilmenite and minor proportions of amphibole. The rocks dominantly range in composition from typical gabbro to olivine gabbro. Less common occurrences of clinopyroxenite (+/- olivine) and anorthosite are also observed. Fe-Ti oxide abundances are highest for the clinopyroxenite layers. Fe-Ti oxides are typically interstitial and may form a network texture where abundant.

4.5 Marginal zone (MGZ/LZ)

The MGZ/LZ in the Jianshan Block of the Panzhihua intrusion is ± 40 m thick and is bound by the main Fe-Ti oxide ore layer below and the MZa ore layer above. The MGZ/LZ is a texturally and compositionally heterogeneous zone, which is comprised of microgabbro, olivine microgabbro, gabbroic rocks and pegmatoidal gabbros. The microgabbros typically have fine grain size < 0.3 mm whereas gabbroic rocks have a gain size 1-2 mm. Pegmatoidal zones have grain size of ± 10 mm. The microgabbro (including olivine microgabbro) is the dominant rock type comprising the MGZ/LZ. Olivine microgabbro is more abundant at the upper regions of the zone. Olivine generally occurs as phenocrysts (Figure 4.6 c and d) within a fine grained matrix comprised of plagioclase, clinopyroxene and Fe-Ti oxides (Figure 4.6). Olivine phenocrysts are typically recrystallised along their margins

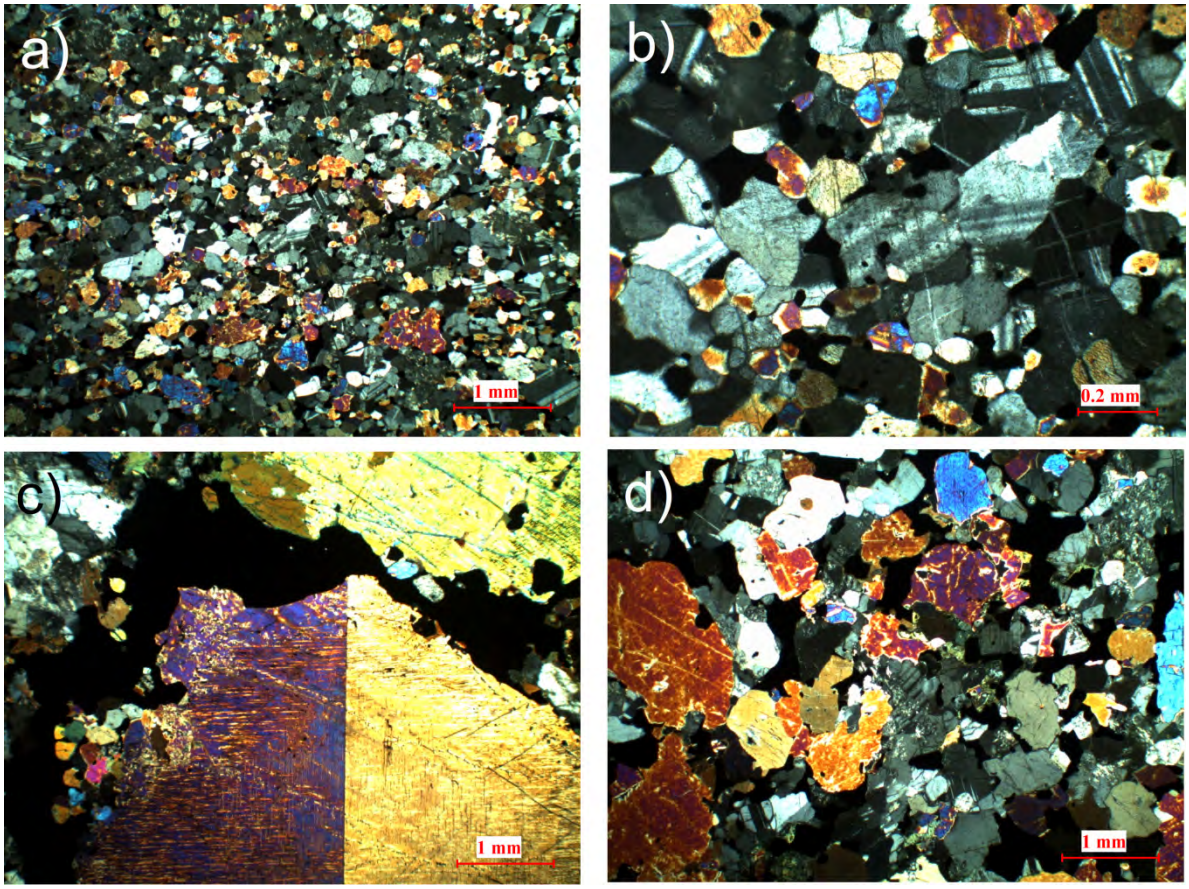

Figure 4.5 Photomicrographs of textures of the Panzhihua gabbroic rocks. a) Microgabbro from the MGZ/LZ Sample BT-01). b) Higher power image of a microgabbro showing annealing of silicate grains (Sample BT-01). c) Pegmatoidal gabbro from the MGZ/LZ. Note the re-crystallisation along the clinopyroxene grains boundary (Sample BT-02). d) Typical gabbro from the MZa comprised of plagioclase, clinopyroxene and interstitial Fe-Ti oxides (Sample BT-13).

(Figure 4.6 d). The fine grained matrix is characterised by grains with straight boundaries meeting at triple junctions (Figure 4.6 b). Coarse grains within pegmatoidal zones are commonly recrystallised along their margins (Figure 4.5 c).

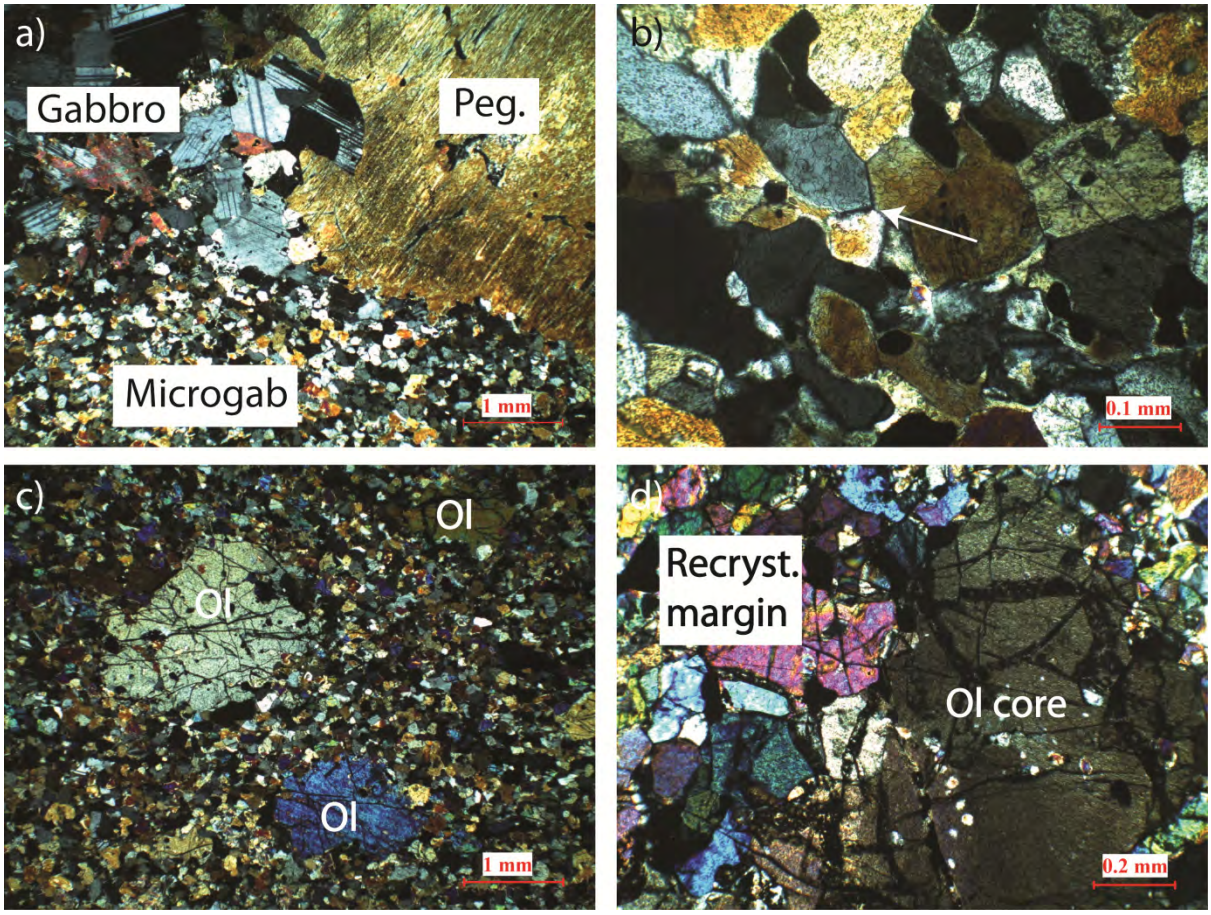

Figure 4.6 Photomicrographs of the MGZ. a) Gabbro, microgabbro and a pegmatoidal clinopyroxene grain together (Sample BT-03 B). b) High power image of the microgabbro showing straight grain boundaries meeting at triple junctions (arrow) (Sample BT-03 B). c) Microgabbro with olivine phenocrysts (ol) (Sample BT-03 X). d) Olivine phenocryst with recrystallised margin (Sample BT-03 X).

4.6 Silicate rim textures within the Fe-Ti oxide ore layers

Fe-Ti oxide ore layers contain variable proportions of silicates including plagioclase, clinopyroxene, olivine and amphibole. Apatite is notably absent from ore layers. Modal abundances range and show no trends through ore layers. For example the silicate abundances for the main ore layer are: plagioclase – 3-17 vol. %; clinopyroxene – 6-16 vol. %; olivine – 1-5 vol. % and amphibole – 2-8 vol.

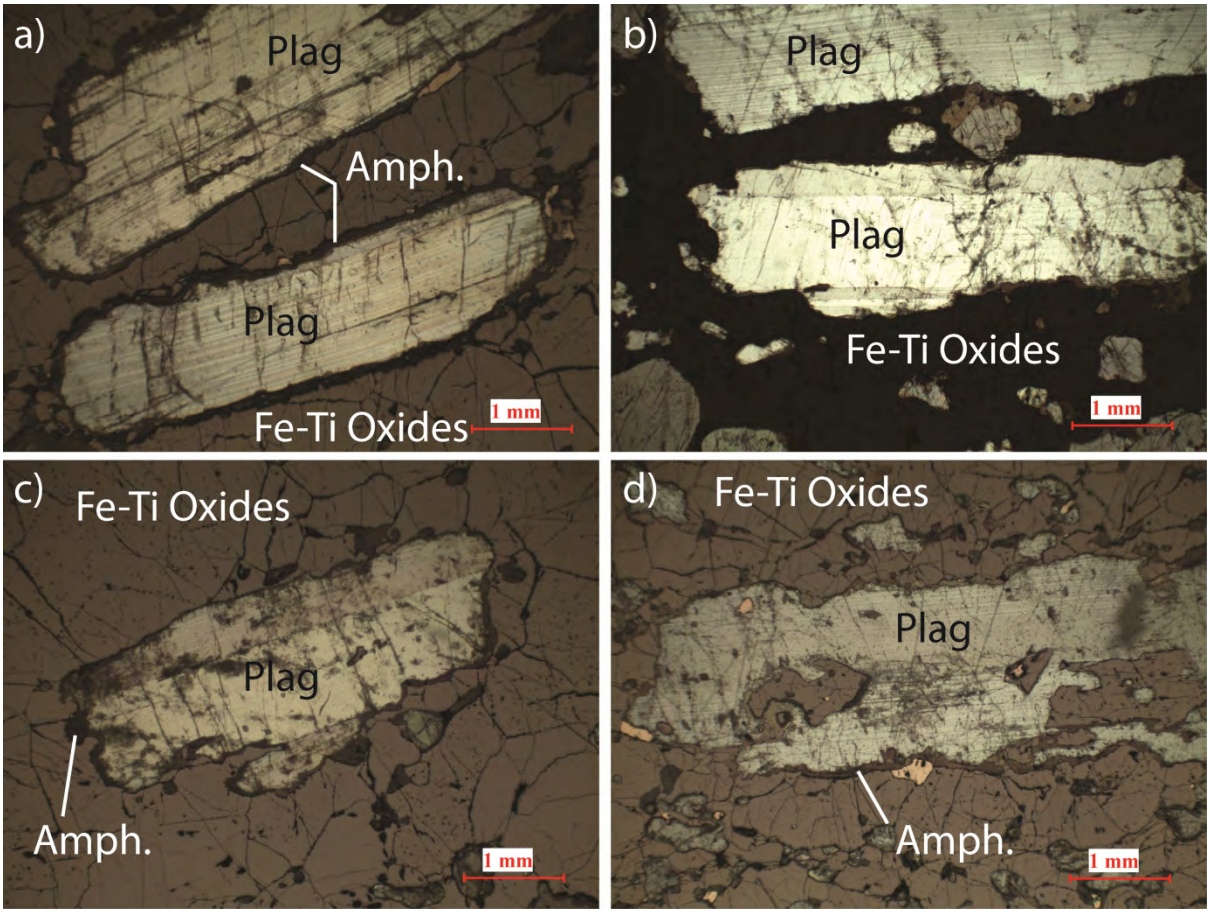

Figure 4.7 Photomicrographs of plagioclase laths within Fe-Ti oxide ore layers from the Jianshan section, Panzhihua intrusion. a) Distinct plagioclase laths with minor resorption at the lath terminations, in particular the upper grain (Sample BT-05). b) Plagioclase laths with minor resorption at the lath terminations and margins (Sample BT-05). c) Plagioclase lath showing resorption along the grain margins (Sample BT-06). d) Highly resorped plagioclase lath showing effects of significant consumption after crystallisation (Sample BT-17).

%. Silicate grains (plagioclase and clinopyroxene) within the massive ore layers are characterised by rounded corners (Figure 4.7) and are commonly embayed where in contact with Fe-Ti oxides (Figure 4.8 c-g), although commonly retain original lath shape (Figure 4.7). Rounded grains range in size but are commonly observed < 0.2 mm in size and down to 0.05 mm (Figure 4.8 a and b). Coarse plagioclase typically retains original lath shapes but show significant rounding and embayment structures (Figure 4.7 and 4.8 g). Associated with the rounding and embayment of plagioclase and clinopyroxene primocrysts are rims of amphibole, olivine, rare pleonaste and rare plagioclase (Figure 4.7; 4.8; 4.9; 4.11). Amphibole is the dominant rim observed and forms a relatively thin (+/- 0.06 mm

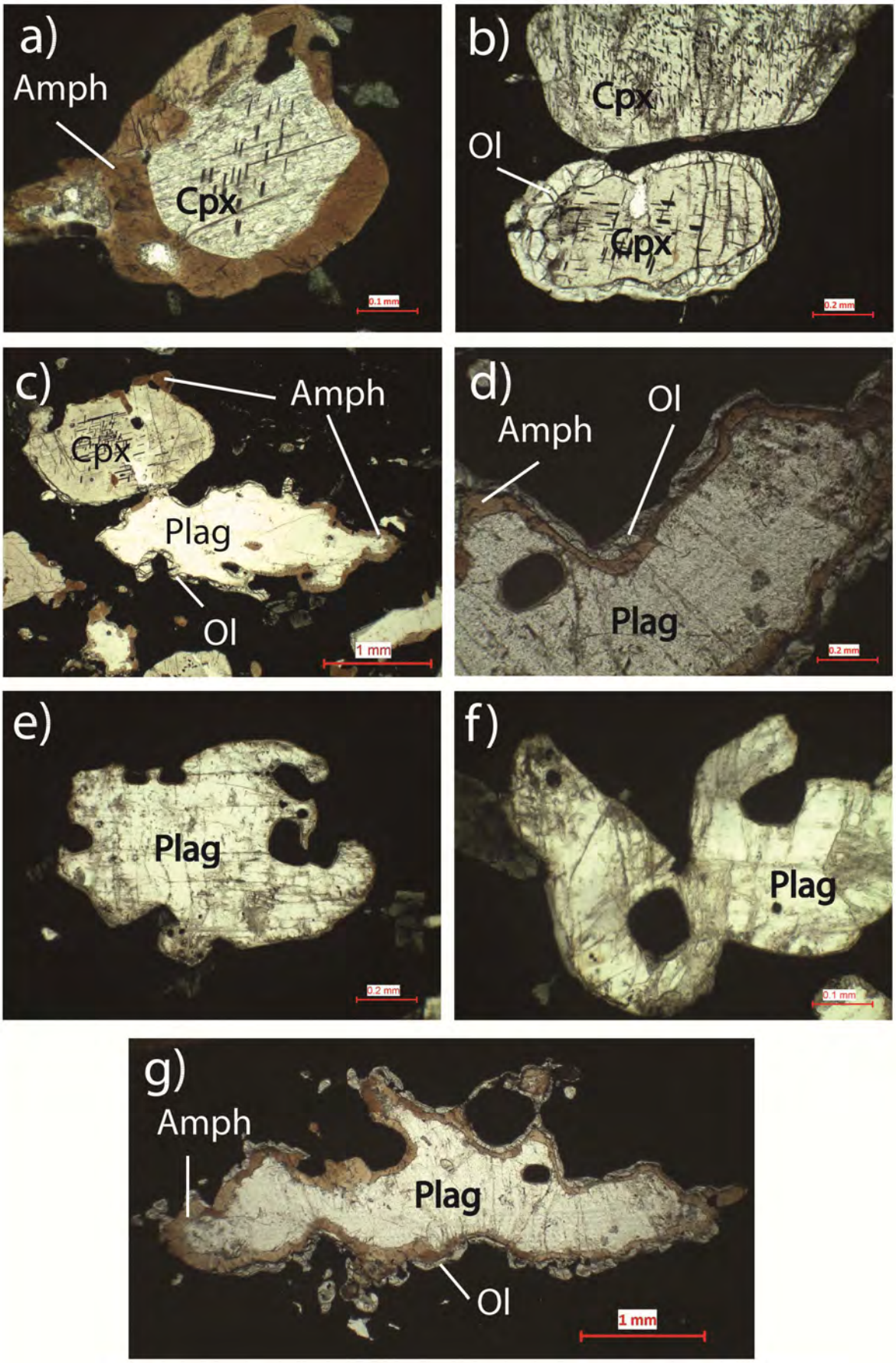

Figure 4.8 See caption overleaf.

Figure 4.8 Photomicrographs of distinct reaction rim textures from the Fe-To oxide ore layers at the Jianshan Block, Panzhihua intrusion. a) Rounded resorped clinopyroxene grain with ilmenite exsolutions with a distinct reaction rim of amphibole. b) Two rounded resorped clinopyroxene grain with reaction rims of olivine of varied thickness. c) Highly resorped/embayed clinopyroxene and plagioclase grains with composite reaction rims of amphibole and olivine. d) Embayed plagioclase grain showing reaction rim of both amphibole and olivine. a)-d) from Sample BT-06. e) and f) highly embayed plagioclase grains (Sample BT-17). g) Highly resorped/embayed plagioclase grain with reaction rim of amphibole and olivine (Sample BT-04).

thick) rim, which either partially or completely surround grains. Olivine forms similar rims and is often altered to serpentine. Composite rims are commonly observed where part of a single silicate grain will have a amphibole rim whereas another area of the same grain has an olivine rim (Figure 4.8 c). Rare occurrences of double rims are also observed where amphibole is observed as a complete rim in contact with the silicate grain and surrounding the amphibole is a complete rim of olivine or pleonaste (Figure 4.8 d. g and Figure 4.9). Pleonaste is not observed in association with olivine as rims.

The common occurrence of rounded Fe-Ti oxide grains included within silicate phases are not inclusions of earlier crystallised Fe-Ti oxide but rather represent embayment structures intersected so that the mouth of the embayment is not observed in the 2D thin section (Figure 4.8 e and f). This is also supported by the occurrence of rims of amphibole between the “included” Fe-Ti oxide and silicate grain, which is similar to the typical amphibole reaction rims observed within embayment structures. Coarse grained (> 0.5 mm) olivine grains within the ore layers are commonly spatially associated with olivine rims forming around other silicate grains (i. e. continuous with the rims). Coarse granular olivine commonly contains inclusions of fine-grained (0.1-0.4 mm) plagioclase (Figure 4.10). Plagioclase has been observed in rare cases (0-3 occurrences per thin section) as either distinct rims (Figure 4.11 a and b) or as grains inter-grown with amphibole (Figure 4.11 c and d). These are discussed further in section 5 for their compositional variation.

Silicate rims are typically poorly developed in the gabbros and are commonly absent. However, the oxide gabbros do contain rare occurrences of reaction rim textures, which have very similar characteristics to the massive ore layers. Silicate grains may be highly irregular and contain similar

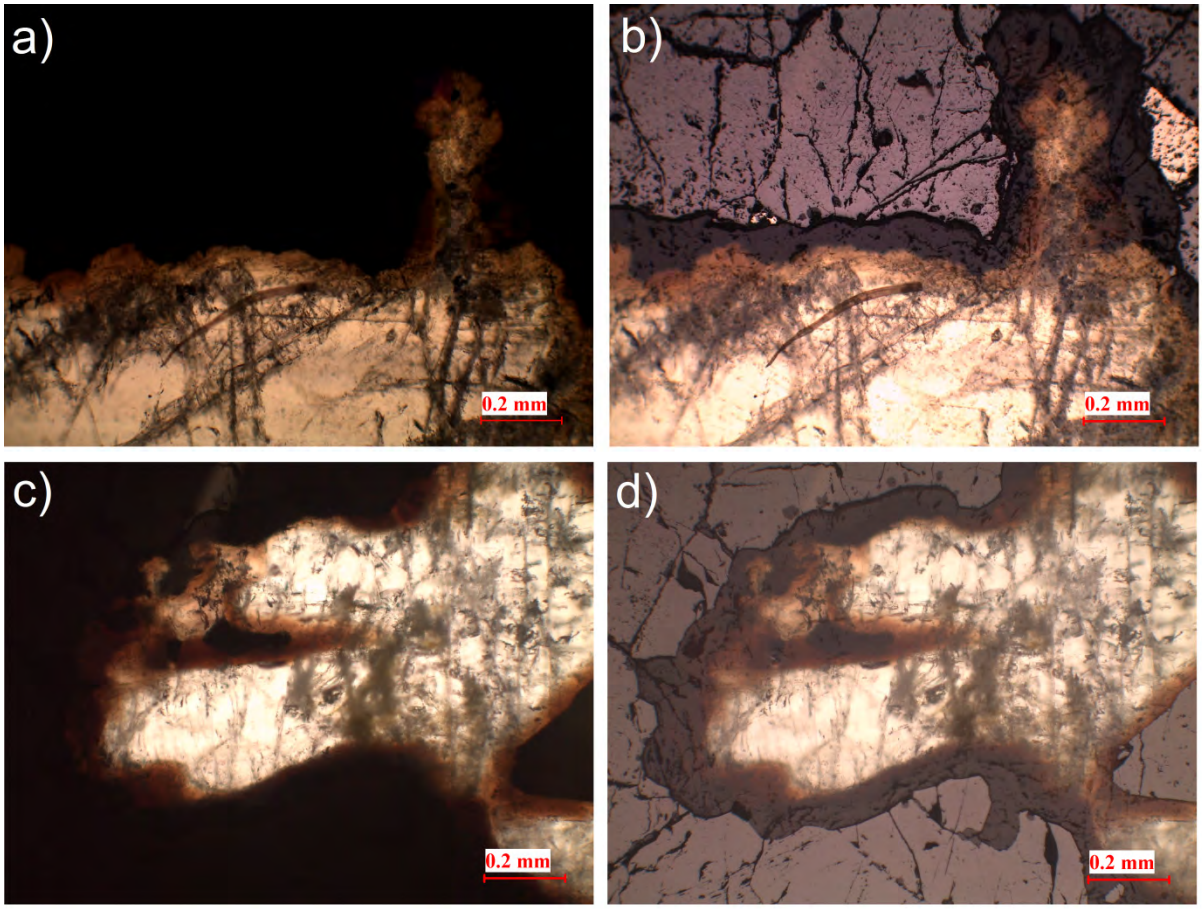

Figure 4.9 Photomicrographs of composite amphibole and pleonaste rims on plagioclase laths. a) Transmitted light photo showing plagioclase with a distinct brown amphibole rim. b) Composite transmitted/reflected light photo of the same grain as in (a) showing the presence of a pleonaste rim surrounding the amphibole rim and in contact with Ti-magnetite. c) Transmitted light photo showing another example of a plagioclase grain with an amphibole rim. d) Composite photo of (c) showing the presence of a pleonaste rim surrounding the amphibole rim. Photomicrographs from sample 05-4.

embayment textures to the ore layers. Amphibole and olivine are observed as rim products and complex rims are common in the oxide-rich gabbros. Oxide-rich gabbroic rocks forming gradational lower contacts of ore layers commonly show similar rim textures and consumption of silicate grains to that described here for the Fe-Ti oxide ore layers.

Table 4.1 Modal abundances of oxides and silicates within the Jianshan Block, Panzhihua intrusion.

Sample#	Zone	Height (m)	Mt	Ilm	Sulph	Silicate	Mt/Ilm
05_1	Main Ore	8	17.6	4.6	2	75.6	3.83
05_2	Main Ore	10	39.3	15	4.3	41.3	2.62
05_3	Main Ore	16	48	11	3.6	37.3	4.36
05_4	Main Ore	23	84.4	6.8	0	8.7	12.41
05_6	Main Ore	35	83	6.3	2	8.6	13.17
05_7	Main Ore	41	69.3	4.5	Trace	26.1	15.4
05_7/8	Main Ore	44	83.3	4.6	Trace	12	18.11
05_8	Main Ore	50	74.3	3.6	0	22	20.64
05_9	Main Ore	54	10	5.3	1.7	82.9	1.89
05_10	Main Ore	60	41.6	6.3	Trace	52	6.6
BT-01	MGZ/LZ	100	7.3	3	0	89.6	2.43
BT-02	MGZ/LZ	115	14	5.3	0.6	80	2.64
BT-03 (D)	MGZ/LZ	141	52.6	15	0.3	32	3.51
BT-03 (F)	MGZ/LZ	144	33.3	9.3	1.3	56	3.58
BT-04	MZa	146.9	89.6	8	0	5.3	11.2
BT-05	MZa	150	68.3	4.3	1.3	26	15.88
BT-06	MZa	160.2	89.3	7	Trace	3.6	12.76
BT-08	MZa	180.4	9	3	0.3	87.6	3
BT-09	MZa	190.5	43.6	5.3	1	50	8.23
BT-10	MZa	200	17.6	3.6	1.3	77.3	4.89
BT-13	MZa	231	9.4	0.3	0	90.1	31.33
BT-17	MZa	265	61	4.6	0.3	33.9	13.26
BT-19	MZa	271	53.3	5	4	37.6	10.66
BT-23	MZa	312	33.3	4	1.6	61.3	8.33
BT-27	MZa	336	58.6	11	1.6	28.6	5.33
BT-30	MZa	352	24.6	13.3	2	60.3	1.85
BT-33	MZa	382	13.6	8	1	77.3	1.7
BT-37	MZa	423	8.7	8.7	0	82.4	1
BT-41	MZa	453	8	8.5	0	83.4	0.94
BT-45	MZa	494	16.2	8.3	1.5	73.9	1.95
BT-48	MZa	504	11.1	8.2	0.7	79.9	1.35
BT-53	MZa	545	14.3	5.2	1	79.3	2.75
BT-64	MZb	1052	5.5	5.9	1.1	87.3	0.93
BT-66	MZb	946	7.2	5	0.2	87.5	1.44
BT-62	MZb	1091	4.3	2.3	0	93.3	1.87
BT-65	MZb	999.2	4	6.3	0.3	89.3	0.63
BT-70	MZb	737.2	1.3	3	0	95.6	0.43
BT-71	MZb	685	2.8	2.2	0	94.8	1.27
BT-72	MZb	632.4	0.6	3.7	0	95.6	0.16
BT-73	MZb	580	2.3	4.6	0	93	0.5
RC-03 B	UZ	1129.7	8.6	3.3	0	88	2.61
UZ-01	UZ	1395	9.5	2.9	0.7	86.7	3.28
UZ-02	UZ	1301.5	7.3	8.6	1	83	0.85
UZ-03	UZ	1208	3.3	3	0	93.6	1.1
UZ-04	UZ	1197	6.3	2.3	0.6	90.6	2.74
UZ-05	UZ	1177	3.6	5.3	0.3	90	0.68
UZ-06	UZ	1145	29.6	4.3	0	66	6.88
UZ-08	UZ	1141	24.3	4.3	0	71.3	5.65

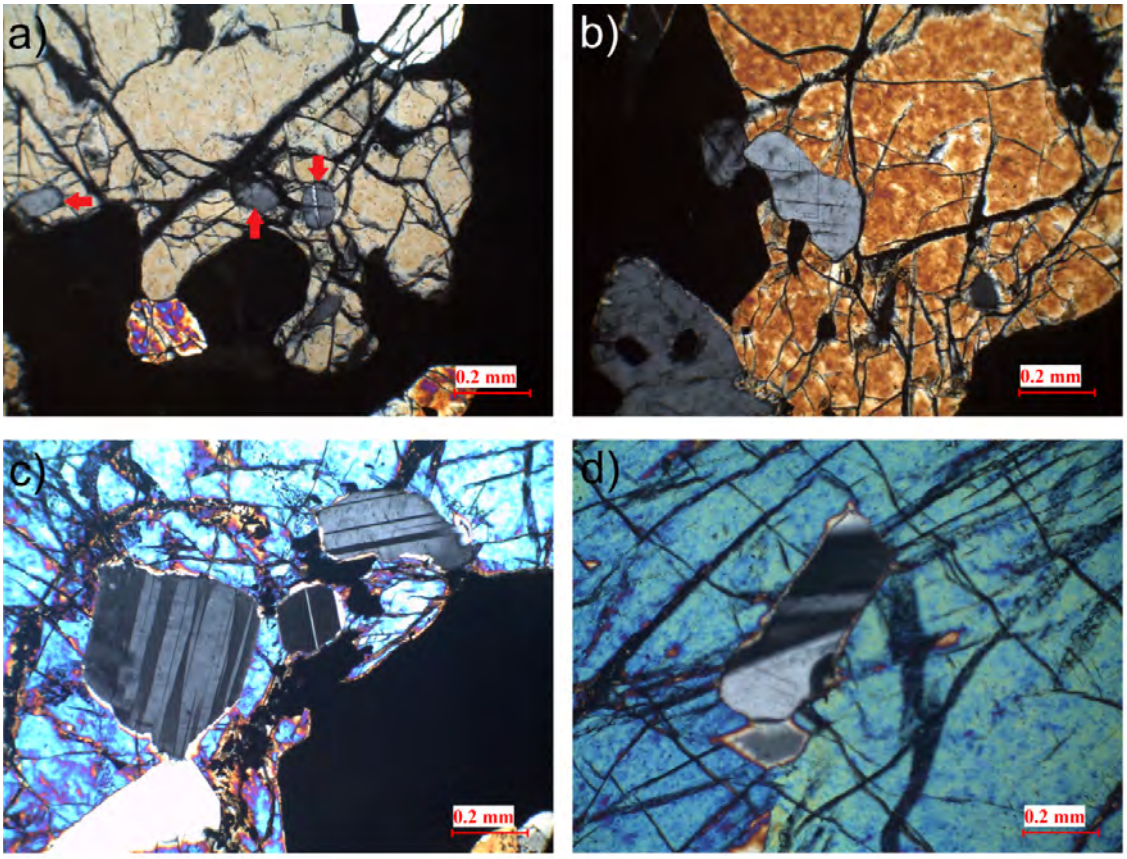

Figure 4.10 Photomicrographs of coarse grained olivine grains in the Fe-Ti oxide ore layers with distinct inclusions of plagioclase. a) and b) from sample BT-19. c) and d) from sample BT-06.

4.7 Fe-Ti oxide abundances and variation

Fe-Ti oxides phases are Ti-magnetite and ilmenite with lesser green spinel also present in some cases. The abundance of Ti-magnetite relative to ilmenite is a particularly important characteristic of the Panzhihua rocks. The ratio of Ti-magnetite/ilmenite (Mt/Ilm) varies with the total abundance of Fe-Ti oxides (Figure 4.12). Modal abundances are presented in Table 4.1.

The rocks of the Panzhihua intrusion are divided into three categories based on the whole-rock Fe_2O_3 wt %: a) massive ore, b) oxide-rich gabbro and c) gabbro. The massive ore rocks typically contain 70-98 vol. % Fe-Ti oxides whereas the oxide gabbro and gabbro contain 30-45 vol. % and 4-30 vol. % respectively (Table 4.1). The ratio of Mt/Ilm changes gradationally from Ti-magnetite dominated in the massive ore to near equal proportions in the gabbros (Figure 4.12). The ratio ranges from Ti-magnetite dominated (10-20) within the massive ore layers to near equal proportions within the gabbroic rocks (1-5). The oxide gabbro contains Mt/Ilm ratio intermediate (5-9) between

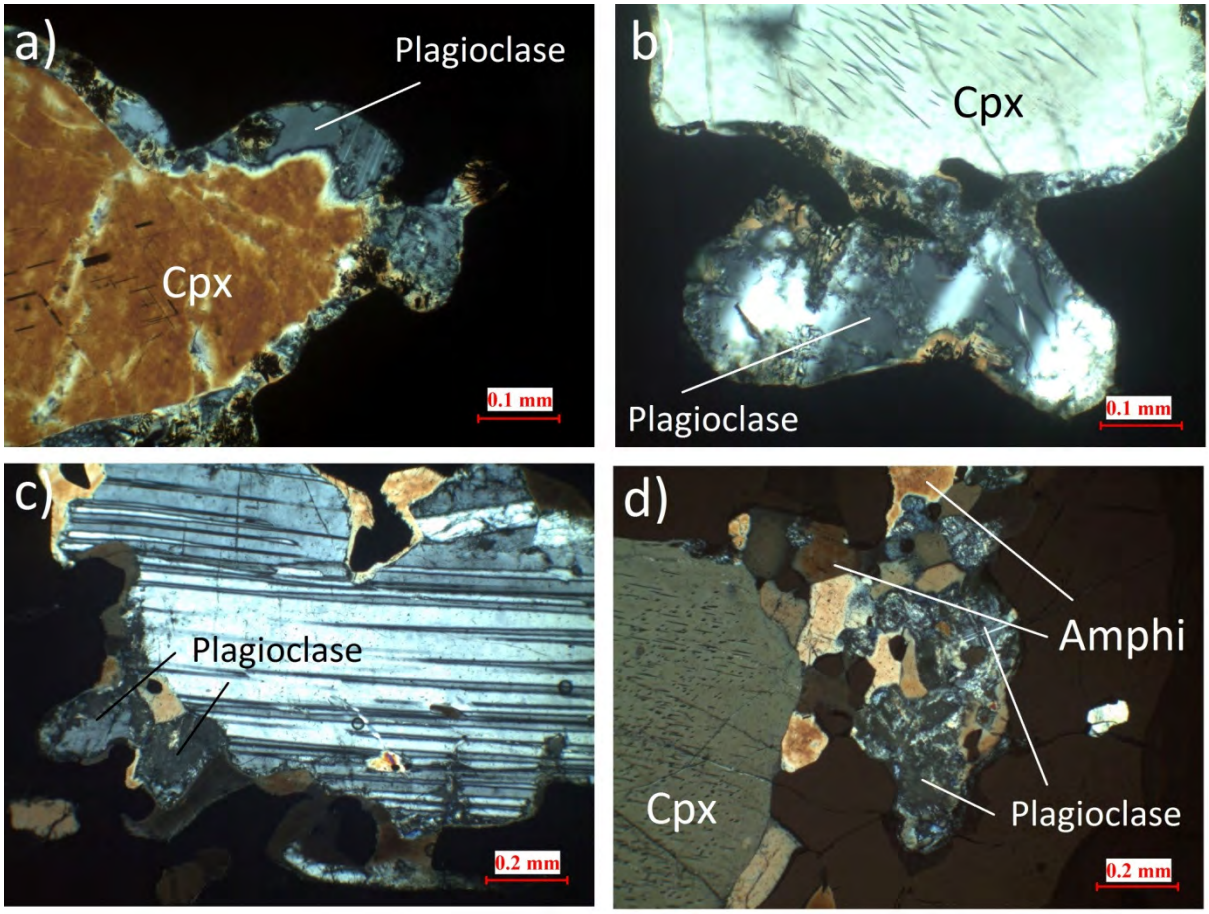

Figure 4.11 Photomicrographs of plagioclase associated with reaction products of silicate primocrysts. a) Plagioclase rim surrounding clinopyroxene primocryst (Sample BT-06). b) Plagioclase grain extending into a rim surrounding clinopyroxene primocryst. c) Plagioclase primocryst with a rim of brown amphibole with included plagioclase grains (as highlighted). d) Plagioclase grain inter-grown with amphibole grain. b) – d) from sample BT-19.

the massive ore and gabbro (Table 4.1). Ti-magnetite clearly dominates over ilmenite within the massive ore layers.

The Mt/Ilm ratio within the main massive ore layer varies with height. The ratio increases with increasing height. The Mt/Ilm ratio increases from 12 at the base of the main ore layer to 20 at the top.

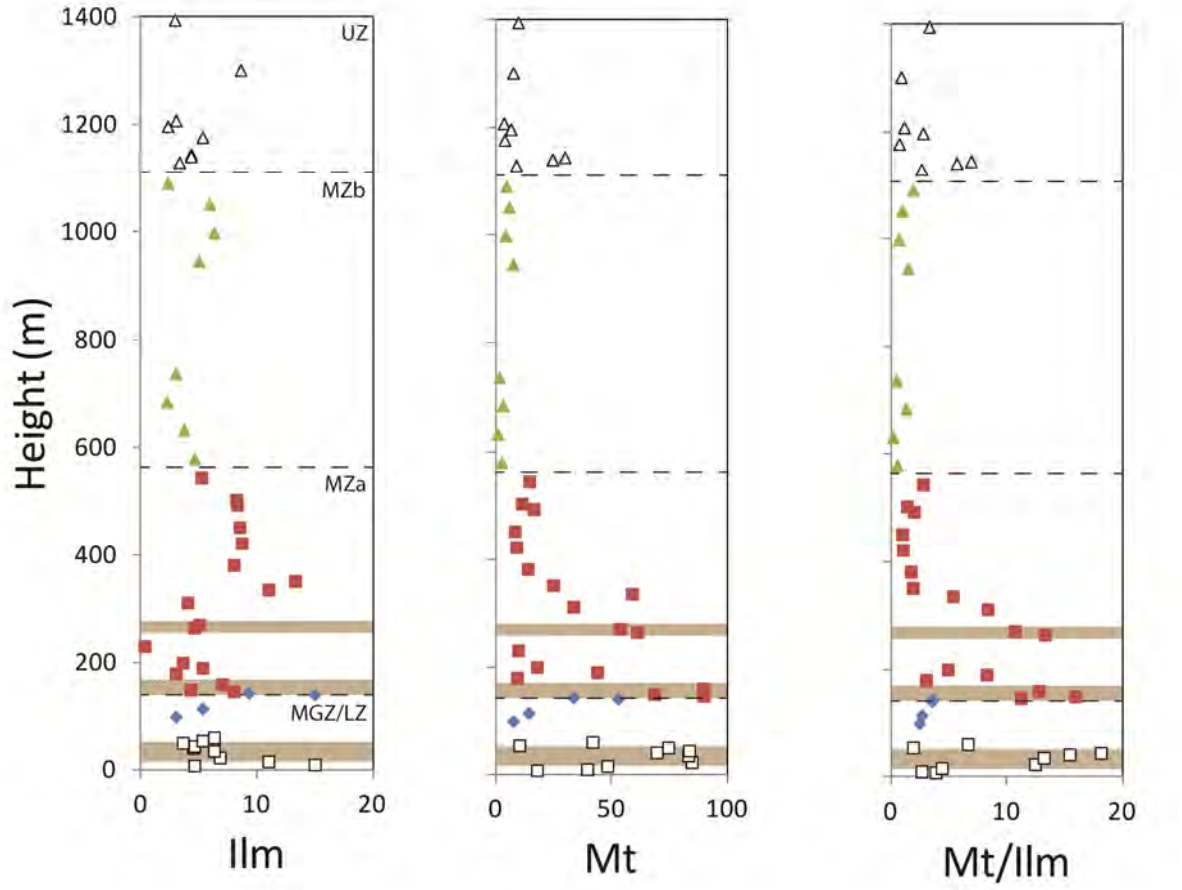

Figure 4.12 Stratigraphic variation of Ti-magnetite (Mt) and Ilmenite (Ilm) for the Jianshan Block, Panzhihua intrusion. Note the distinct decrease in Mt/Ilm at 350 m from the base.

4.8 Microscopic features of the Panzhihua Fe-Ti oxide ore minerals

4.8.1 Massive ore layers

The massive ore layers of the Panzhihua intrusion generally have similar characteristics in terms of the ore mineralogy and are described together below. The massive ore layers contain variable proportions of silicate minerals, ranging from 4 to 32 vol. % (Table 4.1). Silicate minerals are clinopyroxene and plagioclase with lesser olivine and amphibole. The proportion of silicate phases is also variable (i.e. proportion of plagioclase to clinopyroxene), where the ratio of clinopyroxene to plagioclase varies from 0.4 to 5, indicating that the silicate portion of the ore layers may be either plagioclase or clinopyroxene dominated. Sulphide minerals are generally only observed in trace amounts, < 2 vol. % and are generally pyrite, pyrrhotite and pentlandite. Rare occurrence of a green spinel is also observed, typically in trace amounts but may reach up to 5 vol. % in rare occurrences. Silicate minerals generally show the development of reaction rims when in contact with ore

minerals. The ore minerals are dominated by Ti-magnetite (70-90 vol. %) with lesser ilmenite (4-7 vol. %). Ti-magnetite grains are characterised by exsolution of both pleonaste and ulvospinel. Ilmenite grains are typically free of exsolutions apart from the rare occurrence of magnetite lamellae.

Ti-Magnetite and associated exsolution features

Ti-magnetite grains form densely packed aggregates of polygonal grains with straight boundaries and interfacial angles of 120^{o}. Individual polygonal grains are typically 1-4 mm in size and are characterised by abundant cracks/fractures. Exsolution of spinel and ulvospinel within Ti-magnetite grains is ubiquitous (Figure 4.13 a - d).

Spinel exsolution are hercynitic in composition (Pang et al. 2008) and termed pleonaste for the Bushveld Complex rocks (von Gruenewald et al. 1985; Reynolds 1985a); hereafter referred to as pleonaste. The pleonaste exsolution occur in two forms: a) plates/lenses (Figure 4.13 c) and b) internal granules within the Ti-magnetite grains (Figure 4.13 d). Pleonaste plates are concentrated within the core of Ti-magnetite grains and become finer grained toward the margin of the grain. They are notably absent from the margins of Ti-magnetite grains. Pleonaste plates generally range in size from 10-100 µm in length and are typically 5-10 µm in width. Furthermore plates are often observed as chains of very fine blebs of pleonaste. Internal granule exsolution of spinel is also a common feature. Granules typically range in size from 10-40 µm and are similarly concentrated within the core of Ti-magnetite grains.

Ulvospinel exsolution are present in all the massive ore samples analysed as the typical cloth texture with exsolution lamellae intersecting each other at right angles (Figure 4.13 c). The cloth texture is a network of micrometer scale lamellae of ulvospinel (Figure 4.13 c and d). The ulvospinel lamellae intersect each other at right angles and divide the Ti-magnetite grains into micrometer sized cubes and rectangles. This lamellae ulvospinel network varies considerably in size and development where it is often coarse enough to identify at medium power magnification (10-20 x magnification) but in other cases it cannot be identified at high power magnification (50 x magnification). The ulvospinel network typically retains its density up to the margins of the Ti-magnetite grains. Ulvospinel

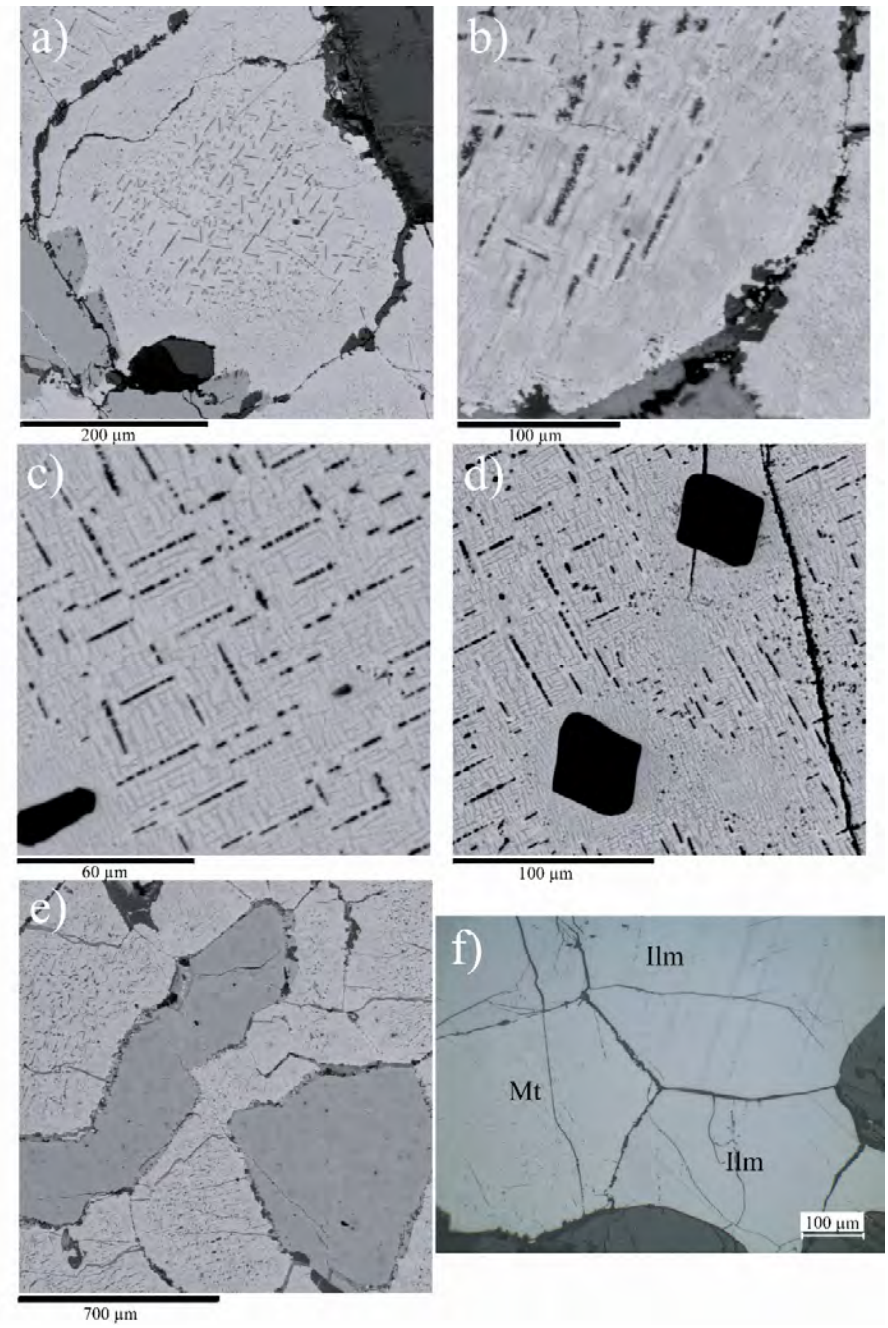

Figure 4.13 Backscatter images of Ti-magnetite exsolution microtextures within the Fe-Ti oxide ore layers from the Jianshan block, Panzhihua intrusion. a) Typical Ti-magnetite grain with exsolutions of pleonaste (black lamellae) in the centre of the grain (Sample 05-7). b) Higher power image showing relatively coarse grained boxwork development of ulvospinel exsolutions surrounding pleonaste lamellae (Sample 05-6). c) High power image showing pleonaste (black lamellae) with the distinct cloth textured ulvospinel (darker grey) (Sample -5-78). d) Image showing distinct cloth textured ulvospinel with two varieties of pleonaste exsolution as blebs and lamellae (Sample 05-78). e) Elongate ilmenite grains forming along Ti-magnetite margins with distinct serrated spinelliferous (pleonaste-rich) margins (Sample 05-6). f) Rare occurrence of polygonal ilmenite in contact with Ti-magnetite, indicating crystallisation prior to annealing.

exsolution commonly form boxwork textures framing spinel plates within the Ti-magnetite (Figure 4.13 b). In these cases the ulvospinel is typically coarser grained relative to the network lamellae.

The Ti-magnetite of the massive ore layers are characterised by the complete absence of ilmenite lamellae. Two exceptions are noted: a) a thin (4 cm thick) massive ore layer in the hangingwall of the MZa ore layer, which contains Ti-magnetite with significant ilmenite lamellae. b) The upper part of the main ore layer of the Nalaqing block.

Granular ilmenite

Ilmenite occurs either as discrete grains or as aggregates of grains. Discrete grains are elongate (Figure 4.13 e) and rarely show straight boundaries with 120^{o} interfacial angles. Aggregates of ilmenite grains have polygonal morphology and interfacial angles of 120^{o}, indicating annealing. Granular ilmenite is rarely observed as polygonal grains with triple junctions with Ti-magnetite grains (Figure 4.13 f).

Ilmenite grain boundaries with Ti-magnetite are typically irregular and serrated due to the development of spinelliferous (pleonaste-rich) ilmenite rims (also observed in the Bushveld Ti-magnetite by Reynolds, 1985). This serrated grain boundary texture is characterised by the presence of abundant fine-grained (< 15 μm) granules of spinel. Spinelliferous margins are not observed where ilmenite grains are polygonal.

Ilmenite grains commonly contain magnetite lamellae, which contain rare micrometer sized granules of spinel.

Variation within massive ore layers

Several variations in the exsolution textures are observed with increasing height in the main ore layer. Granular ilmenite grains are present throughout the massive ore layers and the hosting gabbros, where they occur as either discrete grains or as aggregates. Granular ilmenite concentration is highest at the base of massive ore layers and decreases in abundance upwards. This

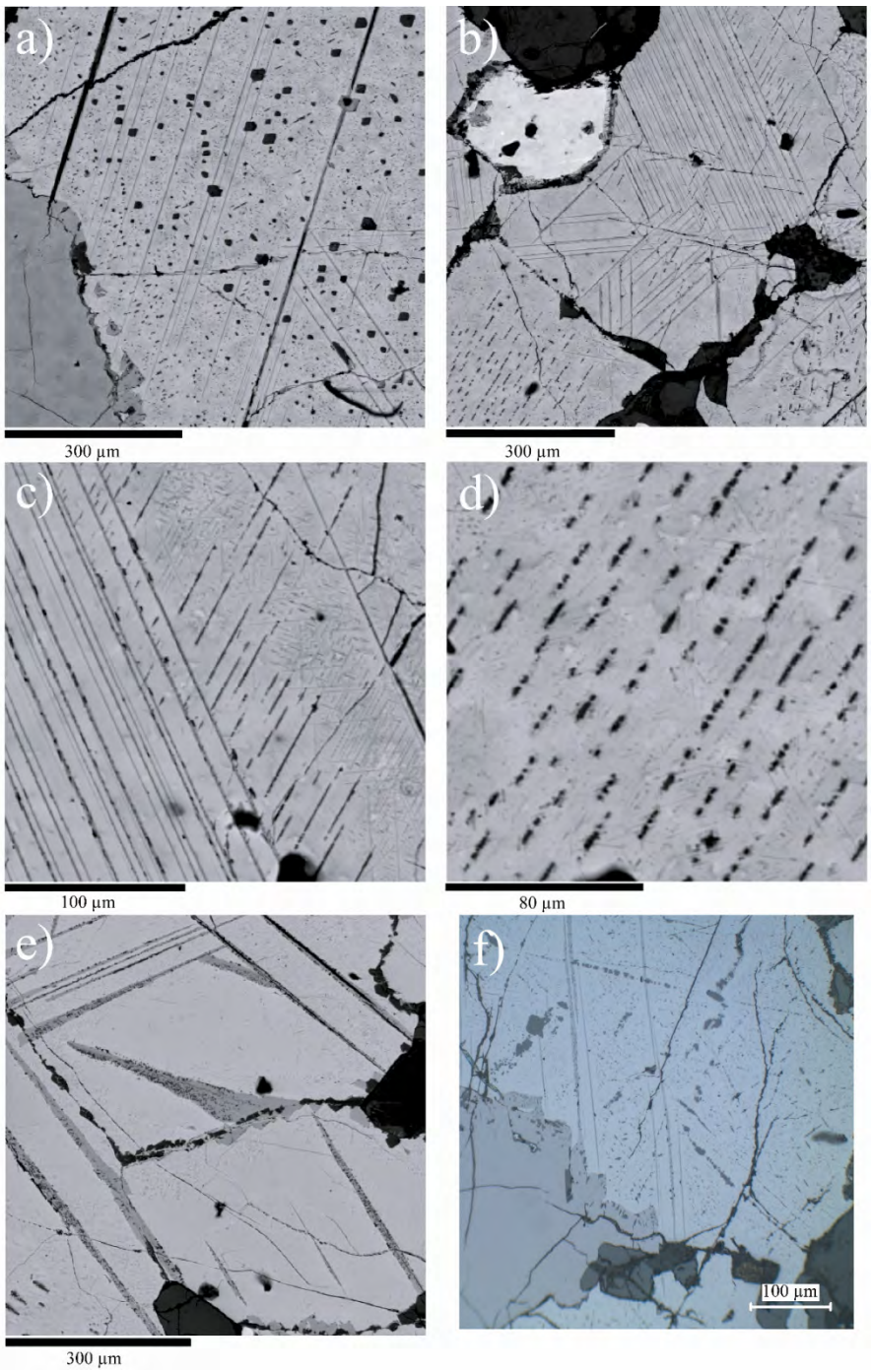

Figure 4.14 Backscatter images of Ti-magnetite exsolution microtextures from the gabbroic rocks of the Jianshan Block, Panzhihua intrusion. a) Relatively low degree of ilmenite lamellae development in an oxide-gabbro. Pleonaste occurs as blebs (Sample 05-2). b) Extensive development of ilmenite lamellae in a typical gabbro from the Jianshan section. Note the variation in the development of ilmenite lamellae: Ti-magnetite grain in bottom-left does not contain extensive ilmenite lamellae (Sample 05-2). c) Extensive development of ilmenite lamellae in a Ti-magnetite grain (Sample 05-2). d) High power image from a Ti-magnetite grain with no trellis/sandwich textured ilmenite lamellae. Note the presence of pleonaste lamellae and the absence of the distinct cloth textured ulvospinel and the minor development of protoilmenite (fine-grained darker grey lamellae) (Sample 05-2). e) Coarse-grained ilmenite lamellae, which contain pleonaste blebs (BT-09). f) Ilmenite lamellae extending from within a Ti-magnetite grain into an ilmenite granule on the grain boundary.

is particularly evident in the main ore layer where the Ti-magnetite/ilmenite ratio increases from 12 at the base up to 20 near the top. This is also evident from the MZa massive ore layer where the ratio increases from 11 toward the base up to 16 nearer the top of the layer.

Spinel plate exsolution within Ti-magnetite grains show a general decrease in size and relative abundance upward in the main ore layer. The average size decreases from 0.04-0.01 mm apart from the base of the main ore layer where the spinel plates are typically <0.03 mm in size.

4.8.2 Gabbro and oxide gabbro

The mineralogy of the gabbroic rocks of the Panzhihua intrusion ranges considerably. The rocks are comprised of plagioclase and clinopyroxene with lesser olivine, amphibole and apatite (MZb only). Ti-magnetite and ilmenite range in modal abundance from 5 vol. % up to 50 vol. %. The gabbros (< 30 wt %; Fe_2O_3) are characterised by low Mt/Ilm ratios (< 1–5). This is a particularly important feature to note as it is far lower than the massive ore layers (10-20).

Ti-Magnetite and associated exsolution features

All of the exsolution features observed within the Ti-magnetite grains of the ore layers are also observed for the gabbros. Ti-magnetite grains are typically polygonal with straight grain boundaries where in contact with each other. Where silicate proportions are high the Ti-magnetite has a distinct interstitial texture. Exsolution of pleonaste occur as both plates and granules within the cores of Ti-magnetite grains where present.

The most notable difference from the massive ore layers is the occurrence of ilmenite lamellae (Figure 4.14 a-f), which are absent in the ore layer Ti-magnetite. The abundance and development varies considerably between and within samples. Ilmenite lamellae form trellis and sandwich textures and are typically < 0.01 mm in width although rare examples are observed up to 0.04 mm in width. These lamellae are always associated with abundant pleonaste granules, which exsolve within the ilmenite lamellae (Figure 4. 14 e). Pleonaste plates are typically absent in the vicinity of ilmenite lamellae and may be completely absent in grains with well developed trellis ilmenite. Ilmenite lamellae are observed cross-cutting pleonaste plates in rare occurrences with no affect on either.

Internal granular exsolutions of ilmenite are also observed in very rare cases. These granules are typically irregular blebs of ilmenite, which contain abundant fine-grained granules of pleonaste. A particularly important feature to note is that ilmenite lamellae are often observed connected to external granular ilmenite grains along the margins of Ti-magnetite (Figure 4.14 f).

The ulvospinel cloth texture is only well developed within grains with low proportions of ilmenite lamellae. Grains containing well developed trellis ilmenite are characterised by the absence of ulvospinel cloth texture with typical right angle lamellae intersections. In most cases the network lamellae intersect each other at 60^{o} and 120^{o} (Figure 4.14 c and d), which is distinctly different in texture to the right angled ulvospinel network observed within the massive ore layer Ti-magnetite.

Granular ilmenite

Granular ilmenite grains are similar to those described for the ore layers. Grain boundaries with Ti-magnetite are typically serrated (similar development of spinelliferous rims to ore layers) and contain abundant pleonaste granules. Chains of pleonaste granules are rarely observed within the ilmenite grains aligned parallel to grain margins. Magnetite lamellae within the ilmenite grains are common. Ilmenite lamellae are commonly observed extending from within Ti-magnetite grains into ilmenite grains.

Variation between oxide gabbro and gabbro with height in the intrusion

Several variations are noted between the oxide gabbros and gabbros. Ilmenite grains are ubiquitous in all rocks; however the Ti-magnetite/ilmenite ratio varies considerably. Oxide gabbros have ratios of ± 10 whereas the gabbros have ratios < 5. Furthermore there is a distinct variation with height in the intrusion. The MGZ/LZ and the base of the MZa oxide gabbros/gabbros have high Ti-magnetite/ilmenite ratios typically > 8 whereas the gabbros from above 350 m from the base are characterised by much lower ratios, which are generally < 3. No oxide gabbros or ore layers are present above this distinct level.

The relative abundance of ilmenite lamellae varies between the oxide gabbros and gabbros. Typically ilmenite lamellae are rare within oxide gabbros and only form sandwich textures. However, ilmenite

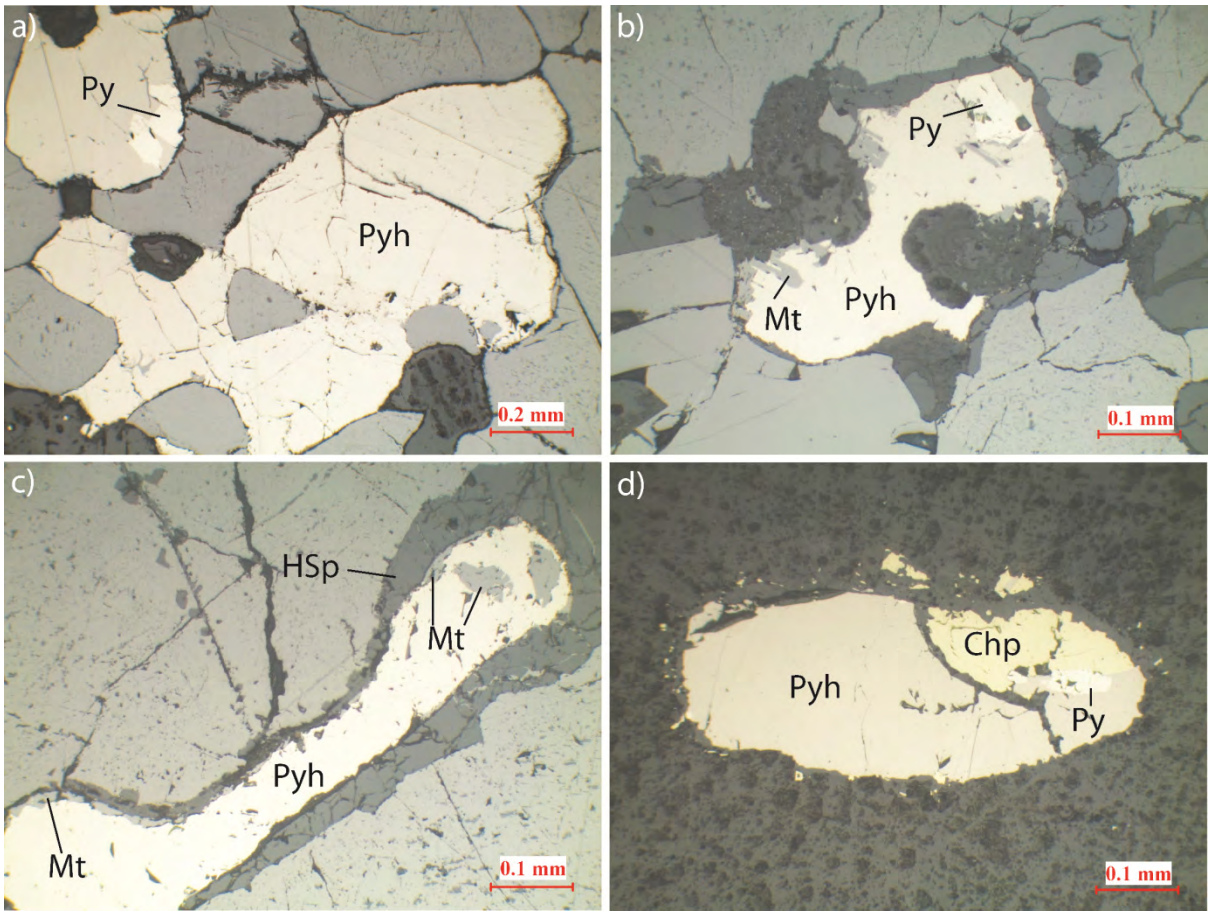

Figure 4.15 Reflected light photomicrographs of the sulphide occurrences within the Panzhihua intrusion. a) Interstitial pyrrhotite (Pyh) with pyrite exsolution (Py) (Sample 05-7). b) Interstitial pyrrhotite (Pyh) with exsolution of pyrite (Py) and magnetite (Mt) (Sample 05-2). c) Interstitial pyrrhotite with exsolutions of magnetite and rimmed by pleonaste (HSp) (Sample 05-7). d) Pyrrhotite (Pyh) bleb included in silicate grain with exsolution of chalcopyrite (Chp) and pyrite (Py) (Sample BT-19).

lamellae within the gabbros are abundant and form well developed trellis textures. The oxide gabbros effectively contain features intermediate between the massive ore rocks and the gabbros.

4.9 Sulphide petrography of oxide ore and gabbroic rocks

Sulphide abundance ranges from 0-4.5 vol. % but generally is < 2 vol. %. Sulphide abundance does not correlate with rock type or chemical trends. Several samples have relatively high sulphide

abundance (> 3 vol. %). Sulphides form either interstitial grains enclosing earlier form oxides and silicates or occur as inclusions within silicate grains. The latter being rare relative to the interstitial sulphides. Interstitial sulphides are typically pyrrhotite (Figure 4.15). Pyrrhotite has exsolved of pyrite (Figure 4.15 a and b) and magnetite (Figure 4.15 c). Magnetite is commonly exsolved along grain boundaries of the sulphide grains. Interstitial sulphides have rims of pleonaste is some occurrences (Figure 4.15 c). Sulphides occurring as inclusions within silicate grains are a similar mineralogy to that described above except for the common occurrence of chalcopyrite as well (Figure 4.15 d).

5. Mineral chemistry

Detailed mineral chemistry studies of the Panzhihua intrusion have been done by Pang et al. (2008a), Pang et al. (2008b) and Pang et al. (2009). These studies have analysed olivine, plagioclase, clinopyroxene, apatite, Ti magnetite and ilmenite over the entire Panzhihua stratigraphy. However detailed analysis of mineral compositional variation through Fe-Ti oxide ore layers has not been done. Presented in this section are mineral composition data for silicates and oxides from the MGZ/LZ, main Fe-Ti oxide ore layer and MZa only in order to constrain the crystallisation of Fe-Ti oxides. Furthermore detailed analyses of reaction rim textures are presented here in order to constrain their development and the implications on Fe-Ti oxide formation.

5.1 Analytical techniques

EPMA data acquisition was performed at Rhodes University, Department of Geology, on a Jeol JXA 8230 Superprobe, using 4 WD spectrometers. Analytical conditions employed were: acceleration voltage 15 kV, probe current 20 nA, counting time 10 sec on peak and 5 sec on background (except for Ni, where the counting time was 20 s and 10 s, respectively). Olivine, pyroxene, amphibole plagioclase and ilmenite were analyzed with spot beam size (< 1 micron). Magnetite was analysed with a 20 micron radius beam in the centre of grains so as to include exsolutions. The standards used for measuring the characteristic Kα radiations were natural minerals: fosteritic olivine sd. for Si and Mg in olivine; fayalite sd. for Fe in all silicates; diopside sd. for Si and Mg in all silicates except olivine; diopside sd. for Ca in olivine; orthoclase sd. for Al in all silicates. In all analyzed minerals the following standards were used: chromite sd. for Cr; rutile sd. for Ti, rhodonite sd. for Mn, orthoclase sd. for K and Al, albite sd. for Na. In most of the cases where an element concentration is below 5%, a large diffracting crystal with high sensitivity was used: LIFL for Ni and Mn in olivine and serpentine; PETL for Ca in olivine, Ti and Cr in most silicates, V in magnetite; TAPL for Na in pyroxene. The ZAF matrix correction method was used for quantification.

5.2 Results - general mineral compositions

5.2.1 Plagioclase

Plagioclase occurs as essentially three populations: a) laths, b) reaction products associated with amphibole and c) fine grains (Figure 5.1). Reaction product plagioclase is described in section 5.3.

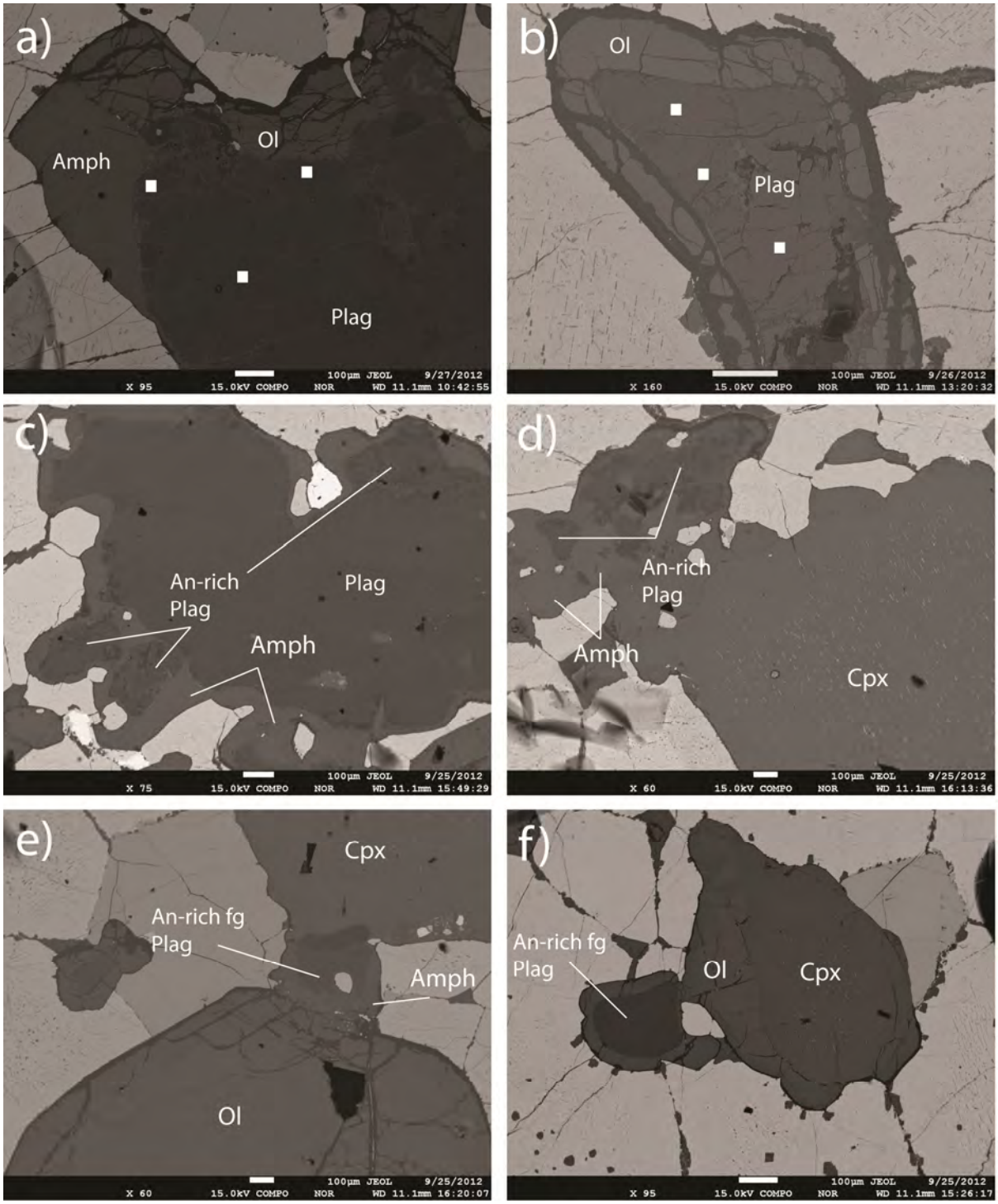

Figure 5.1 Backscatter electron images of plagioclase from the Panzhihua intrusion. a) Plagioclase lath with a rim of amphibole and olivine. White squares represent spot analyses for the plagioclase lath with An contents of An_{51} for the central point and An_{53} and An_{55} for the rim analyses. b) Plagioclase grain with an olivine rim. White squares represent spot analyses, from top to bottom of An_{56}, An_{57} and An_{57}. c) Plagioclase grains associated with reaction products of amphibole. These grains are typically An-enriched An_{73-81} relative to the lath – An_{68}. d) An-enriched plagioclase associated with amphibole reaction product. e) Fine An-enriched plagioclase grain rimmed by amphibole. f) An-enriched plagioclase grain with an olivine rim.

Table 5.1 Plagioclase composition for the Panzhihua intrusion. fg – fine grain

Sample	05_1	05_2	05_3	05_4	05_6	05_7	05_7	05_78	05_8	05_8
Height (m)	8	10	16	23	35	41	41	44	50	50
Occurrence	lath	lath	lath	lath	lath	lath	fg	lath	lath	fg
	n=11	n=2	n=10	n=5	n=10	n=10	n=7	n=13	n=5	n=11
CaO	11.55	11.95	12.00	11.48	11.21	11.27	14.63	11.34	11.31	15.16
K_2O	0.18	0.05	0.21	0.05	0.08	0.10	0.01	0.13	0.08	0.00
Na_2O	5.05	5.01	4.54	4.91	4.94	5.09	4.01	4.80	4.81	3.85
SiO_2	54.29	51.95	53.23	53.97	53.87	54.11	53.32	54.34	54.20	53.69
Al_2O_3	28.47	28.89	29.03	29.93	29.50	29.75	26.89	29.64	29.67	27.58
MnO	0.00	0.03	0.01	0.01	0.01	0.01	0.00	0.01	0.02	0.01
Fe_2O_3	0.28	0.52	0.29	0.04	0.10	0.06	0.13	0.06	0.05	0.15
BaO	0.00	0.00	0.01	0.01	0.01	0.00	0.05	0.01	0.00	0.00
SrO	0.11	0.00	0.11	0.03	0.02	0.01	0.00	0.02	0.01	0.00
Total	99.95	98.41	99.43	100.42	99.74	100.39	99.35	100.35	100.45	100.43
Ca	0.56	0.59	0.59	0.55	0.54	0.54	0.72	0.55	0.55	0.74
K	0.01	0.00	0.01	0.00	0.00	0.01	0.00	0.01	0.00	0.00
Na	0.44	0.45	0.40	0.43	0.43	0.44	0.36	0.42	0.42	0.34
Si	2.46	2.38	2.43	2.43	2.44	2.43	2.45	2.45	2.45	2.44
Al	1.52	1.56	1.56	1.59	1.57	1.58	1.46	1.57	1.58	1.48
Mn	0.00	0.00	0.00	0.00	0.00	0.00	0.00	0.00	0.00	0.00
Fe	0.01	0.02	0.01	0.00	0.00	0.00	0.00	0.00	0.00	0.01
Ba	0.00	0.00	0.00	0.00	0.00	0.00	0.00	0.00	0.00	0.00
Sr	0.00	0.00	0.00	0.00	0.00	0.00	0.00	0.00	0.00	0.00
Sum	5.00	5.00	5.00	5.00	5.00	5.00	5.00	5.00	5.00	5.00
An	56	57	59	56	56	55	67	57	57	69
Range	52-59	57-58	58-62;75	54-60	53-59	51-57	65-70	55-58	55-58	62-69

Table 5.1 continued

Sample	05_9	05_10	BT-01	BT-02	BT-03 (f)	BT-04	BT-05	BT-06	BT-06
Height (m)	54	60	100	115	144	146.9	150	160.2	160.2
Occurrence	lath	lath	lath	lath	lath	lath	lath	lath	fg
	n=14	n=13	n=10	n=11	n=11	n=10	n=11	n=11	n=2
CaO	11.47	11.96	11.22	14.59	11.75	11.49	11.43	11.76	14.02
K_2O	0.20	0.13	0.15	0.27	0.16	0.07	0.13	0.15	0.12
Na_2O	4.99	4.65	5.04	4.08	4.64	4.84	4.90	4.62	3.19
SiO_2	54.16	53.37	54.70	53.54	53.67	53.58	53.96	53.70	50.59
Al_2O_3	28.31	28.70	28.43	26.68	28.60	29.73	29.53	29.76	31.69
MnO	0.01	0.00	0.01	0.00	0.00	0.00	0.01	0.01	0.01
Fe_2O_3	0.33	0.22	0.34	0.24	0.34	0.05	0.08	0.06	0.12
BaO	0.02	0.00	0.01	0.00	0.01	0.01	0.01	0.02	0.01
SrO	0.10	0.00	0.14	0.09	0.14	0.02	0.02	0.01	0.01
Total	99.60	99.03	100.03	99.50	99.32	99.79	100.05	100.09	99.76
Ca	0.56	0.59	0.54	0.72	0.57	0.56	0.55	0.57	0.69
K	0.01	0.01	0.01	0.02	0.01	0.00	0.01	0.01	0.01
Na	0.44	0.41	0.44	0.36	0.41	0.42	0.43	0.41	0.28
Si	2.46	2.44	2.47	2.45	2.45	2.43	2.44	2.43	2.31
Al	1.52	1.55	1.52	1.44	1.54	1.59	1.57	1.59	1.71
Mn	0.00	0.00	0.00	0.00	0.00	0.00	0.00	0.00	0.00
Fe	0.01	0.01	0.01	0.01	0.01	0.00	0.00	0.00	0.00
Ba	0.00	0.00	0.00	0.00	0.00	0.00	0.00	0.00	0.00
Sr	0.00	0.00	0.00	0.00	0.00	0.00	0.00	0.00	0.00
Sum	5.00	5.00	5.00	5.00	5.00	5.00	5.00	5.00	5.00
An	56	59	55	66	58	57	56	58	71
Range	48-59; 85	56-60	54-56	38-99	56-64	56-58	53-59	57-59	70-72

Table 5.1 continued; RP – reaction product; inc – inclusion in olivine

Sample	BT-08 180.365	BT-09	BT-10	BT-13	BT-17	BT-17	BT-17	BT-19	BT-19	BT-19
Height (m)	9	190.5	200	231	265	265	265	271	271	271
Occurrence	lath	lath	lath	lath	lath	inc	fg	lath	RP	inc
	n=7	n=10	n=10	n=10	n=8	n=3	n=5	n=9	n=8	n=1
CaO	10.76	10.63	11.33	11.19	13.06	13.95	14.64	13.15	15.20	12.73
K_2O	0.24	0.15	0.13	0.16	0.07	0.07	0.04	0.06	0.02	0.11
Na_2O	4.84	4.93	4.80	4.71	3.75	3.29	3.21	3.85	2.63	3.91
SiO_2	53.70	53.12	53.09	52.69	50.68	50.52	50.19	51.35	48.74	51.50
Al_2O_3	29.35	29.44	29.88	30.02	31.19	31.64	31.33	30.81	32.42	30.41
MnO	0.01	0.00	0.01	0.00	0.01	0.01	0.01	0.01	0.01	0.00
Fe_2O_3	0.05	0.08	0.05	0.06	0.10	0.11	0.08	0.07	0.10	0.01
BaO	1.35	1.41	1.50	1.16	1.09	0.00	0.01	0.01	0.01	0.00
SrO	0.01	0.01	0.01	0.01	0.01	0.00	0.00	0.02	0.03	0.01
Total	100.31	99.78	100.80	100.00	99.96	99.60	99.52	99.32	99.16	98.69
Ca	0.52	0.52	0.55	0.55	0.64	0.68	0.72	0.64	0.75	0.63
K	0.01	0.01	0.01	0.01	0.00	0.00	0.00	0.00	0.00	0.01
Na	0.43	0.44	0.42	0.42	0.33	0.29	0.29	0.34	0.24	0.35
Si	2.44	2.42	2.40	2.40	2.32	2.31	2.30	2.35	2.25	2.37
Al	1.57	1.58	1.59	1.61	1.68	1.71	1.69	1.66	1.76	1.65
Mn	0.00	0.00	0.00	0.00	0.00	0.00	0.00	0.00	0.00	0.00
Fe	0.00	0.00	0.00	0.00	0.00	0.00	0.00	0.00	0.00	0.00
Ba	0.02	0.03	0.03	0.02	0.02	0.00	0.00	0.00	0.00	0.00
Sr	0.00	0.00	0.00	0.00	0.00	0.00	0.00	0.00	0.00	0.00
Sum	5.00	5.00	5.00	5.00	5.00	5.00	5.00	5.00	5.00	5.00
An	55	54	57	57	66	70	72	65	76	64
Range	53-61	50-59	56-58	55-59	61-69	69-72	67-76	63-68	73-81	64

Table 5.1 continued

Sample	BT-23	BT-27	BT-30	BT-33	BT-37	BT-41	BT-45	BT-48	BT-53
Height (m)	312	336	352	382	423	453	494	504	545
Occurrence	lath	lath	lath	lath	lath	lath	lath	lath	lath
	n=9	n=9	n=9	n=9	n=3	n=2	n=10	n=6	n=3
CaO	11.18	12.00	10.84	10.75	10.84	10.82	10.50	9.29	10.39
K_2O	0.12	0.06	0.14	0.18	0.16	0.14	0.20	0.21	0.23
Na_2O	4.65	4.33	4.94	4.94	5.07	4.96	4.94	6.03	5.20
SiO_2	52.73	52.07	53.12	53.26	52.68	52.99	53.58	54.97	53.17
Al_2O_3	29.47	29.99	29.18	29.33	28.83	28.97	28.98	27.72	28.47
MnO	0.00	0.01	0.01	0.01	0.00	0.01	0.01	0.02	0.00
Fe_2O_3	0.06	0.07	0.07	0.05	0.08	0.10	0.06	0.06	0.08
BaO	1.49	1.49	1.47	1.47	1.74	1.12	1.14	0.94	1.67
SrO	0.01	0.01	0.02	0.01	0.00	0.01	0.01	0.02	0.01
Total	99.71	100.02	99.79	100.00	99.40	99.12	99.44	99.25	99.22
Ca	0.55	0.59	0.53	0.52	0.53	0.53	0.51	0.45	0.51
K	0.01	0.00	0.01	0.01	0.01	0.01	0.01	0.01	0.01
Na	0.41	0.38	0.44	0.44	0.45	0.44	0.44	0.53	0.46
Si	2.41	2.38	2.42	2.43	2.42	2.43	2.45	2.50	2.44
Al	1.59	1.62	1.57	1.57	1.56	1.57	1.56	1.49	1.54
Mn	0.00	0.00	0.00	0.00	0.00	0.00	0.00	0.00	0.00
Fe	0.00	0.00	0.00	0.00	0.00	0.00	0.00	0.00	0.00
Ba	0.03	0.03	0.03	0.03	0.03	0.02	0.02	0.02	0.03
Sr	0.00	0.00	0.00	0.00	0.00	0.00	0.00	0.00	0.00
Sum	5.00	5.00	5.00	5.00	5.00	5.00	5.00	5.00	5.00
An	57	61	55	55	54	55	54	46	52
Range	54-59	54-70	48-57	53-57	54-55	55	53-56	43-48	51-54

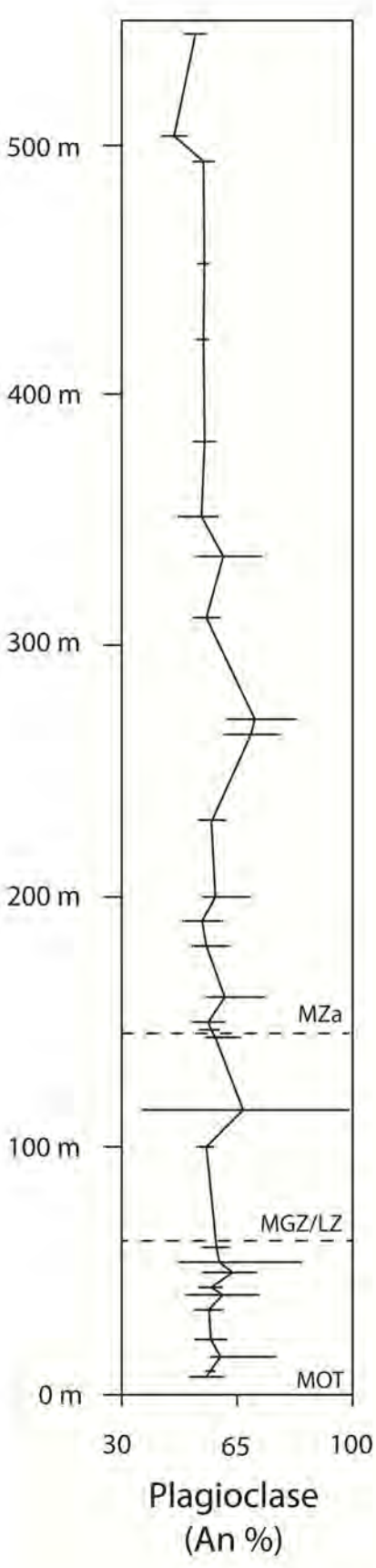

Figure 5.2 Compositional variation of plagioclase laths analysed in this study. The trend line represents the average composition for each sample. MOT – Main ore transect.

Plagioclase lath composition ranges from An_{56} to An_{66} with the exception of one more evolved sample in the upper part of the section (An_{48}). Individual plagioclase laths generally show limited variation (1-2 mol % An) and no significant zoning of grains is observed between cores and rims (Figure 5.1 b). With the exception in rare cases where minor reversed zoning is observed; e.g. Figure 5.1 a. In these cases minor increase in An content is observed at the rims of grains; An increase of 2-4 mol. % An. There is significant variation in the An mol % for individual samples (up to 7 mol %). Sample BT-02 (pegmatoid) has a range in An content from An_{38} to An_{99}. Ranges in An contents for individual samples in given in Table 1 and illustrated in Figure 5.2. Several samples have anomalous high An analyses: e. g. sample 05-9 – An_{85}, with no apparent correlation to grain morphology; i. e. rim vs. core. Fe_2O_3 content of plagioclase is low throughout and no correlation of An content with Fe_2O_3 is observed (Figure 5.3 a). Gabbroic rocks within the MGZ/LZ contain the highest Fe_2O_3 contents (02.-0.5 %). Fe_2O_3 contents of plagioclase within Fe-Ti oxide ore layers are low < 0.1 %. An content shows some minor positive correlation with clinopyroxene Mg# and TiO_2 content (Figure 5.3 b and c).

Plagioclase included within olivine grains is limited to Fe-Ti oxide ore layers. The plagioclase has either similar composition to laths within the same sample (BT-19) or slightly higher An content (BT-17). Fine-grained plagioclase (e.g. Figure 5.1 e and f) analysed from the MZa Fe-Ti oxide ore layers has significantly higher An content (6-12 mol % An) relative to the laths within the same sample.

5.2.2 Clinopyroxene

Clinopyroxene from the Panzhihua intrusion is primarily diopside to augite and has restricted variation in composition (Figure 5.4; data table given in Appendix C). The average end member composition is $En_{42}Fs_{11}Wo_{47}$, which is augite. The Mg# of the clinopyroxene ranges from 77-82 with no variation between the Fe-Ti oxide ores vs. gabbroic rocks. However there is a notable variation in the TiO_2 content between the ore vs. gabbro. Variation in composition within a single sample is generally 1-2 mol. % Mg#. Cr_2O_3 contents are low and below detection limit. TiO_2 contents range from 0.6-1.7 % and are the highest for the Fe-Ti oxide ore layers within the MZa (1.4-1.7 %). There is no correlation of the Mg# with An content.

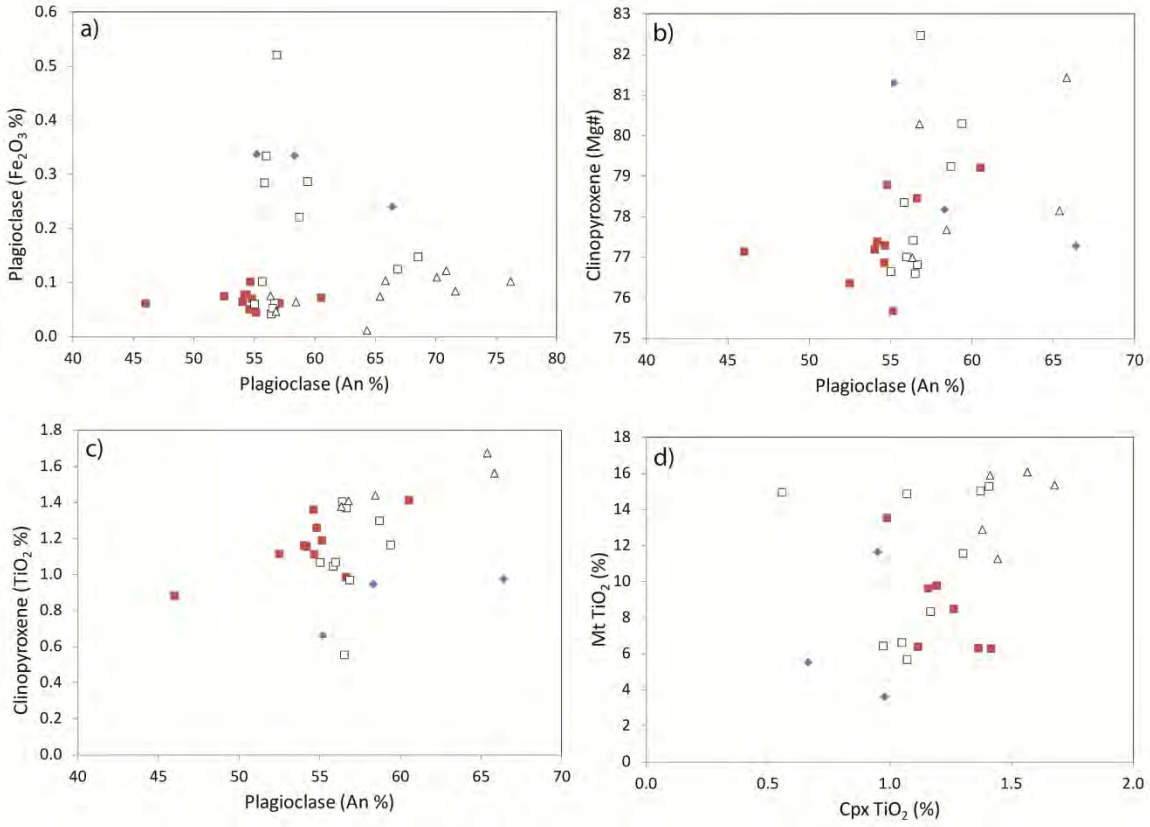

Figure 5.3 Binary plots of major and trace element compositions for the gabbroic and oxide ore rocks of the Panzhihua intrusion. a) Plagioclase An mol. % vs. Fe_2O_3 wt %. b) Plagioclase An mol. % vs. Clinopyroxene Mg#. C) Plagioclase An mol. % vs Clinopyroxene TiO_2 wt %. d) Clinopyroxene TiO_2 wt % vs. Magnetite TiO_2 wt %. Open squares: Main ore intersection. Open triangles: Ore layers from MZa. Solid squares: Gabbroic rocks of the MZa. Blue Diamonds: Gabbroic rocks of MGZ/LZ.

5.2.3 Ti-magnetite

Ti-magnetite ranges significantly in composition between the Fe-Ti oxide ore layers and gabbroic rocks (Appendix D). TiO_2 content ranges from 3.6-16 % with the highest contents for the Fe-Ti oxide ores. MgO, Al_2O_3 and MnO all show a positive correlation with TiO_2, indicating that the Ti-magnetite within the Fe-Ti oxides ores have higher MgO, Al_2O_3 and MnO relative to the gabbroic rocks (Figure 5.5). V_2O_3 and Cr_2O_3 contents are both very low are generally below detection.

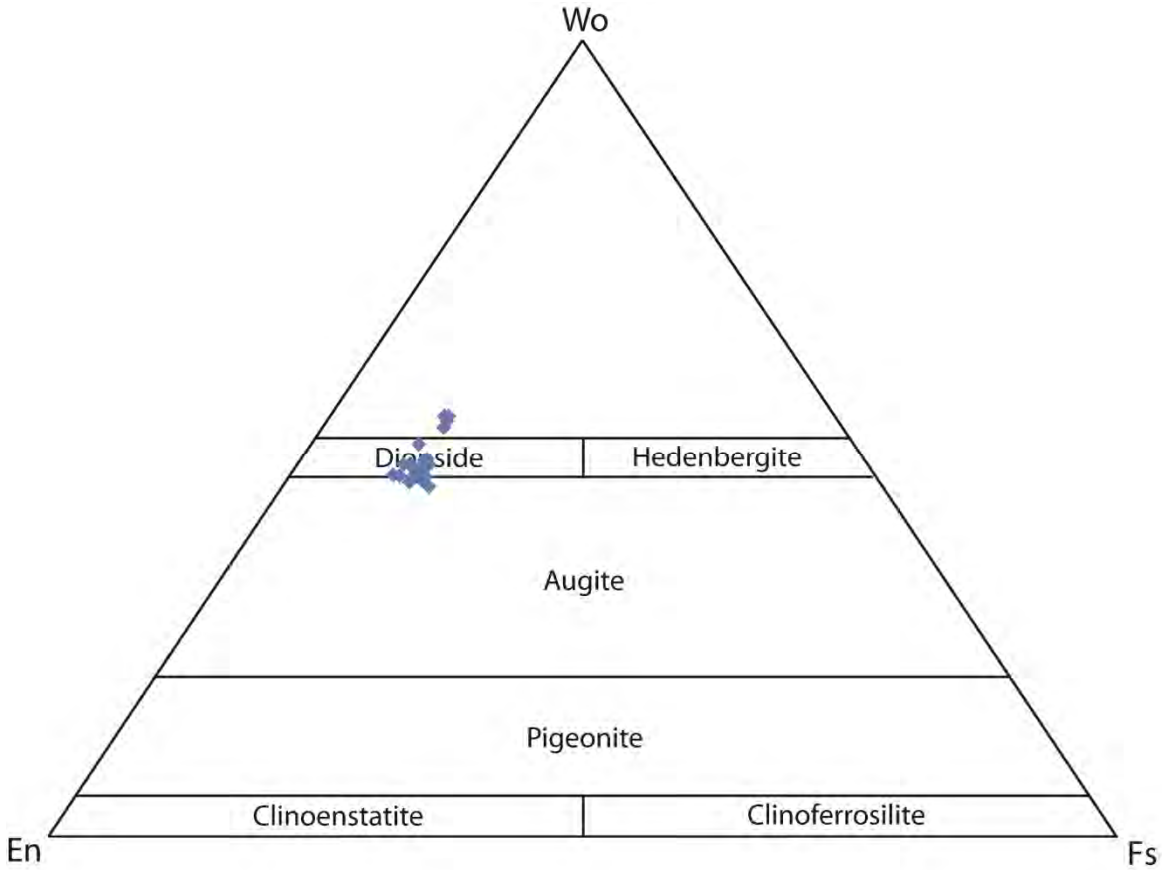

Figure 5.4 Ternary diagram showing the compositional ranges for Ca-Mg-Fe clinopyroxenes with the accepted names (after Morimoto et al. 1988). Clinopyroxene from the Panzhihua intrusion plots within a limited range between augite and diopside with several points just above the diopside field. A full table of analytical results for clinopyroxene is given in Appendix C.

5.2.4 Ilmenite

Ilmenite from the Fe-Ti oxide ore layers has higher MgO (> 6 %) and TiO_2 (> 55 %) relative to the gabbroic rocks (< 4.5 %) and (< 55 %) respectively. Cr and V concentrations are below detection limits. MnO ranges from 0.06-0.6 % and shows no distinct variation between ore and gabbros or stratigraphic height. Data for ilmenite analysed in this study are given in Appendix E.

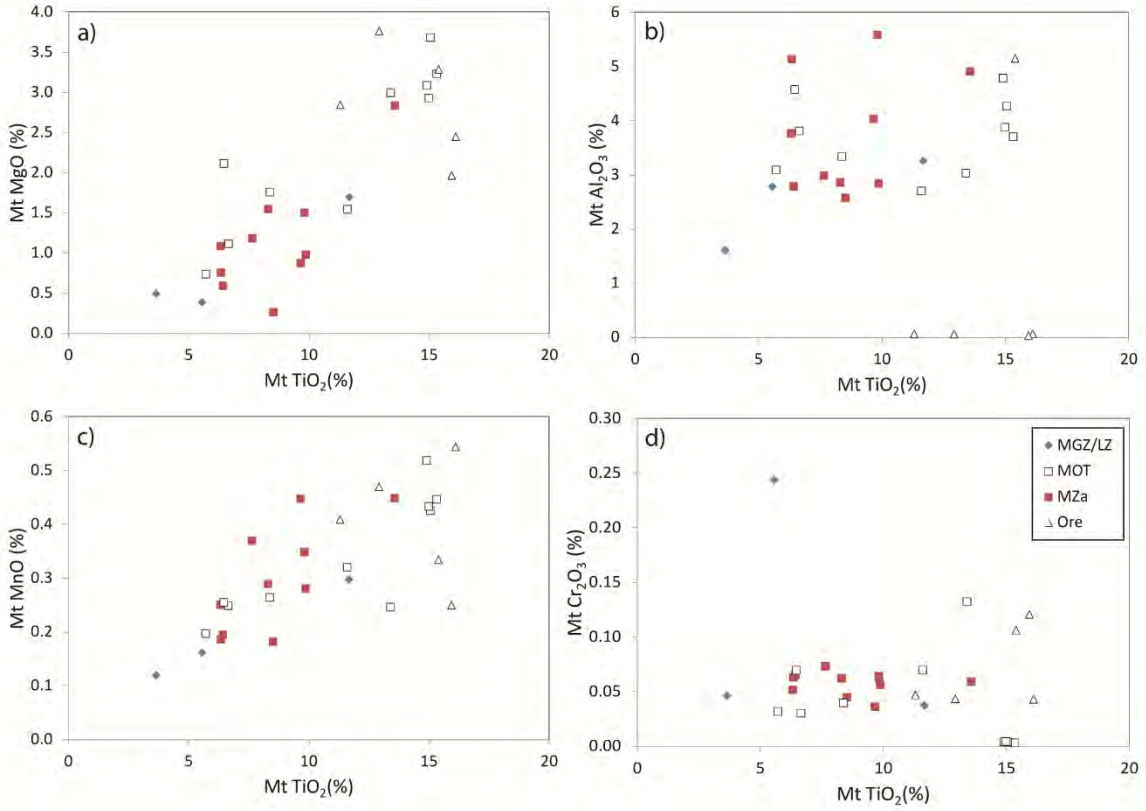

Figure 5.5 Binary variation diagrams for Ti-magnetite from the Panzhihua intrusion. a) TiO_2 vs. MgO, b) TiO_2 vs. Al_2O_3, c) TiO_2 vs. MnO and d) TiO_2 vs. Cr_2O_3.

5.3 Reaction rims

Amphibole has been analysed from the Fe-Ti oxide ore layers only with specific interest in the composition of amphibole rims on plagioclase and clinopyroxene grains. The amphibole is characterised by relatively high TiO_2 (4.75-5.91 %), FeO_T (8-10 %) and Al_2O_3 (12-14 %) and relatively low SiO_2 (42 %) and Na_2O (0.1 %) (Table 5.2). Fe^{3+} and Fe^{2+} were recalculated from analysed FeO using the method described by Holland and Blundy (1994). The Mg# ($Mg/Mg+FeO_T$) ranges from 70-76. The amphibole can be classified as Na-poor kaersutite based on the classification scheme of Leake et al. (1997). No compositional variation between amphibole as rims on plagioclase vs. rims on clinopyroxene is observed.

Olivine has been analysed from the ore layers only with specific interest in the composition of olivine rims vs. olivine grains (Figure 5.6; Table 5.3). Olivine composition of rims and grains ranges from Fo_{73} grains have a slightly more Mg-rich composition of Fo_{79} – Fo_{85}. In particular the comparison of

Table 5.2 Amphibole composition of reaction rims surrounding silicates in Fe-Ti oxide ore layers.

Sample	05_4	05_6	05_7	05_78	05_8	BT-04	BT-05	BT-06	BT-17	BT-19
	n=6	n=14	n=6	n=5	n=7	n=9	n=9	n=4	n=6	n=8
Al_2O_3	13.65	13.90	13.17	14.26	13.66	13.61	12.22	13.53	13.41	13.86
CaO	12.88	12.57	12.63	12.87	12.86	12.85	11.24	12.90	12.85	12.94
K_2O	0.81	0.74	1.03	0.80	0.91	0.65	0.69	0.91	0.76	0.67
SiO_2	41.99	42.24	42.21	42.39	42.26	42.05	42.12	42.39	42.35	42.00
MgO	14.27	13.67	12.99	13.59	13.81	13.98	17.06	13.41	13.95	14.27
Fe_2O_3	2.41	2.16	0.30	1.57	1.01	2.01	8.70	1.94	2.08	2.52
FeO	5.82	7.01	9.44	7.00	7.39	6.16	1.28	7.53	6.83	5.44
MnO	0.06	0.08	0.07	0.10	0.07	0.08	0.11	0.11	0.06	0.08
Cr_2O_3	0.00	0.00	0.00	0.01	0.01	0.01	0.01	0.00	0.01	0.01
TiO_2	5.32	5.07	5.91	4.88	5.66	5.25	4.75	5.19	5.57	5.12
Na_2O	0.10	0.10	0.10	0.10	0.11	0.12	0.10	0.10	0.10	0.11
H_2O	2.00	2.00	2.00	2.00	2.00	2.00	2.00	2.00	2.00	2.00
Total	99.31	99.56	99.85	99.57	99.74	98.76	100.29	100.01	99.97	99.02
Ca	1.99	1.94	1.96	1.98	1.98	1.99	1.70	1.99	1.98	2.00
K	0.15	0.14	0.19	0.15	0.17	0.12	0.12	0.17	0.14	0.12
Si	6.05	6.08	6.12	6.10	6.08	6.08	5.96	6.10	6.08	6.05
Mg	3.06	2.94	2.81	2.91	2.96	3.02	3.60	2.88	2.99	3.06
Fe^{3+}	0.29	0.24	0.03	0.18	0.12	0.25	0.87	0.20	0.23	0.32
Fe^{2+}	0.71	0.88	1.15	0.85	0.89	0.75	0.33	0.94	0.84	0.65
Mn	0.01	0.01	0.01	0.01	0.01	0.01	0.01	0.01	0.01	0.01
Cr	0.00	0.00	0.00	0.00	0.00	0.00	0.00	0.00	0.00	0.00
Al	2.32	2.36	2.25	2.42	2.32	2.32	2.04	2.30	2.27	2.35
Ti	0.58	0.55	0.65	0.53	0.61	0.57	0.51	0.56	0.60	0.55
Na	0.03	0.03	0.03	0.03	0.03	0.03	0.03	0.03	0.03	0.03
Sum	15.17	15.16	15.20	15.16	15.18	15.14	15.18	15.19	15.16	15.14
Mg#	76	73	70	74	75	75	75	72	74	76

to Fo_{85}. Olivine grains have a range of Fo_{73} to Fo_{80} whereas the olivine rims surrounding silicate olivine grains vs. olivine rim compositions from individual samples shows that the olivine rims are always slightly more Mg-rich (1-6 mol.% Fo; Table 5.3). Olivine occurs as rims on both plagioclase and clinopyroxene (Figure 5.1 a, b, e, f), however there is no compositional variation between rims on differing silicate host grains. NiO contents are low for both olivine grains and rims (< 0.05 %).

Table 5.3 Olivine composition for the Fe-Ti oxide ore layers of the Panzhihua intrusion, including coarse grains and reaction rims.

	05_4 Grain n=3	05_4 Rim n=6	05_6 Grain n=6	05_6 Rim n=2	05_7 Rim n=8	05_78 Grain n=3	05_78 Rim n=7	05_8 Grain n=4	05_8 Rim n=4	BT-04 Grain n=3
MgO	42.52	44.30	41.06	43.36	42.35	41.29	43.31	42.46	44.16	41.83
SiO_2	39.01	39.30	38.94	39.11	38.74	38.77	39.41	38.85	39.13	38.88
FeO	18.96	16.72	20.22	18.53	19.51	19.50	17.89	18.93	17.34	18.57
MnO	0.36	0.30	0.35	0.30	0.35	0.37	0.35	0.34	0.29	0.38
NiO	0.01	0.01	0.02	0.00	0.02	0.01	0.01	0.01	0.02	0.00
CaO	0.00	0.00	0.00	0.00	0.00	0.00	0.00	0.00	0.00	0.00
Total	100.86	100.64	100.58	101.30	100.96	99.95	100.97	100.60	100.93	99.66
Mg	1.60	1.66	1.56	1.62	1.60	1.58	1.62	1.61	1.65	1.60
Si	0.99	0.99	1.00	0.98	0.98	0.99	0.99	0.99	0.98	1.00
Fe	0.40	0.35	0.43	0.39	0.41	0.42	0.38	0.40	0.36	0.40
Mn	0.01	0.01	0.01	0.01	0.01	0.01	0.01	0.01	0.01	0.01
Ni	0.00	0.00	0.00	0.00	0.00	0.00	0.00	0.00	0.00	0.00
Ca	0.00	0.00	0.00	0.00	0.00	0.00	0.00	0.00	0.00	0.00
Sum	3.00	3.00	3.00	3.00	3.00	3.00	3.00	3.00	3.00	3.00
Fo	80	83	78	81	79	79	81	80	82	80

Table 5.3 continued

	BT-04 Rim n=9	BT-05 Grain n=3	BT-05 Rim n=6	BT-06 Grain n=3	BT-06 Rim n=9	BT-17 Grain n=4	BT-17 Rim n=5	BT-19 Grain n=5	BT-19 Rim n=3
MgO	44.42	42.71	43.34	37.90	41.92	40.64	43.99	41.82	45.60
SiO2	39.52	38.96	39.15	38.14	38.93	38.70	39.55	38.86	39.64
FeO	15.80	18.81	18.18	24.76	19.81	20.31	16.66	19.71	14.90
MnO	0.27	0.32	0.34	0.50	0.38	0.34	0.23	0.35	0.26
NiO	0.01	0.02	0.01	0.00	0.01	0.03	0.02	0.01	0.02
CaO	0.00	0.00	0.00	0.00	0.00	0.00	0.00	0.00	0.00
Total	100.03	100.82	101.02	101.31	101.05	100.02	100.44	100.76	100.42
Mg	1.67	1.61	1.63	1.46	1.58	1.56	1.65	1.59	1.70
Si	0.99	0.99	0.98	0.99	0.99	1.00	0.99	0.99	0.99
Fe	0.33	0.40	0.38	0.54	0.42	0.44	0.35	0.42	0.31
Mn	0.01	0.01	0.01	0.01	0.01	0.01	0.00	0.01	0.01
Ni	0.00	0.00	0.00	0.00	0.00	0.00	0.00	0.00	0.00
Ca	0.00	0.00	0.00	0.00	0.00	0.00	0.00	0.00	0.00
Sum	3.00	3.00	3.00	3.00	3.00	3.00	3.00	3.00	3.00
Fo	83	80	81	73	79	78	82	79	85

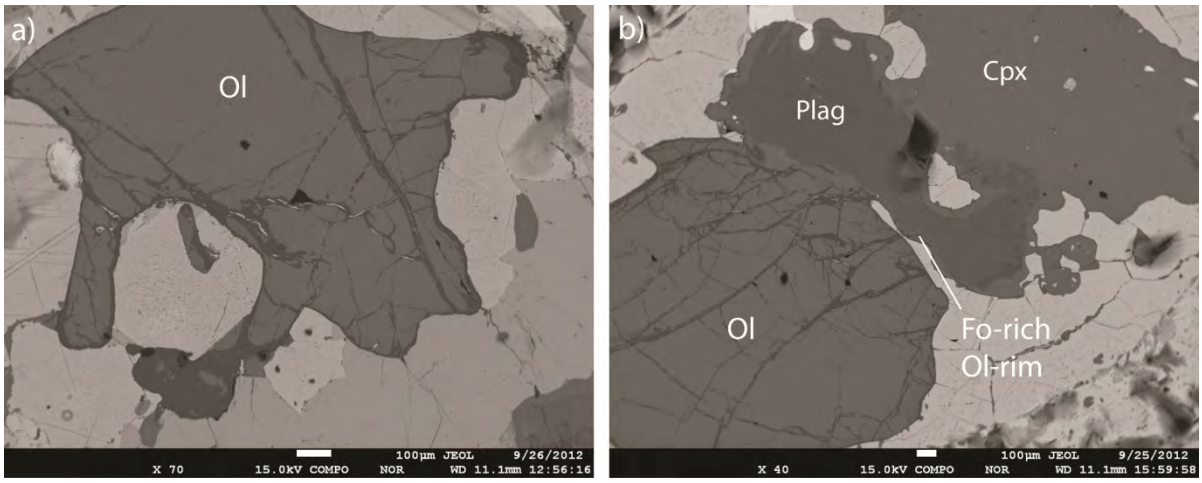

Figure 5.6 Coarse olivine grains. a) Coarse olivine partially enclosing a Ti-magnetite grain within the main ore layer. b) Coarse olivine grain and Fo-enriched olivine rim on a plagioclase lath from an ore layer within the MZa (sample BT-19).

Plagioclase observed as reaction products are rare and only analysed from sample BT-19 (Figure 5.1 c and d). In sample BT-19 there is a significant increase in An content for the plagioclase overgrowths (11 mol % An).

5.4 Stratigraphic variations

Plagioclase lath composition generally shows little variation over the stratigraphy of the lower Panzhihua intrusion (Figure 5.7). A distinct increase in An content of plagioclase laths is observed for the upper MZa ore layer where An content increases from An_{57} in the underlying gabbroic rocks to An_{66} within the ore layer and subsequent decrease to An_{57} in the gabbroic rock above the ore layer (Figure 5.7 b). Fe_2O_3 content of plagioclase is high for the gabbroic rocks above and below the main ore layer and the gabbroic rocks of the MGZ/LZ (Figure 5.7 c). No correlation is observed with increase An content in the upper MZa ore layer. Clinopyroxene Mg# is generally consistent and shows no distinct increases/decreases (Figure 5.7 d). TiO_2 content of clinopyroxene is generally higher within ore layers and this is also evident by an increase in TiO_2 content of the upper MZa ore layer (Figure 5.7 e). TiO_2 content varies considerably and is highest for ore layers (Figure 5.7 f)

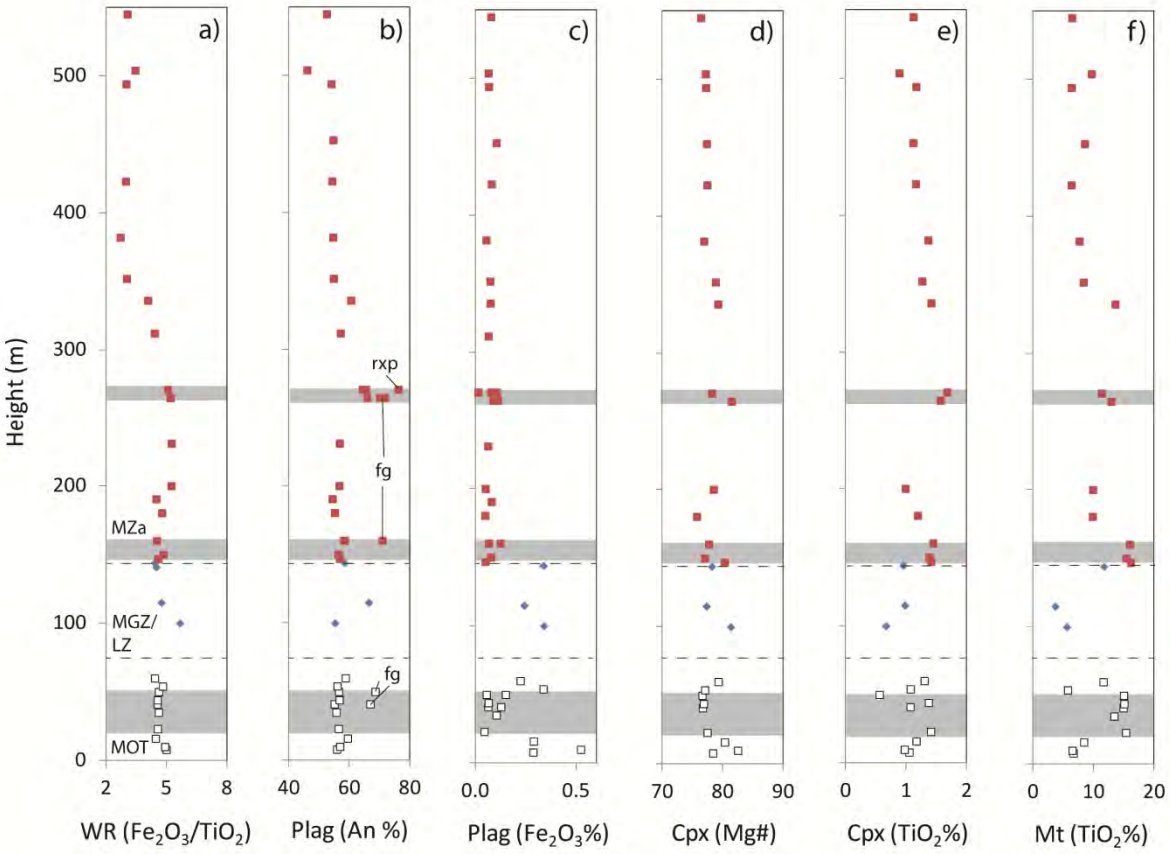

Figure 5.7 Stratigraphic variation of mineral phases analysed in this study.

5.5 Discussion on reactions forming rims on silicate within Fe-Ti oxide ore layers

Reactions related to the formation of rims or coronas in natural rocks have been discussed in numerous papers (e.g. van Lamoen, 1979; Acquafredda et al. 1992; Larikova and Zaraisky 2009). The principal debate in many studies is whether individual reactions form in an open or closed system. van Lamoen (1979) suggests that opaque oxide-silicate reaction rims/coronas forming in gabbroic and Fe-Ti oxide ore rocks from Finland occur in an open system. Coronas and reactions described by van Lamoen (1979) are very similar to those observed in this study and will be used here for comparison. Reactions are discussed in order to explain the development of reaction product assemblages observed at the Panzhihua intrusion. The reactions are based on the assumption that the minerals analysed are the reactant and product phases involved in formation. Such an assumption is only true if no sub-solidus re-equilibration of the primary mineral phases occurred.

Table 5.4 Summary of Reactant grains and reaction rim assemblages

Grain	Rim	Rim	Grain
Plagioclase	Amphibole		Fe-Ti Oxide
Plagioclase	Amphibole+Olivine		Fe-Ti Oxide
Plagioclase	Amphibole	Olivine	Fe-Ti Oxide
Plagioclase	Olivine		Fe-Ti Oxide
Plagioclase	Amphibole	Pleonaste	Fe-Ti Oxide
Clinopyroxene	Amphibole		Fe-Ti Oxide
Clinopyroxene	Amphibole+Olivine		Fe-Ti Oxide
Clinopyroxene	Amphibole	Olivine	Fe-Ti Oxide
Clinopyroxene	Plagioclase (± Amphibole)		Fe-Ti Oxide

Two principal reactions are observed at the Panzhihua intrusion: 1) opaque oxide-plagioclase and 2) opaque oxide-clinopyroxene. In both cases the reactant mineral assemblage is similar, including: most commonly kaersutite and Fo-enriched olivine with lesser An-enriched plagioclase, pleonaste and very rare clinopyroxene. A summary of reactants and product phases is given in Table 5.4.

5.5.1 Opaque oxide-plagioclase reactions

The reaction of plagioclase and a fluid phase is expressed in equation (1) (after van Lamoen, 1979). Furthermore the reaction of magnetite and a fluid phase is expressed in equation (2) (after van Lamoen, 1979):

Plagioclase Fluid

$(Na_{0.44}Ca_{0.56}Al_{1.60}Si_{2.40}O_8) + (0.64Fe+0.95Mg+0.34H_2O) \longrightarrow$ (1)

Hornblende Spinel Fluid

$0.34(Na_{0.84}Ca_{1.81}Fe_{1.57}Mg_{2.64}Al_{2.70}Si_{6.08}O_{22}(OH)) + 0.15(Fe_{0.7}Mg_{0.34}Al_{1.93}O_4) + (0.15Na+0.06Ca+0.39Al+0.33Si)$

Magnetite Fluid

$(Fe_{2.63}Mg_{0.03}Al_{0.16}Ti_{0.13}O_4) + (0.14Na+0.30Ca0.41Mg+0.26Al+0.98Si+0.16H_2O) \longrightarrow$ (2)

Hornblende Fluid

$0.16(Na_{0.84}Ca_{1.83}Fe_{1.51}Mg_{2.72}Ti_{0.18}Al_{2.62}Si_{6.10}O_{22}(OH)_2) + (2.39Fe0.10Ti+0.24O_2)$

In both cases the fluid phase is H_2O-bearing in order to account for the formation of hornblende as the dominant product phase. This is very similar to the reactions observed at the Panzhihua intrusion. Opaque oxide-plagioclase reactions at Panzhihua are most commonly associated with amphibole reaction products and less commonly amphibole and spinel. Reactions given in equations

(1) and (2) can account for these associations, although the amphibole at Panzhihua is more Ti-rich than a typical hornblende. However olivine is also commonly observed as a product phase associated with opaque oxide-plagioclase reactions. Olivine cannot be accounted for in equations (1) and (2) as the Mg all goes into hornblende. A combination of equations (1) and (2) gives the typical reaction product assemblage observed at Panzhihua with the exception of olivine. The lack of olivine produced by this reaction is due to the lack of Mg available for olivine formation. Equations (3) and (4) show two further scenarios for fluid phases reacting with plagioclase.

Plagioclase Fluid

$$(Na_{0.44}Ca_{0.56}Al_{1.60}Si_{2.40}O_8) + (1.26Fe+1.59Mg+0.65O_2) \longrightarrow$$

(3)

Orthpyroxene Spinel Fluid

$$2.38(Fe_{0.37}Mg_{0.59}Al_{0.04}Si_{0.98}O_3) + 0.54(Fe_{0.7}Mg_{0.34}Al_{1.93}O_4) + (0.44Na+0.56Ca+0.46Al)$$

Plagioclase Fluid

$$(Na_{0.44}Ca_{0.56}Al_{2.64}Si_{2.40}O_8) + (0.27Fe+0.41Mg+0.19Ca) \longrightarrow$$

(4)

Orthpyroxene Anorthite Fluid

$$0.70(Fe_{0.39}Mg_{0.56}Al_{0.03}Si_{0.98}O_8) + 0.77(Na_{0.02}Ca_{0.98}Al_{1.98}Si_{2.02}O_8) + (0.42Na)$$

Equations (3) and (4) show that in the absence of H_2O in the fluid phase no amphibole is produced as a reaction product and Mg-rich silicate (orthopyroxene) is produced in its place. Furthermore in equation (4) anorthite is produced from reaction with a fluid phase with lower Mg relative to equation (3) where spinel is produced.

These reactions suggest that the composition of products produced during opaque oxide-plagioclase reactions are essentially controlled by the composition of the fluid phase. Furthermore these reactions clearly occur within an open system as a fluid phase is produced in all the reactions. These reactions place some constraints on the fluid phase driving the formation of reaction products at the Panzhihua intrusion. In order to account for the common association of kaersutite (amphibole) and olivine the fluid phase must be H_2O-bearing and must be very Mg-rich. The less common association of kaersutite with An-rich plagioclase indicates a H_2O-bearing Ca-rich fluid.

5.5.2 Opaque oxide-clinopyroxene reactions

The reaction of clinopyroxene and a fluid phase is expressed in equation (5) (after van Lamoen, 1979).

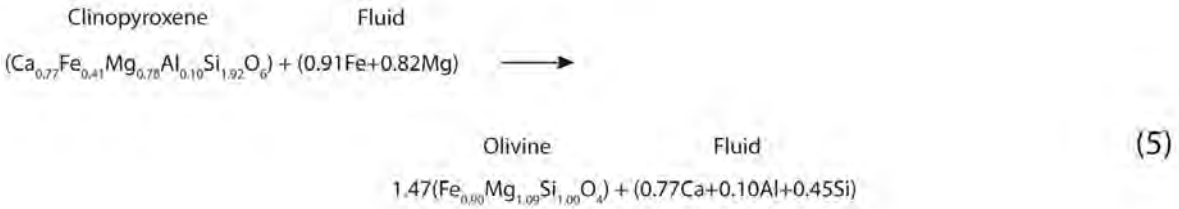

(5)

In this case clinopyroxene reacts with a fluid phase producing olivine as a reaction product. This is a common feature of the Panzhihua intrusion. A combination and equations (2) and (5) indicates that along with olivine crystallisation, as a result of clinopyroxene reaction, amphibole is also associated with opaque oxide-clinopyroxene reactions due to magnetite reaction with a H_2O-bearing fluid phase. Again in this case an H_2O-bearing fluid phase is required in order to account for amphibole occurrence.

5.5.3 Panzhihua reactant and product mineral compositions

Reactions for mineral compositions analysed at the Panzhihua intrusion are expressed in equations (6)-(10). All these reactions take place in association with magnetite reaction given in equation (2). It is immediately apparent that the fluid phase required to form the reactions products is highly variable. All of the reactions (6)-(10) may occur within a single sample at Panzhihua. Reactions involving plagioclase (6)-(8) require a Mg and Fe –rich liquid to produce olivine and amphibole reaction products. Fe is easily sourced from concurrent reaction of magnetite, however Mg concentration is low in magnetite and plagioclase. This implies that these reactions occur in an open system where Mg is sourced from elsewhere. No other reactions presented for the Panzhihua compositions or those presented by van Lamoen (1979) (equations (1)-(5)) produce significant Mg in the fluid phase. This implies that Mg is externally derived. The formation of kaersutite amphibole from either plagioclase or clinopyroxene requires addition of Ti in the fluid phase. This is similar to Fe and can be sourced from concurrent magnetite reaction. In reaction (8) An-enriched plagioclase is observed as a reactant phase. This requires Ca in the fluid phase. Ca must be sourced from outside the magnetite-plagioclase reaction. Ca is produced by reaction (9) where olivine forms from clinopyroxene reaction. This may suggest that there is some interaction between fluids produced

from the reactions (6)-(10). In order to account for the production of An-enriched plagioclase associated with clinopyroxene reactions a Na+Al fluid phase is required (reaction (10)). Na and Al are typically produced by plagioclase reactions (6)-(8) and further suggest interaction by fluid produced in the various reactions.

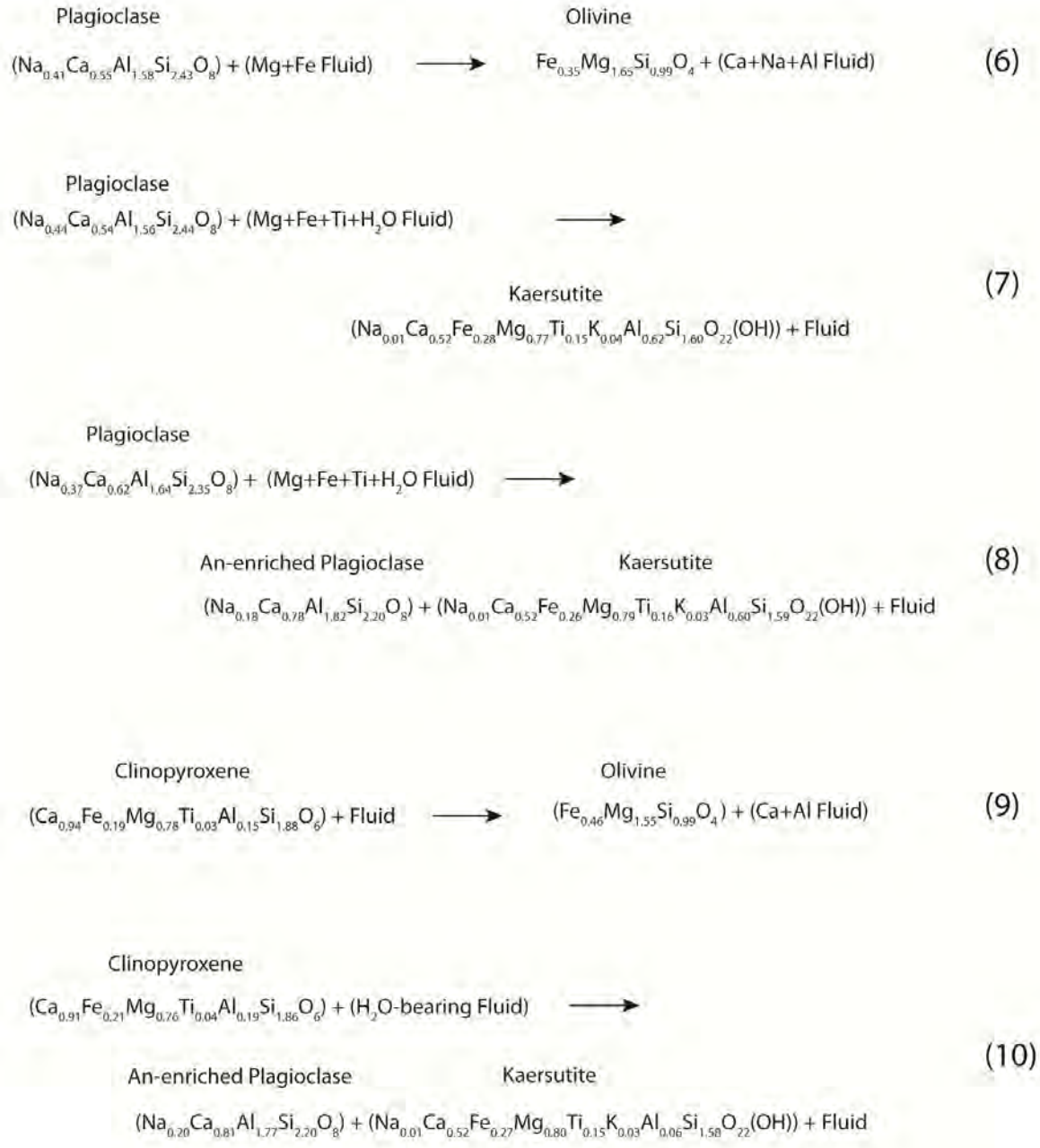

5.5.4 Conclusions for reaction rim formation

The petrographic and mineral composition data discussed above and reactions expressed for the development of reaction rims indicate several conclusions about their formation. The reaction

assemblages formed from the reaction of primary minerals facilitated by a reactant medium of a fluid phase. The fluid phase has variable composition; however the dominance of kaersutite amphibole as a reaction product indicates that the fluid phase was H_2O-rich. Reaction products must form essentially as allochemical systems involving mass transfer between the reactant primary minerals within the reaction assemblage and between the reaction assemblage and the surroundings. Overall reaction product assemblage within a sample likely involved the net gain of at least H_2O and Mg. The high Ti content of amphiboles and the addition of Fe of plagioclase reactions indicate significant involvement of Ti-magnetite in the reaction. TiO_2 and Al_2O_3 contents of calcic amphiboles can be used to determine the temperature and depth of formation using the thermobarometer of Ernst and Liu (1998). The TiO_2 content of the kaersutite observed as reaction products at the Panzhihua intrusion is significantly high (4 wt %) than the TiO_2 content of hornblende produced in the Fe-Ti oxide ore rock described by van Lamoen (1979). This suggests that the amphibole at the Panzhihua intrusion formed at significantly higher temperatures. This is discussed further in section 9.3.4 with implications for Fe-Ti oxide ore forming processes.

6. Whole-rock geochemistry

The following section presents results for whole-rock geochemical analysis of the Jianshan and Nalaqing Blocks, Panzhihua intrusion. Major element, trace element, PGE and Sr-Nd isotope variations are presented and illustrated along with analytical techniques used to analyse powders. Full data sets for the whole-rock geochemistry are presented in Appendix B.

6.1 Analytical techniques

6.1.1 Major element geochemistry

Major Element geochemistry was done through XRF analysis at the Department of Geological Sciences, University of Cape Town, South Africa. Samples were analysed by a X'Unique XRF spectrometer for Fe, Mn, Ti, Ca, K, S, P, Si, Al, Mg and Na. Major elements were determined using fusion disks prepared with LiT-LiM flux in the proportion 57:43 and LiBr as releasing agent. Intensity data are collected using the Phillips X40 software. Spectral overlap corrections are made for Br on Al, Cr on Mn, Al and Ca on Mg, and Mg and Ca on Na. Matrix corrections are made on all elements using the de Jongh model in the X40 software along with theoretical alpha coefficients, which are calculated using Phillips on-line ALPHAS programme.

6.1.2 Trace element geochemistry

Trace elements for the main Fe-Ti oxide ore intersection, MGZ/LZ and MZa were analysed at the Department of Geological Sciences, University of Cape Town, by solution inductively coupled plasma mass spectrometry (ICP-MS) on a Perkin-Elmer ELAN 6000 system. Appendix B presents data on the analyses of procedural blanks and international standards for the trace element analyses. Trace elements for the MZb and UZ were analysed at by wave-length dispersive X-ray fluorescence spectrometry at the Department of Geology, Rhodes University. A full trace element data set is presented in Appendix B.

Duplicate samples from the MGZ/LZ, Main ore layer and MZa were run for trace elements on the XRF at Rhodes University for comparison with ICP-MS data obtained. Figure 6.1 (a-f) illustrates the results of XRF vs. ICP-MS data. In general the absolute concentrations of trace elements are

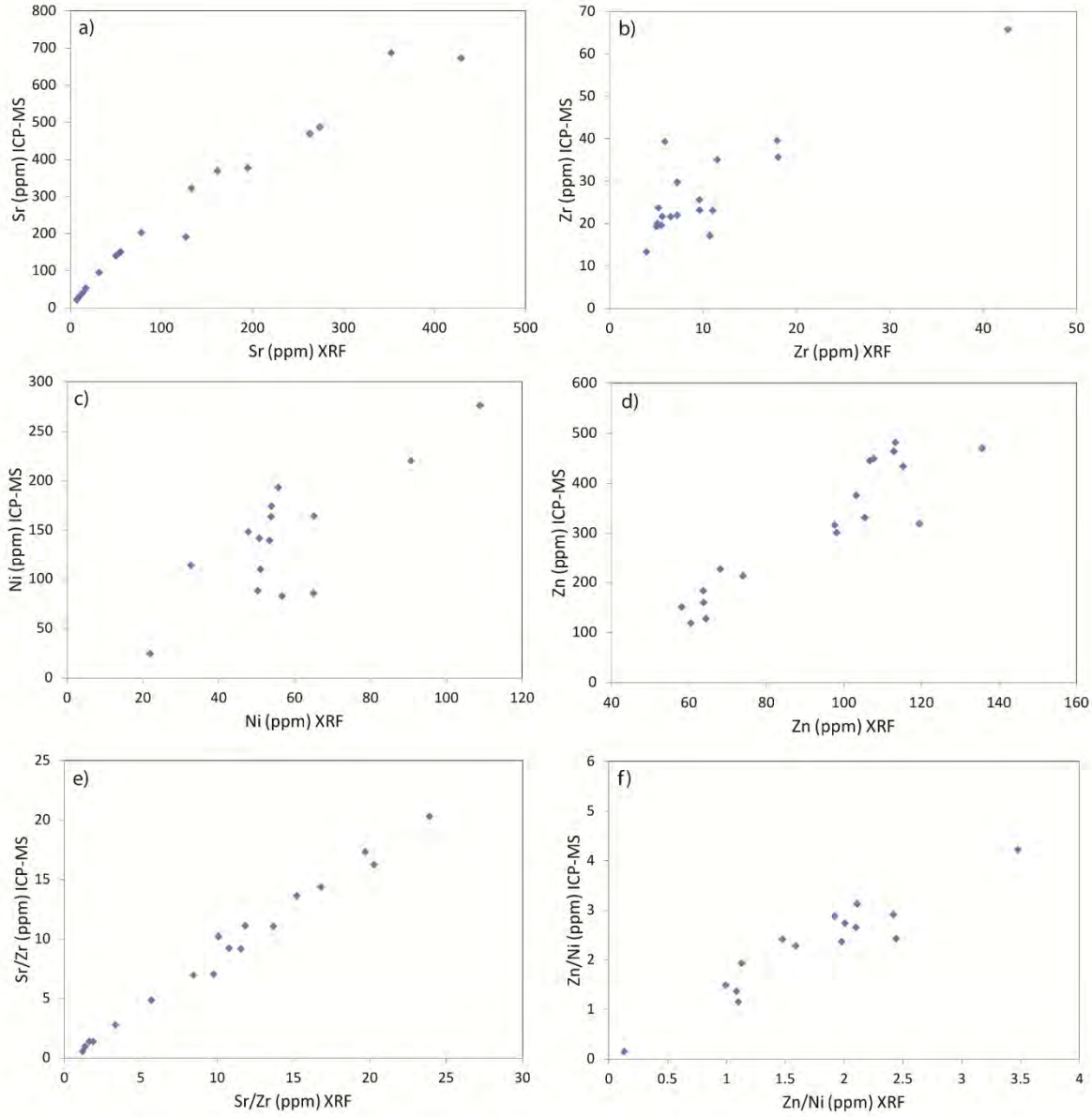

Figure 6.1 Comparison of whole-rock trace element geochemical analysis of XRF vs. ICP-MS.

somewhat different but show good positive correlation. This implies that although the concentrations are different the overall trends would be similar for XRF and ICP-MS data. Comparison of trace element ratios shows even better positive correlations. However direct comparison of trace element concentrations of XRF vs. ICP-MS results is not appropriate as the concentrations do not correlate. For example Zn concentrations (Figure 6.1 d) have a maximum of 135 ppm for XRF and a maximum of 482 ppm for ICP-MS. Direct comparison of ICP-MS data for the MGZ/LZ and MZa with XRF data for the MZb and UZ needs to be done with care. However, overall trends shown by XRF in comparison with ICP-MS are appropriate. Cu could not be analysed for ICP-

MS (technical difficulties at the laboratory used) and therefore XRF Cu data is used. Cu is only used for comparison with PGE data.

6.1.3 Platinum group element geochemistry

A total of 25 samples were selected from the main Fe-Ti oxide ore layer, MGZ/LZ and MZa for PGE analysis (Table 6.1) at the University of Quebec at Chicoutimi, Canada. Analytical procedures followed those of Savard et al. (2010).

6.1.4 Sr and Nd isotope geochemistry

A total of 27 samples covering the entire stratigraphy of the intrusion were selected for whole-rock Sr and Nd isotopic analysis (Table 6.2). Nd and Sr isotopic compositions, and Sm and Nd concentrations were analysed by isotope dilution at the CNRS in Rennes, France, following the procedure of Kirkland et al. (2011). Rb-Sr ratios were determined independently on separate whole rock splits from the same samples by ICP-MS at the University of Cape Town as described above.

6.1.5 O-isotope geochemistry

Oxygen isotope ratios were measured in the stable isotope laboratory at the Department of Geological Sciences at the University of Cape Town, South Africa. Extraction of O from plagioclase and magnetite was performed using conventional ClF_3 line. The method for oxygen extraction and the facilities at UCT are explained in further detail by Harris and Ashwal (2002) and Fagereng et al. (2008).

6.2 Whole-rock geochemical results

6.2.1 Major and trace element variation

Major element variation

Concentrations of major elements for the Panzhihua intrusion are given in Appendix B. There are large variations in SiO_2 (0-58 wt %), Fe_2O_3 (3-73 wt %) and TiO_2 (0.5-16 wt %). Concentrations of SiO_2

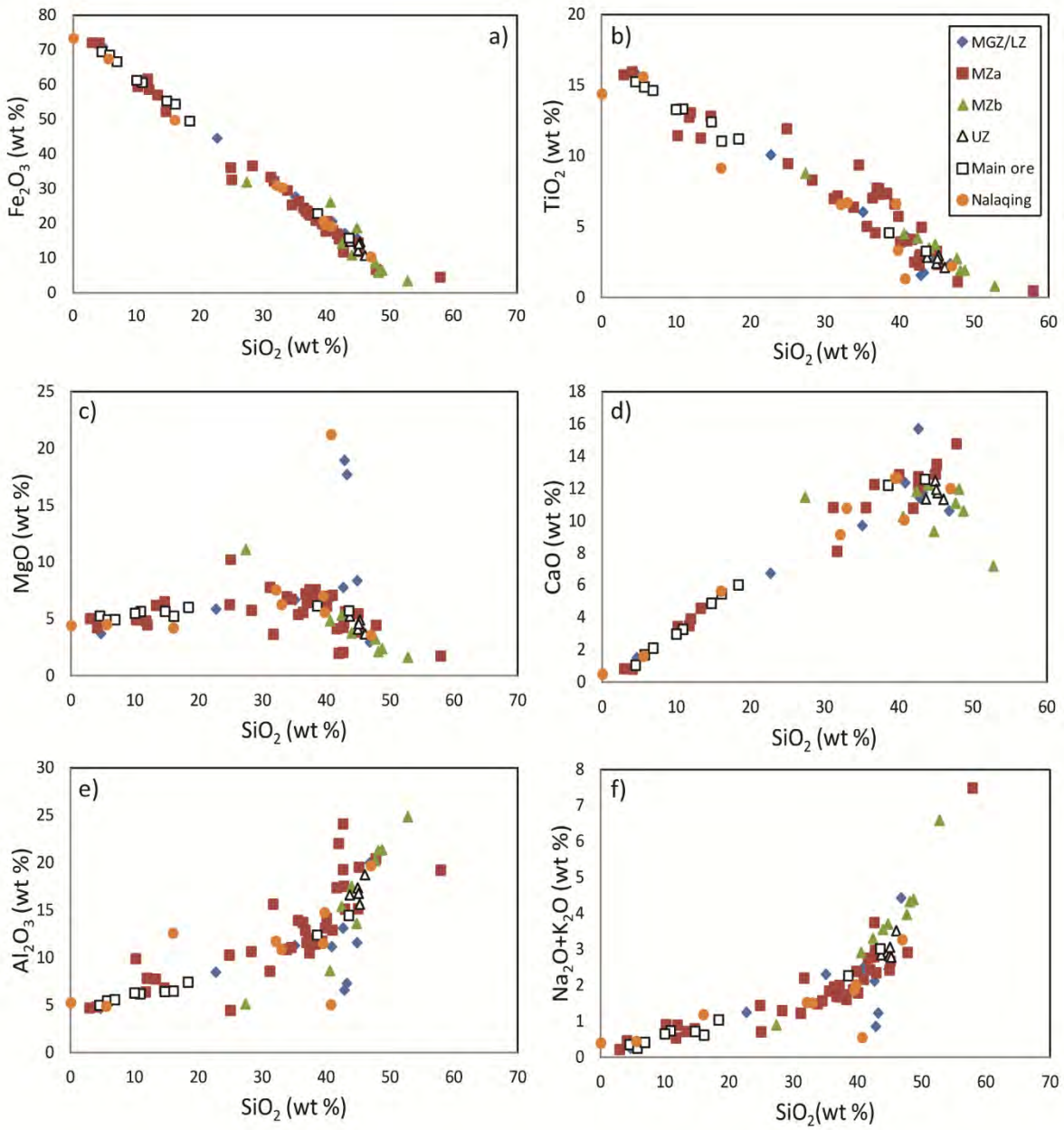

Figure 6.2 Whole-rock major element oxide variation diagrams for SiO_2, Fe_2O_3, MgO TiO_2, CaO, Al_2O_3 and Na_2O+K_2O for the Jianshan and Nalaqing Blocks, Panzhihua intrusion.

are negatively correlated with Fe_2O_3 and TiO_2 (Figure 6.2 a and b). It is particularly noteworthy that diagrams of SiO_2, Fe_2O_3, and V with TiO_2 (Figure 6.2 a, b and 6.3) all show two distinct trends. Rocks of the upper MZa and MZb plot on a high-Ti trend whereas rocks from the MGZ/LZ, Main ore layer, lower MZa and UZ plot on a low-Ti trend. MgO concentrations are low and show no obvious trends (Figure 6.2 c). SiO_2 concentrations are positively correlated with Al_2O_3 and CaO (Figure 6.2 d and e).

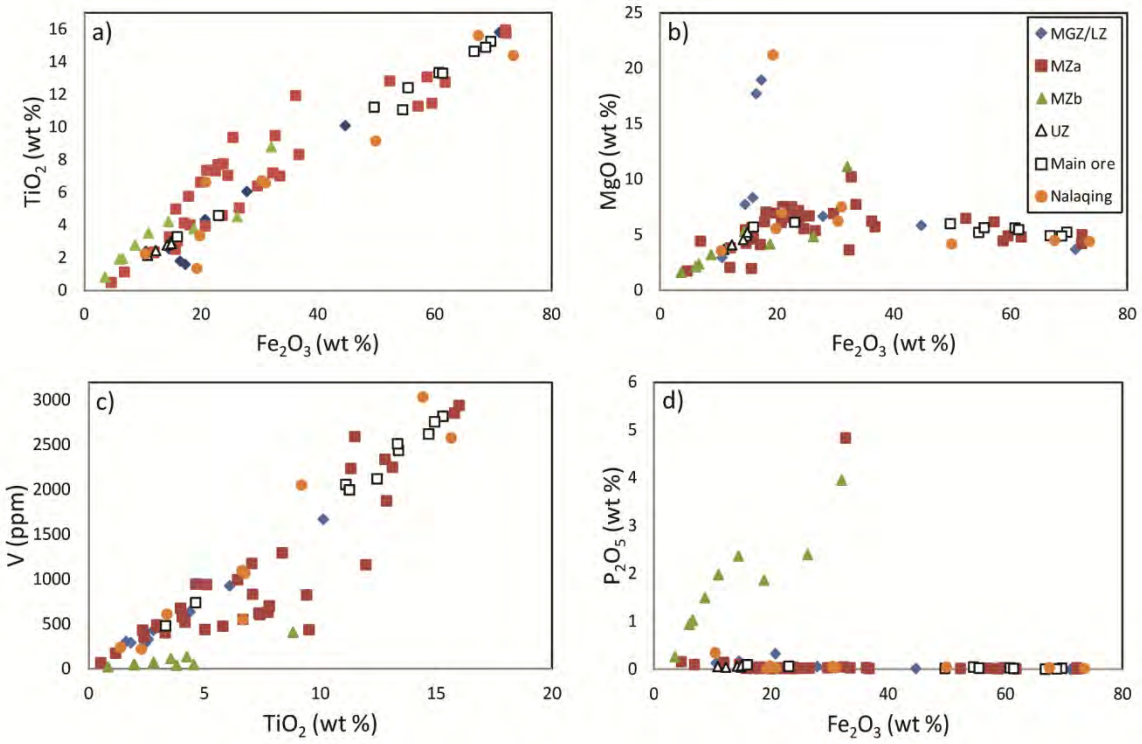

Figure 6.3 Whole-rock major element oxide variation diagrams for Fe_2O_3, TiO_2, MgO, V and P_2O_5 for the Jianshan and Nalaqing Blocks, Panzhihua intrusion.

Furthermore Na_2O+K_2O also show a positive correlation with SiO_2 (Figure 6.2 f). P_2O_5 concentrations are typically low apart from the MZb where there is a positive correlation with Fe_2O_3 (Figure 6.3 d).

Trace element variation

Concentrations of trace elements are presented in Appendix B. V, Co and Zn are all positively correlated with one another (Figure 6.4 a-c). Cr shows no correlation with V (Figure 6.4 b). Cr concentration of the Panzhihua rocks is relatively low with an average of, 43 ppm (2-320 ppm) for the MZa, 14 ppm (8-24 ppm) for the MZb and 180 ppm (18-1380 ppm) for the UZ with the exception of the MGZ/LZ which has an average of 445 ppm (9-1835 ppm). High concentration of Cr is always associated with ultramafic rocks such as clinopyroxenite in the MGZ/LZ (Appendix B). High field strength elements (HFSE) show no correlation with V. Incompatible elements such as Nb-Ta and Zr-Hf show strong positive correlation (Figure 6.4 d and f). Zr-Nb plot shows two indistinct trends (Figure 6.4 e).

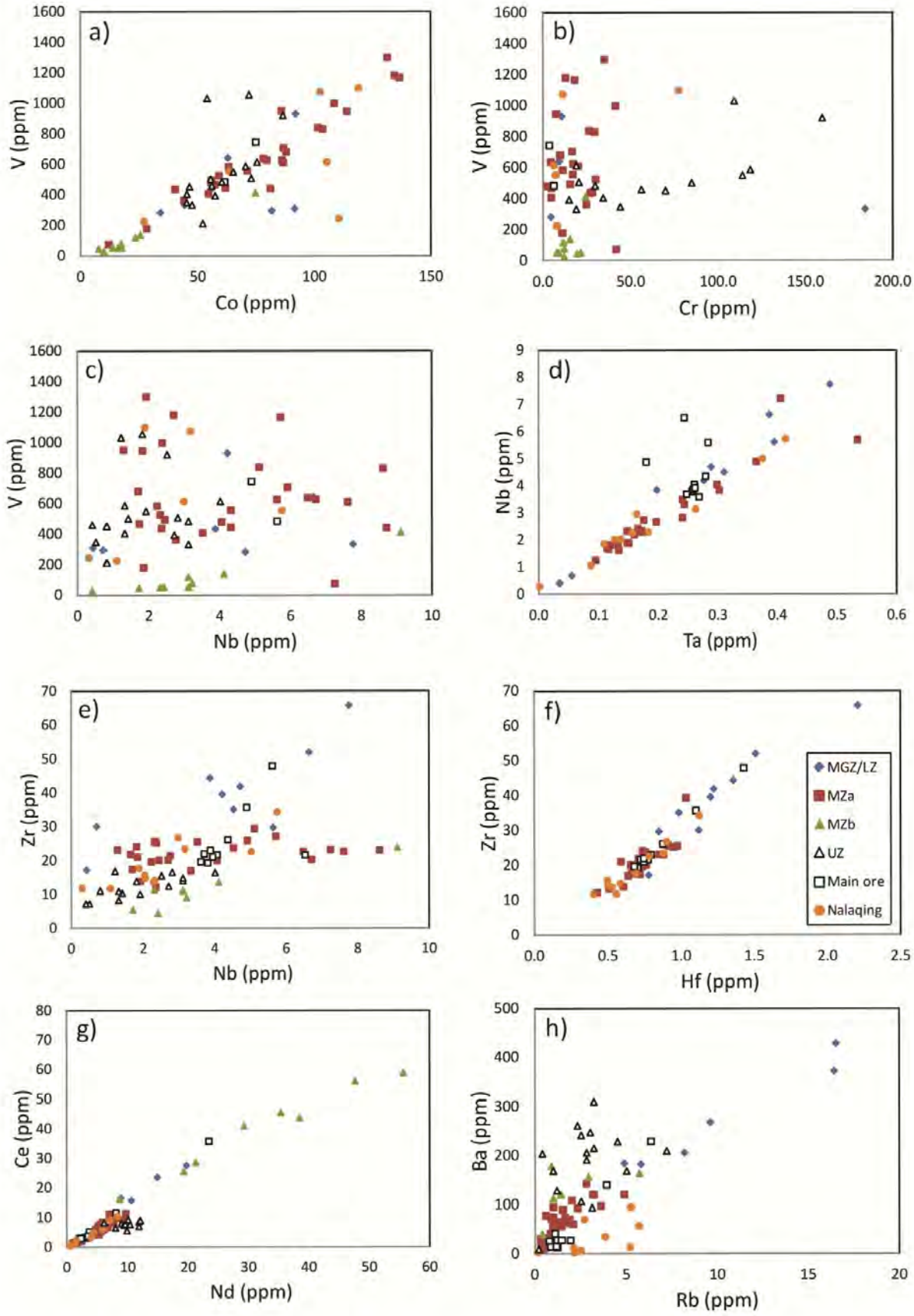

Figure 6.4 Trace element variation diagrams for the Jianshan and Nalaqing Blocks, Panzhihua intrusion. Symbols are the same as in Figure 6.2 and 6.3.

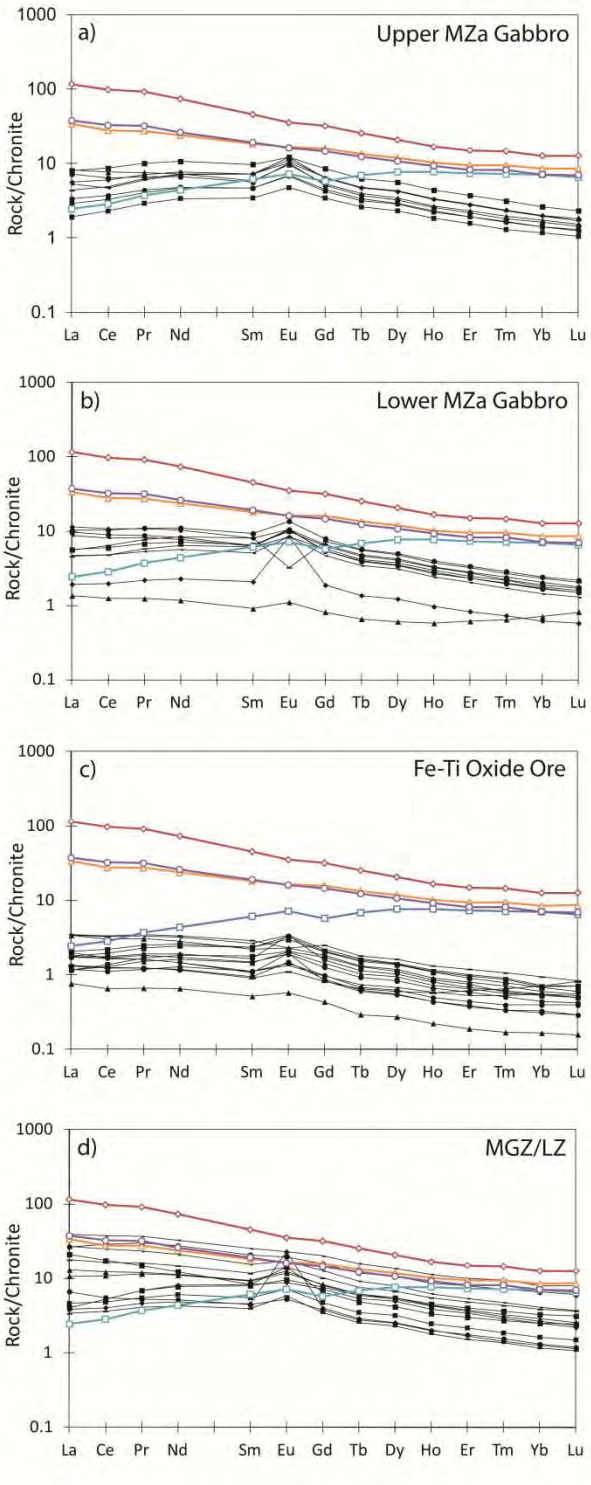

Figure 6.5 Chondrite-normalised REE profiles for the MGZ/LZ, Fe-Ti oxide ores, Lower MZa Gabbro and Upper MZa gabbro. Average REE profiles for the Emeishan extrusive rocks are plotted for comparison and are discussed in section 8. Open symbols represent average compositions of: LREE depleted picrite (Blue squares; Wang et al. 2007), picrites (Orange triangles; Li et al. 2010), low-Ti basalt (Purple circles; Xiao et al. 2004) and high-Ti basalt (Brown diamonds; Xiao et al. 2004).

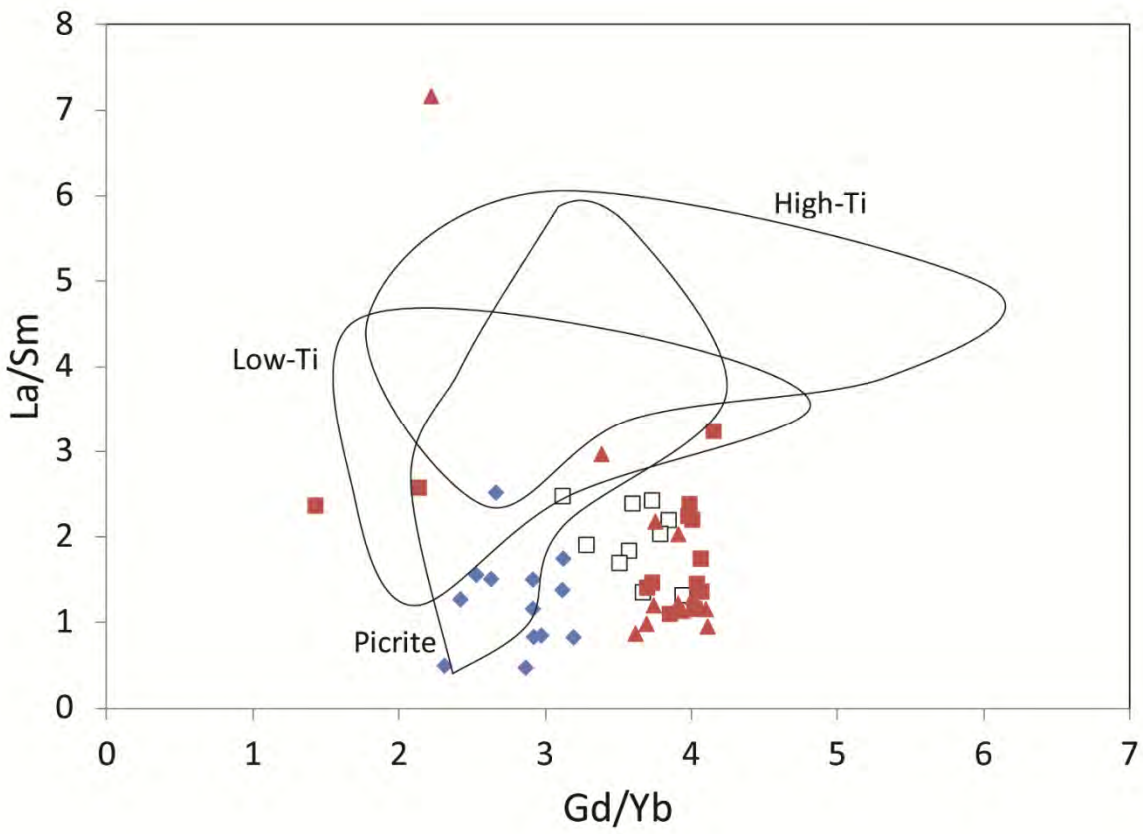

Figure 6.6 La/Sm vs. Gd/Yb for the Panzhihua intrusion and comparison with Emeishan extrusive lavas: picrite (field after Wang et al. 2007, Li et al. 2010, Zhang et al. 2006), high-Ti basalt (field after Xiao et al. 2004, Wang et al. 2007, Song et al. 2009) and low-Ti basalt (field after, Xiao et al. 2004, Wang et al. 2007, Song et al. 2009). Symbols: Blue diamond's – MGZ/LZ; Open squares – Fe-Ti oxide ore; Brown squares and triangles – MZa gabbro.

REE concentrations are generally low throughout the intrusion apart from the MZb where REE show a positive correlation with P_2O_5. REE are enriched in the MGZ/LZ (Figure 6.5d). Chondrite-normalised REE diagrams shows a general enrichment of LREE relative to HREE with $(La/Lu)_N$ ratios ranging from 1.5-6, 1.3-8.6 and 1.5-6.5 for the MGZ/LZ, Oxide Ores and MZa gabbro respectively (Figure 6.5 and 6.6). One outlier with a ratio of 12 (Sample BT-24) is noted in the upper MZa gabbro (Figure 6.6). LREE ratios are relatively low, e.g. $(La/Sm)_N$ – 0.8-1.7 for the MGZ/LZ (with an outlier of 2.5); 0.6-1.5 for the MZa gabbro and 0.7-1.6 for the Oxide ores (Figure 6.6). HREE ratios such as $(Gd/Yb)_N$ have ratios of 2.3-3.1, 3-3.2 and 2.6-3.1 for the MGZ/LZ, MZa gabbro and Oxide ores respectively. Two oxide ore samples have lower $(Gd/Yb)_N$ ratios of 1.1 and 1.7 (Figure 6.6).

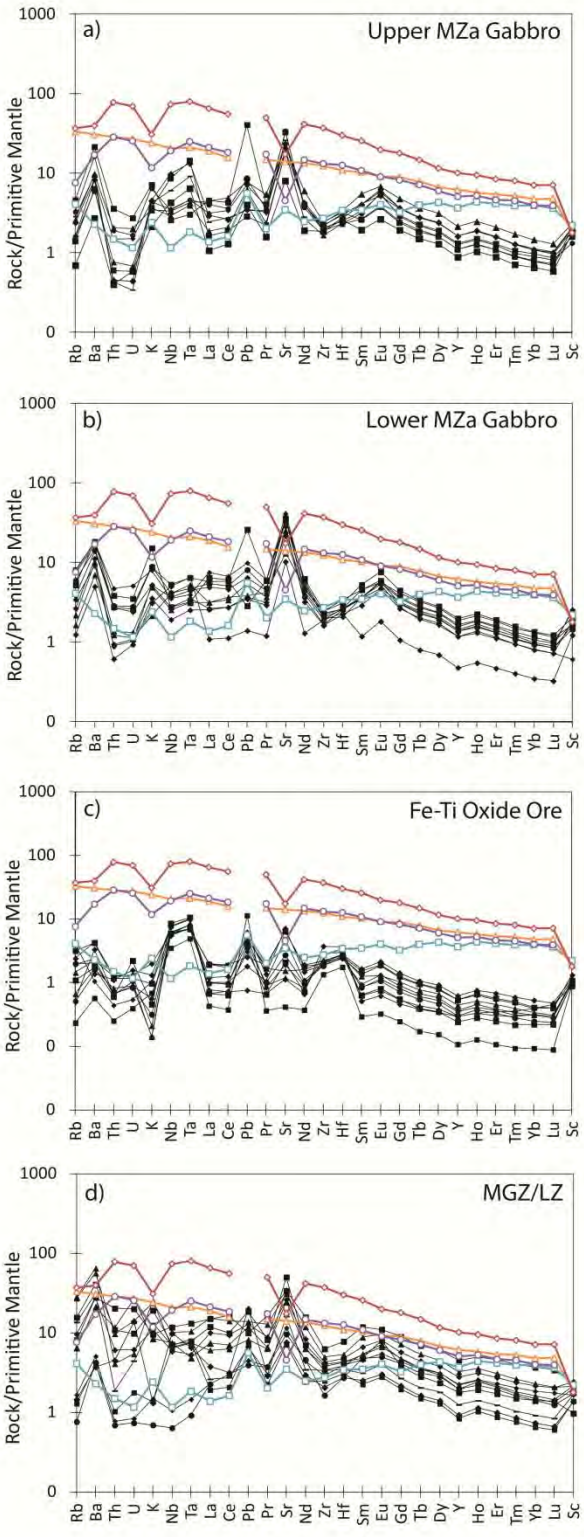

Figure 6.7 Primitive mantle-normalised trace element diagrams for the MGZ/LZ, Fe-Ti oxide ores, Lower MZa Gabbro and Upper MZa gabbro. Average primitive-mantle normalised values for the Emeishan extrusive rocks are plotted for comparison and are discussed in section 8. Open symbols represent average compositions of: LREE depleted picrite (Blue squares; Wang et al. 2007), picrites (Orange triangles; Li et al. 2010), low-Ti basalt (Purple circles; Xiao et al. 2004) and high-Ti basalt (Brown diamonds; Xiao et al. 2004).

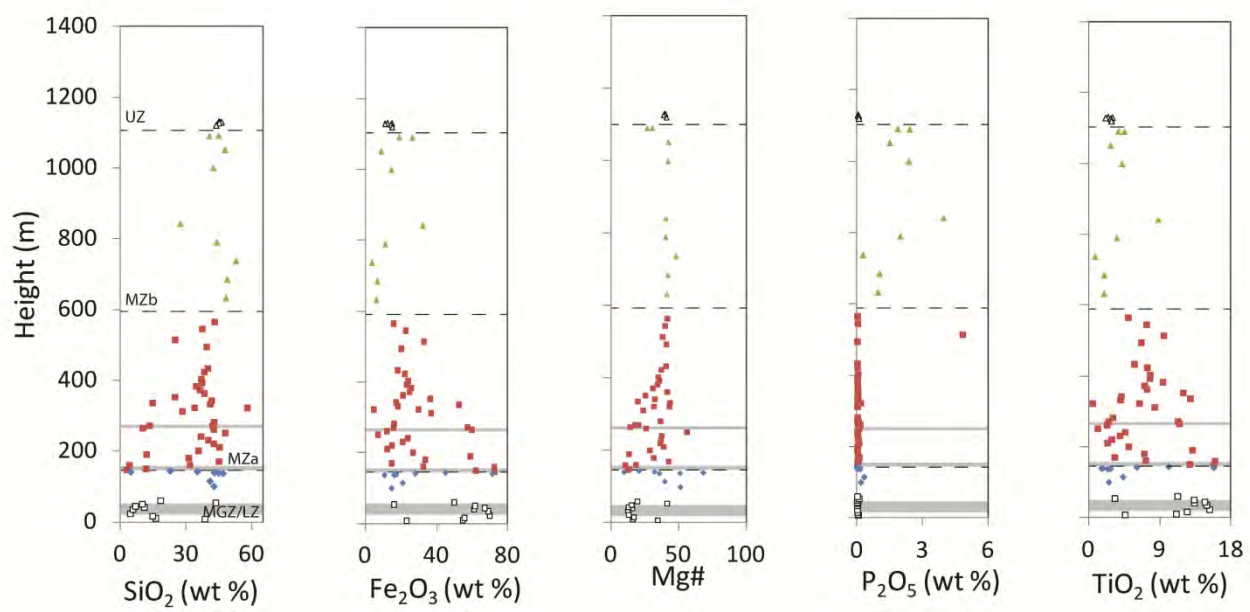

Figure 6.8 Whole-rock major element oxide stratigraphic variations through the Jianshan Block, Panzhihua intrusion. Symbols are the same as in Figure 6.2 and 6.3.

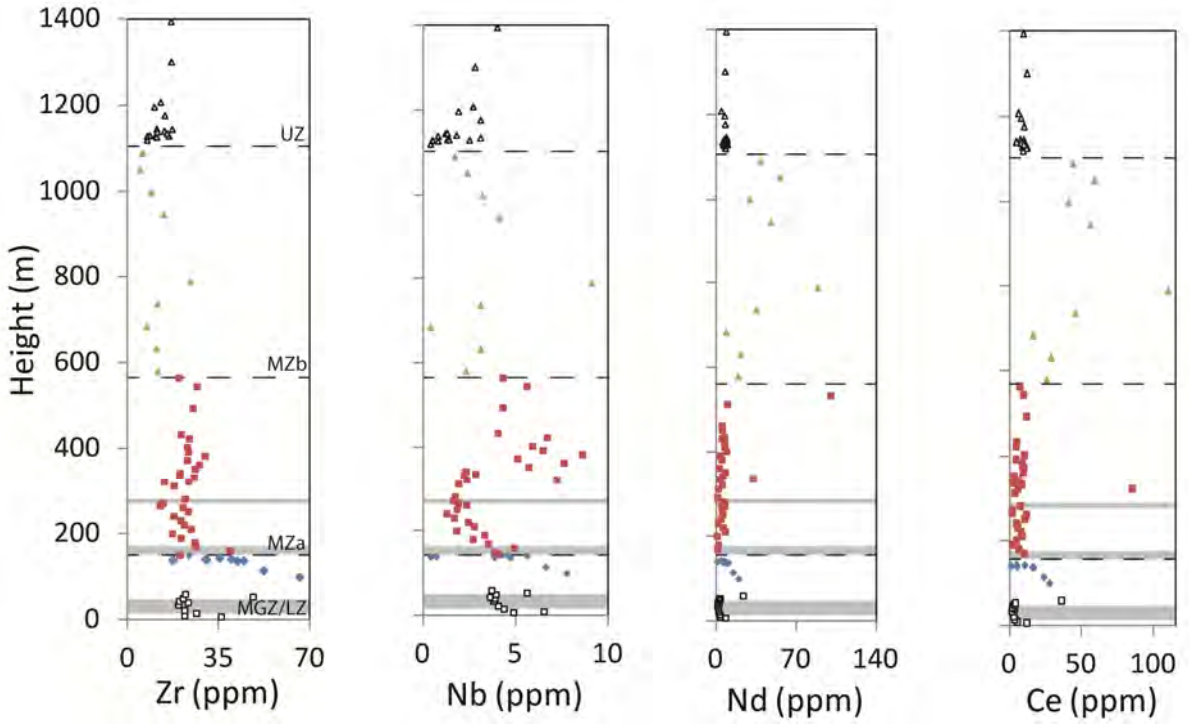

Figure 6.9 Selected trace element (V, Co, Cr, Sr) stratigraphic variation for the Jianshan Block, Panzhihua intrusion. Symbols are the same as in Figure 6.2 and 6.3.

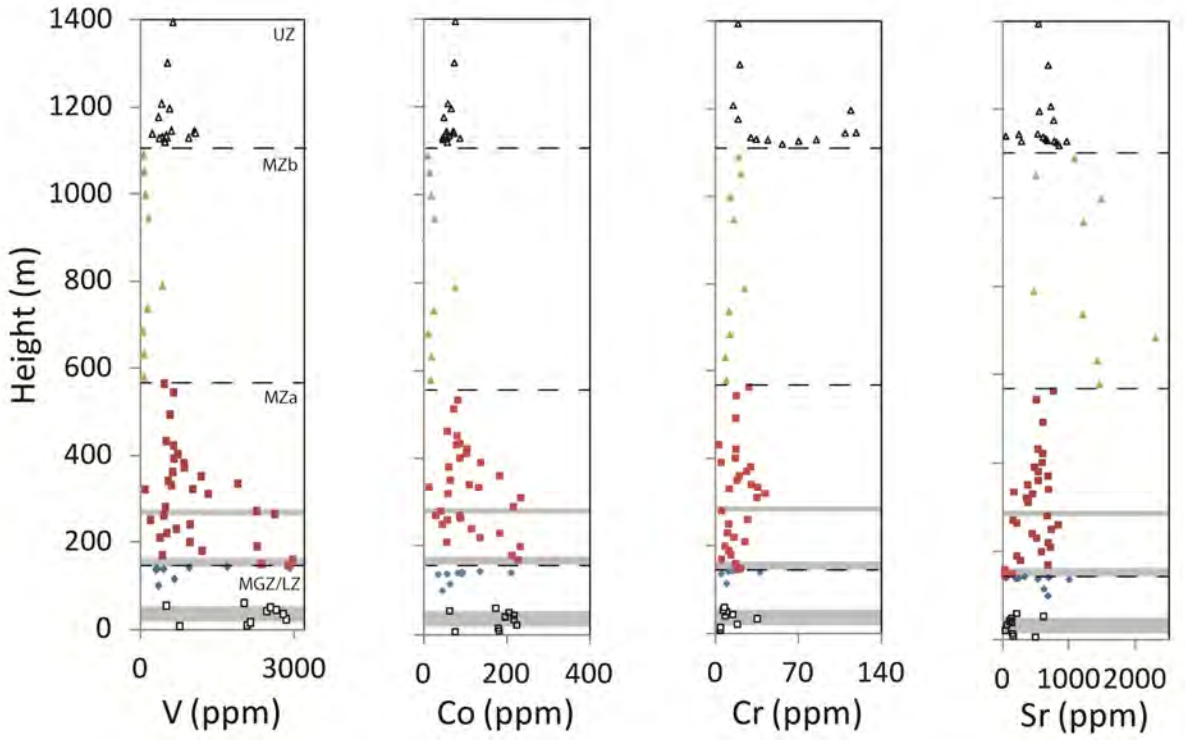

Figure 6.10 Selected trace element (Zr, Nb, Nd, Ce) stratigraphic variation for the Jianshan Block, Panzhihua intrusion. Symbols are the same as in Figure 6.2 and 6.3.

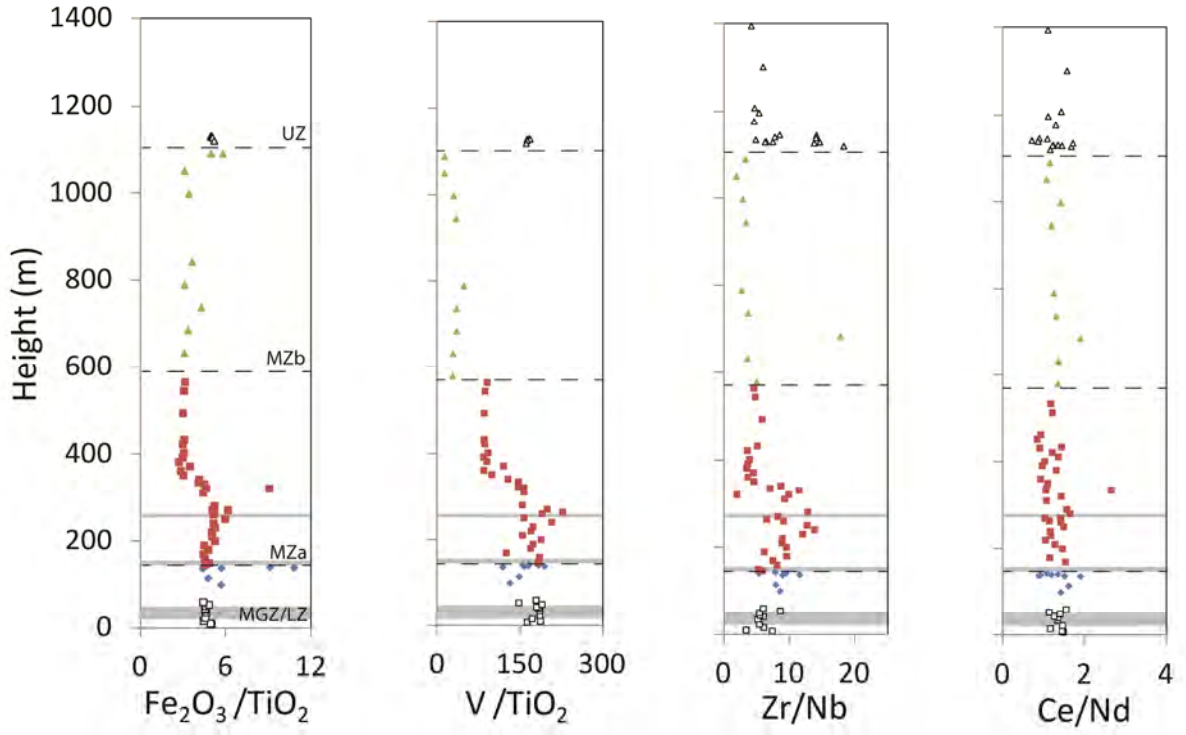

Figure 6.11 Stratigraphic variation for selected major and trace element ratios for the Jianshan Block, Panzhihua intrusion. Symbols are the same as in Figure 6.2 and 6.3.

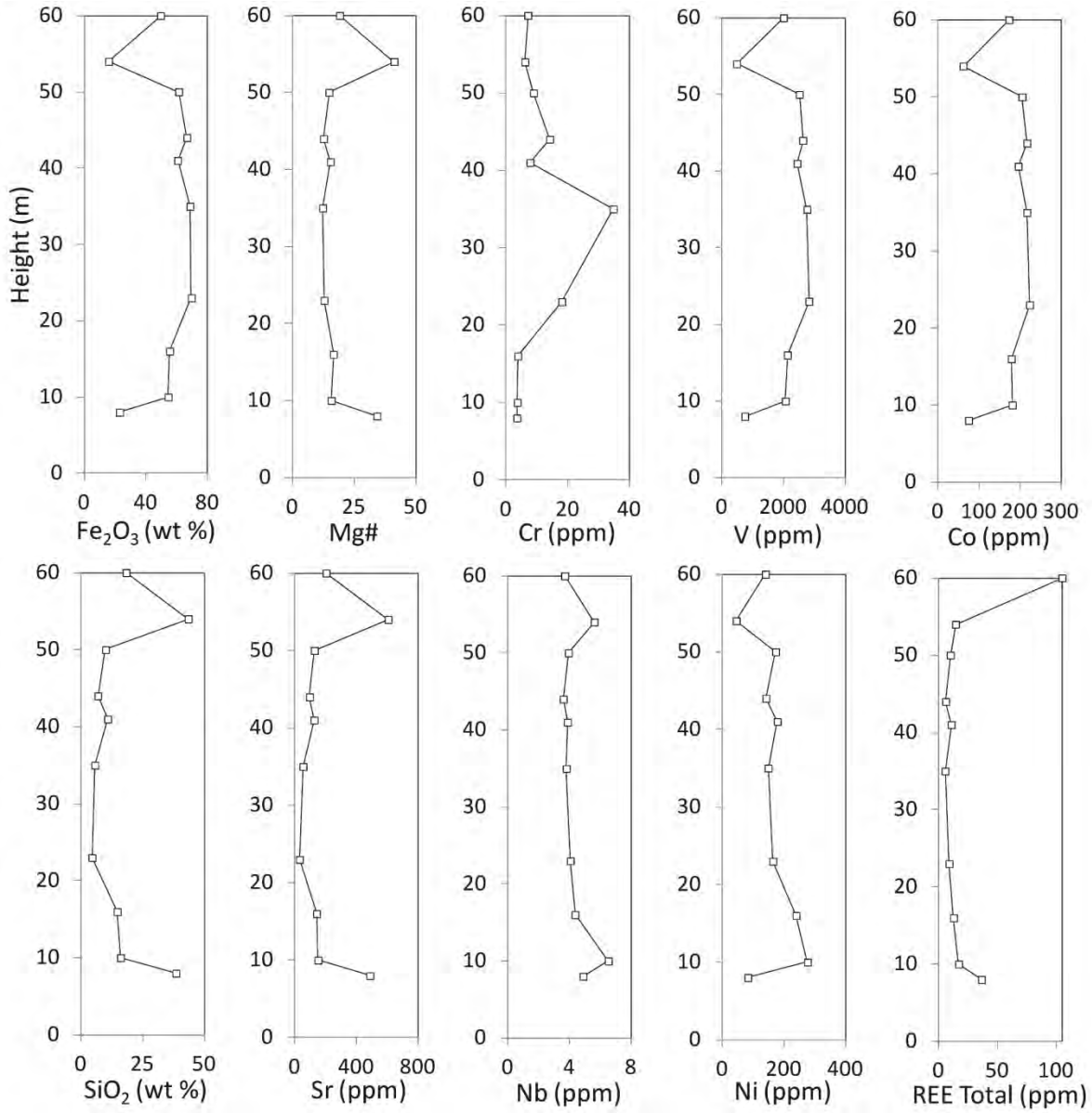

Figure 6.12 Selected whole-rock geochemical variation for the main Fe-Ti oxide ore layer, Jianshan Block, Panzhihua intrusion.

Extended primitive mantle normalised trace element diagrams show several similarities for the MGZ/LZ, MZa gabbro and Oxide ores (Figure 6.7). All samples are characterised by strong positive Sr and Ba anomalies. All samples also show a negative Y anomaly. Generally Zr-Hf show negative anomalies except in the oxide ore samples where Zr-Hf shows a distinct positive anomaly. The oxide ore samples have very distinct trace element patterns (Figure 6.7). Most notably strong positive Nb-Ta and Zr-Hf anomalies and a strong negative K anomaly. Nb-Ta shows a flat pattern apart from the

oxide ores and several samples from the upper MZa gabbro. The lower and upper MZa gabbro also shows a negative Th-U anomaly.

Major and trace element stratigraphic variation

Several distinct stratigraphic variations are described here, which have bearing on the evolution of the magma chamber. SiO_2 (Figure 6.8), Al_2O_3 and CaO have similar patterns, which are highly variable in the MGZ/LZ, Main ore and MZa but concentrations are higher and less variable above this level (+/- 350 m). Similarly the Fe_2O_3 and TiO_2 (Figure 6.8) concentrations are high but variable (7-72 wt % and 0.5-16 wt % respectively) in the lower 300 m of the intrusion but decrease above this level (3.5-30 wt % and 0.8-10 wt % respectively). Mg# is similarly variable (10-68) in the lower 300 m and is more consistent (30-40) above this level (Figure 6.8). High concentrations P_2O_5 are only noted in the MZb.

Transition metals (V, Co, Zn) have similar patterns (Figure 6.9) to Fe_2O_3. However Cr concentrations show no correlation with Fe_2O_3. Cr concentrations are generally low (< 50 ppm) apart from the UZ. Sr has the highest concentrations in the MZb as expected due to the more leucocratic nature of the rocks (Figure 6.9). Incompatible trace elements typically have low concentrations throughout the intrusion except for the MGZ/LZ where concentrations are higher (Figure 6.10). REE concentrations are high within the MZb. Nb and Ta concentrations show a marked increase at the 300 m level (Figure 6.10).

Major and trace element ratios further highlight the distinct break in geochemical patterns at 300 m (Figure 6.11). Fe_2O_3/TiO_2, V/TiO_2 and Zr/Nb all show distinct decreases. Two distinct trends of Fe_2O_3-TiO_2 were identified in Figure 6.3, the high-Ti trend occurs above 350 m level. Incompatible element ratios such as Ce/Nd show no variation and are consistent throughout the intrusion.

Main ore variation

The main ore intersection shows an increase in Fe_2O_3 content from 22 wt % at the base to 55 wt % below the massive ore and up to 70 wt % within the massive ore layer itself (Figure 6.12). SiO_2

Table 6.1 Sulphide and PGE concentrations in the gabbroic and Fe-Ti oxide ore rocks on the Panzhihua intrusion. See Appendix F for the concentrations of analytical standards used.

Sample	Rock Type	Sulphide Abundance (%)	Ni (ppm)	Cu (ppm)	Ru (ppb)	Rh (ppb)	Pd (ppb)	Os (ppb)	Ir (ppb)	Pt (ppb)
05-01	Oxide-rich Gabbro	2	56	128	<LD	<LD	0.78	<LD	<LD	-
05-02	Oxide-rich Gabbro	4.3	108	285	<LD	<LD	1.15	<LD	<LD	0.14
05-04	Fe-Ti Oxide Ore	0	53	50	<LD	<LD	0.95	<LD	<LD	0.15
05-06	Fe-Ti Oxide Ore	2	47	67	<LD	<LD	1.11	<LD	<LD	0.43
05-78	Fe-Ti Oxide Ore	Trace	50	88	<LD	<LD	0.78	<LD	<LD	0.16
05-10	Oxide-rich Gabbro	Trace	53	29	<LD	<LD	0.47	<LD	<LD	-
BT-01	Microgabbro	Trace	64	126	<LD	0.14	5.11	<LD	0.27	7.10
BT-02	Pegmatoid	0.6	56	na	<LD	<LD	0.64	<LD	<LD	0.10
BT-03 (a)	Microgabbro	Trace	19.	na	<LD	<LD	-	<LD	<LD	-
BT-03 (c)	Microgabbro	Trace	475	17	3.53	0.88	3.86	2.57	1.93	12.52
BT-03 (d)	Fe-Ti Oxide Ore	0.3	55	28	<LD	<LD	0.91	<LD	<LD	0.32
BT-03 (e)	Microgabbro	Trace	50	61	<LD	<LD	0.67	<LD	<LD	0.15
BT-03 (f)	Microgabbro	1.3	50	42	<LD	<LD	0.70	<LD	<LD	0.17
BT-04	Fe-Ti Oxide Ore	0	53	43	<LD	<LD	0.84	<LD	<LD	0.21
BT-05	Fe-Ti Oxide Ore	1.3	65	164	<LD	<LD	1.11	<LD	0.03	0.83
BT-06	Fe-Ti Oxide Ore	Trace	32	22	<LD	<LD	0.80	<LD	<LD	0.14
BT-07	Gabbro	Trace	16	na	<LD	<LD	-	<LD	<LD	-
BT-10	Gabbro	1.3	61	na	<LD	<LD	-	<LD	<LD	-
BT-13	Gabbro	0	40	na	<LD	<LD	-	<LD	<LD	-
BT-19	Fe-Ti Oxide Ore	4	90	152	0.17	0.22	4.95	<LD	0.14	5.88
BT-25	Gabbro	Trace	21	41	<LD	<LD	1.78	<LD	<LD	1.53
BT-30	Gabbro	2	15	21	<LD	<LD	1.02	<LD	<LD	0.97
BT-34	Gabbro	Trace	2	17	<LD	<LD	0.50	<LD	<LD	-
BT-38	Gabbro	Trace	-	na	<LD	<LD	-	<LD	<LD	-
BT-45	Gabbro	1.5	-	na	<LD	<LD	-	<LD	<LD	-

content and Mg# show an excellent negative correlation compared with Fe_2O_3. Cr content is low (< 40 ppm) and show no correlation with Fe_2O_3 or SiO_2. V and Co show excellent positive correlation with Fe_2O_3 (Figure 6.12). Sr an Nb shows good correlation with SiO_2 (Figure 6.12). Similar trends not shown in Figure 6.12 are also noted for Zr, Y and Hf. Total REE also show correlation with SiO_2 content except for sample 05-10, which has high REE content. Ni content does not show correlation with SiO_2 content, which is consistent with the low abundance of olivine within the main ore intersection (< 3 vol. %).

6.2.2 Ni, Cu, Cr and platinum group elements (PGE)

The concentrations of Cr, Ni, Cu and PGEs are illustrated in Figure 6.13 and given in Table 6.1. Ni concentrations are generally < 75 ppm with the exception of micro-ultramafics in the MGZ/LZ (> 400 ppm). Cu concentrations show a range of 17-280 ppm and are generally correlated with the modal abundance of sulphides (Table 6.1). Cr concentrations are generally low < 50 ppm, again with the exception of micro-ultramafics in the MGZ/LZ typically having higher Cr contents (> 1500 ppm). One

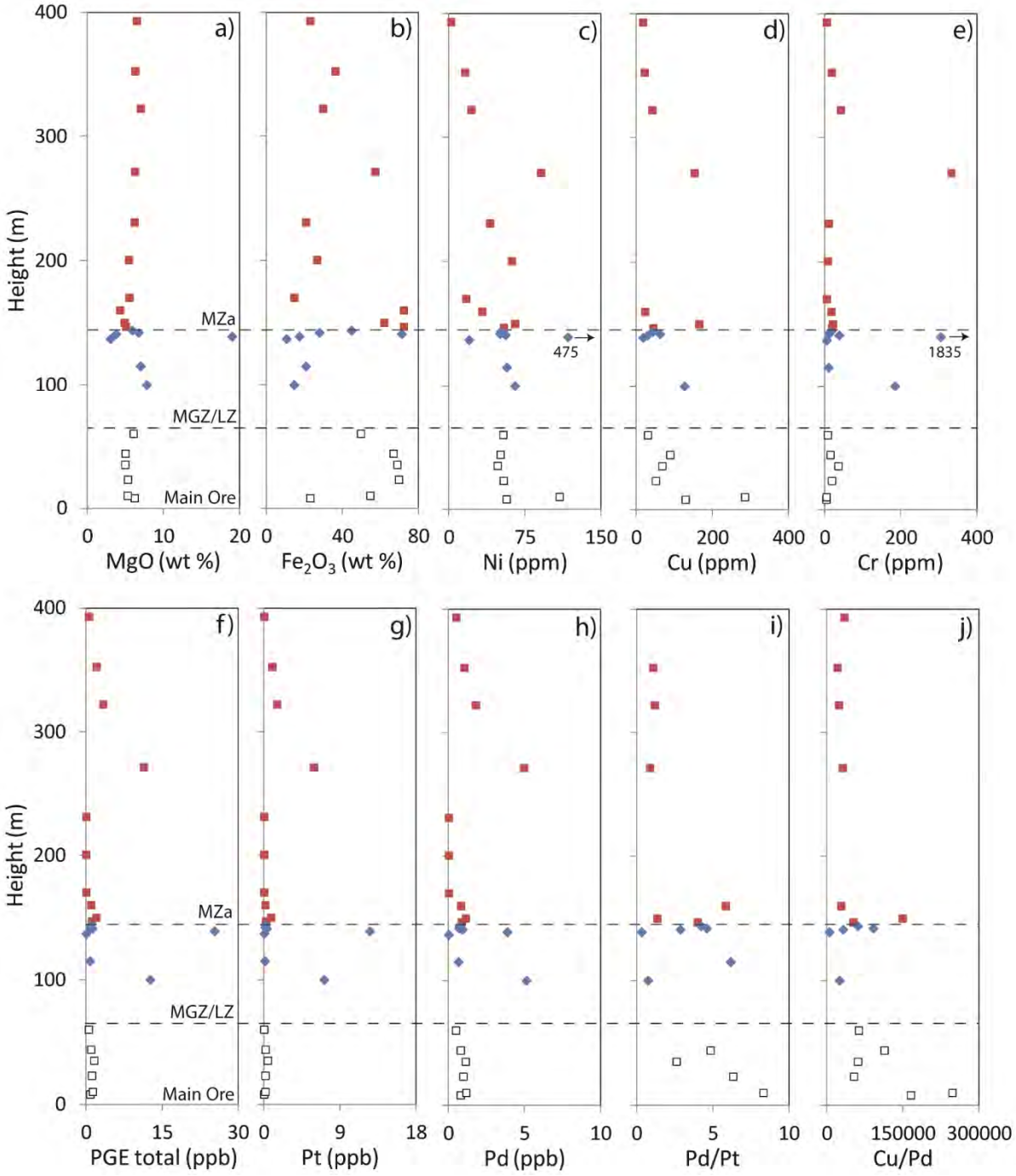

Figure 6.13 Stratigraphic variation of MgO, Fe_2O_3 Ni, Cr, Cu and PGEs for the main Fe-Ti oxide ore transect (main ore), MGZ/LZ and MZa.

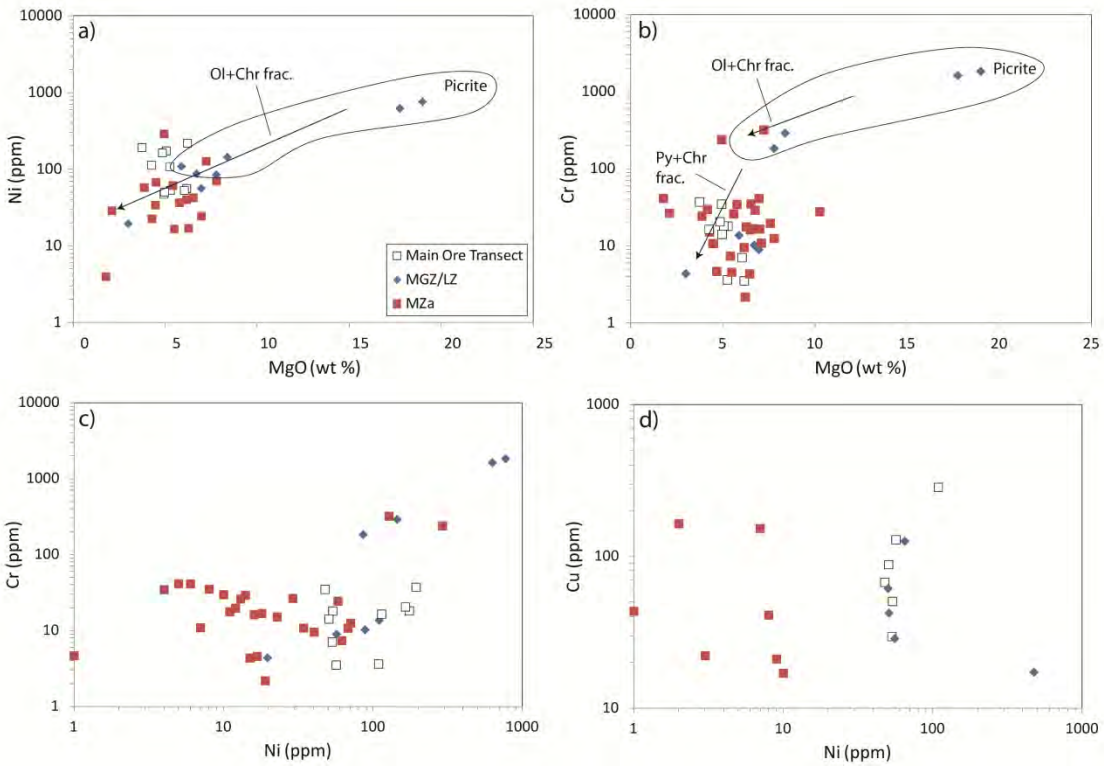

Figure 6.14 Whole-rock geochemical variation diagrams for the main Fe-Ti oxide ore transect, MGZ/LZ and MZa of the Panzhihua intrusion. a) Ni vs. MgO showing good correlation with picrites evolution. b) Cr vs. MgO showing correlation of Cr with MgO but lower Cr than the typical olivine + chromite fractionation trend. c) Cr vs. Ni showing correlation. d) Cu vs. Ni showing no correlation. Picrite field in a and b is after Li et al. (2010).

exception is a Fe-Ti oxide ore layer in the MZa (sample BT-19), which has 331 ppm Cr. PGE abundances are generally very low (< 2 ppb), with the exception of three samples with > 10 ppb total PGE. Generally only Pt and Pd are above detection limit (Table 6.1). Cu/Pd ratios are variable for the main ore transect and MGZ/LZ and generally constant and lower for the MZa. Fe_2O_3, Ni, Cu, Cr and PGEs show a correlation in the MZa but no correlations are noted for the main ore transect and MGZ/LZ.

Ni and Cr are plotted against MgO in Figure 6.14 (a and b) with the field for Emeishan picrites included for comparison. Samples from the Panzhihua intrusion cluster at the low MgO and low Cr, Ni end of the Emeishan picrite field apart for the micro-ultramafic samples with high MgO. Cr and Ni show positive correlation but no correlation of Ni and Cu is observed (Figure 6.14 c and d). Total PGE abundance show a positive correlation with Cr but only a weak correlation with Cu is observed (Figure 6.15 a and b). Pt and Pd also show a positive correlation (Figure 6.15 c) with a broad range of

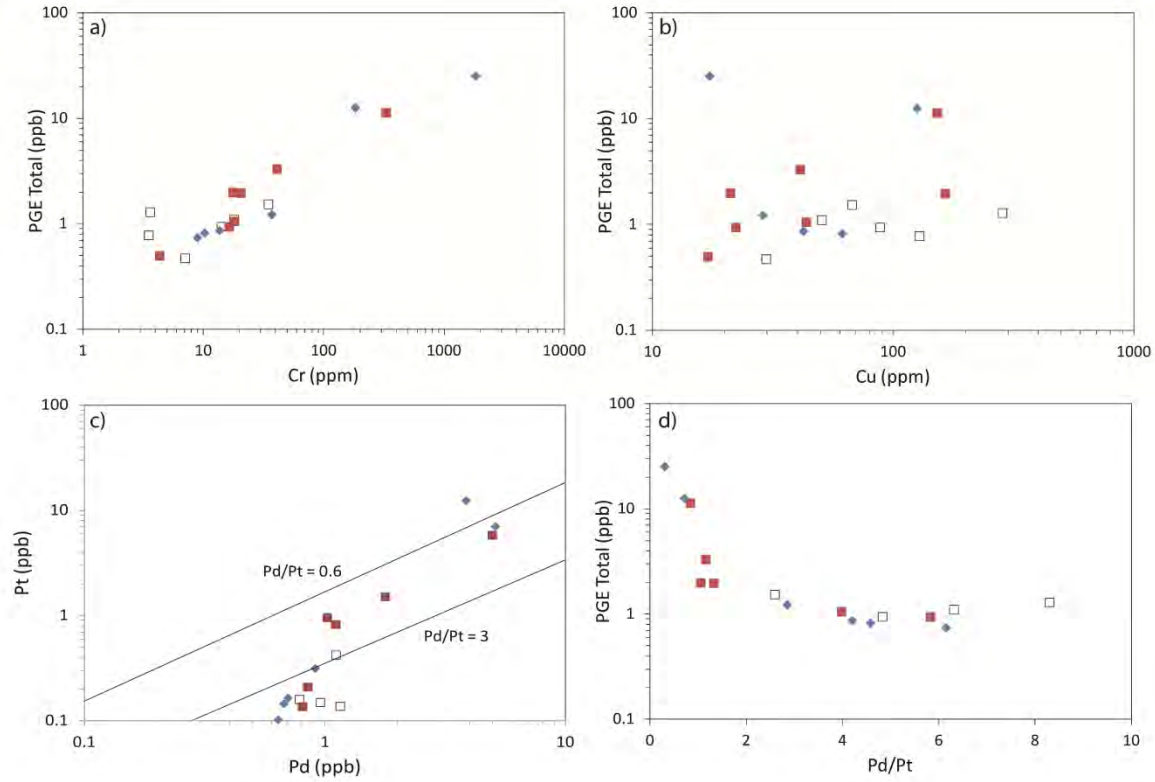

Figure 6.15 PGE variation diagrams. a) PGE vs. Cr showing a good correlation. b) PGE vs. Cu showing weak correlation. c) Pt vs. Pd with typical mantle Pd/Pt range = 0.6 indicated along with a Pd/t = 3 trend. d) PGE vs. Pd/Pt showing low Pd/Pt ratios typically related to the higher total PGE samples.

Pd/Pt = 0.6 (typical mantle value) to 8.5. Samples containing > 10 ppb have low Pd/Pt (< 1) whereas samples with low total PGE abundance have high Pd/Pt (up to 8.5) (Figure 6.15 d). Cu/Pd ratios are similarly high relative to the typical mantle range (7000-10000; Taylor and McLennan, 1985). Discussed later in section 8.4 for the evolution of the Panzhihua parent magma.

Primitive mantle-normalised profiles for three samples with mostly detectable PGE concentrations are illustrated in Figure 6.16 along with the fields for Emeishan picrite and high-Ti basalt. The gabbroic and Fe-Ti oxide samples plot within the high-Ti basalt field with enriched Pt and Pd values. Sample BT-03 (c) (micro-ultramafic in the MGZ/LZ) plots within the picritic field with a relatively flat profile.

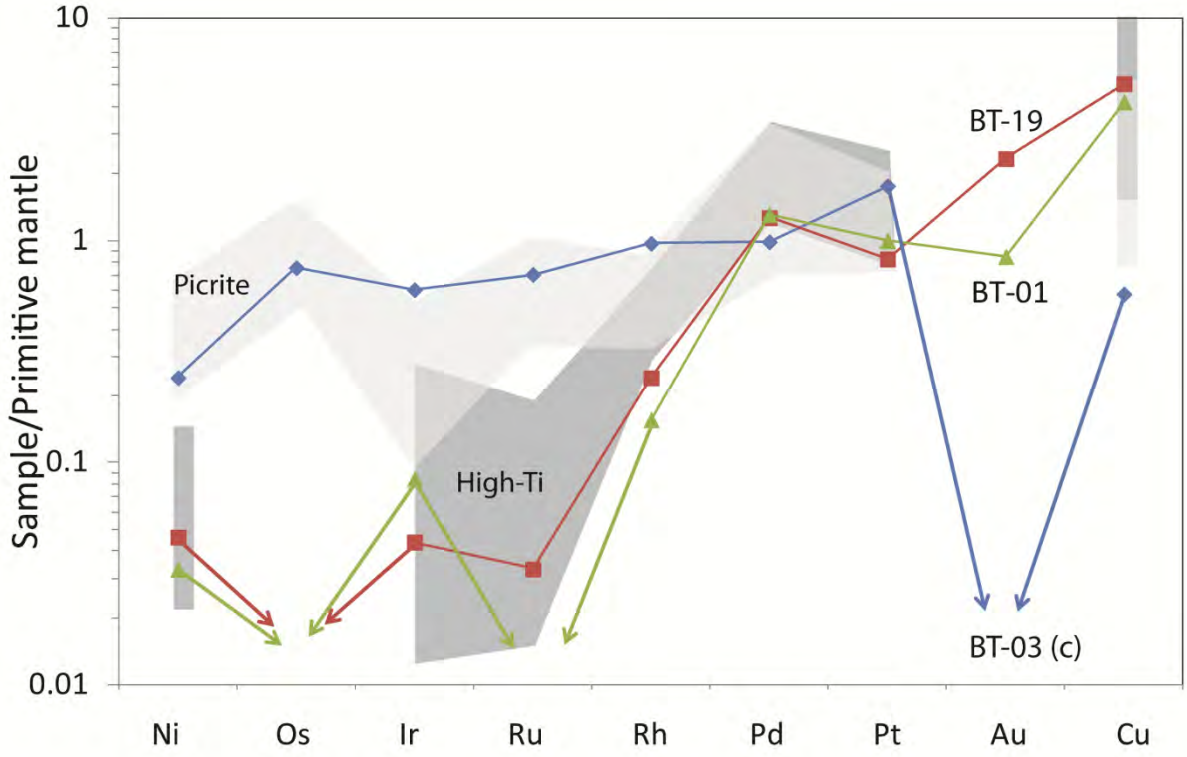

Figure 6.16 Primitive mantle-normalised profiles for samples BT-19, BT-01 and BT-03 (c). Picrite field is after Li et al. 2012 and the High-Ti basalt field is after Song et al. (2009).

6.2.3 Sr and Nd radiogenic isotopes

Whole-rock initial Sr and Nd isotope data show no distinct variations through the Panzhihua intrusion (Figure 6.17). Initial Sr ratios in the Fe-Ti oxides ores and MZa gabbros have values of $(^{87}Sr/^{86}Sr)_i$: 0.7043-0.7046 and 0.7041-0.7045 respectively. The MGZ/LZ rocks are characterised by a higher $(^{87}Sr/^{86}Sr)_i$ of 0.7054. $\varepsilon_{Nd}(i)$ values similarly show little variation for the Fe-Ti oxides ores and gabbros with values of: 2.6-3.5 and 2.1-3.7 respectively. The MGZ/LZ again is characterised by enriched $\varepsilon_{Nd}(i)$: -0.6 to 1.6. Isotope data are given in Table 6.2.

Sr-Nd isotope data for the Fe-Ti oxide ore and MZa gabbro all plot within the Emeishan High-Ti basalt field (Figure 6.18). Samples from the MGZ/LZ, enriched relative to the ore and gabbro samples, still plot within the typical isotopic range of the High-Ti basalt and overlap with the Low-Ti basalt field toward the more enriched section of the Figure 6.18.

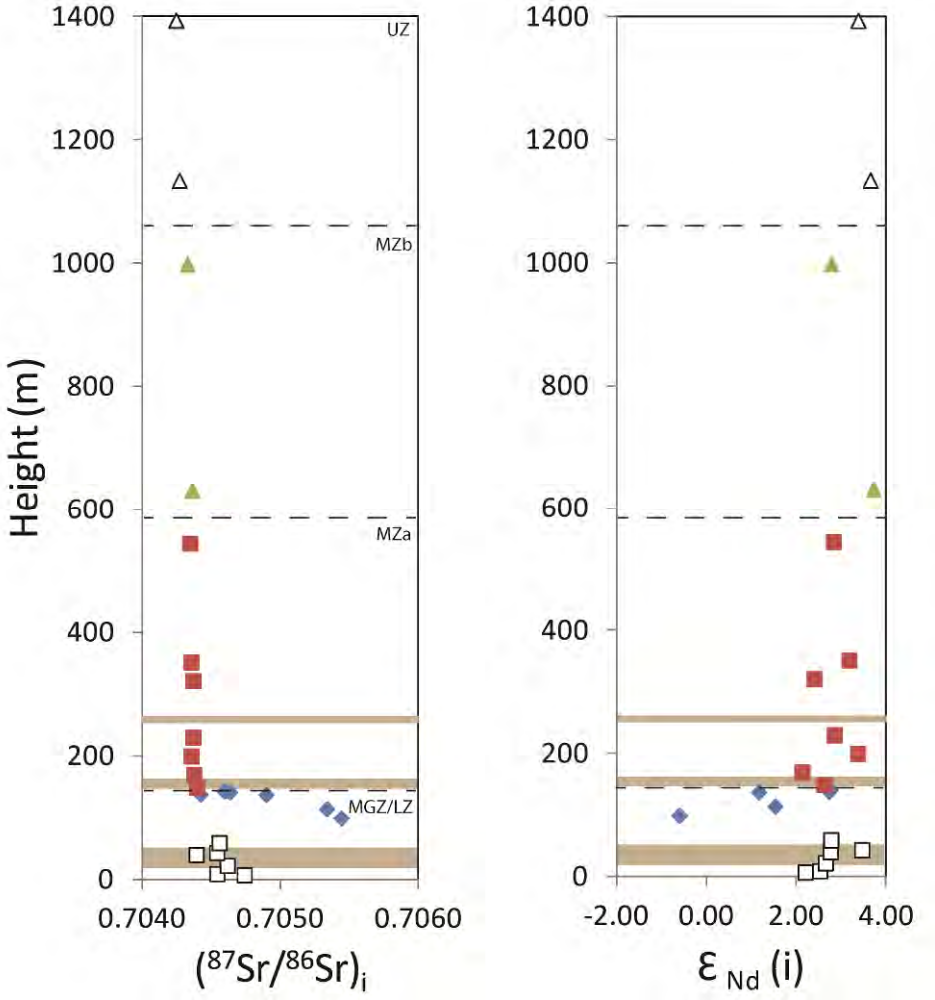

Figure 6.17 stratigraphic variations for whole-rock Sr and Nd isotopes, Jianshan Block, Panzhihua intrusion. Symbols are the same as in Figure 6.2 and 6.3. Grey bars represent Fe-Ti oxide ore layers sampled in this study.

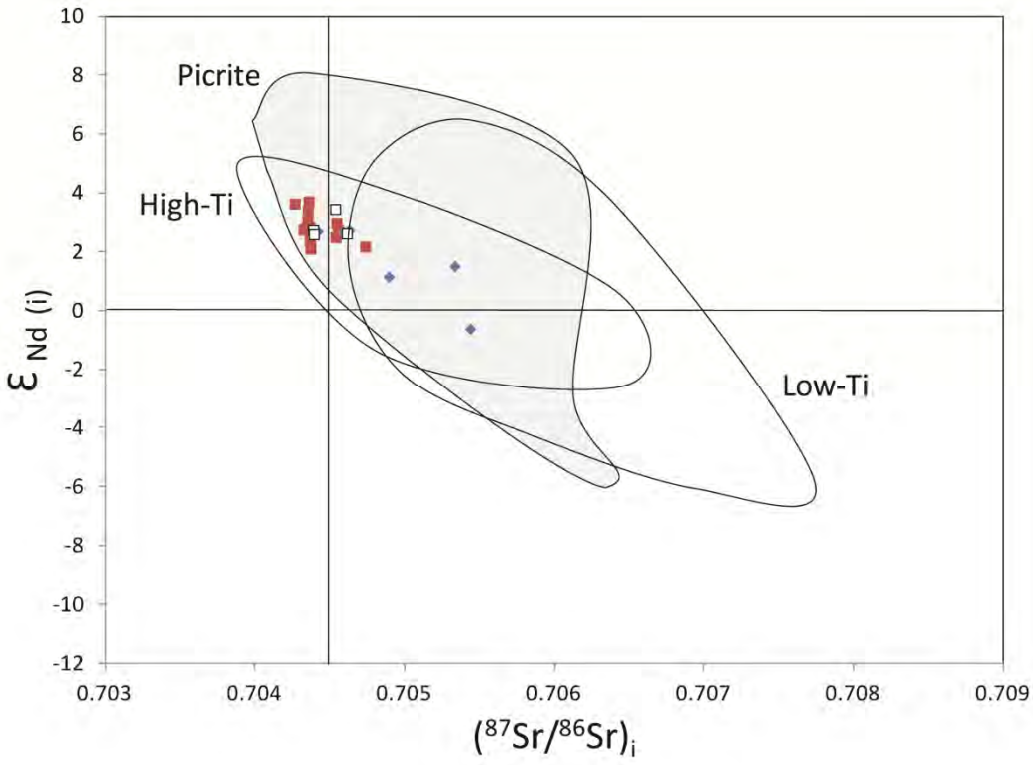

Figure 6.18 Sr-Nd isotope variation for the Jianshan Block, Panzhihua intrusion and comparison with Emeishan extrusive lavas: picrites (field after Zhang et al. 2006, Wang et al. 2007, Li et al. 2010), high-Ti basalt (field after Xu et al. 2001, Xiao et al. 2004, Wang et al. 2007) and low-Ti basalt (field after Xu et al. 2001, Xiao et al. 2004, Wang et al. 2007). Symbols: Blue diamond's – MGZ/LZ; Open squares – Fe-Ti oxide ore; Brown squares – MZa gabbro.

6.2.4 Oxygen isotope geochemistry

Four samples were selected from the main ore transect as part of a pilot study for O-isotope geochemistry of mineral separates. Two gabbroic rocks, one from above the main ore and one from below, along with two samples from within the ore layer were selected for analysis. Ti-magnetite and plagioclase were separated and each was analysed for O-isotope ratios. Plagioclase in the gabbroic rocks has ^{18}O of 8.2 and 8.4 ‰ below and above the ore layer respectively. Plagioclase from the Fe-Ti oxide ore samples has ^{18}O of 8.2 and 8.9 ‰. Ti-magnetite for the gabbroic rocks has ^{18}O of 3.8 and 2.9 ‰ below and above the ore layer respectively. Ti-magnetite with the ore has ^{18}O of 5.9 and 3.6 ‰. O-isotope data are given in Table 3.

Table 6.2 Sr and Nd isotope geochemistry for the gabbroic and Fe-Ti oxide ores of the Panzhihua intrusion. Initial isotope ratios calculated for 260 Ma.

Sample	Rock Type	Rb	Sr	(87Sr/86Sr)m	(87Sr/86Sr)i	error (2se)	Sm	Nd	(143Nd/144Nd)m	(143Nd/144Nd)i	error (2se)	Ɛ Nd i
05-1	Oxide-rich Gabbro	3.90	488	0.704767	0.704738	0.00001	2.18	7.97	0.512688	0.512415	0.000006	2.19
05-2	Oxide-rich Gabbro	0.88	151	0.704561	0.704540	0.00001	1.02	3.69	0.512711	0.512432	0.000006	2.51
O5-4	Fe-Ti Oxide Ore	0.87	30.6	0.704719	0.704614	0.000011	0.51	2.01	0.512691	0.512438	0.000006	2.63
O5-7	Fe-Ti Oxide Ore	1.44	126	0.704432	0.704390	0.000009	0.67	2.40	0.512715	0.512444	0.000006	2.75
05-78	Fe-Ti Oxide Ore	1.16	96.1	0.704582	0.704537	0.00001	0.38	1.36	0.512763	0.512480	0.000006	3.45
05-10	Oxide-rich Gabbro	1.09	204	0.704575	0.704555	0.000008	5.84	23.4	0.512741	0.512445	0.000006	2.76
BT-01	Microgabbro	4.87	674	0.705464	0.705438	0.000015	4.81	19.7	0.512521	0.512272	0.000006	-0.61
BT-02	Pegmatoid	16.4	616	0.705431	0.705333	0.000011	3.57	14.8	0.512628	0.512381	0.000006	1.52
BT-03 (b)	Microgabbro	5.78	524	0.704936	0.704895	0.000011	2.70	10.5	0.512627	0.512362	0.000006	1.16
BT-03 (c)	Microgabbro	0.46	192	0.704428	0.704419	0.000009	1.93	5.76	0.512781	0.512442	0.000005	2.72
BT-03 (d)	Fe-Ti Oxide Ore	0.66	41.8	-	-	-	0.26	0.91	-	-	-	-
BT-03 (e)	Microgabbro	17	688.0	0.704719	0.704631	0.00001	2.12	7.88	0.512722	0.512444	0.000006	2.75
BT-03 (f)	Microgabbro	8.17	323	0.704686	0.704593	0.000012	1.28	4.32	0.512744	0.512441	0.000005	2.68
BT-04	Fe-Ti Oxide Ore	0.4	23.70	-	-	-	0.26	1.04	-	-	-	-
BT-05	Fe-Ti Oxide Ore	0.32	142	0.704402	0.704394	0.000009	0.54	1.85	0.512731	0.512437	0.000006	2.61
BT-06	Fe-Ti Oxide Ore	0.3	22.50	-	-	-	0.21	0.83	-	-	-	-
BT-07	Gabbro	3.14	673	0.704389	0.704372	0.000009	2.15	7.84	0.512689	0.512412	0.000006	2.12
BT-10	Gabbro	1.61	576	0.704364	0.704353	0.000013	1.18	4.02	0.512773	0.512475	0.000006	3.35
BT-13	Gabbro	1.32	503	0.704375	0.704366	0.00001	1.51	5.07	0.512752	0.512449	0.000007	2.84
BT-19	Fe-Ti Oxide Ore	0.63	148	-	-	-	0.54	1.76	-	-	-	-
BT-25	Gabbro	1.42	378	0.704380	0.704366	0.000011	1.68	5.44	0.512737	0.512425	0.000006	2.38
BT-30	Gabbro	0.84	370	0.704360	0.704352	0.000011	1.07	3.29	0.512794	0.512465	0.000006	3.16
BT-53	Gabbro	1.3	499.1	0.704353	0.704343	0.000011	-	7.2	0.512783	0.512448	0.000006	2.82
BT-65	Gabbro	1	1479.5	0.704328	0.704325	0.000011	-	29.2	0.512673	0.512445	0.000005	2.77
BT-72	Gabbro	1	1419	0.704361	0.704359	0.00001	-	21.2	0.512718	0.512493	0.000013	3.71
UZ-11	Gabbro	0.4	641.3	0.704268	0.704266	0.00001	-	5.7	0.512799	0.512489	0.000006	3.63
UZ-01	Gabbro	2.8	531.6	0.704262	0.704243	0.00001	-	8.7	0.512769	0.512476	0.000007	3.36

Table 6.3 O-Isotopes for plagioclase and Ti-magnetite separates from gabbroic and Fe-Ti oxide ore layers.

Sample	Rock Type	Stratigraphic Position	Plagioclase ^{18}O	Ti-magnetite ^{18}O
05-1	Gabbro	± 15 m below main ore	8.2	3.8
05-9	Gabbro	± 5 m above main ore	8.4	2.9
05-6	Fe-Ti Oxide ore	Middle of ore layer	8.9	5.9
05-78	Fe-Ti Oxide ore	Middle of ore layer	8.2	3.6

7. fO_2 and H_2O modeling implications for Fe-Ti oxide crystallisation: high-Ti vs. low-Ti basalt as parental for the Panzhihua intrusion

Variations in fO_2 and H_2O have significant effects on the crystallisation of ferrobasaltic magmas (e.g. Toplis and Carroll, 1995; Botcharnikov et al. 2008). High fO_2 favours the crystallisation of magnetite-ulvospinel (Mt-Uv) over ilmenite and can result in the early crystallisation of Mt-Uv (Toplis and Carroll, 1995). Ilmenite crystallisation has been shown to be controlled by the TiO_2 content of the parent magma rather than fO_2 like Mt-Uv. High H_2O contents of ferrobasaltic magma depress the crystallisation temperature of silicate minerals, plagioclase in particular, and can also result in the early crystallisation of Fe-Ti oxides. Clinopyroxene crystallisation is controlled by the CaO/FeO_T ratio of the parent magma (Snyder et al. 20030, which results in either earlier crystallisation prior to Fe-Ti oxides or later crystallisation after Fe-Ti oxides. Recent work on the Panzhihua intrusion has produced two separate models for the crystallisation of the intrusion: 1) low-Ti, high CaO and low H_2O (0.5 wt %) parent magma (equivalent to Emeishan low-Ti basalt) at FMQ (e.g. Ganino et al. 2008) and 2) high-Ti, low CaO and higher H_2O (> 1.5 wt %) parent magma (equivalent to Emeishan high-Ti basalt) at FMQ+1.5 (e.g. Pang et al. 200b; Zhang et al. 2012). Modeling of these parent magma compositions produces significantly different results.

Present here is detailed fO_2 and H_2O modeling for average compositions of both Emeishan high-Ti and low-Ti ferrobasalts in order to constrain the effects on crystallisation sequences for Emeishan ultramafic-mafic layered intrusions. Modeling is consistent with numerous experimental studies on the ferrobasaltic magmas from other localities; e. g. Skaergaard intrusion – Botcharnikov et al. (2008). Modeling is compared with the geology of the Panzhihua intrusion in order to constrain the crystallisation of the gabbroic rocks and the Fe-Ti oxides ore layers. The gabbroic rocks at the Panzhihua intrusion can be best explained by crystallisation from a parent magma similar to that of the high-Ti Emeishan basalt at moderate H_2O contents (0.5-1 wt %) but at the lower end of TiO_2 content for typical high-Ti basalts (2.5 wt % TiO_2). Distinct silicate disequilibrium textures in the Fe-Ti oxide ore layers suggest that an influx of H_2O may be responsible for changing the crystallisation path. An increase in H_2O during crystallisation of gabbroic rocks will result in the depression of silicate liquidus temperatures and resultant disequilibrium with the liquid. Continued cooling of the magma with high H_2O then results in precipitation of Mt-Uv alone.

The H_2O content of parent magmas for mafic layered intrusions associated with the ELIP is an important variable. H_2O alters the crystallisation sequence of the basaltic magmas so that at high H_2O and fO_2 Mt-Uv crystallises earlier than plagioclase and clinopyroxene. Furthermore, the addition of H_2O to an anhydrous magma can explain silicate disequilibrium texture observed in the Fe-Ti oxide ore layers.

7.1 Introduction to crystallisation modeling

Fe- and Ti-rich basaltic magmas evolve by differentiation processes following the typical tholeiitic Fenner trend (Fenner, 1929). Early stages of evolution are characterised by an increase in FeO and TiO_2 at relatively constant SiO_2. Later stages of evolution are characterised by strong depletion of FeO and TiO_2 at the onset of Fe-Ti oxide crystallisation with resultant increase in SiO_2. The timing of Fe-Ti oxide crystallisation is strongly dependant on the conditions of the magma system, in particular fO_2 (e. g. Toplis and Carroll, 1995). Significant Fe-enrichment is mostly confined to plutonic/layered intrusions where differentiation results in the upper zones becoming enriched in Fe and Ti (e.g. Skaergaard intrusion). The rarity of Fe-enriched extrusive rocks is interpreted to be the result of the high density of such magmas (Sparks et al. 1980), although examples are known, such as the Columbia River Flood basalts (12-17 wt % total Fe; Lange, 2002). The eruption of these dense Fe-rich magmas is attributed to a high initial volatile content (> 4 wt %) (Lange, 2002). The Emeishan flood basalts have total Fe concentrations of 9-14 wt % (Xiao et al. 2004) and are an example of Fe-rich flood basalts. Recent experimental work of Botcharnikov et al. (2008) has shown that the concentration of volatiles within the ferrobasaltic magmas has significant effects on the differentiation paths leading to a calc-alkaline evolutionary trend due to the early crystallisation of Fe-Ti oxides.

The Panzhihua intrusion contains significant Fe-Ti oxide ore layers, implying significant Fe-enrichment of the parent magma. Recent studies on the intrusion have modeled magma compositions believed to represent parent magmas in order to constrain the formation of massive Fe-Ti oxide ore layers. Pang et al. (2008b) and Hou et al. (2012) modeled a representative parent composition for the Panzhihua and Taihe intrusions respectively at conditions of P= 3 kb, fO_2 marked by FMQ and an initial bulk H_2O of 1.5 wt %. Ganino et al. (2008) also modeled a representative composition of an Emeishan basalt at FMQ, although it contains significantly less TiO_2 (2.6 wt %) relative to the composition used by Pang et al. (2008b) (4.85 wt %) and Hou et al. (2012) (4.1 wt %). Furthermore Ganino et al. (2008) model the magma with low bulk initial H_2O (0.5 wt % H_2O), using

methods developed by Dixon et al. (2002) such that the Ce concentrations were used to estimate H_2O contents. The results from these two modeling studies are very different. Pang et al. (2008b) and Hou et al. (2012) show that Fe-Ti oxides crystallise early whereas Ganino et al. (2008) show that Fe-Ti oxides crystallised late, after significant crystallisation of olivine, plagioclase and clinopyroxene. These studies form the basis of the current study. A further important factor influencing the crystallisation of ferrobasaltic magma (not discussed by Pang et al. 2008b or Ganino et al. 2008) is the CaO/FeO_T and CaO/TiO_2 ratios of the parent magma. Snyder et al. (1993) showed that at low ratios clinopyroxene crystallises late, after Fe-Ti oxides. The parent composition used by Pang et al. (2008b) has low CaO/FeO_T and CaO/TiO_2 ratios whereas the parent composition used by Ganino et al. (2008) has high ratios. Figure 7.1 presents a summary mineral abundances and mineral compositions from Zhou et al. (2005) and Pang et al. (2009) for comparison with modeling predictions in later discussions.

7.2 Objectives for crystallisation modeling

The objectives of the modeling presented in this study are to constrain the parent magma composition with respect to bulk composition, in terms specifically of the influence of a) CaO/FeO_T and CaO/TiO_2 ratios, b) oxygen fugacity, c) water content, and to evaluate these effects in terms of the timing and mechanism for Fe-Ti oxide crystallization in light of observations from the ferrogabbros and Fe-Ti oxide ore layers of the Panzhihua intrusion. Fe-Ti oxides at the Panzhihua intrusion have been interpreted to crystallise late after silicate crystallisation (Zhou et al. 2005; Zhou et al. 2008; section 9.1). The silicates are interpreted to crystallise prior to extensive Ti-magnetite crystallisation forming ore layers (Zhou et al. 2005; Zhou et al. 2008; section 9.1). This is fundamental in the understanding of ore forming processes at the Panzhihua Intrusion. Silicate phases are not in equilibrium with later liquids crystallising Fe-Ti oxides. The effect of varying fO_2 and H_2O is discussed in order to account for early crystallisation of silicates with later crystallisation of extensive Fe-Ti oxides.

7.3 Modeling conditions

Modeling was done using the PELE version 7.04 (Boudreau 1999). Pang et al. (2008a) suggested that the Panzhihua intrusion crystallised at a depth equivalent to 5 kb based on the Al_2O_3 content of Ti-magnetite grains. However, Ganino et al. (2008) showed that the footwall carbonates were buried to

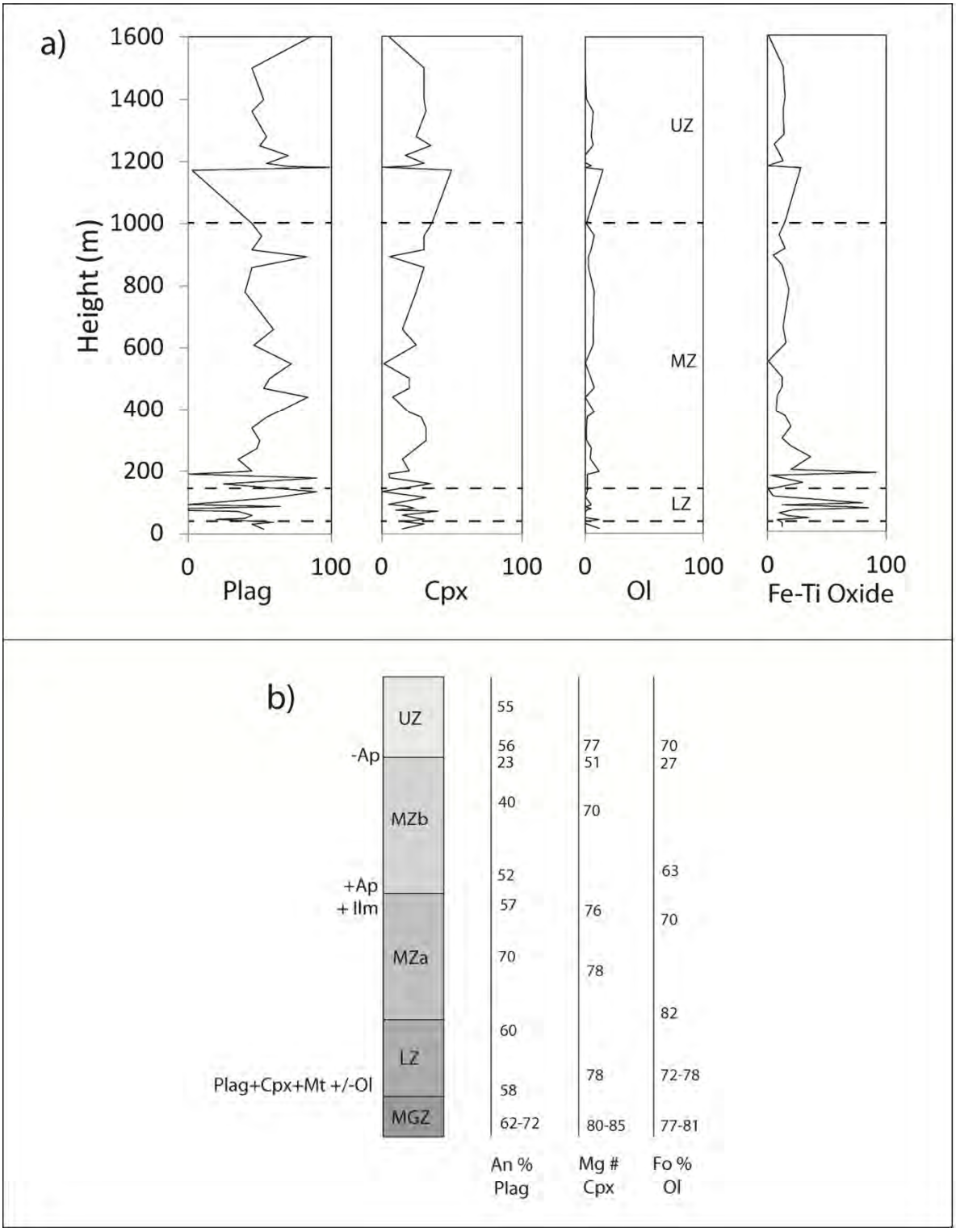

Figure 7.1 a) Modal abundance of mineral phases for the Zujiabaobao Block of the Panzhihua intrusion after Zhou et al. (2005). b) Mineral compositional variation over the stratigraphy of the Jianshan Block of the Panzhihua intrusion after Pang et al. (2009).

a depth of approximately 2 kb. This latter estimate of 2 kb is used here due to the possibility of Ti-magnetite having crystallised at depth prior to emplacement, and hence potentially not being representative of emplacement conditions; however, the pressure (depth) of crystallisation does not significantly affect the crystallisation sequence. Temperature increments were set at 5^{o}C for an isobaric system undergoing fractionation. A variety of oxygen buffers were used including FMQ, FMQ+1, FMQ+2 and FMQ+3. Furthermore initial H_2O was modeled at 0, 0.5, 1, 2, 3 and 5 wt %. The parent magma compositions were renormalised to accommodate variable amounts of H_2O added to the composition.

By fixing the fO_2 buffer (FMQ-FMQ+3) during differentiation the modeled system is essentially open to oxygen. In a closed system, the precipitation of Mt-Uv would in itself lower the Fe^{3+}/Fe^{2+} ratio of the system and result in more reducing conditions. The consequence is that precipitation of large quantities of Mt-Uv is not possible as oxidizing conditions are required and Mt-Uv crystallisation produces more reducing conditions. Model runs closed to oxygen, in the absence of a fO_2 buffer, do not result in Mt-Uv crystallisation and a system closed to oxygen does not result in extensive Mt-Uv precipitation. For this reason the fO_2 was set using the buffers described above.

7.4 Constraints of PELE software

Several papers report experimental work that is not in agreement with the predictions of modeling software such as MELTS and PELE, in particular for hydrous and highly oxidizing conditions (e.g. Toplis and Carroll 1995 and Gaillard et al. 2003). These variables form the basis of the current study and the validity of discussion based on PELE modeling needs to be assessed. In order to constrain uncertainties of the PELE software, I present PELE recreated models for experimental results.

The experimental results of Toplis and Carroll (1995) are used in order to constrain the uncertainties for highly oxidising conditions at anhydrous compositions (Figure 7.2 a and c). It is immediately apparent that the Mt-Uv stability curve is significantly different at highly oxidizing conditions (> FMQ+1). Experimental results show that Mt-Uv becomes stable at higher temperatures under oxidising conditions and that Mt-Uv is the first oxide phase to crystallise above FMQ (Figure 7.2 c). Modeling software (PELE) shows Mt-Uv becoming stable at significantly lower temperatures at highly oxidizing conditions. This is at odds with what is expected and implies that modeling software

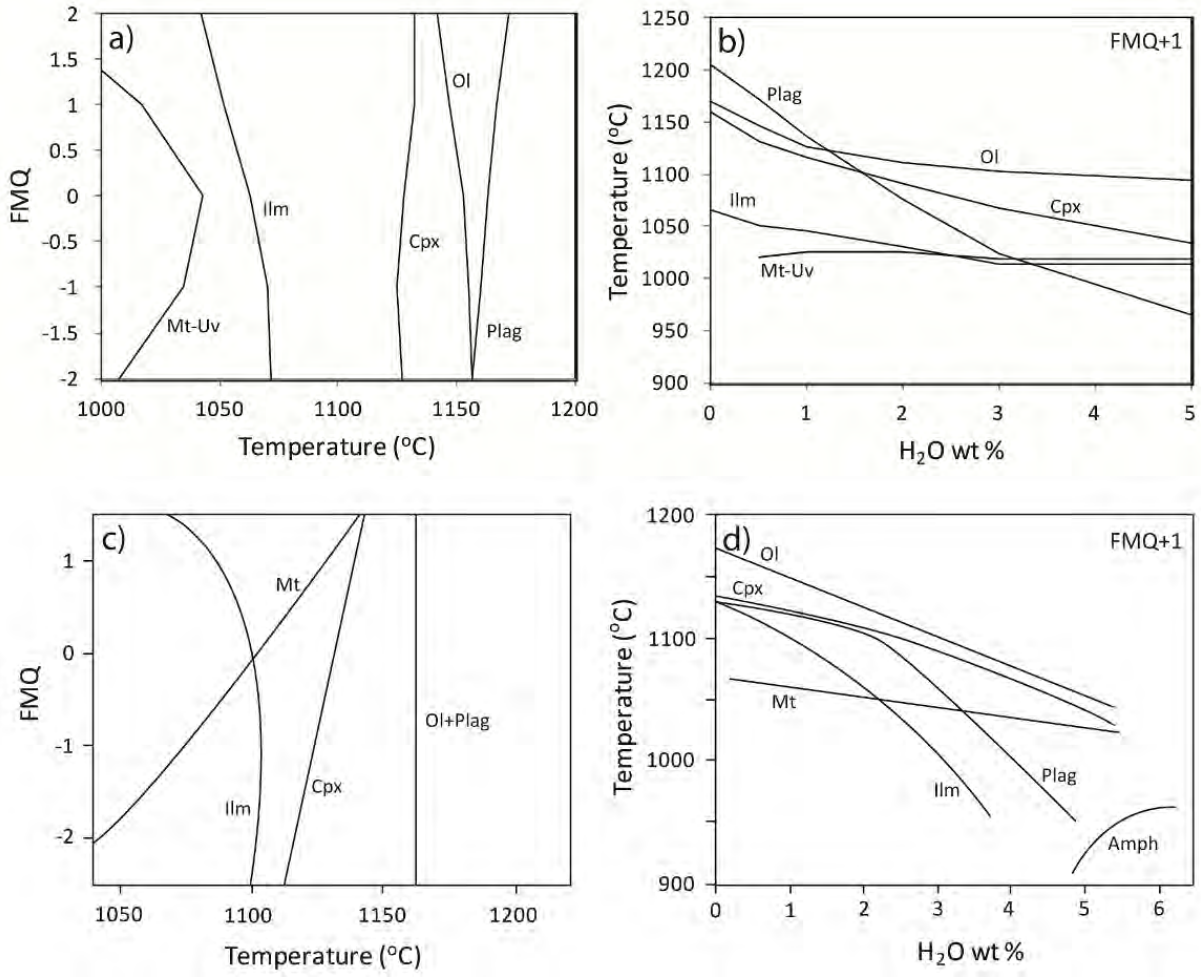

Figure 7.2 a) Recreated modeling derived phase equilibria for the experiments of Toplis and Carroll (1995). b) Recreated modeling derived phase equilibria for the experiments of Botcharnikov et al. (2008). c) Phase equilibria of the experiments of Toplis and Carroll (1995). d) Phase equilibria as determined by Botcharnikov et al. (2008).

is not reliable for oxide phase stability at highly oxidizing conditions. Silicate stability curves, in particular olivine and plagioclase, also show some variation from experimental results at highly oxidising conditions. This further suggests that PELE has significant errors for highly oxidizing conditions. Therefore discussion on results of PELE modeling at highly oxidising conditions is not valid.

In order to constrain the uncertainties of hydrous compositions, the experiments of Botcharnikov et al. (2008) are also recreated using the PELE software (Figure 7.2 b and d). The fO_2 was set using the

oxygen buffer FMQ+1 (upper limit of PELE reliability for oxide stability predictions) and modeled parent magma compositions at various initial H_2O contents (Figure 7.2 b and d). The PELE model created is somewhat more reliable than that for highly oxidizing conditions. The major difference of the PELE model is the crystallisation of plagioclase and ilmenite at lower H_2O contents (< 1.5 wt %). This suggests that plagioclase stability at low H_2O contents may be over estimated using PELE (in terms of temperature of crystallisation). This needs to be taken into account for later discussions. Error bars (calculated by difference between crystallisation temperature of PELE vs experimental results of Botcharnikov et al. 2008) for olivine are generally low; 4^{o}C at anhydrous conditions and increase to 29 ^{o}C at 5 wt % H_2O. Clinopyroxene is also generally relatively consistent with experimental work with errors ranging from 12 to 26 ^{o}C. As discussed above plagioclase crystallisation for anhydrous compositions is significantly over estimated with an error of 73 ^{o}C. However at hydrous conditions > 0.5 wt % the errors range from 14 to 36 ^{o}C. Mt-Uv is generally in good agreement with errors of 16 to 35 ^{o}C. Ilmenite crystallisation shows the greatest errors and ranges from 30-60 ^{o}C.

However the overall trends of both the silicates and Mt-Uv are similar to experimental results, in particular the decrease in stability of silicate phases and the relatively constant crystallisation temperature of Mt-Uv. The ilmenite stability curve is significantly different to that of experimental results of Botcharnikov et al. (2008). This needs to be taken into account in later discussions. It is noteworthy to point out here that PELE does not predict amphibole stability. However experimental results shows that amphibole is only stable at low temperatures and very high H_2O contents (> 5 wt %) (Figure 7.2 d).

Therefore while PELE software has large uncertainties at highly oxidising conditions the trends predicted at high H_2O contents are consistent (with the exception of ilmenite) with experimental work.

7.5 Parent magma composition

Selection of parent magmas for modeling of the evolution of the Panzhihua intrusion is particularly important as subtle variations in TiO_2 content and CaO/FeO_T can have significant affects on the crystallisation sequence. Emeishan basalts vary significantly in terms of TiO_2 and have been divided

Table 7.1 Modeled average parent magma compositions for high-Ti and low-Ti Emeishan basalt after Xiao et al. (2004) and comparison with compositions modeled in studies of Ganino et al. (2008) and Pang et al. (2008b). Compositions modeled by Toplis and Carroll (1995) and the estimated composition of the Skaergaard intrusion (Hoover, 1989) are also given for comparison.

	Low-Ti basalt	High-Ti basalt	Ganino et al. (2008)	Pang et al. (2008b)	Toplis and Carroll (1995)	Hoover (1989)
SiO_2	51.48	51.72	47.50	45.83	48.30	49.62
TiO_2	1.71	4.37	2.70	4.85	2.90	2.61
Al_2O_3	13.91	13.49	14.00	15.62	14.90	13.25
Fe_2O_3	1.66	2.16	1.77	2.23	1.85	
FeO	9.29	11.09	10.55	11.36	11.43	13.03*
MnO	0.16	0.21	0.00	0.23	0.00	0.22
MgO	6.90	4.94	7.10	7.18	6.50	7.23
CaO	11.22	7.26	10.60	7.52	10.90	10.13
Na_2O	2.71	3.39	2.70	3.26	2.70	2.39
K_2O	0.73	0.93	1.70	1.41	0.30	0.45
P_2O_5	0.24	0.42	0.30	0.51	0.00	0.22
Total	100.00	99.98	98.92	100.00	99.78	99.15

***Total Fe as FeO

into high-Ti and low-Ti groups (e. g. Xu et al. 2001; Xiao et al. 2004). Along with this variation in TiO_2 content there is a notable variation in CaO/FeO_T ratio; high-Ti basalts have low ratios whereas the low-Ti basalts have high ratios. Parent magma compositions used in previous studies (Ganino et al. 2008; Pang et al. 2008b) are presented in Table 1 along with the average composition of low-Ti and high-Ti basalt from Xiao et al. (2004). The composition used by Pang et al. (2008b) is a typical high-Ti basalt composition. However the composition used by Ganino et al. (2008) is more similar to low-Ti basalt.

The interpretation of the MGZ as a chilled margin suggests that this zone may represent a parental magma for the Panzhihua intrusion. However the heterogeneous rock compositions (e.g. olivine gabbro, gabbro, clinopyroxenite, wehrlite) observed in the MGZ makes it difficult to use the MGZ as a parental magma composition. Numerous authors have suggested that the Panzhihua intrusion crystallised from a high-Ti basalt parent (e. g. Zhou et al. 2005; Zhang et al. 2009). I present here crystallisation modeling for parent magma compositions represented by both the average high-Ti basalt and average low-Ti basalt compositions listed in Table 1. Average compositions of Emeishan basalts are preferred over preferentially selecting a single analysis.

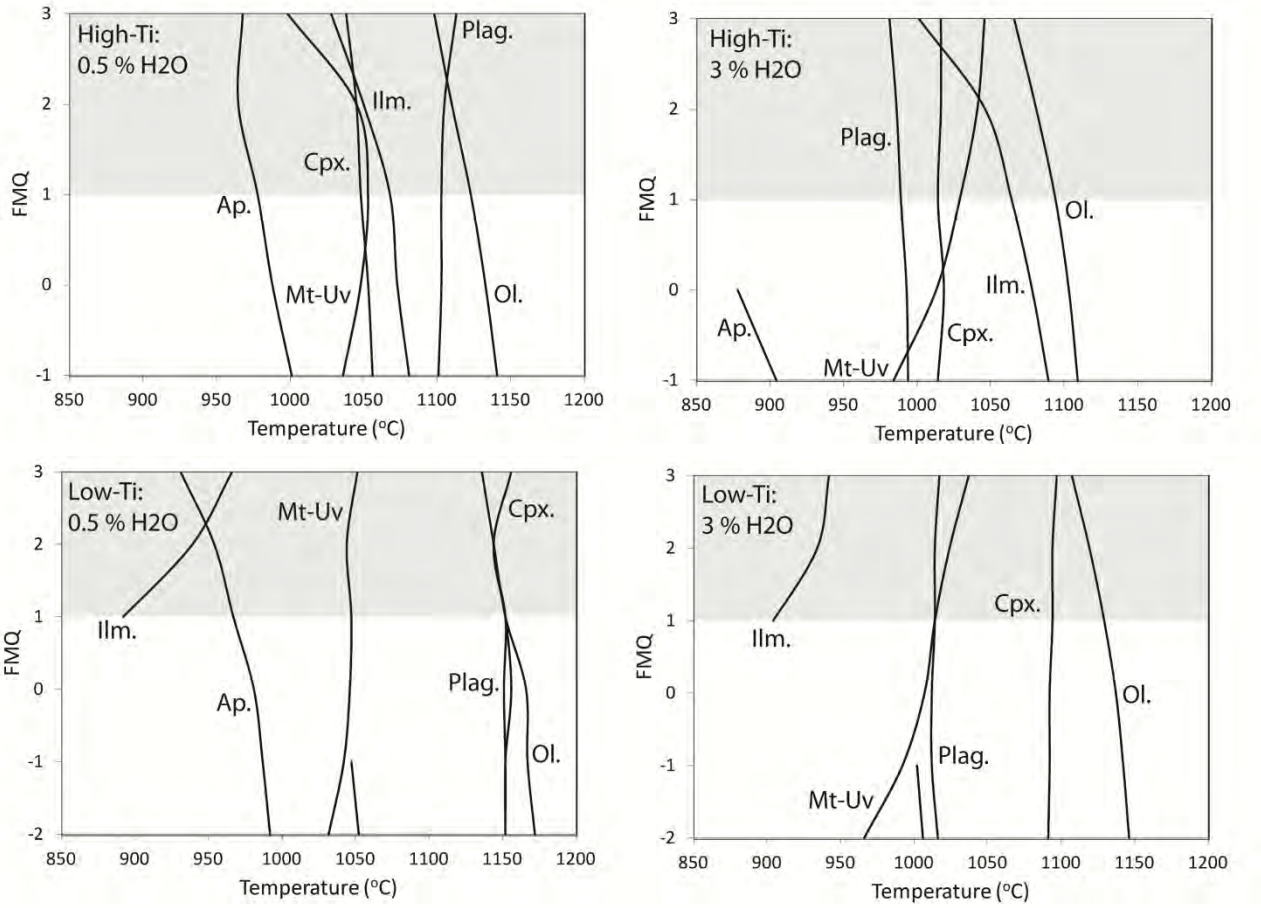

Figure 7.3 Modeling derived phase equilibria for average high-Ti and low-Ti Emeishan basalt compositions as a function of fO_2 with temperature at 0.5 and 3 wt % H_2O for each composition. Note the distinct relationship of Fe-Ti oxides for the high-Ti compositions: Mt-Uv crystallises prior to ilmenite at high fO_2. Areas highlighted in grey represent areas of unreliability for the PELE software (i.e. highly oxidising conditions; see section 7.4 in the text for discussions).

7.6 Thermodynamic modeling predictions

7.6.1 Crystallisation sequence

The crystallisation sequence for both the average high-Ti and low-Ti Emeishan basalt compositions have been modeled at FMQ – FMQ+3 and at initial H_2O wt % of 0-3. The results are illustrated in Figures 7.3 and 7.4. Several significant variations are highlighted in descriptions for each composition below.

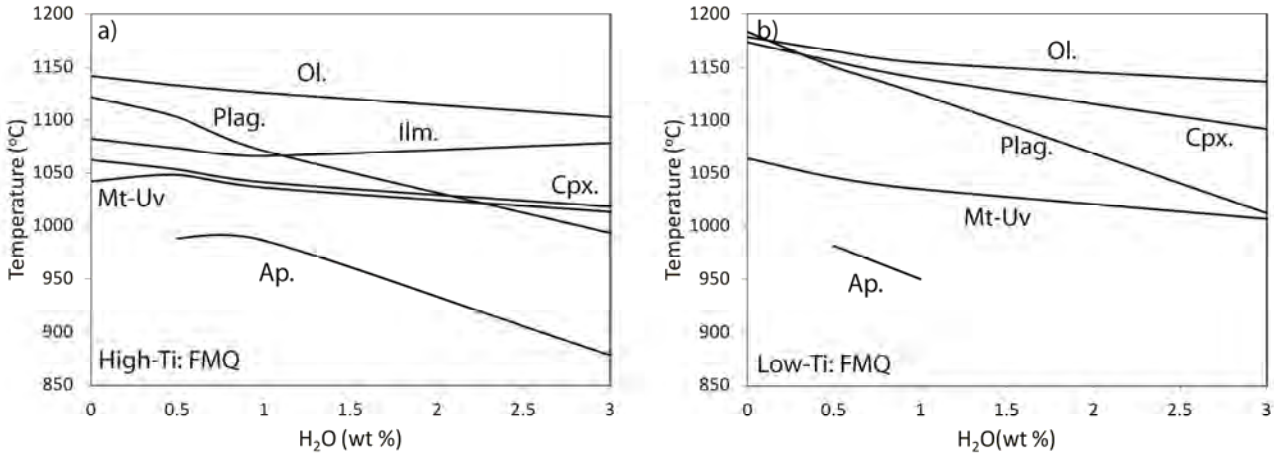

Figure 7.4 Modeling derived phase equilibria for average a) high-Ti and b) low-Ti Emeishan basalt compositions as a function of H_2O with temperature at FMQ. Note the significant depression of plagioclase and clinopyroxene crystallisation temperature with increasing H_2O content for both high-Ti and low-Ti basalt compositions.

Parent 1: High-Ti basalt

The crystallisation sequence of the high-Ti basalt composition varies with both changes in fO_2 and H_2O wt %. Figure 7.3 shows at low H_2O (0.5 wt %) the sequence is olivine-plagioclase-ilmenite-clinopyroxene - Mt-Uv – apatite. At high fO_2 (FMQ+3) there is a subtle change such that plagioclase crystallises prior to olivine and clinopyroxene prior to ilmenite and Mt-Uv. However, as observed above the software does not correctly predict Mt-Uv crystallisation at highly oxidizing conditions and therefore the trends observed are likely not correct. At high H_2O content (3 wt %) the crystallisation temperature of the silicates is significantly depressed (Figure 7.3). The general crystallisation sequence changes to olivine-Fe-Ti oxide-clinopyroxene-plagioclase-apatite. Figure 7.4 (a) shows the clear depression of plagioclase crystallisation temperature from 1125-1500^{o}C at 0.5 wt % H_2O to < 1000^{o}C at 3 wt % H_2O, which results in the earlier appearance of Fe-Ti oxides in the crystallisation sequence.

Parent 2: Low-Ti basalt

The crystallisation sequence of the low-Ti basalt composition at low H_2O (0.5 wt %) is characterised by the crystallisation of olivine, plagioclase and clinopyroxene within 10-15^{o}C of each other. Fe-Ti oxides crystallise at significantly lower temperatures; ± 100^{o}C lower (Figure 7.3). Ilmenite crystallises first at low fO_2 (< FMQ) and Mt-Uv at higher fO_2 (> FMQ). This is more consistent with experimental

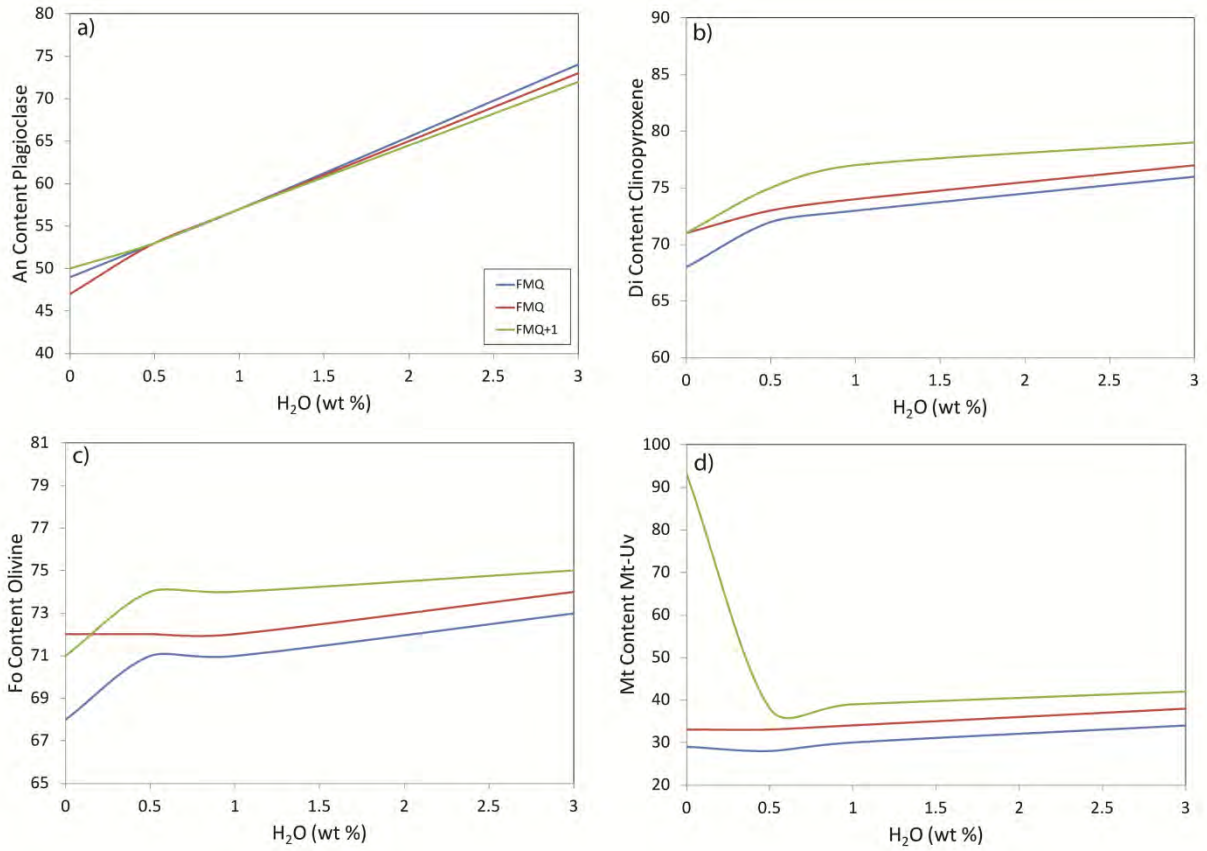

Figure 7.5 Modeled compositions of the first occurrences of mineral phases for the high-Ti basalt parent magma with increasing H_2O and fO_2. a) An content of plagioclase shows significant variation with H_2O content but no variation with increasing fO_2. b) Di content of clinopyroxene showing minor variation with both H_2O and fO_2. c) and d) Fo content of olivine and Mt content of Mt-Uv respectively showing minor variation with increasing fO_2 and no variation with H_2O.

results of Toplis and Carroll (1995). Ilmenite does not crystallise at fO_2 conditions represented by FMQ. At higher H_2O content (3 wt %; Figure 7.3) the crystallisation temperature of silicate phases is depressed, in particular plagioclase, which crystallises after Mt-Uv at fO_2 conditions > FMQ. The affects of H_2O on the crystallisation sequence is further highlighted in Figure 7.4 b. The main differences in the crystallisation sequence of the low-Ti basaltic liquid (as compared to high-Ti basaltic liquid) are the earlier appearance of clinopyroxene and the later occurrence of ilmenite.

7.6.2 Mineral compositional variation

The data presented here are for the compositions of the first appearance of any given mineral phase. Evolution of the mineral compositions with differentiation of the magma is presented below in section 7.6.3.

Parent 1: High-Ti basalt

The initial composition of crystallising phases varies with fO_2 and the initial H_2O content of the parent magma. An content of plagioclase (Figure 7.5 a) shows a significant variation with respect to H_2O content of the magma but is not affected by fO_2. At 0% initial H_2O content, plagioclase has a composition of An_{49}-An_{52} in contrast to An_{70}-An_{74} at 3% initial H_2O. Clinopyroxene shows a similar variation but the compositional change is not as significant as plagioclase. At low initial H_2O clinopyroxene has composition of Di_{68}-Di_{79} but at higher initial H_2O content the composition is Di_{76}-Di_{85} (Figure 7.5 b). Clinopyroxene also shows a minor variation with fO_2, at higher fO_2 conditions the clinopyroxene has a higher Di content. Olivine and Mt-Uv show no correlation with H_2O content but do show significant variation with fO_2 (Figure 7.5 d). At fO_2 conditions represented by FMQ-1 olivine has a composition of Fo_{68}-Fo_{73} (Figure 7.5 c). The Fo content of olivine increases with increasing fO_2.

Parent 2: Low-Ti basalt

The composition of plagioclase crystallising from the Low-Ti parent compositions shows a similar trend to that described above, with significant increase in An content with increasing H_2O wt %. The An content increases from An_{69}-An_{72} at low H_2O (0 wt %) to An_{83} at high H_2O (3 wt %) (Figure 7.6 a). These compositions are more primitive (more calcic) relative to the plagioclase crystallising from the high-Ti parent composition. Clinopyroxene, olivine and Mt-Uv show no trend with H_2O content of the parent magma and show only minor variation in composition with changing fO_2 conditions (Figure 7.6 b-d). Except for Mt-Uv, which show a significant change in composition with increasing fO_2 conditions (Figure 7.6 d). At low fO_2 (FMQ-1) Mt-Uv has a composition of Mt_{20}-Mt_{32}.

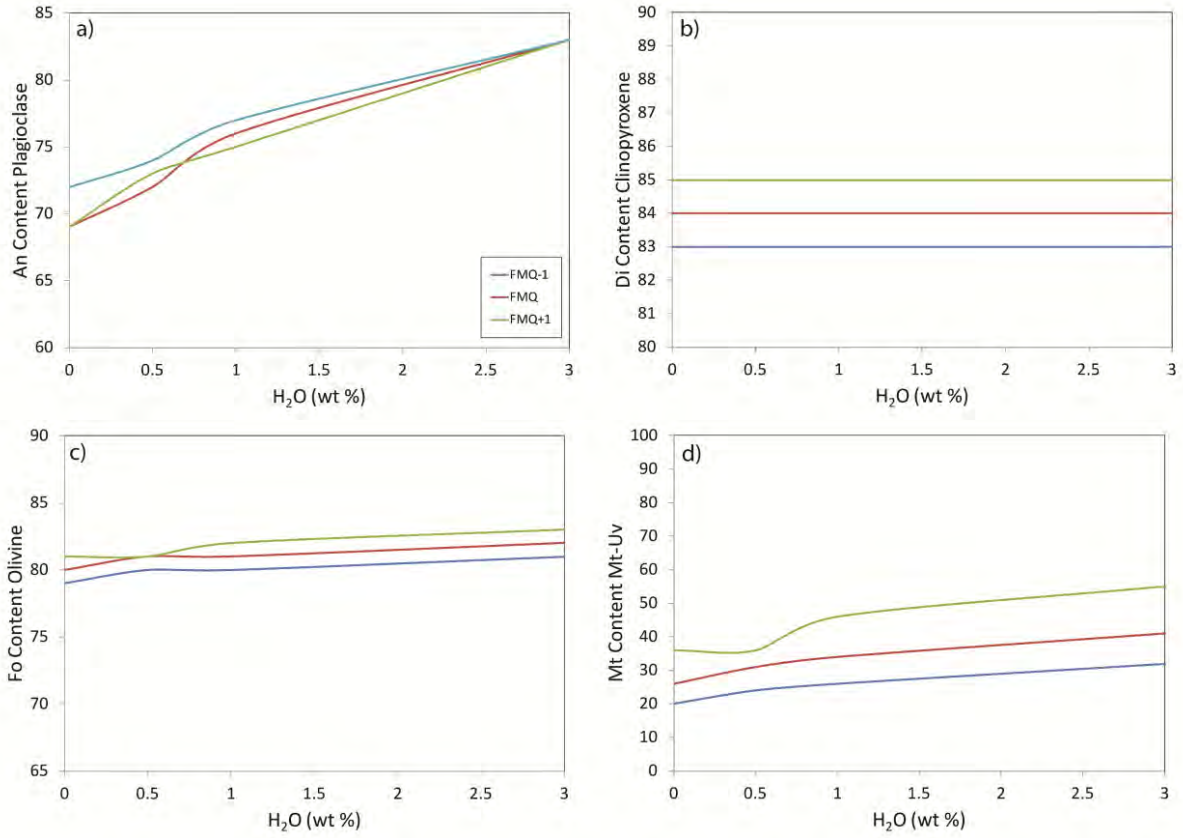

Figure 7.6 Modeled compositions of the first occurrences of mineral phases for the low-Ti basalt parent magma with increasing H_2O and fO_2. a) An content of plagioclase showing a distinct relationship with H_2O. Also note the significantly higher An content relative to that of the high-Ti basalt composition (Figure 7.5 a). b), c) and d) clinopyroxene, olivine and Mt-Uv composition of the low-Ti basalt parent magma respectively; showing no trend with H_2O and minor variation with fO_2.

7.6.3 Evolution of mineral compositions with differentiation

Parent 1: High-Ti basalt

Figures 7.7 and 7.8 illustrate the evolution of olivine, plagioclase, clinopyroxene and Mt-Uv during cooling of high-Ti parent magma at 0.5 % H_2O and 3 % H_2O. At 0.5 % H_2O; olivine initially evolves to lower Fo content as expected but there is a clear inflection point related to the onset of Fe-Ti oxide crystallisation (Figure 7.7 a). The Fo content of olivine at low fO_2 (< FMQ) remains constant after the onset of Fe-Ti oxide crystallisation whereas at high fO_2 (>FMQ) the Fo content increases. Plagioclase shows a typical evolution from high An (An_{54}) at high temperature to low An (An_{30}) at later stages of crystallisation (Figure 7.7 b). Di content of clinopyroxene remains relatively constant with decreasing

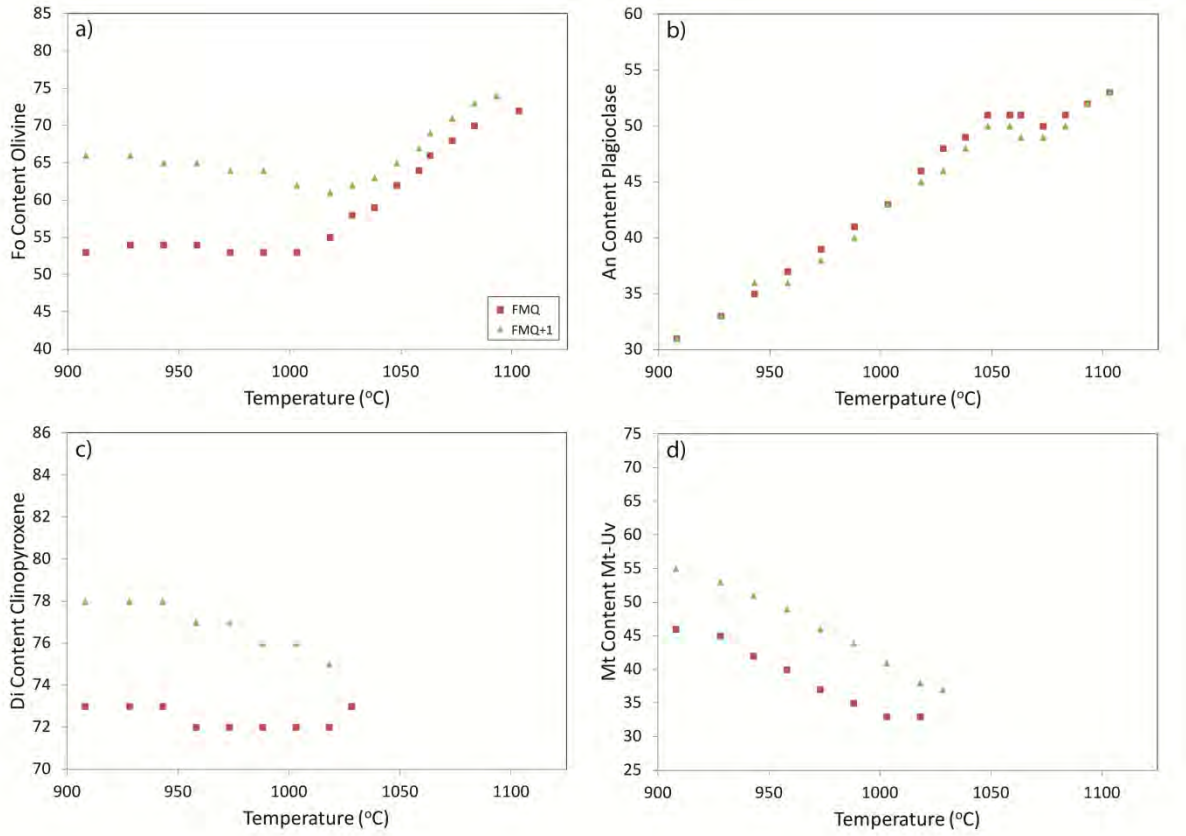

Figure 7.7 Composition of mineral phases as a function of fO_2 with decreasing temperature for a high-Ti parent magma with 0.5 wt % H_2O.

temperature Figure 7.7. Mt content of Mt-Uv increases in Mt at all fO_2 conditions modeled. Furthermore the Mt content is higher at higher fO_2 conditions (Figure 7.7 d). At high H_2O contents olivine shows initial minor evolution to lower Fo contents followed by a gap of ± 40°C where no olivine crystallises. Olivine resumes crystallisation after this gap and remains constant in composition down to 900°C (Figure 7.8 a). Mt content of Mt-Uv shows a minor increases in content with decreasing temperature and shows a minor increase in Mt content with increased fO_2 (Figure 7.8 b). Di content of clinopyroxene remains constant with decreasing temperature (Figure 7.8 c). Plagioclase crystallises at significantly lower temperatures at higher H_2O as described previously. An content of plagioclase shows a typical evolution from high An (An_{74}) at high temperature to low An (An_{57}) at low temperature (Figure 7.8 d).

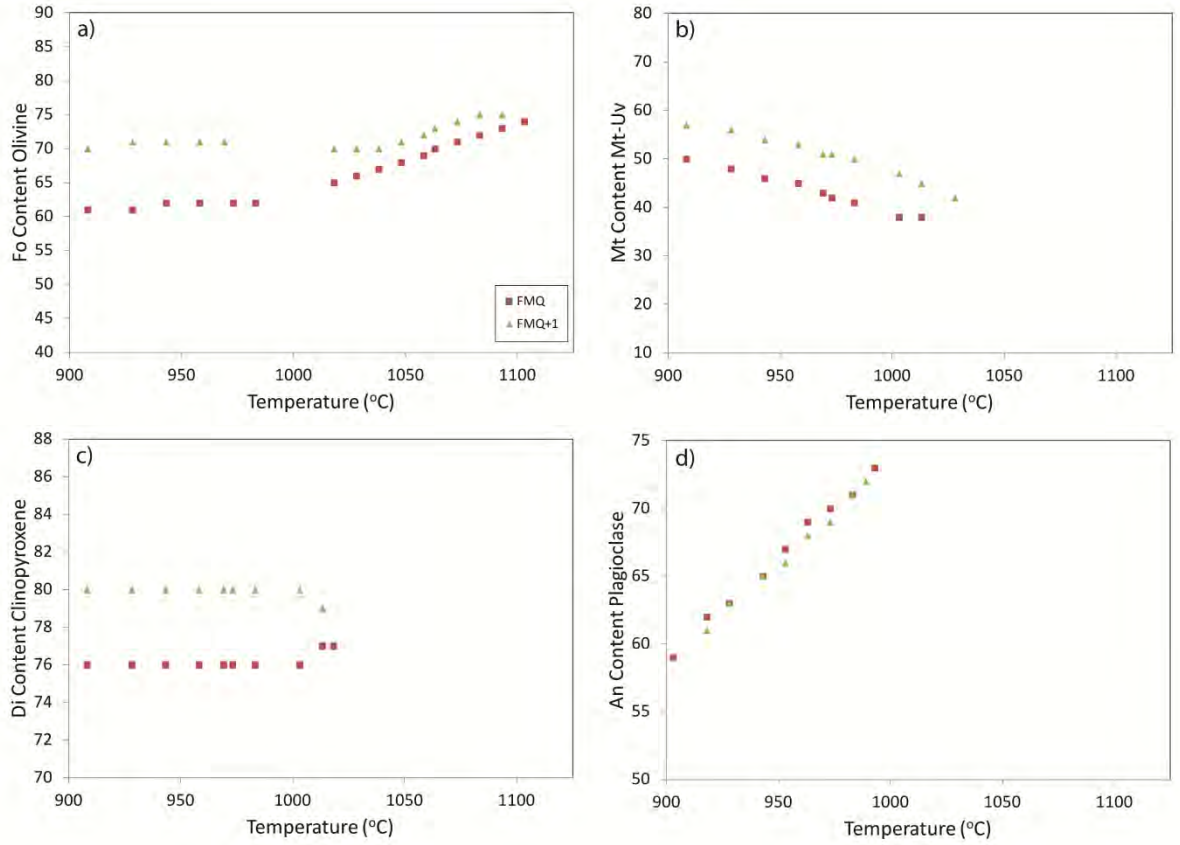

Figure 7.8 Composition of mineral phases as a function of fO_2 with decreasing temperature for a high-Ti parent magma with 3 wt % H_2O.

Parent 2: Low-Ti basalt

Figures 7.9 and 7.10 illustrate the evolution of olivine, plagioclase, clinopyroxene and Mt-Uv during cooling and crystallisation of the Low-Ti basalt parent magma. At low H_2O content (0.5 wt %; Figure 7.9) olivine and clinopyroxene initially evolve to lower Fo and Di contents respectively. However at the onset of Mt-Uv crystallisation (1050°C; Figure 7.9 d) the trends change and generally show increases in Fo and Di content with decreasing temperature. Fo and Di contents of olivine and clinopyroxene are also affected by the fO_2 conditions. At higher fO_2 conditions the Fo and Di contents are slightly higher. Plagioclase shows a constant decrease in An content with cooling and shows no variation with fO_2 conditions (Figure 7.9 b). Mt-Uv generally shows an increase in Mt content with cooling (Figure 7.9 d).

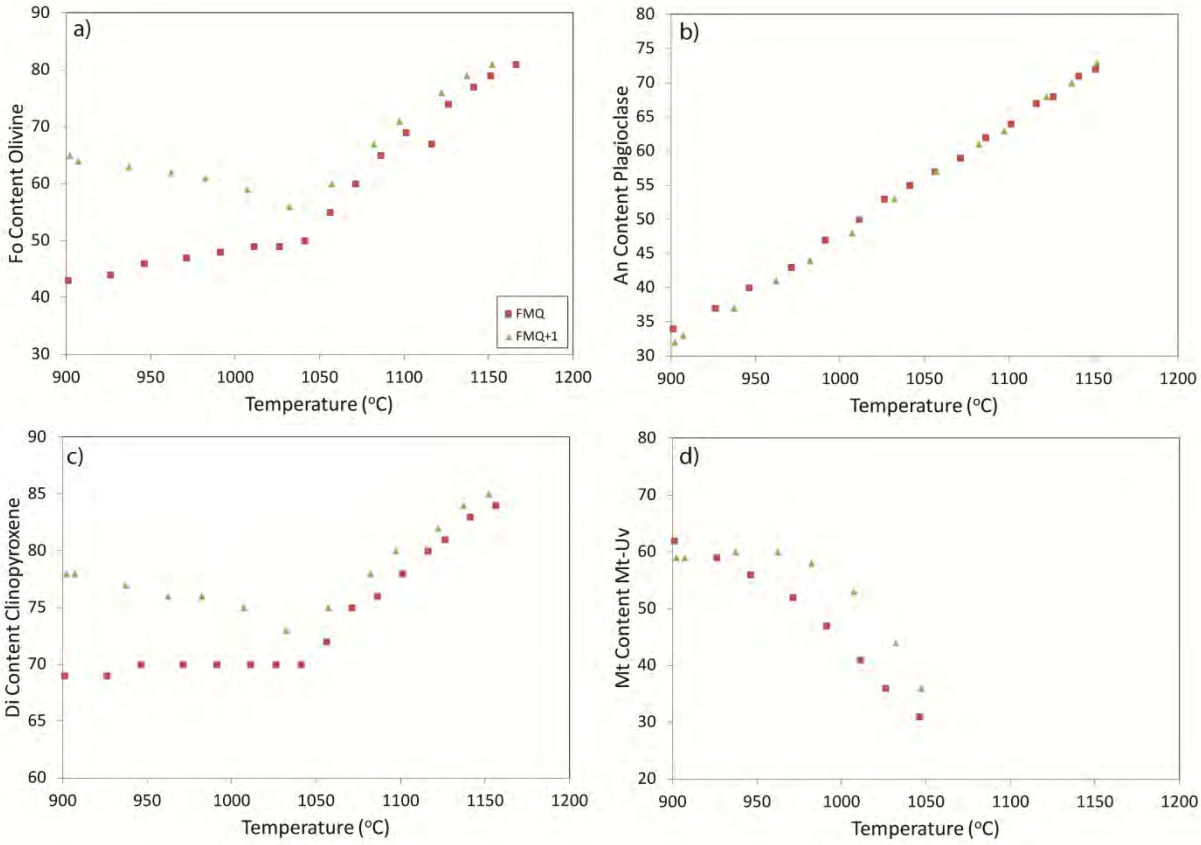

Figure 7.9 Composition of mineral phases as a function of fO_2 with decreasing temperature for a low-Ti parent magma with 0.5 wt % H_2O.

Olivine, clinopyroxene and plagioclase show similar trends at high H_2O content (3 wt %) of the parent magma (Figure 7.10 a, b and c), although the crystallisation temperature of plagioclase is significantly lower. Mt-Uv increases in Mt content with cooling at low fO_2 conditions (FMQ).

7.6.4 Fe-enrichment in the liquid

Fe-enrichment in the liquid is controlled by the timing of Fe-Ti oxide crystallisation. Fe-enrichment trends are similar for both the high- and low-Ti parent magmas and are described together. Fe-

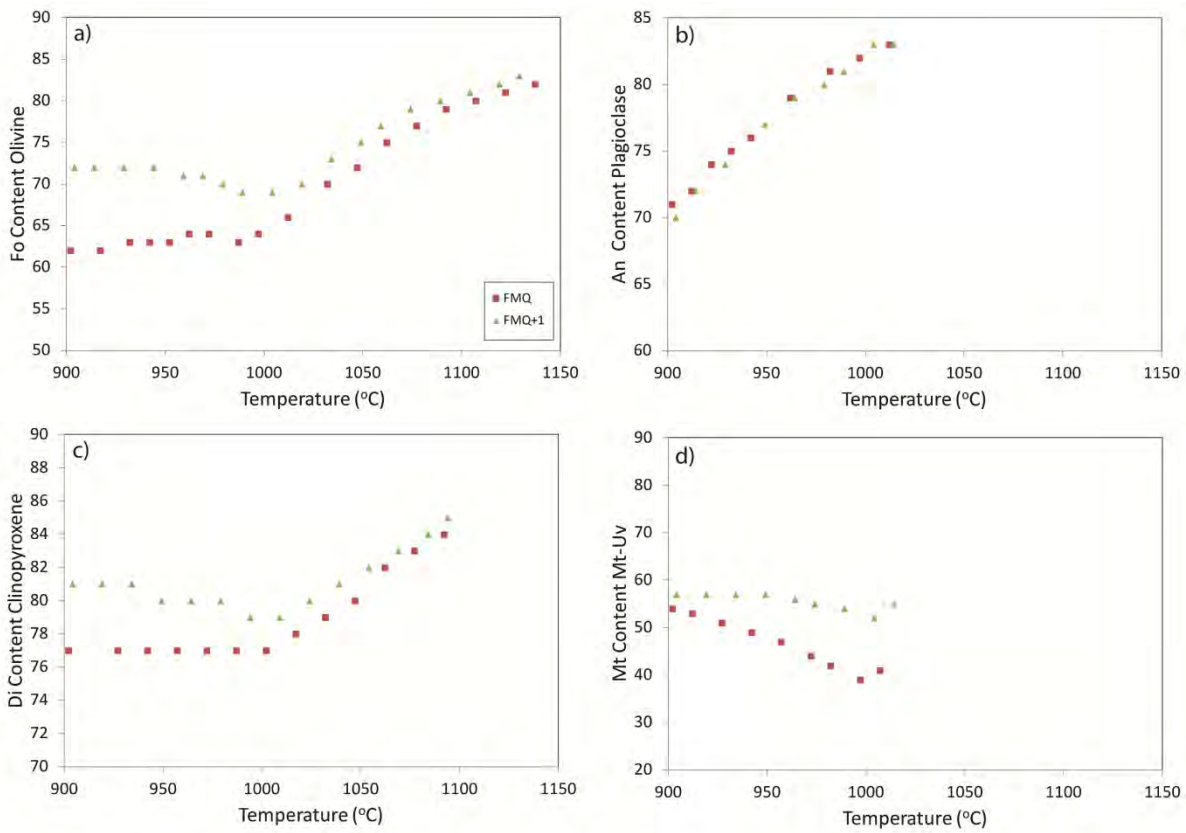

Figure 7.10 Composition of mineral phases as a function of fO_2 with decreasing temperature for a low-Ti parent magma with 3 wt % H_2O.

enrichment in the liquid is only observed for parent magmas with low H_2O content (< 0.5 wt %;) (Figure 7.11).

7.7 Factors affecting the crystallisation sequence of the Emeishan basaltic magmas

Toplis and Carroll (1995) showed experimentally that ilmenite crystallises prior to Mt-Uv at low fO_2 conditions (< FMQ) whereas Mt-Uv crystallises prior to ilmenite at high fO_2 (> FMQ). The large positive $\Delta T/\Delta fO_2$ slope for Mt-Uv is interpreted to represent a direct control of Mt-Uv crystallisation by fO_2. However, the crystallisation of ilmenite as the first Fe-Ti oxide phase is controlled by the melt TiO_2 content rather than fO_2 (Toplis and Carroll, 1995). Ilmenite saturation at 1100°C for MORB magmas has been calculated at 4.5-5.5 wt % TiO_2 (Delong and Chatelain, 1990). Synder et al. (1993) showed experimentally that the crystallisation of clinopyroxene is controlled by the CaO/FeO_T and CaO/TiO_2 ratios of the parent magma. Clinopyroxene crystallises after Fe-Ti oxides at low CaO/FeO_T and CaO/TiO_2 ratios. Botcharnikov et al. (2008) showed experimentally that the crystallisation of

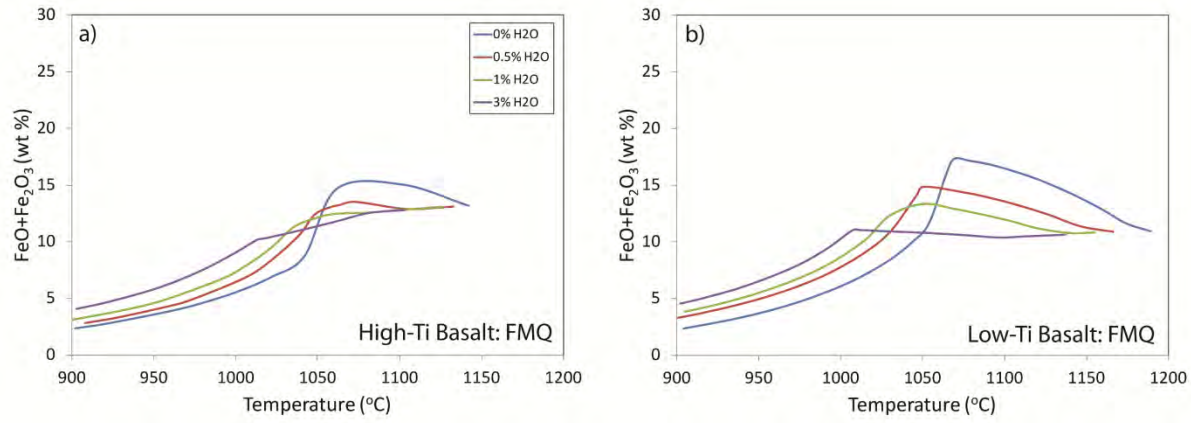

Figure 7.11 $FeO+Fe_2O_3$ (concentration in liquid) vs. temperature for high- Ti and low-Ti basalt parent magmas showing Fe-enrichment and lack of as a result of varying H_2O content of the parent magma.

silicates, in particular plagioclase, are significantly affected by the H_2O content of the parent magma. High H_2O contents results in significantly lower crystallisation temperatures for plagioclase. In general all of these previous observations from experimental studies have been reproduced here for the Emeishan high-Ti and low-Ti basaltic magmas. Three main factors influence the crystallisation sequence of the Emeishan ferrobasaltic magmas: 1) Major element composition, in particular TiO_2 and CaO contents and 3) H_2O content.

The Emeishan basalts vary significantly in major element composition, in particular the TiO_2 and CaO contents. Emeishan high-Ti basalt is characterised by high TiO_2 (3.5-5 wt %) and low CaO (3-10 wt %) whereas the low-Ti basalt is characterised by low TiO_2 (1.2-2 wt %) and high CaO (7.5-13 wt %) (Xiao et al. 2004). This results in significantly different crystallisation sequences for the high-Ti vs. low-Ti Emeishan basalts. Modeled high-Ti basalt composition has a crystallisation sequence at FMQ of ol.-plag.-ilm.-cpx.-mt-uv.-ap. Ilmenite crystallises early as a result of high TiO_2 content and clinopyroxene crystallises late as a result of low CaO/FeO_T and CaO/TiO_2 ratios. Ilmenite crystallises from the high-Ti basalt at FMQ and 0.5 wt % H_2O at 1073°C and TiO_2 of 5.2 wt %, which is consistent with the data from Delong and Chatelain (1990). Modeling shows that low-Ti Emeishan basalt crystallises clinopyroxene early as a result of higher CaO/FeO_T and CaO/TiO_2 ratios. This is also confirmed by petrographic descriptions of Emeishan basalt where low-Ti basalt are typically characterised by clinopyroxene phenocrysts whereas the high-Ti basalts are dominated by plagioclase phenocrysts (Xu et al. 2001).Furthermore, ilmenite crystallises late in the low-Ti basalt sequence due to the significantly lower TiO_2 content.

Modeled variation in H_2O content of the average high-Ti and low-Ti Emeishan basaltic compositions shows a significant depression of the crystallisation temperature of plagioclase. Plagioclase crystallises early for high-Ti compositions with low H_2O (0.5 wt %) content whereas at high H_2O (3 wt %) plagioclase crystallises last apart for apatite. A similar trend is observed for the low-Ti composition except that ilmenite crystallises late in this case. The variation in crystallisation temperature of plagioclase is accompanied by a large variation in An content. At low H_2O when plagioclase crystallises early the An content is generally low whereas at higher H_2O content and later crystallisation the An content is significantly higher. Furthermore the An content of plagioclase crystallising from the low-Ti basalt parent, which has higher CaO content, is significantly more calcic than that crystallising from the high-Ti basalt parent. Plagioclase composition can be used as a proxy for estimating the initial CaO content for the Panzhihua intrusion and possibly the H_2O content.

Modeling presented here provides constraints on the crystallisation of Fe-Ti oxides and resultant silicate disequilibrium. As discussed above H_2O significantly reduces the crystallisation temperature of silicate phases (Figure 7.3 and 7.4). The gabbroic rocks likely crystallised from a parent magma with low H_2O. Minor increases in H_2O content will result in a significant change in the crystallisation sequence. An increase in H_2O will result in conditions favoring significant Mt-Uv crystallisation along with minor olivine. I suggest that hydration may be an important mechanism for the stability of Mt-Uv over silicate phases.

7.8 Effects of H_2O on Fe-enrichment in the liquid and comparison with the Skaergaard intrusion

Basaltic/gabbroic intrusions such as the Bushveld, Stillwater and Skaergaard are characterised by Fe-enrichment in the liquid during differentiation (Fenner trend). This is indicated by the presence of Fe-Ti oxide free cumulate rocks at the base of the intrusion. The Skaergaard intrusion is a particularly well studied example of a ferrobasaltic magma showing distinct Fe-enrichment resulting in later crystallisation of Fe-Ti oxides. The liquid line of descent for the Skaergaard intrusion, presented by Hunter and Sparks (1987), is used here for comparison with modeling results for the Emeishan basaltic magma.

Modeled relationships between $FeO+Fe_2O_3$ and SiO_2 are presented in Figure 7.12, along with the Skaergaard trend calculated by Hunter and Sparks (1987). Dry magma compositions show Fe-

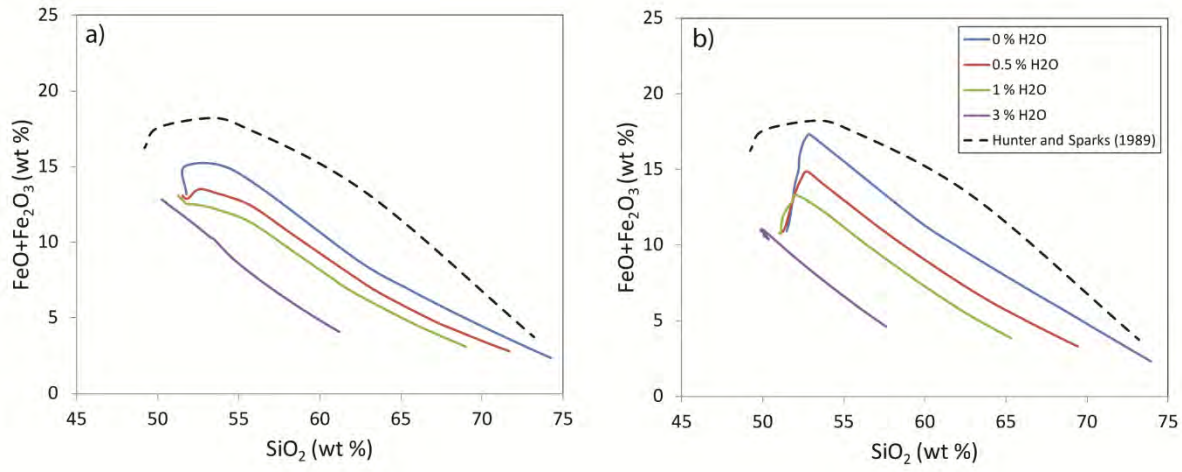

Figure 7.12 $FeO+Fe_2O_3$ vs. SiO_2 for high-Ti (a) and low-Ti (b) basalt parent magmas at FMQ showing the liquid line of descent and comparison with Hunter and Sparks (1987) trend for the Skaergaard Intrusion.

enrichment up to 15-20 wt % for high-Ti parent and 17-24 wt % for low-Ti parent. These trends are similar for the Skaergaard trend with initial increase in FeO_T at relatively constant SiO_2 content with subsequent decrease in FeO_T and increase in SiO_2 at the onset of Fe-Ti oxide crystallisation. Change in the H_2O content of the magma results in the depression of Fe-enrichment. This is particularly evident for the high-Ti basalt where the addition of small amounts of H_2O results in the absence of a Fe-enrichment trend. For the low-Ti parent addition of H_2O decreases the amount of Fe-enrichment but the trend remains similar up to 3 wt % for the parent magma where no Fe-enrichment occurs.

The trends of Fe-enrichment with H_2O are consistent with experimental work of Sisson and Grove (1993), Berndt et al. (2005) and Botcharnikov et al. (2008). Where Fe-Ti oxides crystallises early no Fe-enrichment occurs whereas late crystallization of Fe-Ti oxides is typically preceded by substantial plagioclase crystallisation and associated Fe-enrichment in the liquid. The liquid line of descent during the differentiation of Emeishan ferrobasalt in a magma chamber is significantly affected by the presence and abundance of H_2O. The Fe-enrichment trend, known as the Fenner trend, is typical of tholeiitic basalts whereas the absence of Fe-enrichment is usually characteristic of calc-alkaline magmas. The Emeishan basaltic rocks have been classified as tholeiitic, which comprise 95 % of the extrusive flood volcanism of the Emeishan large igneous province (Xu et al. 2001; Xiao et al. 2004).

The Skaergaard intrusion is characterised by a typical Fe-enrichment trend, which culminates in the crystallisation of ferrogabbros in the Upper Zone (UZ). The Lower Zone (LZ) of the Skaergaard intrusion is comprised of three sub-zones where the upper LZc is characterised by the occurrence of Ti-magnetite (McBirney, 1996). The underlying LZa and LZb represent an 800 m thick sequence of gabbroic rocks with no Fe-Ti oxide phases (McBirney, 1996). Hunter and Sparks (1987) calculated a liquid line of descent for the differentiation of the Skaergaard intrusion where the initial liquid becomes enriched in FeO_T at relatively constant SiO_2. This Fe-enrichment is essentially produced by the formation of the gabbroic rocks of the LZa and LZb. The onset of Ti-magnetite crystallisation in the LZc scavenges Fe from the liquid resulting in a decrease in FeO_T and subsequent increase in SiO_2 in the liquid at this level. This represents the typical Fenner trend for the differentiation of tholeiitic basalt. Botcharnikov et al. (2008) interpreted this to indicate that the Skaergaard parent magma had low H_2O content (< 0.5 wt %), which accounts for significant crystallisation of Fe-Ti oxide free cumulate rocks. The gabbroic rocks of the Panzhihua intrusion are characterised by the occurrence of Fe-Ti oxides throughout the intrusion (Zhou et al. 2005; Pang et al. 2008a; this study). No Fe-Ti oxide free rocks are present at the base of the intrusion such as at the Skaergaard intrusion. This suggests that the parent magma for the Panzhihua intrusion either contained significant H_2O in order to depress the crystallisation of silicate phases: > 1 wt % for high-Ti parent and > 3 wt % for low-Ti parent or was slightly more evolved than the typical Emeishan basaltic compositions. This further highlights the importance of H_2O in the evolution of the Emeishan magmas as the presence/abundance will affect the evolution of the liquid in a magma chamber. While the parent magma for the Panzhihua intrusion is typical tholeiitic basalt, the lack of Fe-Ti oxide free cumulates suggests that the liquid evolves along a calc-alkaline differentiation trend.

7.9 Modeling constraints on the crystallisation of the Panzhihua gabbros

The gabbroic rocks of the Panzhihua intrusion are composed of dominantly plagioclase and clinopyroxene with interstitial Fe-Ti oxide minerals. Minor amounts of olivine and hornblende are also observed. Apatite is present within the MZb only as small grains occurring in association with Fe-Ti oxide in the interstitial spaces. The general absence of olivine and lack of olivine cumulate rocks at the base of the intrusion imply that some crystallisation and fractionation of olivine has occurred prior to the formation of the Panzhihua intrusion. Modeling crystallisation sequences (Figure 7.3) indicates that two possible scenarios may produce a gabbroic rock similar to that described above. 1) Low-Ti basaltic parent magma with H_2O of 0-2.5 wt % at fO_2 of FMQ-FMQ+3. This represents almost all modeled H_2O and fO_2 variations for the low-Ti parent magma. This is due

to the high CaO/FeO_T ratio of the low-Ti basalt. 2) The high-Ti parent magma will only crystallise the observed Panzhihua gabbroic sequence at high fO_2 (> FMQ+2) and low H_2O (0-1 wt %). Fe-Ti oxides crystallises before clinopyroxene at all other fO_2 conditions. However, as discussed previously the PELE software does not work at highly oxidising conditions (> FMQ+1). One major problem with the crystallisation from low-Ti parent magma in terms of reconciling modeled and observed petrography is the large temperature gap between the crystallisation of silicates and that of Fe-Ti oxides. Approximately 50 % crystallisation is required before Fe-Ti oxides begin to crystallise. This implies that a significant amount of Fe-Ti oxide poor gabbroic rocks should be present at the base of the Panzhihua intrusion, which is not the case. Alternatively the absence of ilmenite as a primary early crystallising phase at the Panzhihua intrusion may suggest that the parent magma for the gabbroic rocks had slightly lower TiO_2 content than typical high-Ti basalt. A high-Ti Emeishan basaltic parent composition with slightly lower TiO_2 content can then account for the mineral assemblage of the Panzhihua gabbroic rocks.

Pang et al. (2009) presented detailed mineralogical data for the Panzhihua intrusion. Comparison of these data with the modeled compositions provides further constraints on the genesis of the gabbroic rocks at the Panzhihua intrusion. The clinopyroxene at the Panzhihua intrusion is somewhat more complex than simple diopside-hedenbergite solid solution, as calculated by modeling software, which makes comparison difficult. Ti-magnetite at the Panzhihua intrusion has undergone significant sub-solidus re-equilibration with ilmenite and silicates (Pang et al. 2008a) and is similarly difficult to compare with modeled compositions. However, plagioclase and olivine compositions from the Lower Zone (LZ) gabbros provide useful comparison. Plagioclase composition of the LZ gabbro is An_{58}-An_{60} (Pang et al. 2009). Olivine composition ranges from Fo_{72} to Fo_{78} for the LZ gabbro (Pang et al. 2009). Low-Ti basalt crystallises plagioclase with more primitive/calcic compositions, always > An_{68} (Figure 7.6 a). Again this is a reflection of the higher CaO content of the low-Ti parent magma. However, the high-Ti basalt crystallises plagioclase with more sodic compositions. The composition of An_{60} is produced by a high-Ti basalt with 1 wt % H_2O (Figure 7.5 a). Fo content of olivine indicates two possible scenarios for crystallisation: 1) low-Ti basalt at low fO_2 (< FMQ) or 2) high-Ti basalt at relatively high fO_2 (FMQ-FMQ+2).

Comparison of the petrography and mineral composition of the Panzhihua gabbroic rocks with that of modeled average high-Ti and low-Ti basaltic compositions suggests that neither the average high-

Ti nor low-Ti basalt compositions fit the mineralogy of the Panzhihua gabbroic rocks. Although the low An content of plagioclase favours the high-Ti parent. The average TiO_2 content of high-Ti basalt is very high resulting in early crystallisation of ilmenite prior to clinopyroxene. The generally low FeO_T and TiO_2 contents of the low-Ti basalt require significant Fe-enrichment prior to the crystallisation of Fe-Ti oxides. This suggests that the parent magma for the Panzhihua gabbroic rocks was either: 1) low-Ti basalt parent, which has undergone significant Fe-enrichment by fractionation prior to intrusion at the current level or 2) composition similar to high-Ti basalt but with lower TiO_2. Further PELE modeling of a high-Ti Emeishan basalt with relative low TiO_2 content (2.5 wt % TiO_2; lower range of TiO_2 contents for Emeishan high-Ti basalt; Xu et al. 2001) is consistent with the gabbroic rocks of the Panzhihua intrusion. I suggest that the parent magma for the gabbroic rocks of the Panzhihua intrusion was likely similar to typical high-Ti basalt but at the lower range of TiO_2 contents and low H_2O content (< 1 wt %).

Pang et al. (2008b) suggests that the Fe-Ti oxides at the Panzhihua intrusion crystallised at fO_2 conditions of FMQ and 1.5 wt % H_2O for the parent magma. These arguments were made for the early crystallisation of Fe-Ti oxides and the formation of Fe-Ti oxide ore layers. The Fe-Ti oxides within the gabbroic rocks are clearly interstitial and must crystallise at lower H_2O contents. However it is again noteworthy that minor increases in H_2O content would favour the crystallisation of Fe-Ti oxides over plagioclase and clinopyroxene. This is discussed further below for modeling constraints on Fe-Ti oxide ore genesis.

7.10 Modeling constraints of the genesis of Fe-Ti oxide ore layers

The formation of Fe-Ti oxide ores at the Panzhihua intrusion is currently under much debate. Ganino et al. (2008) suggested that the parent magma was similar to low-Ti basalt (Table 1) with high CaO and lower TiO_2. They further suggested that an increase in fO_2 related to the interaction of hot magma with footwall carbonates resulted in the crystallisation of Mt-Uv and the formation of ore layers. Modeling presented here favours a parent magma similar to the high-Ti basalt composition at the lower end of TiO_2 content. Ganino et al. (2008) also showed that the release of CO_2 from the footwall carbonates and the addition of 10 wt % CO_2 can increase the fO_2 by an order of magnitude. This favours an interpretation for (at least locally) high fO_2 during the crystallisation of gabbroic rocks. Furthermore Iacono-Marziano et al. (2008) observed experimentally that olivine and plagioclase are consumed during extensive carbonate assimilation while extensive clinopyroxene

crystallisation is favoured. Silicate disequilibrium observed in the Fe-Ti oxide ore layers may be linked to this process. However massive clinopyroxene crystallisation should be expected to occur in association with the footwall (as suggested by Iacono-Marziano et al. 2008) at Panzhihua, which is not observed. Furthermore clinopyroxene is similarly resorped within Fe-Ti oxide ore layers, which does not favour disequilibrium by carbonate assimilation.

Pang et al. (2008b) interpreted Fe-Ti oxide inclusions in olivine to indicate early crystallisation of Fe-Ti oxides. Pang et al. (2008b) modeled a high-Ti parent magma at FMQ and showed that Fe-Ti oxides crystallise early at high H_2O contents (> 1.5 wt %). This is confirmed in modeling presented here for high-Ti parent magma. Section 4.3 presents descriptions of silicate disequilibrium textures within the Fe-Ti oxide ore layers. Plagioclase and clinopyroxene within ore layers show distinct resorption and rims of hornblende and olivine developed at contacts with Fe-Ti oxides. Silicate disequilibrium clearly indicates that Fe-Ti oxides did not crystallise first but rather formed after silicate grains at conditions where silicates are no longer stable. A similar interpretation of early silicate crystallisation is made by Zhou et al. (2005) and Zhou et al. (2008). Fe-Ti oxide inclusions in olivine in the MGZ described by Pang et al. (2008b) are significantly different in composition with high Cr_2O_3 contents, similar to Ti-magnetite described from the Xinjie ultramafic-mafic intrusion (Wang et al. 2008). The high Cr contents and their presence within olivine phenocrysts, which are trapped in the chilled margin, are more consistent with the crystallisation of olivine en route to the current magma chamber (Zhou et al. 2013). Minor crystallisation of Cr-rich spinel is also consistent with early crystallisation of olivine, most of which were likely lost at some stage en route to the surface. Zhou et al. (2005) also suggest that the Panzhihua parent magma has undergone some fractionation en route to the chamber. Furthermore numerous recent studies have suggested that the Emeishan basaltic magmas form by the fractionation of olivine and minor Cr-spinel from picritic magmas (e. g. Tao et al. 2008; Zhou et al. 2013). Therefore the Cr-spinel-bearing olivine phenocrysts observed within the MGZ of the Panzhihua intrusion may also be interpreted to represent early crystallisation and differentiation of the parent magma from a picritic magma.

Ganino et al. (2008) suggested that an increase in fO_2 can result in 6-8 % crystallisation of Mt-Uv, which if efficiently segregated from the crystallising magma and settled to the base of the chamber could account for the extensive ore bodies at the Panzhihua intrusion. Crystallisation of a high-Ti Emeishan basaltic composition at low H_2O (< 1 %) followed by a later influx of H_2O can produce a

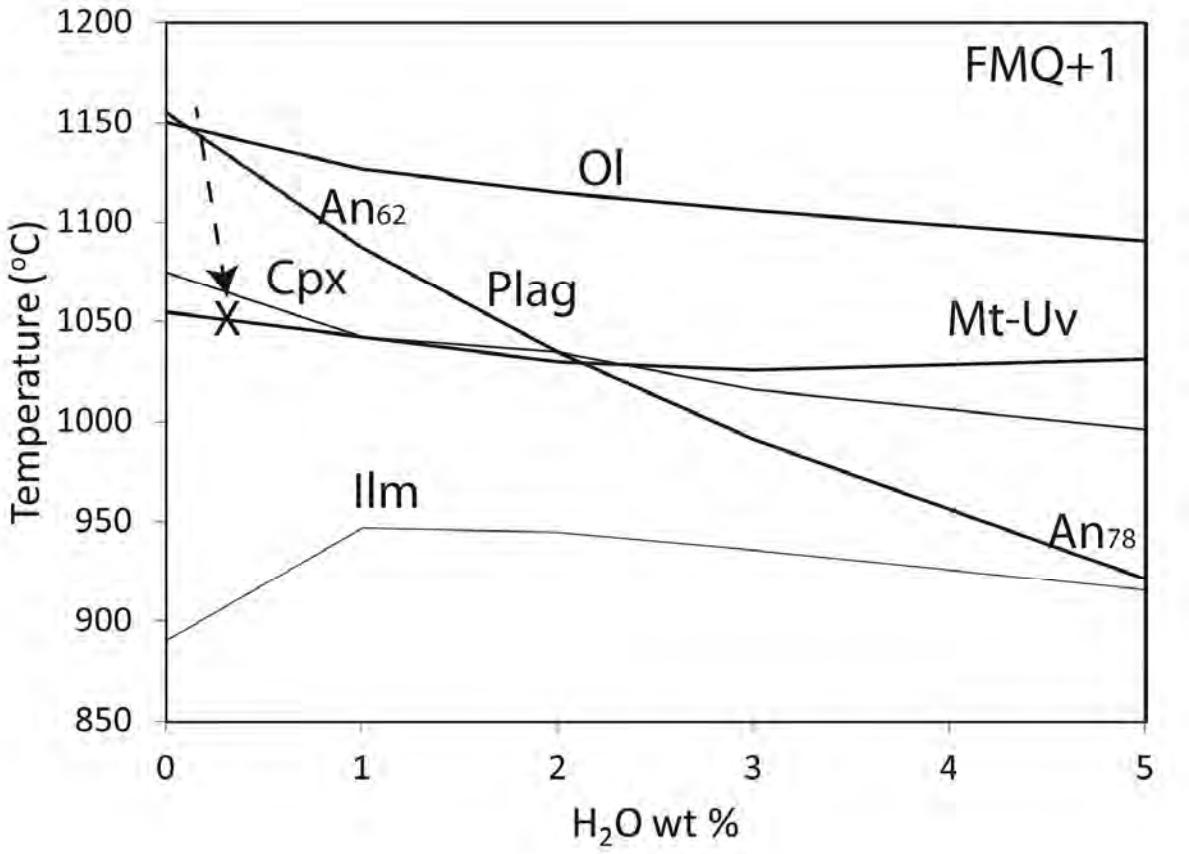

Figure 7.13 Proposed model for the formation of Fe-Ti oxides ore layers by the addition of a later H_2O-rich fluid phase/magma. Point X represents the composition of the liquid, which becomes enriched in H_2O (see text for discussion).

similar effect to that described by Ganino et al. (2008) although this is the result of silicate instability rather than increasing Fe-Ti oxide stability. Figure 7.13 presents modeled variation of an Emeishan high-Ti basalt with 2.5 wt % TiO_2 (as discussed earlier) at various initial H_2O contents. Crystallisation of the magma at low H_2O results in the typical mineral assemblage of the gabbroic rocks (Figure 7.13). A later influx of H_2O will result in the instability of silicates.

Further modeling of the liquid composition at point X (with 3 wt % H_2O as a result of the influx of H_2O) in Figure 7.13 indicates that ± 5-6 % Mt-Uv crystallises in the absence of any silicate phases. Concentration of this amount of Mt-Uv can account for the formation of extensive ore layers. Furthermore the increase in H_2O will result in the consumption of silicate grains. I suggest that an

influx in H_2O can account for large scale Fe-Ti oxide crystallisation as a result of silicate instability. Further discussion on the potential source of H_2O is discussed in section 9.2. I simply demonstrate here that an influx of H_2O causes silicate instability and resultant crystallisation of 5-6 % Mt-Uv alone.

7.11 Implications for the crystallisation of other Fe-Ti oxide ore-bearing intrusions of the ELIP

The main Fe-Ti oxide ore-bearing layered intrusions of the ELIP are the Panzhihua, Baima, Hongge, Taihe and Xinjie intrusions (Pang et al. 2010). The Baima intrusion is composed of gabbroic rocks only, with Fe-Ti oxides ore layers dominantly occurring at the base of the intrusion (Shellnutt and Pang, 2012), similar to the Panzhihua intrusion. However, the Hongge and Xinjie intrusions are composed of dominantly ultramafic clinopyroxenite with minor olivine (Bai et al. 2012; Zhong et al. 2004). Fe-Ti oxide ore layers in these cases are hosted within clinopyroxenite rather than gabbros and are only present within the upper half of the intrusions. Modeling results presented in section 7 indicate that, in order to crystallise clinopyroxene early the parent magma must have a high CaO/FeO_T ratio. This would imply that the parent magmas for these intrusions are more similar to that of the modeled low-Ti Emeishan basalt, with its high CaO/FeO_T. Furthermore, in order to produce clinopyroxenite with low abundance of plagioclase, the H_2O content of the parent magma must be high enough to depress the plagioclase crystallisation temperature (> 2 wt %) (Figure 7.4). Zhou et al (2008) and Zhang et al. (2009) suggested that the Emeishan large Fe-Ti oxide-bearing mafic intrusions formed from parental magmas similar to high-Ti basalt whereas the smaller Ni-Cu-PGE ultramafic intrusions crystallised from low-Ti basalt parent magmas. I agree with this but modeling presented here provides further constraints on the parental magmas for the large Fe-Ti oxide-bearing intrusions. In particular the Hongge and Xinjie intrusions, which contain ultramafic lower halves dominated by clinopyroxenite. Clinopyroxene cystallises early for magmas with high CaO/FeO_T ratios, similar to the low-Ti Emeishan basalt. This implies that any ultramafic rocks related to the Emeishan layered intrusions crystallised from a parental magma with high CaO/FeO_T; i. e. low-Ti basalt or picrite. This is consistent with recent work of Bai et al. (2012) who suggest that the parent magma for the Hongge intrusion had high CaO (± 11 wt %). The low proportion of plagioclase in the Hongge intrusion may also favour a parent magma with high H_2O content in order to depress the crystallisation temperature sufficiently so that only olivine and clinopyroxene crystallise from the magma.

7.12 Conclusions

The CaO and TiO_2 contents of Emeishan basaltic magmas have a significant effect on the resultant crystallisation sequences for ultramafic-mafic layered intrusions. High CaO contents for the low-Ti Emeishan basalts results in early crystallisation of clinopyroxene while the low CaO content of the high-Ti basalt results in clinopyroxene typically crystallising after Fe-Ti oxide. Furthermore the CaO content of the parent magma also effects the composition of plagioclase. Low-Ti basaltic magmas crystallises more calcic plagioclase relative to the high-Ti magmas. TiO_2 content of the parent magmas also controls the occurrence of ilmenite. Ilmenite crystallises out of a liquid with ± 5 wt % TiO_2. fO_2 and H_2O also have significant effects on the crystallisation sequence of the Emeishan basaltic magma. Mt-Uv is favoured over ilmenite at high fO_2 as shown previously by Toplis and Carroll (1995). The most important variable for the timing of Fe-Ti oxide crystallisation, along with fO_2, is H_2O content of the parent magma. Increasing H_2O contents significantly depresses the crystallisation temperature of silicates, which results in the early crystallisation of Fe-Ti oxides at high H_2O content (> 1.5 wt %) of the parent magma. The H_2O content of the Emeishan basaltic magmas can alter the differentiation path of the associated intrusion. Magmas with low H_2O generally follow the typical Fenner Fe-enrichment trend whereas those with higher H_2O contents follow a more calc-alkaline trend of differentiation.

Comparison of fO_2 and H_2O modeling of high-Ti and low-Ti basaltic magmas with that of the gabbroic rocks of the Panzhihua intrusion favour a parental magma similar to the high-Ti basaltic magma but at the low end of TiO_2 contents (± 2.5 wt % TiO_2). This interpretation is in agreement with numerous geochemical studies on the ultramafic-mafic layered intrusions in SW China (e.g. Zhou et al. 2008; Pang et al. 2010). Furthermore modeling suggest that the gabbroic rocks crystallised at low to moderate fO_2 (FMQ-FMQ+1) and moderate H_2O content (± 0.5-1 wt % H_2O). I suggest that the formation of Fe-Ti oxide ore layers can result from an influx of H_2O or H_2O-rich magma. Recent studies suggest that the Panzhihua parent magma was originally picritic and evolved at depth through fractionation to a basaltic composition (this study section 9.1; Zhou et al.2013). Furthermore Pang et al. (2009) showed that at least two or three pulses of magma filled the current chamber. H_2O will increase in residual liquid during fractional crystallisation. Magma evolving at depth would have increased H_2O contents as evolution continued. It may be reasonable to suggest that a late stage magma pulse from depth would have high H_2O contents as a result of the concentration of H_2O in the residual liquid. The influx of H_2O-rich liquid or fluid into the partially

crystallised Panzhihua intrusion can account for the occurrence of large scale Fe-Ti oxide ore layers with distinct consumed silicate grains.

8. Petrogenesis of the Panzhihua parent magma

8.1 Parent magma

Numerous studies have suggested that Fe-Ti oxide ore-bearing mafic intrusions in the PANXI region crystallised from parental magmas similar to that of the Emeishan high-Ti basalt (e.g. Zhou et al. 2005; Pang et al. 2008a; 2008b; Zhou et al. 2008; Zhang et al. 2009; this study). Furthermore, recent studies have suggested that these basaltic parent magmas to ELIP layered intrusions are related to the Emeishan picritic magmas through fractionation of olivine ± chromite (Zhang et al. 2009; Wang et al. 2012; Bai et al. 2012). In particular, Zhang et al. (2009) calculated the MgO content (12 wt %) of liquids in equilibrium with the most primitive olivine (Fo_{82}) compositions at the Panzhihua intrusion, which are interpreted to have crystallised from ferro-picritic magma.

Comparison of the trace element characteristics of the Panzhihua intrusion favour an interpretation of a parental magma formed through the differentiation of picritic magma. The average chondrite-normalised REE concentrations for high-Ti, low-Ti and picritic magmas are plotted in Figure 6.5 for comparison with the rocks of the Panzhihua intrusion. The relatively flat REE patterns, in particular for the MGZ/LZ (Figure 6.5), are similar to those of the Song Da LREE-depleted picrites (Wang et al. 2007). LREE patterns of the MZa gabbroic rocks are also similar but HREE patterns are depleted relative to the Song Da LREE-depleted picrites. REE patterns are significantly depleted relative to typical high-Ti Emeishan basalt, which is expected for cumulate rocks likely having lost a portion of evolved interstitial liquid. Trace element spidergram patterns show a similar trend such that primitive mantle-normalised trace element concentrations of the Panzhihua intrusion are similar to those of the Song Da LREE-depleted picrite (Figure 6.7). In particular, distinct negative Th-U and positive Pb anomalies for all the Panzhihua rocks match well with the LREE-depleted Song Da picrite.

Sr-Nd isotopes show that the Panzhihua intrusion plots within a field of overlap between picrite and high-Ti basalt and trend toward more evolved isotopic compositions (Figure 8.1).

Comparison of trace element characteristics of the Panzhihua intrusion with those of the ELIP lava is also consistent with a picritic parent magma of the Panzhihua intrusion, which has undergone differentiation prior to emplacement into the current chamber. Plots of Ni and Cr vs. MgO indicate

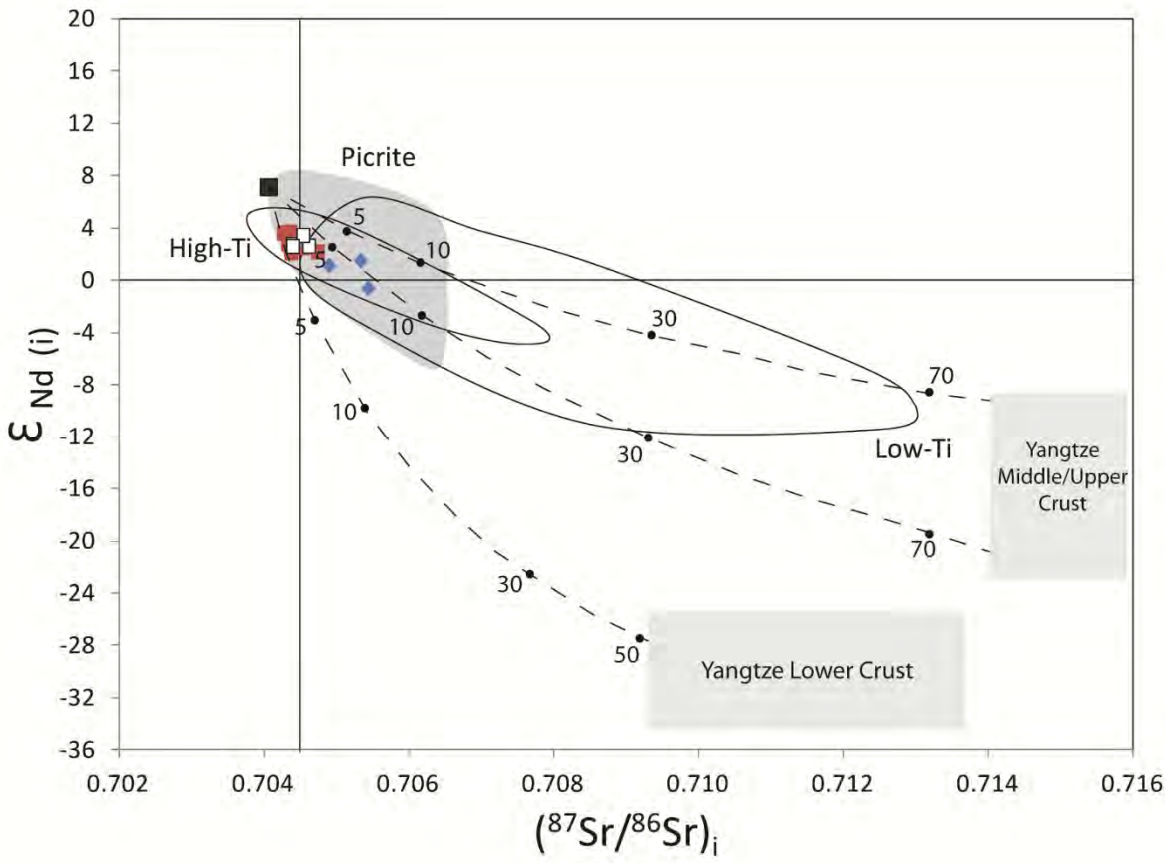

Figure 8.1 Initial (at 260 Ma) Sr and Nd isotopic compositions for the Panzhihua intrusion and comparison with picrites (field after Zhang et al. 2006, Wang et al. 2007, Li et al. 2010), high-Ti basalt (field after Xu et al. 2001, Xiao et al. 2004, Wang et al. 2007) and low-Ti basalt (field after Xu et al. 2001, Xiao et al. 2004, Wang et al. 2007). Crustal contamination models are modified after Wang et al. (2007). Symbols: diamonds – MGZ/LZ; open squares – Fe-Ti oxide ore; solid squares – gabbro.

that olivine and chromite are likely the dominant fractionating phases (Figure 6.14 a and b). The Panzhihua rocks generally plot at slightly lower Cr relative to MgO and this may indicate a proportion of sulphide fractionation as suggested by Song et al. (2009) for Emeishan lavas. Wang et al. (2012) have made a similar interpretation for the gabbroic rocks of the Nantianwan intrusion (ELIP). Bai et al. (2012) make a similar interpretation of differentiated picritic parent magmas for the Hongge intrusion (ELIP) based on mantle-normalised PGE patterns. Tao et al. (2008) interpreted the parent magma composition of the Limahe intrusion as moderately fractionated picrite based on olivine compositions. Based on evidence presented here as well as evidence presented by Zhang et al. (2009) we interpret the parent magma of the Panzhihua intrusion to be a differentiated picrite.

Direct evidence for picritic parent magma for the Panzhihua intrusion is given by sample BT-03 (c). This sample is PGE undepleted and has a primitive mantle-normalised PGE profile similar to typical Emeishan picrites (Figure 6.16). Furthermore the sample is a micro-clinopyroxenite rock within the marginal zone of the Panzhihua intrusion with whole-rock major element geochemistry comparable to typical Emeishan picrite lavas. Therefore this sample may represent an earlier pulse of picrite magma, which was not been subjected to evolution at depth forming the first/early stages of the Panzhihua intrusion.

8.2 Crustal contamination

In general the Panzhihua intrusion shows little Sr-Nd isotopic variation and typically plots in the field of overlap between Emeishan picrite and high-Ti basalt (with the exception of several samples from the MGZ) (Figure 8.1). The MGZ (0-40 m thick; Zhou et al. 2005) microgabbro has been interpreted to represent the chilled margin of the Panzhihua intrusion (e.g. Pang et al. 2008b). Enriched Sr-Nd isotope ratios for the MGZ may be consistent with minor contamination of earlier magmas by footwall material. Sr-Nd isotopic ratios for the main ore transect (0.7043-0.7047) plot within the typical field of high-Ti basalt (Figure 8.1) and do not indicate significant crustal contamination. The ^{18}O of the magma forming the main ore layer and associated gabbroic rocks is difficult to determine precisely based on the limited data set presented in section 6.2.4 but estimations are made in order to constrain crustal contamination. The limited data set presented here is similar to unpublished data of Pang (2008) for the LZ and MZa gabbroic and ore rocks. The plagioclase and Ti-magnetite ^{18}O values correspond to a temperature of 760^{o}C, using the fractionation equation of Chiba et al. (1989). This is significantly lower than the temperature of crystallisation of these mineral phases (1050-1150^{o}C; Figure 7.13), as predicted by PELE modeling in section 7, but this is expected in slowly cooled igneous rocks as the closure temperature for diffusion of oxygen in plagioclase and Ti-magnetite is 500-550^{o}C, depending on the H_2O content (Giletti, 1986; Sharp, 1991). Fractionation factors of Zhao and Xheng (2002) between magnetite and magma (-3.34 ‰) and plagioclase and magma (+ 0.06 ‰) leads to an estimate of magma ^{18}O of 7.4 ‰ (average magnetite Table 6.3) and 8.4 ‰ (average plagioclase Table 6.3). These values are significantly above the values of 5.7 expected for mantle-derived magmas (e.g. Eiler, 2001). This implies some degree of crustal contamination either en route to the chamber or within the chamber as a result of footwall or roof rock interaction. Ganino et al. (2013) present simple mixing models using data from this study along with their own data from the contact aureole for the final magma ^{18}O of 7.4-8.4 ‰ and that of a footwall contaminant (either dolostone or marl or sandstone). The contaminants contain 16, 13 and

4 times less Sr than the gabbro making contamination by footwall unable to significantly affect the Sr-Nd isotopic ratios (Ganino et al. 2013). Further calculations suggest that an increase of initial $^{87}Sr/^{86}Sr$ from 0.704-0.705 requires assimilation of 20 wt % marls or 600 wt % dolostone. (Ganino et al. 2013). For this reason Ganino et al. (2013) suggested that footwall contamination will not affect the initial $^{87}Sr/^{86}Sr$ ratio of the Panzhihua parent magmas. Ganino et al. (2013) goes on to calculate that 8-13 % assimilation of carbonate footwall is required to account for the calculated high ^{18}O ratios of the Panzhihua parent magma forming the gabbros and Fe-Ti oxide ore layers.

This implies that the enriched Sr-Nd isotope ratios of the MGZ microgabbro are not related to footwall contamination but rather to contamination at depth prior to intrusion at the current level. This could only be possible if the initial pulse feeding the current chamber was small and formed the MGZ rocks only where later uncontaminated pulses of magma form the overlying cumulate gabbroic rocks. In this way one may account for the absence of enriched Sr-Nd isotopic ratios for the gabbroic rocks.

This brings the interpretation of the microgabbro as a chilled margin (e.g. Pang et al. 2008a) to the Panzhihua parent magma into contestation. While the microgabbro may form a thermal insulator for later pulses of magma (i.e. later pulses of magma do not chill against cold country rock) it is unlikely that it represents a chilled margin for the Panzhihua parent magma forming the overlying cumulate rocks, which have Sr-Nd isotopic ratios unaffected by crustal contamination. As discussed above footwall contamination by carbonate material cannot account for the enriched Sr-Nd isotopic ratios of the MGZ. This implies that crustal contamination of the parent magma for the MGZ rocks must have occurred at depth en route to the current chamber. The formation of the MGZ is discussed in detail in section 9.1.2.

This interpretation of the microgabbro as an early magma pulse unrelated to the later cumulate forming magmas has further implications for potential footwall interaction of the later magmas. Based on the interpretation above that the MGZ forms from a contaminated magma and is not parental to the gabbroic cumulate rocks. Several further constraints may be placed on contamination processes. The early formation of the MGZ would result in the formation of a thermal insulator between later pulses of magma and the footwall. The ability of later pulses of magma to

interact with the footwall carbonates then becomes difficult due to the formation of the MGZ rocks. This then leads back to the high ^{18}O values of the cumulate rocks. The original implication of low Sr contents of footwall carbonates being unable to significantly enrich initial $^{87}Sr/^{86}Sr$ ratios has now led to a conclusion that elevated ^{18}O is not likely caused by interaction with the footwall of the intrusion. Two alternate hypotheses may account for elevated ^{18}O, which is most likely the result of carbonate contamination (lack of correlation with enriched Sr-Nd isotopes). 1) Interaction with carbonate, which would have formed the roof of the original intrusion. The upper contact of the Panzhihua intrusion is fault controlled and the upper portion has been lost making this hypothesis difficult to evaluate. 2) Interaction with carbonate at depth en route to the current chamber. The crustal rocks underlying the Panzhihua are similarly difficult to constrain. Therefore while either of these two alternative hypotheses are viable they are equally as difficult to evaluate. However what does seem clear is that carbonate contamination has occurred at some stage during the evolution of the cumulate forming parental magmas, which is unlikely from footwall interaction.

The formation of the MGZ is discussed further in section 9.1.2 with specific reference to variations in incompatible element concentrations and Sr-Nd ratios across the zone.

8.3 Controls on PGE distribution in the Panzhihua intrusion

PGE concentrations in the Panzhihua intrusion are generally significantly lower (total PGEs below detection limit to 12 ppb with the exception of BT-03 (c) – 24 ppb; Table 6.1) than coeval Emeishan picrite (total PGE- 26 ppb; Wang et al. 2007), suggesting PGE depletion of the parent magma at depth. PGE distribution in mafic rocks is generally controlled by sulphides, oxides/silicates or discrete PGMs. Chalcophile elements Ni, Cu and PGE strongly partition into sulphide liquid due to their high partition coefficients (e. g. 10^4-10^5 for PGE; Fleet et al. 1996). The positive, albeit highly scattered, correlation of PGE with Cu (Fig. 6.15 b) may indicate a sulphide control on the PGEs within the intrusion. In particular, sample BT-19 contains 11 ppb PGE and disseminated sulphides (4 vol. %; Table 6.1), suggesting a sulphide control on the PGEs for this Fe-Ti oxide ore layer. However, the sulphide abundance at the base of the main Fe-Ti oxide ore layer is similarly high (4.5 vol. %; Table 6.1) and no PGE enrichment is observed. This indicates that while sulphide liquid controls the PGE distribution in some cases, the presence of locally high proportions of sulphides within the Panzhihua intrusion does not correspond to high proportions of PGEs.

PGE abundance shows a good positive correlation with Cr abundance (Fig. 6.15 a), indicating a potential oxide control on the PGE distribution; PGEs have commonly been associated with chromitite layers in layered mafic intrusions (such as the UG2 chromitite in the Bushveld Complex; Maier and Barnes, 2008). Although chromite is completely absent from the Panzhihua intrusion, Cr is also compatible in magnetite (e.g. Cawthorn and McCarthy, 1980). PGE-enriched magnetitites have been documented at the Stella intrusion (South Africa) (Maier et al. 2003) but in fact, the main Fe-Ti oxide ore layer (magnetitite layer) at the Panzhihua intrusion contains relatively low PGE abundances, as well as low Cr contents. This indicates that neither the PGE nor the Cr distribution is controlled by the Fe-Ti oxide phases.

The correlation of PGEs with Cr could suggest the presence of chromite with associated PGE as an accessory phase in the main body of the Panzhihua intrusion. However, chromite is only reported as inclusions in rare olivine near the base of the intrusion (Pang et al. 2008b), where both the olivine and the chromite are thought to be xenocrystic (Zhou et al. 2013; this study). The relatively high PGE concentrations of the MGZ/LZ samples observed in this study may result from the association of PGMs with oxide phases included within xenocrystic olivine grains. Alternatively, the Cr-PGE correlation may be an artefact of earlier depletion of PGE and Cr related to the fractionation of chromite prior to emplacement.

Although locally the PGE distribution is likely controlled by sulphide (e.g. sample BT-19), the occurrence of sulphide does not always result in enhanced PGE concentration. Conversely, two samples from the MGZ/LZ have relatively high PGE abundance (12 ppb and 25 ppb; Table 6.1) but no association with sulphides. This implies the occurrence of multiple sulphide liquids. This is also consistent with the weak correlation of Cu and PGE. Specifically, the occurrence of sulphide-bearing samples near the base of the intrusion in the footwall-proximal rocks (samples 05-1 and 05-2; Table 6.1) is superficially consistent with S-saturation induced by local footwall assimilation. This process is the keystone of the mineralisation model proposed by Ganino et al. (2008). However, the fact that these sulphides are particularly low in PGE, in spite of the apparent available PGE nearby (as noted earlier in this paragraph), requires that if indeed these sulphides were derived by footwall assimilation effects, that this was a very localised and limited process, with a resultant low R-factor, and not a pervasive intimate interaction of magma and footwall.

8.4 Depletion of PGEs : S-saturated vs. S-undersaturated magmas

The primitive mantle contains ± 250 ppm S (McDonough and Sun, 1995) and requires at least 18 % (Naldrett et al. 2010) or 25 % (Keays, 1995) partial melting to produce S-undersaturated basaltic magma. Song et al. (2009) suggested that the ELIP lavas were produced from a moderately S-depleted (± 200 ppm) mantle, implying slightly lower degrees of partial melting required to produce S-undersaturated magmas. Zhang et al. (2006) and Wang et al. (2007) suggested that the ELIP basaltic magmas formed by low degrees of partial melting; 2-7 % and 8 % respectively. Wang et al. (2007) suggested higher degrees of partial melting for picritic magmas (20 %), indicating that the picrite magma is close to the S-saturated/S-undersaturated threshold. Emeishan flood basalts may be either PGE-depleted or –undepleted (Song et al. 2009), whereas Emeishan picrite is generally PGE-undepleted (Li et al. 2012). The Panzhihua intrusion is PGE-depleted relative to the typical PGE concentration of Emeishan picrite, with the exception of sample BT-03 (c), as discussed above.

PGE depletion of the Emeishan magmas may have occurred in both S-undersaturated and S-saturated conditions, driven by chromite and sulphide liquid fractionation, respectively (Song et al. 2009). The discrimination between PGE depletion for S-saturated vs. S-undersaturated magmas is possible using various trace elements and PGEs and provides constraints on the evolution of the Panzhihua parent magma. Pt has a higher partition co-efficient than Pd for mafic minerals; for example chromite has $D^{cr\text{-}sil\ liq}$ for Pt = 3.3 and for Pd = 0.14-1.6 (Puchtel and Humayan, 2001 and Richter et al. 2004). This preferential enrichment in Pt over Pd by a factor of 2 (as compared to about 0.1 by sulphide fractionation) can result in a significant increase in Pd/Pt ratio from the typical mantle ratio of 0.6 (Taylor and McLennan, 1985) with fractionation of mafic minerals where S-saturation has not been achieved.

Alternatively the heterogeneous nature of the Pd/Pt ratio observed for the Panzhihua intrusion may simply imply late stage hydrothermal alteration and mobilisation of Pt and Pd. Tang et al. (2011) describe negative Pt anomalies from the Tianyu intrusion (NW, China), which are interpreted to result from late stage post-magmatic hydrothermal alteration. The samples with Pt anomalies are sulphide-rich and also characterised by higher degrees of serpentinisation. Negative Pt anomalies are not observed for the PGE-rich samples from the Panzhihua intrusion and in general the Panzhihua rocks do not show significant serpentinisation. Barnes and Liu (2012) showed that while Pt and Pd can be highly mobile under the right conditions for sulphide-rich rocks, they are near-

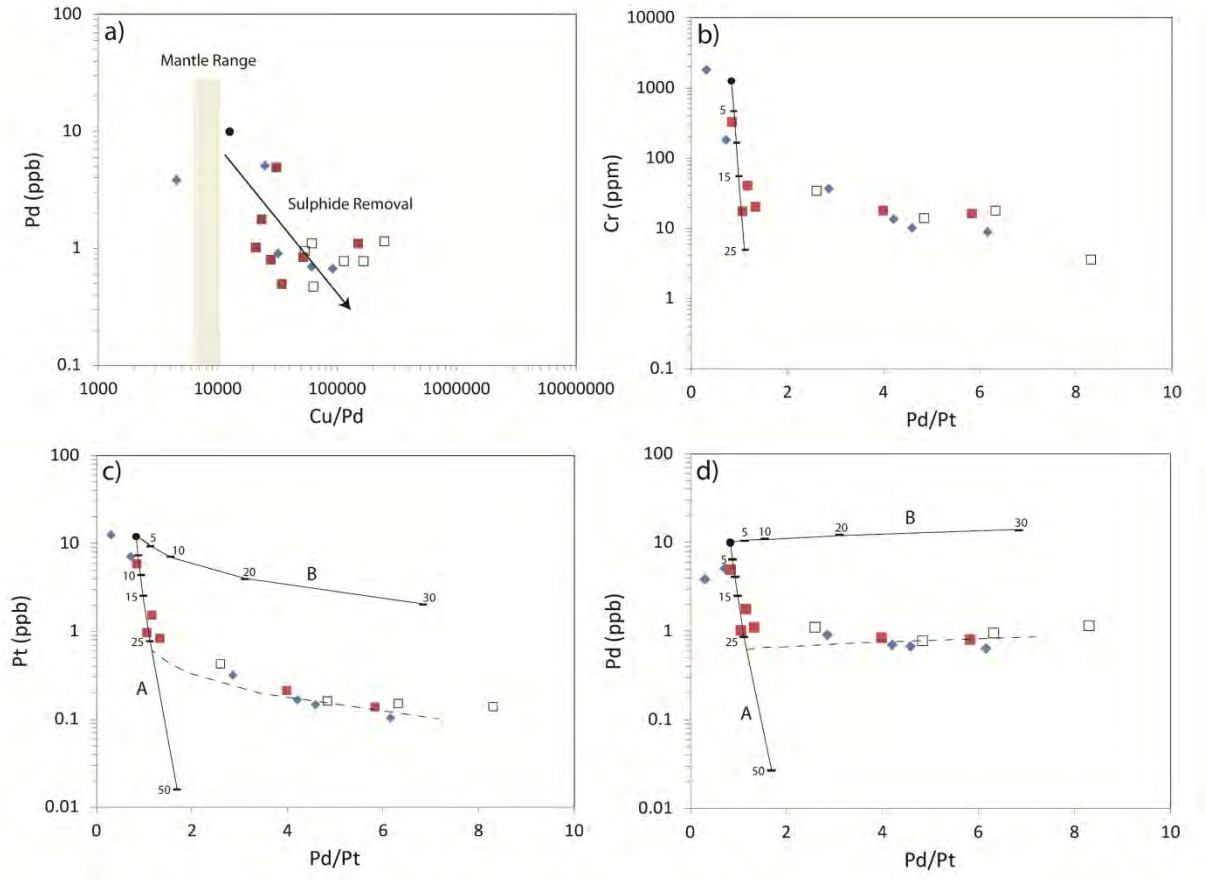

Figure 8.2 Fractional Crystallisation models for the Panzhihua intrusion based on modeling average total PGE concentrations of picrites (Wang et al. 2007). a) Pd vs. Cu/Pd showing the typical trend of sulphide removal. Solid circle represents the average composition of Emeishan picrite. b) Cr vs. Pd/Pt showing models of Cr depletion for Emeishan picrite. c) and d) Pt and Pd (respectively) vs. Pd/Pt showing models A and B described in text for fractionation of an Emeishan picrite. Symbols: diamonds – MGZ/LZ; open squares – Fe-Ti oxide ore; solid squares – gabbro.

immobile in silicate rocks. In these cases of hydrothermal alteration Pd is generally more mobile than Pt, which would result in lowering the Pd/Pt ratio rather than an increase as observed at the Panzhihua intrusion. The sulphide-rich PGE undepleted rocks of the Panzhihua intrusion (e.g. sample BT-19) show a minor increase in Pd/Pt implying that the elevated Pd/Pt ratio for the Panzhihua rocks is not a result of late stage post-magmatic hydrothermal alteration.

Olivine and chromite fractionation would also be reflected by significant Ni and Cr depletion respectively in a sulphide-free system. Similarly, Pd is much more compatible than Cu in sulphide liquid (e.g. Fleet et al. 1991, Barnes and Picard, 1993 and Fleet et al. 1996) (Figure 8.2 a), whereas both elements are strongly incompatible with silicate and oxide solids. Enrichment in Cu/Pd ratio of the residual magma is therefore characteristic of sulphide extraction (e.g. Maier & Barnes, 1999).

The effects of fractionation of a sulphide liquid and of olivine and chromite fractionation from a S-undersaturated liquid can thus potentially be distinguished. The positive correlations of Cr and Ni with MgO and Cr with Ni (Figure 6.14 a-c), indicate that mafic mineral fractionation has played a part in the differentiation of the parent picritic magma, as expected. The generally high Pd/Pt ratio may suggest a stage of PGE depletion occurring under S-undersaturated conditions. The absence of any correlation between Ni and Cu (Figure 6.14 d) also supports the absence of a sulphide liquid during this stage. However, in addition to the evidence for sulphide-free PGE and metal redistribution, sulphide removal (S-saturation) is indicated by the high Cu/Pd ratios. The large scale depletion of PGEs in the Panzhihua intrusion also strongly favours a stage of major PGE depletion related to sulphide removal from S-saturated magma.

Therefore the strong depletion in PGEs and high Cu/Pd ratios indicates a PGE depletion event, presumably at depth, related to sulphide segregation, whereas the high Pd/Pt ratios indicate a separate stage of PGE depletion related to fractionation of mafic silicates from S-undersaturated magma. Correlations of Ni, Cr and MgO indicate a significant proportion for silicate and oxide fractionation at depth (i.e. prior to emplacement) as well.

8.5 PGE and Cr Depletion: Modeling fractionation of picritic parent magma

Two models (Model A and Model B; Figure 8.2) are presented here for PGE depletion of a typical Emeishan picritic magma with Cr = 1266 ppm, Pt = 12 ppb and Pd = 10 ppb (concentrations from Wang et al. 2007) in order to further constrain the evolution of the Panzhihua parent magma.

Model A: a sulphide-present system, involving depletion of PGEs from a S-saturated magma (Figure 8.2 c and d). In order to constrain the proportion of mafic silicate fractionation as well as sulphide

fractionation we present here a model of fractionation of 96 % olivine, 4 % chromite and 0.15 % sulphide. The proportion of olivine:chromite is taken from cotectic proportions of modeled picrite parent magma as predicted using the modeling software PELE (Boudreau, 1999). A similar olivine:chromite cotectic proportion is used by Wang et al. (2012). The proportion of sulphide fractionation is taken as 0.15 %, which is based on the typical S content of basaltic melts saturated with S-liquid (e.g. Jugo et al. 2005). Partition coefficients for Cr, Pt and Pd in olivine, chromite and sulphide liquid are taken from Ely and Neal (2003), Puchtel and Humayum (2001) and Fleet et al. (1994). Model A is illustrated in Figure 8.2 (b, c and d). Cr, Pt and Pd modeling indicates that approximately 25 % fractional crystallisation is required in order to account for the PGE depletion observed at the Panzhihua intrusion. This model cannot, however, account for the increase in the Pd/Pt ratio, due to the strong compatibility of both Pt and Pd in sulphide liquid. This proportion of fractionation is consistent with interpretations from other Fe-Ti oxide-bearing intrusion in the ELIP, such as 22 % fractionation of a picritic magma at the Hongge intrusion (Bai et al. 2012).

Model B: a sulphide-absent system, involving depletion of PGEs from a S-undersaturated magma (Figure 8.2). Song et al. (2009) showed that in order to increase the Pd/Pt ratio to > 1 with concurrent decrease in Pt abundances, there needs to have been fractionation of mafic minerals or a combination of mafic minerals and Pt-rich alloys, in the absence of sulphide. Model B is presented in Figure 8.2 (c and d) is based on the fractionation of mafic minerals along with laurite and Os-Ir-Ru alloys with bulk partition co-efficients for Pt and Pd of 6 and 0.1 respectively (Model 2 of Song et al. 2009) from a parent magma with Pt and Pd concentrations similar to Model A. Model B clearly shows a significant increase in Pd/Pt with fractionation but cannot account the major depletion of PGEs in the Panzhihua intrusion. A two-stage evolution of sulphide-present and sulphide-absent processes is therefore envisioned.

8.6 Petrogenetic model

Two key characteristics need to be explained in a petrogenetic model for the evolution of the Panzhihua parent magma. These include: 1) major depletion of PGEs and high Cu/Pd ratio related to sulphide separation from a S-saturated magma and 2) high Pd/Pt and correlation of MgO, Cr and Ni interpreted to be related to an artefact of a S-undersaturated stage of fractionation.

S-saturation of an originally S-undersaturated magma may occur through three processes: a) silicate fractionation, b) magma mixing or 3) assimilation. Two potential scenarios are outlined here in order to account for both S-saturated and S-undersaturated fractionation. Models presented below (Figure 8.3) begin with the generation of a S-undersaturated picritic melt through 20% partial melting of the mantle.

1. Early fractionation of olivine and chromite along with early saturation of PGMs (e.g. Pt-rich alloy; Song et al. 2009) from S-undersaturated picritic magma (Figure 8.3 a). This will result in increased Pd/Pt and correlation of MgO with Cr and Ni. This significant fractionation of olivine and chromite (up to 35 % Model B; Figure 8.2) then results in S-saturation of the magma and the separation of a sulphide liquid. The sulphide liquid will quickly scavenge PGEs resulting in major depletion of PGEs and increased Cu/Pd in the residual liquid. Bai et al. (2012) calculate, using a typical Emeishan picrite composition, that ± 42 % fractional crystallisation is required in order to produce S-saturation in the absence of externally derived sulphur. This is slightly higher than that shown in Model B (Figure 8.2) and may suggest that some minor contamination is also required in order to produce S-saturation of the magma. Sr-Nd isotopes of the gabbroic rocks show very minor enrichment relative to the typical picrite composition, which may suggest minor contamination (< 2.5 %) at depth.

   This model will result in the formation of ultramafic cumulates in the plumbing system beneath the Panzhihua intrusion. In particular PGMs would be present as inclusions in olivine and potentially chromite as a result of early S-undersaturated stage of evolution. Furthermore PGE-rich interstitial sulphides should also be present as a result of S-saturation due to fractional crystallisation.
2. Early S-saturation induced by assimilation of crustal materials, results in sulphide liquid separation and depletion of PGEs and increased Cu/Pd (Figure 8.3 b). This stage of early S-saturation will then need to be followed by later S-undersaturated conditions in order to account for high Pd/Pt ratios. Mavrogenes and O'Neill (1999) showed that during the essentially adiabatic rise of a S-saturated mafic magma the sulphur concentration at sulphur saturation (SCSS) is significantly increased due to the decrease in pressure, which can result in an originally S-saturated magma becoming S-undersaturated. It may be suggested that an initial S-saturated stage of PGE depletion (Model A; Figure 8.2) due to sulphide segregation at depth was followed by a later S-undersaturated stage of PGE depletion (Model B; Figure 8.2) at shallower depth due to a pressure decrease and an increase in the SCSS. This is shown in Figure 8.2 (c and d) where an initial stage of fractionation including sulphide removal, which scavenges PGEs is followed by a later stage of S-undersaturated PGE

depletion (Model B dashed line). PGE depletion is controlled by the removal of sulphide liquid at this stage. Fractionation of mafic minerals may also occur but is not required. The major controlling factor for this model would then be the early S-saturation, which is likely dominantly controlled by contamination (possibly some fractional crystallisation as well). In general the Panzhihua intrusion does not show significant contamination, with the exception of the MGZ rocks. It was suggested earlier that these rocks represent an earlier contaminated pulse of magma unrelated to later pulses for gabbroic rocks. If this is the case then early contamination of this magma at depth will result in the separation of a sulphide liquid, which may become trapped at some level in the conduit. Later uncontaminated S-undersaturated magma pulses passing through the same conduit would have their PGEs scavenged by this earlier developed sulphide liquid resulting in significant upgrading of a potential PGE-rich sulphide deposit forming in the plumbing system of the Panzhihua intrusion. This is similar to the interpretations of Wang et al. (2010) for the early stages of development of the Jinbaoshan intrusion. Numerous other studies of layered intrusions in the ELIP have also suggested S-saturation by crustal contamination e.g. Hongge intrusion (Bai et al. 2012), Baimazhai intrusion (Wang et al 2006) and Limahe intrusion (Tao et al. 2008).

This model requires the initial formation of a massive sulphide deposit deep within the plumbing system as well as the formation of ultramafic cumulates at a higher level with associated PGMs.

Ultramafic Ni-Cu-PGE sulphide-bearing intrusions are present within the ELIP spatially associated with mafic Fe-Ti oxide-bearing intrusions. Sulphide PGE-bearing ores in the ELIP occur in two settings. 1) Olivine primocrysts with interstitial chromite and sulphides (e.g. Jinbaoshan), where S-saturation is interpreted to result from fractional crystallisation (Wang et al. 2010). 2) Massive sulphide ore bodies generally in direct contact with footwall rocks, where S-saturation is interpreted to result from crustal contamination; e.g. Limahe (Tao et al. 2008) and Baimazhai (Wang et al. 2006). S-saturation in known ultramafic layered intrusion in the region is achieved through either fractional crystallisation or crustal contamination. This implies that both models proposed above may account for the evolution of layered intrusions in the region.

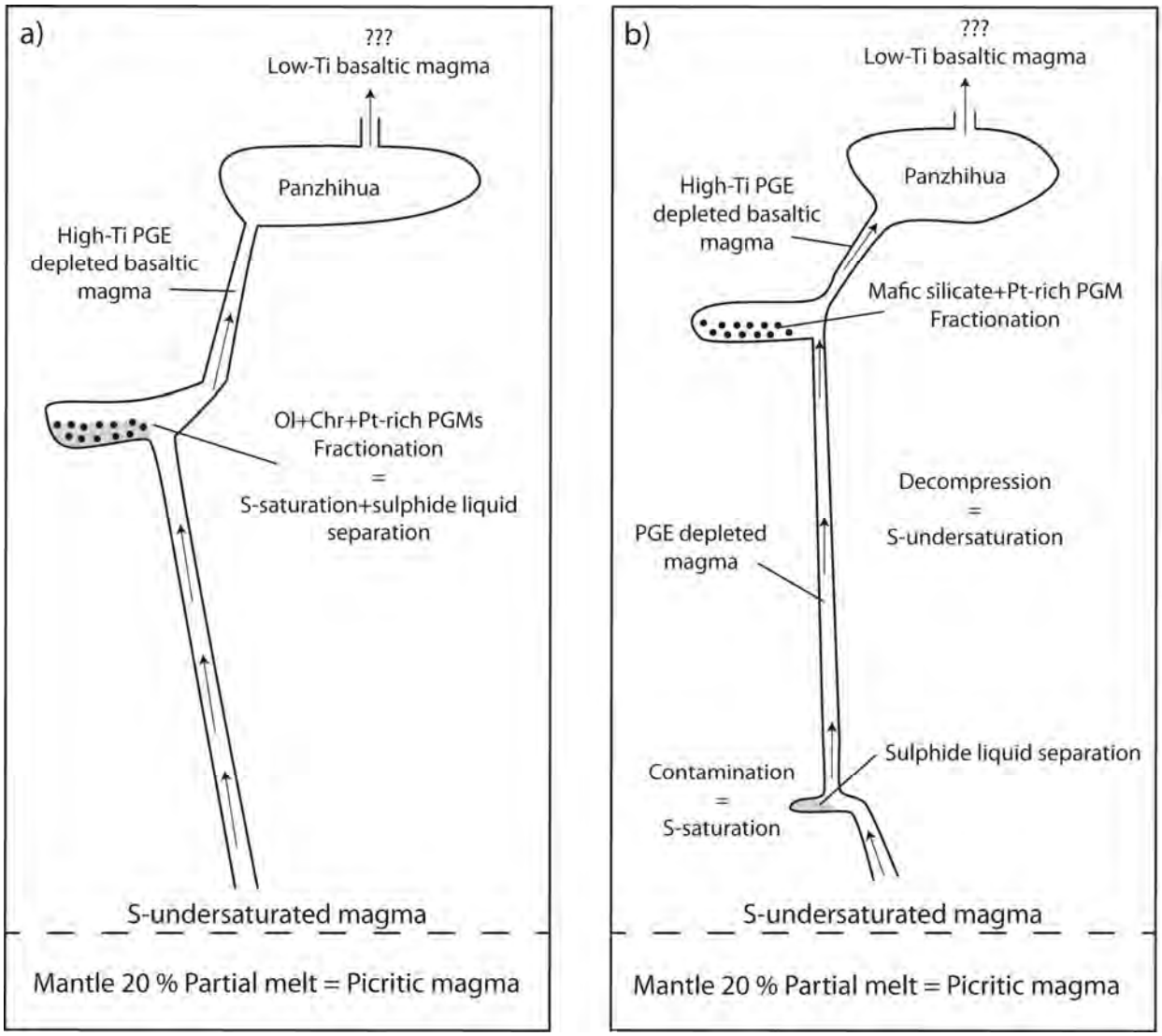

Figure 8.3 Simplified illustrations of the petrogenetic models proposed for the evolution of the parent magma for the Panzhihua intrusion. a) Early silicate fractionation inducing S-saturation. b) Early crustal contamination inducing S-saturation.

8.7 Conclusions

The main conclusions of the current section are summarised here:

1. The Panzhihua intrusion parent magma is a PGE-depleted basaltic magma, which has evolved from picritic magma through fractionation at depth in a plumbing system.
2. PGE depletion results from S-saturation at depth due to a combination of olivine (± chromite) fractionation and assimilation of crustal material in a plumbing system.

3. Fe-Ti oxides do not concentrate PGEs within the Panzhihua intrusion.
4. Major depletion of PGEs of the Panzhihua parent magma suggests that a PGE-rich sulphide ore deposit may be present at depth below the Panzhihua intrusion.

The Panzhihua intrusion represents part of a larger feeder/plumbing system related to ELIP volcanism. The related fractionation at depth would crystallise ultramafic cumulate rocks with PGE-rich sulphides. Numerous smaller ultramafic sills within the PANXI area may represent these early staging chambers, which subsequently feed PGE-depleted evolved magmas to shallower depths or as extrusive rocks on the surface. Any magma escaping from the Panzhihua chamber and extruding at the surface would be a highly PGE depleted low-Ti type Emeishan basalt.

9. Petrogenesis of the Panzhihua intrusion and Fe-Ti oxide ore layers

9.1 Petrogenesis of the Panzhihua intrusion

9.1.1 Mineralogical controls on whole-rock geochemistry

Large variations in whole-rock major and trace element geochemistry are controlled by the cumulus mineralogy of the Panzhihua gabbros and ore rocks. In particular the strong negative correlation of SiO_2 and Fe_2O_3 (Figure 6.2 a) indicates the strong control on the geochemistry by Fe-Ti oxides. Fe-Ti oxides phases include Ti-magnetite and ilmenite. The Fe-Ti oxide ore rocks are dominated by Ti-magnetite over ilmenite whereas the gabbroic rocks typically contain equal proportions of Ti-magnetite: ilmenite. Two distinct trends of Fe_2O_3/TiO_2 and V/TiO_2 indicate a high-Ti trend and a low-Ti trend. These two separate trends are interpreted to represent a Ti-magnetite control only (low-Ti trend) and a Ti-magnetite and ilmenite control (high-Ti trend) (Zhou et al. 2005; Pang et al. 2008a; this study). The gradational change from a low-Ti trend to a high-Ti trend at ± 270 m stratigraphic height implies that ilmenite becomes a cumulus phase at this level. Nb-Ta are compatible in ilmenite and concurrent increase in whole-rock Nb-Ta at ± 270 m is consistent with the occurrence of cumulus ilmenite at this level (Figure 9.1). This implies that ilmenite occurring within the lower 270 m of the Panzhihua intrusion is not cumulus and is likely the product of oxidation exsolution and expulsion from Ti-magnetite grains, which is consistent with further discussion below in section 9.1.3. Furthermore the occurrence of ilmenite lamellae exsolved within Ti-magnetite grains extending into external granules of ilmenite favours this interpretation.

Whole-rock Fe_2O_3 within the main Fe-Ti oxide ore layer is all contained within Ti-magnetite. The generally low concentrations of trace elements (e.g. V; Cr – below detection limit on the microprobe) within the Ti-magnetite makes evaluation of variation trends through the main ore layer difficult. However whole-rock Fe_2O_3 (total Fe) can be used as a normalising factor for evaluation of trace elements compatible in Ti-magnetite (Figure 9.2). Similarly, Sr is highly incompatible in Ti-magnetite and should not show similar trends to the compatible elements, as is observed in Figure 9.2. Generally trace elements compatible in Ti-magnetite (e.g. V; Co; Zn) all have constant ratios with Fe_2O_3 implying that there is no chemical variation trends for Ti-magnetite through the main Fe-Ti oxide ore layer for these elements. Cr contents are generally very low but

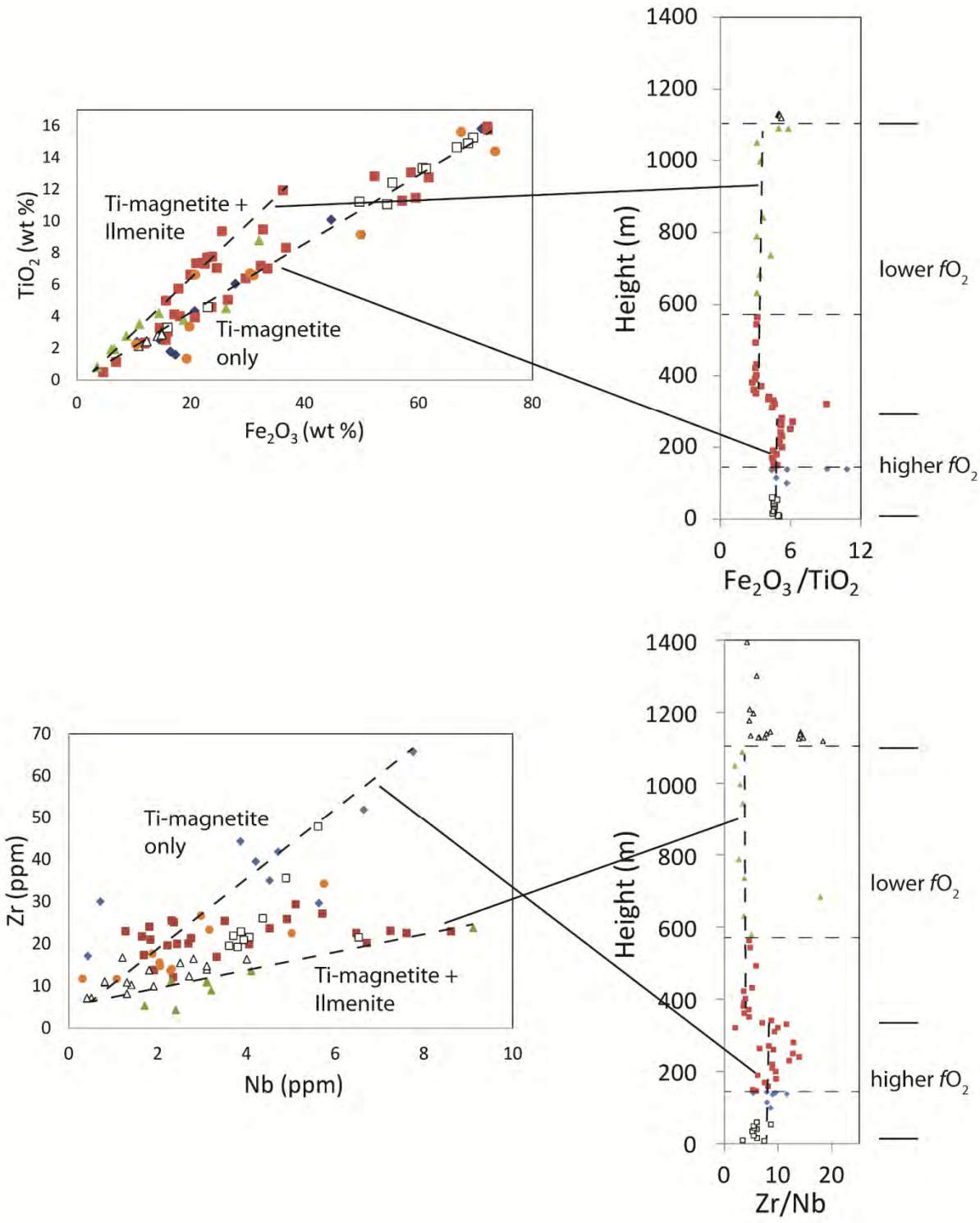

Figure 9.1 Whole-rock geochemical variations of selected chemical ratios for the Panzhihua intrusion showing the stratigraphic occurrence of cumulus ilmenite, indicated by changes in the Fe_2O_3/TiO_2 and Zr/Nb ratios. The absence of cumulus ilmenite indicates that the lower part of the intrusion crystallised at higher fO_2 conditions relative to the upper MZa and MZb.

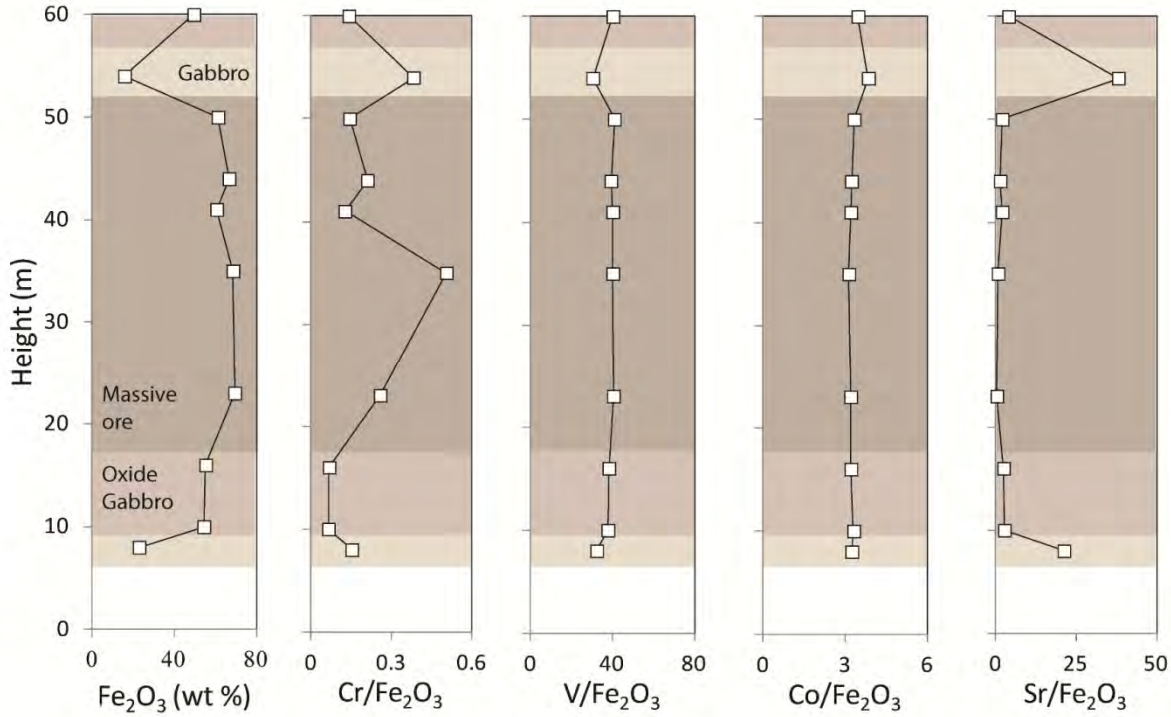

Figure 9.2 Selected whole-rock geochemical major and trace element ratios for the main Fe-Ti oxide ore layer, Panzhihua intrusion.

show some variation for Ti-magnetite within the main ore layer with highest values within the centre (Figure 9.2). Ti-magnetite ore layers at the Panzhihua intrusion (Pang et al. 2008a) and numerous other intrusions around the world (e.g. Bushveld Complex; Cawthorn and McCarthy, 1980) have been interpreted to form by fractional crystallisation and gravitational settling to the floor of a chamber. Cawthorn and McCarthy (1980) showed that compatible elements in Ti-magnetite (e.g. Cr, V) typically have high concentrations at the base of individual layers are decreases rapidly upwards. Compatible element trends across the 40 m thick main ore layer at Panzhihua do not show any upward decrease in concentration. This suggests that it is unlikely that the main ore layer formed by simple early crystallisation and fractional crystallisation from a single pulse of magma.

Incompatible trace element concentrations are generally low for the gabbroic rocks (e.g. Zr < 40 ppm). This is consistent with the cumulate nature of the gabbroic rocks and likely loss of interstitial liquid. P_2O_5 and REE concentrations are significantly higher in the MZb gabbroic rocks. This is consistent with the occurrence of apatite within the gabbroic rocks of this zone. The very low concentration of P_2O_5 and REEs in the Fe-Ti oxide ore layers, in particular, is consistent with the

complete absence of apatite from ore layers, which is an important feature not note and is discussed later in discussion on liquid immiscibility.

9.1.2 Formation of the marginal zone (MGZ)

The MGZ of the Panzhihua intrusion has, in the past, been interpreted to represent a chilled margin based on the fine-grained nature of the rocks and the close proximity of the footwall rocks (Pang et al. 2008a). However, as shown by Latypov et al. (2007) chilled margins are very rarely preserved in layered intrusions due to intense remelting by heat flux from the interior of the chamber. This results in texturally and compositionally heterogeneous marginal zones (e.g. Latypov, 2003; Latypov et al. 2007). Furthermore in section 8.2 the MGZ was interpreted to form from early contaminated magmas, based on the inconsistency between O-isotope and Sr-Nd isotope ratios. Recent work on marginal zones of layered intrusions show that they typically form as secondary chilled margins through complex processes and are characterised by reversals in the typical geochemical evolution (i.e. increasing MgO away from the margins) (e.g. Latypov et al. 2011; Egorova and Latypov, 2012a and 2012b). Numerous models exist in order to explain marginal zone reversals; e.g. contamination of magma in the chamber, prolonged or multiple injections into the magma chamber, compositional stratification of magma in the chamber.

The formation of the MGZ at the Panzhihua intrusion can be explained by its geological and petrological features including: 1) upward decrease in incompatible elements (Figure 9.3). 2) Upward decrease in initial $^{87}Sr/^{86}Sr$ and increase in initial ƐNd (Figure 9.3). 3) Bound by Fe-Ti oxide ore layers at both the upper and lower contacts. 4) Fine-grained nature where grains have straight boundaries and meet at triple junctions (Figure 4.2 b and 4.3 c). 5) Occurrence of olivine phenocrysts (1.5 mm) within the fine-grained MGZ rocks, which are recrystallised around the margins (Figure 4.3). 6) Gradational change in grain size and Fe_2O_3 content at the top of the MGZ (Figure 9.3).

The upward decrease in incompatible elements in a marginal zone is typically explained by an upward increase in cumulate phases due to slower cooling away from the contact with cold country rock. The decrease in incompatible elements upward is attributed to the return of evolved interstitial liquid back into the main magma chamber by compaction of the cumulate pile (e.g. Tait and Jaupart, 1996). The high concentration of incompatible elements near the footwall contact is

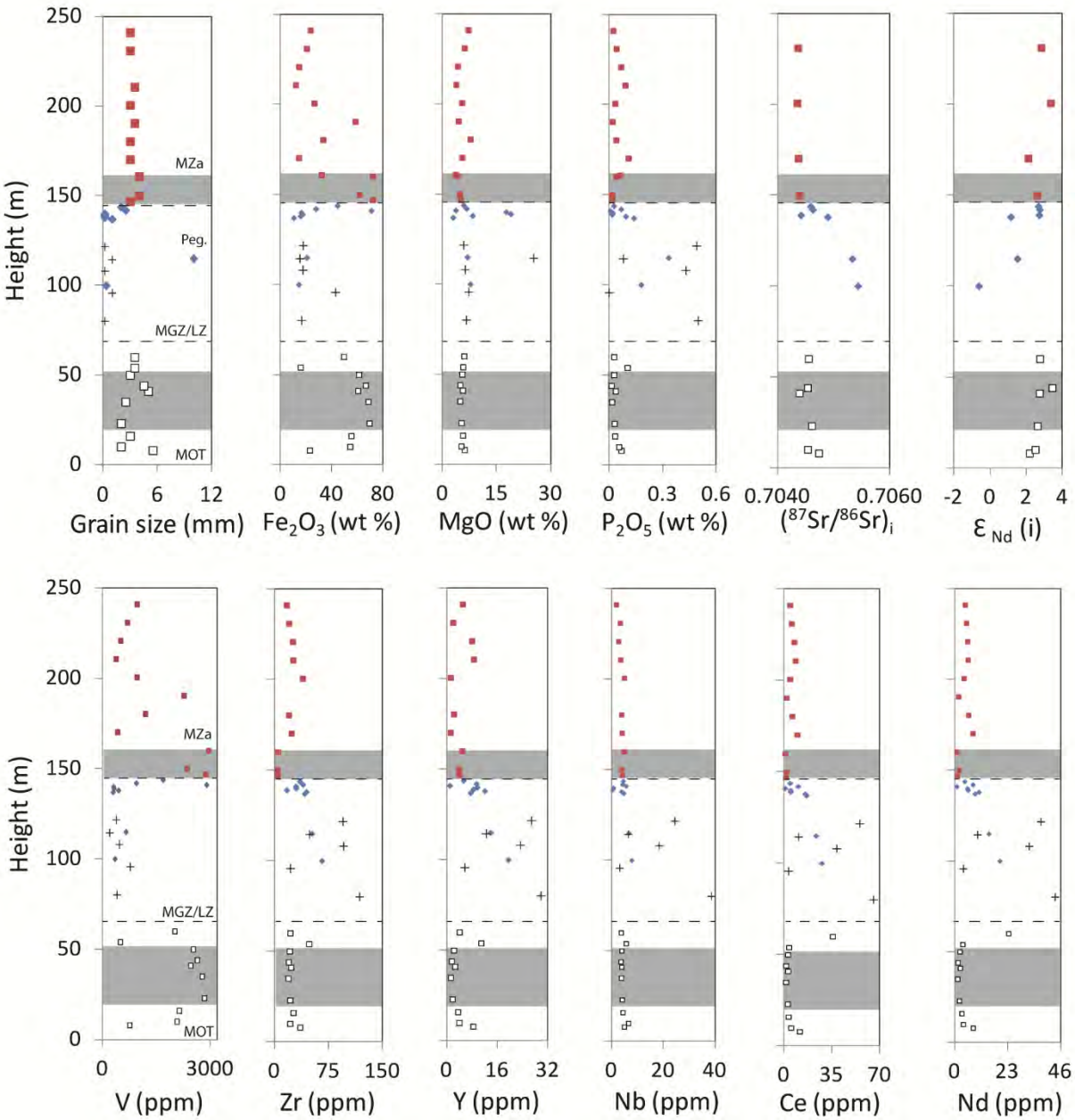

Figure 9.3 Whole-rock geochemical stratigraphic variations with specific interest in the MGZ/LZ and under/over-lying units. Plus symbols in the MGZ/LZ zone are from Pang (2008).

then due to supercooling at the immediate margin, which effectively quenches the magma and forms a chilled margin. This can be achieved in a closed system by a single pulse of magma. Alternatively, Latypov et al. (2011) suggests that a similar incompatible element trend can be accomplished by removing an evolved liquid boundary layer from the in situ growing cumulus

minerals by magma continuously flowing along the base of the intrusion, i.e. in an open system (also suggested by Hill et al. 1995). Latypov et al. (2011) goes on to explain that this process will become more effective away from the contact because a decrease in the rate of crystallisation (i.e. magma hotter away from the footwall contact), which allows for more effective removal of the evolved interstitial liquid. Discrimination of closed vs. open system processes is not possible based on the incompatible elements trends alone.

The most important characteristic of the MGZ at Panzhihua is the upward gradational change in Sr-Nd isotope ratios. It was discussed in section 8.2 that the carbonate footwall of the Panzhihua intrusion has Sr concentrations too low to significantly change the initial $^{87}Sr/^{86}Sr$ ratio. Furthermore one may also suggest that if the enriched Sr-Nd isotope ratios resulted from footwall contamination the ratios should be homogenous across the chilled margin. Sorensen and Wilson (1995) described a similar upward gradational change in Sr-Nd isotope ratios, at the Fongen-Hyllingen layered intrusion (Norway), from enriched values near the contact. Egorova and Latypov (2012a) interpret this trend to strongly favour an interpretation of open system formation by multiple pulses of magma with progressively less degrees of contamination. A similar interpretation is made for the Panzhihua MGZ. Contamination in this case must occur at depth in the plumbing system prior to intrusion at the current level. This further favours interpretations in section 8.2. Furthermore an interpretation of open system behaviour suggests that the upward decrease in incompatible element concentrations is more likely the result of the removal of an evolved liquid boundary layer by magma continuously flowing along the base of the open system chamber (e.g. Latypov et al. 2011).

The MGZ at the Panzhihua intrusion is bound by two large Fe-Ti oxide ore layers. There is gradational change in the grain size and Fe_2O_3 content at the top contact (Figure 9.3). This zone of gradational change is highly heterogeneous and contains zones of fine-grained rocks and zones of coarser grained rocks. Furthermore distinct xenoliths of fine grained MGZ rocks are observed within the massive Fe-T oxide sections within this zone (Figure 2.12). This suggests interaction of the Fe-Ti oxide ore layer with the underlying marginal rocks and that the MZa ore layer formed by a later large volume pulse of magma, which effectively terminates processes forming the marginal zone. A similar contact between marginal rocks and a chromitite layer is described by Egorova and Latypov (2012b) for the Imandra layered intrusion (Russia). In this case the irregular contact was interpreted to result from thermo-chemical erosion of the marginal rocks, which would have formed the footwall to the

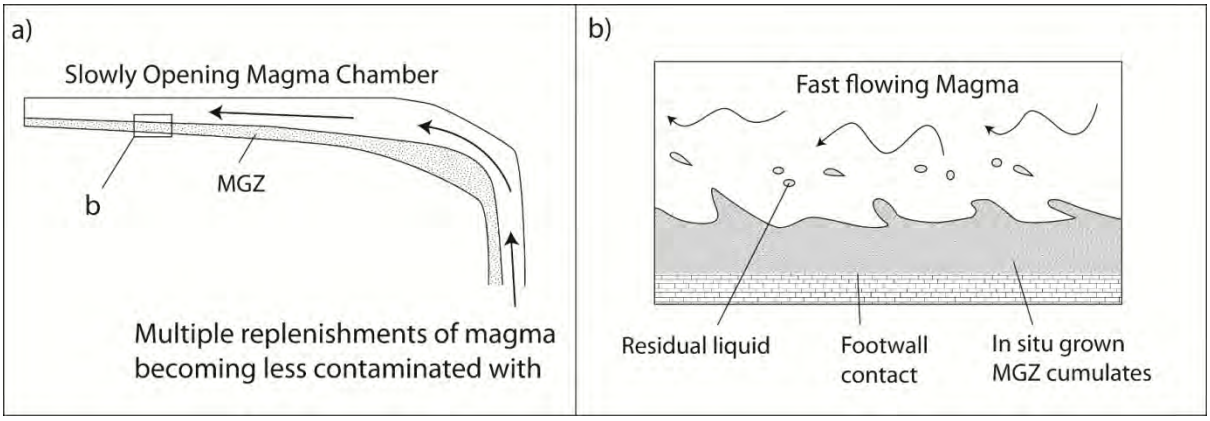

Figure 9.4 Simplified illustration of the formation of the MGZ/LZ, with specific interest in the upward decrease in incompatible element concentration as a result of continuous flowing magma along the base of the chamber. Illustration modified after Egorova and Latypov (2012b).

later large volume influx of magma forming the overlying layered series of the Imandra intrusion (Egorova and Latypov, 2012b). A similar interpretation of irregular contacts between chromitite layers and underlying cumulates is made by O'Driscoll (2010) for the Rum layered suite (Scotland). Therefore the upper contact of the MGZ rocks with the MZa ore layer is likely an unconformable contact due to significant thermo-chemical erosion of the MGZ/LZ rocks and interaction with a new pulse of magma. This is discussed further in section 9.3 for the petrogenesis of the Fe-Ti oxide ore layers.

New large volume pulses of magma significantly increase the chamber size and result in significant textural modification of the underlying rocks, which is achieved by partial melting, compaction and recrystallisation (e.g. Latypov et al. 2011). Mineral grain boundaries in the Panzhihua MGZ rocks are straight and meet at triple junctions clearly indicating significant recrystallisation after their formation. Furthermore olivine phenocrysts are partially recrystallised further indicating a stage of significant compaction and recrystallisation (Figure 4.3). Therefore the fine grain size of the marginal zone rocks does not indicate a chilled margin as suggested by Pang et al. (2008a).

The main ore layer occurring below the MGZ rocks is likely not in situ. This is suggested by the significantly coarser grain size, low concentrations of incompatible elements and the distinct break

in Sr-Nd isotope ratios. This is discussed further in section 9.3 on the petrogenesis of the Fe-Ti oxide ore layers.

The MGZ rocks are interpreted to form in two successive stages in an open system. Firstly, intrusion of basaltic magma between the footwall carbonate and unknown roof rocks results in the initial opening of the Panzhihua chamber. The initial chamber is slowly infilled by progressively less contaminated magma with variable proportions of olivine phenocrysts (Figure 9.4). Decreasing rates of solidification inwards, results in more effective removal of an evolved boundary layer by continuously flowing magma along the base of the chamber (Figure 9.4). The second stage of development begins with a large volume pulse of magma, which effectively terminates the development of the MGZ rocks. This later pulse of magma results in significant recrystallisation of the MGZ rocks due to compaction and remelting. Therefore the MGZ rocks effectively formed in an open system.

9.1.3 Empirical evidence for fO_2 variation

Ganino et al. (2008) presented evidence for an increase in fO_2 as a mechanism for the formation of Fe-Ti oxide ore layers as a result of the interaction of the magma with the footwall carbonates. The contrasting Fe_2O_3/TiO_2 ratios with stratigraphic height and the contrasting exsolution textures between the ore rocks and gabbroic rocks support the notion of variation in fO_2 at the Panzhihua intrusion. Specifically, the two distinct trends observed in whole-rock bivariant plots of Fe_2O_3 vs. TiO_2 and TiO_2 vs. V (Figure 9.1) have been interpreted to represent a Ti-magnetite-controlled trend and a Ti-magnetite + ilmenite-controlled trend (Zhou et al., 2005; this study). Fe_2O_3/TiO_2 ratios plotted against stratigraphic height clearly show that the lower ± 270 m of the intrusion is controlled by Ti-magnetite accumulation and the upper parts are controlled by both Ti-magnetite + ilmenite. This is also supported by the evidence from the variation of Mt/Ilm wherein the lower part of the intrusion is characterised by variable but Ti-magnetite-dominated ratios. Toplis and Carroll (1995) showed that Ti-magnetite-dominated oxide assemblages crystallise at high fO_2 conditions in excess of FMQ, whereas those containing cumulus Ti-magnetite and ilmenite crystallise at fO_2 at FMQ. The data in this case therefore indicate that the lower ± 270 m of the intrusion crystallised at high fO_2 conditions relative to the upper parts of the intrusion (above 270 m) where ilmenite is also an important cumulus phase.

An important observation indicating varying fO_2 conditions is that of the ilmenite exsolution lamellae within Ti-magnetite grains. It has been shown (e.g. Lindsley, 1962) that the solubility of ilmenite in magnetite at high temperature is far too low to account for the observed quantities thereof. High proportion of ilmenite lamellae within Ti-magnetite has been explained by simultaneous oxidation and exsolution of the magnetite-ulvospinel solid solution. Furthermore it has been shown that differing degrees of oxidation and diffusion of Mt-Uv solid solution can result in a variety of exsolution textures (Buddington and Lindsley, 1964). They described increasing degrees of oxidation and exsolution resulting in a systematic progression of exsolution intergrowth textures: 1) single phase homogenous spinel, 2) trellis intergrowths of thin ilmenite lamellae in all sets of (111) planes of the host, 3) sandwich intergrowths of relatively thick ilmenite lamellae, 4) granules of ilmenite developing within the host grain (internal granular exsolution) and 5) granules or lamellae of ilmenite on the external borders of magnetite grains (external granular exsolution). This continuous series of ilmenite exsolution fits well with observations from the Panzhihua rocks. The gabbroic rocks are characterised by abundant ilmenite lamellae typically showing well-developed trellis textures. In contrast, the oxide gabbros contain much lower proportions of ilmenite lamellae which typically show sandwich textures, although trellis textures are also observed. The massive ores are typically characterised by the complete absence of ilmenite lamellae intergrowths. Similar observations were made by von Gruenewaldt et al. (1985) for magnetitites from the Upper Zone of the Bushveld Complex, which were interpreted, along with compositional data from Klemm et al. (1985), to reflect higher prevailing fO_2 conditions during the crystallisation of the ore rocks. For the ore rocks, early (high temperature) oxidation of magnetite-ulvospinel solid solution results in ilmenite exsolution and its diffusion to grain boundaries, a decrease in the ulvospinel content, and cloth-textured ulvospinel exsolutions forming later at relatively low temperatures (von Gruenewaldt et al. 1985). Conversely, where the high temperature setting is less oxidizing, ilmenite exsolution is less and ulvospinel cloth textures form, with later oxidation to protoilmenite (ilmenite thereby forming as a result of oxidation of ulvospinel cloth-textured exsolutions), as is seen in the gabbroic rocks at Panzhihua. Diffusion of protoilmenite results in the composite lamellar intergrowths observed in the gabbroic rocks (von Gruenewaldt et al. 1985).

Evidence presented here indicates that the lower ± 270 m of the intrusion crystallised at relatively high fO_2 conditions, likely > FMQ+1, whereas above ± 270 m where cumulus ilmenite is observed the fO_2 conditions were more likely close to FMQ. Furthermore, within the lower ± 270 m there is a distinct variation in the fO_2 conditions, as indicated by the variation in the Ti-magnetite exsolution

textures. Fe-Ti oxide ore rocks crystallised at higher fO_2 conditions relative to the associated gabbroic rocks. This is consistent with the model for Fe-Ti oxide ore formation presented by Ganino et al. (2008).

9.1.4 H_2O content of the parent magma

The crystallisation temperature and composition of plagioclase is affected by two key characteristics of the parent magma composition: a) CaO/FeO and b) initial H_2O content. Parent magmas with high CaO/FeO favour early crystallisation of clinopyroxene (as a result of high CaO) with subsequent late crystallisation of plagioclase (e. g. Snyder et al. 1993). In particular for the Emeishan low-Ti basalt, which is characterised by high CaO/FeO relative to the high-Ti basalt, clinopyroxene crystallises early followed by later crystallisation of plagioclase (section 7.6.1). H_2O content of the parent magma also significantly affects the crystallisation temperature of plagioclase (Botcharnikov et al. 2008; this study: section 7.8). Increasing H_2O content of the parent magma significantly depresses the crystallisation temperature of plagioclase and to a lesser extent clinopyroxene. In both cases where plagioclase crystallises later, the composition is more calcic. The Panzhihua intrusion parent magma was interpreted to be similar to typical high-Ti Emeishan basaltic magma, although on the lower end of TiO_2 range (section 7.9). Models for the crystallisation of plagioclase are presented in section 7 (Figure 7.5 a and 7.6 a) for both high-Ti and low-Ti basaltic magmas. The initial plagioclase composition of the Panzhihua intrusion can be used as a proxy to estimate the bulk H_2O content of the parent magma.

The H_2O content of the parent magma for the Panzhihua intrusion has been estimated by two previous studies. Pang et al. (2008b) suggested that the Fe-Ti oxides in ore rocks crystallise early and showed that this is possibly for a high-Ti Emeishan basaltic magma with > 1.5 wt % H_2O. Ganino et al. (2008) used a technique developed by Dixon et al. (2002) using known H_2O/Ce variations for undegassed oceanic basalts and suggested that the parent magma had 0.2-0.7 wt % H_2O. In section 7.9 I suggested that the Panzhihua gabbroic rocks crystallised from high-Ti Emeishan basaltic parent magma with ± 1 wt % based on the average plagioclase composition of gabbroic rocks presented by Pang et al. (2009). Sample BT-01 analysed in this study is a microgabbro from the MGZ interpreted to represent the earliest pulses of magma forming the Panzhihua intrusion. This sample has a plagioclase composition of An_{57} with minor intra-sample variation (2 mol. %). This composition represents the initial composition of plagioclase to crystallise from the Panzhihua parent magmas

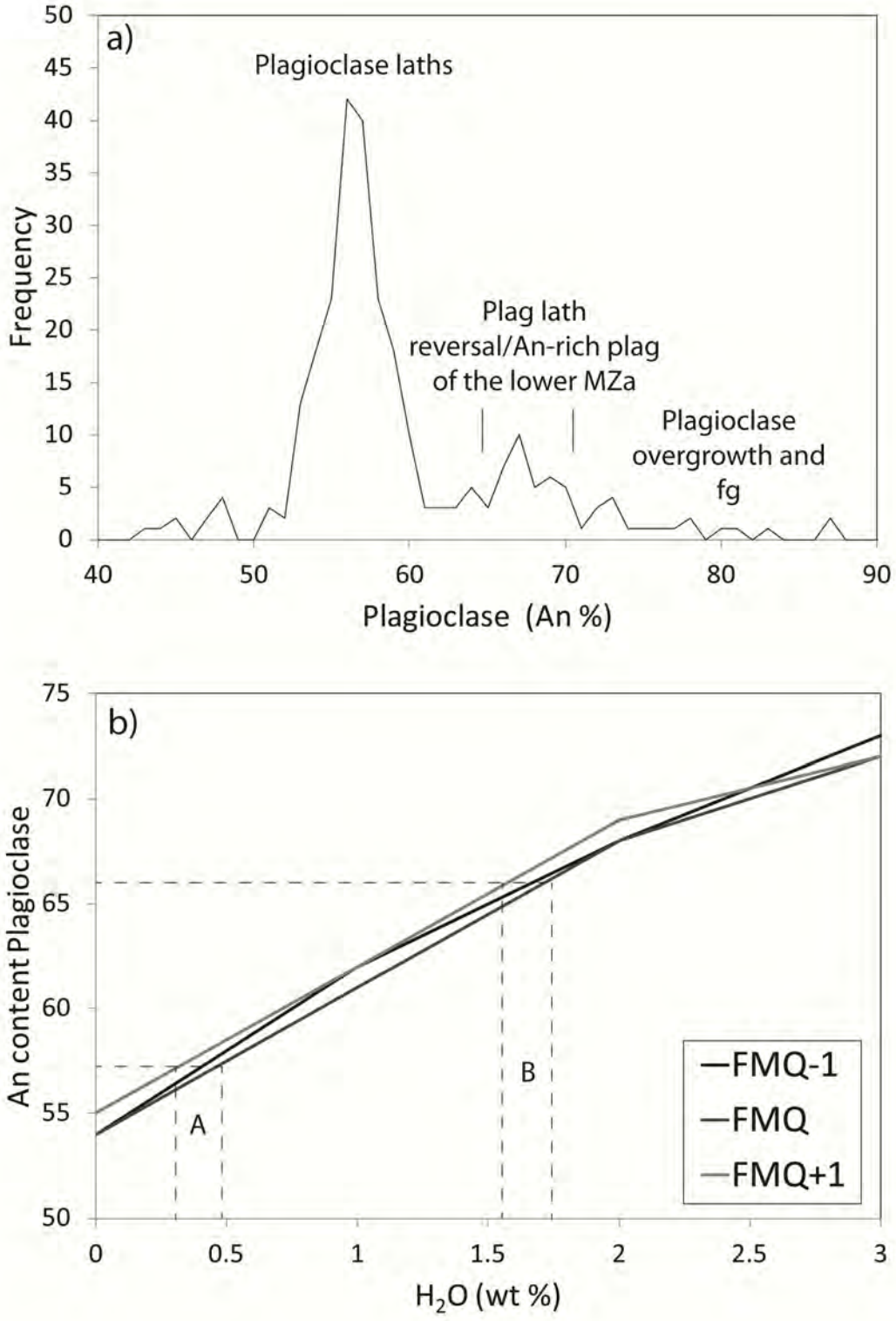

Figure 9.5 a) Figure illustrating the plagioclase composition given as An content vs. the frequency for the entire data set of this study. b) Modeled compositional variation of plagioclase as a function of fO_2 and H_2O. A – Composition of plagioclase from microgabbro and gabbroic rocks of the lower MZa. B – Composition of plagioclase from the MZa reversal (section 9.1.5).

and can be used to estimate the bulk H_2O content of the magma. Furthermore the average composition of the Panzhihua gabbroic rocks from the MZa is also An_{57} (Figure 9.5 a). New plagioclase composition models produced by PELE using a high-Ti basaltic composition with 2.5 wt % TiO_2 (interpreted as parental in section 7.9) are presented in Figure 9.5 b. The composition of An_{57} corresponds to an initial H_2O content of ± 0.3-0.5 wt % (Figure 9.5 b). This is in agreement with the earlier estimate of Ganino et al. (2008) for the gabbroic rocks of the Panzhihua intrusion.

The composition of plagioclase can be used as a tool for estimating the bulk H_2O content of parent magmas for mafic intrusions or extrusions given that: a) the major element chemistry of the parent magma is known and b) the initial plagioclase composition is known.

9.1.5 Multiple replenishments of magma

The cumulate gabbroic rocks of the Panzhihua intrusion clearly form from at least three pulses of magma, which is indicated by two major reversals in the mineral compositions, one within the MZa and one defining the base of the UZ (Pang et al. 2009). The reversal in the MZa is also observed in this study and is spatially associated with a Fe-Ti oxide ore layer (Figure 5.6). No concurrent increase in clinopyroxene Mg# is observed in this study or by Pang et al. (2009). However reversals in clinopyroxene trace elements (Ti and V) and plagioclase trace element (Fe) is also observed (Pang et al. 2009; this study for Ti in clinopyroxene). Pang et al. (2009) interpreted this reversal in major and trace element compositions to indicate a new pulse of more primitive magma, even more primitive than earlier pulses due to the significant increase in plagioclase An content. As discussed above in section 9.1.4 H_2O content of a parent magma will also significantly influence the An content of plagioclase. Mixing between resident and primitive magmas will produce a hybrid melt with higher Mg/Fe (Mg#) and Ca/Na, which should result in concurrent increases in the Mg# of pyroxene and An content of plagioclase (Namur et al. 2010). This is not observed for the MZa reversal at the Panzhihua intrusion. Ti, V and Fe all typically enrich in residual liquids during early crystallisation of an anhydrous tholeiitic basaltic magma. Similarly H_2O also enriches during crystallisation of anhydrous mineral phases during the early stages of basaltic evolution. Therefore I suggest here that the reversal in mineral compositions within the MZa may result from a more evolved magma, rather than a more primitive one, with high concentrations of Ti, V, Fe and most importantly H_2O as a result of fractionation at depth prior to emplacement. The highest An content of plagioclase analysed for primocryst laths of the reversal in this study is An_{66} (Table 5.1). This corresponds to a H_2O content of

1.55-1.75 wt % (Figure 9.5 b). The crystallisation sequence of a magma with ± 1.5 wt % H_2O is ol + plag+ cpx + Mt-Uv and can be observed in Figure 9.6. A further conclusion is that the Panzhihua intrusion is essentially an open system forming from multiple pulses of magma with varying H_2O contents.

9.2 Petrogenesis of the Fe-Ti oxide ore layers

9.2.1 Timing of Fe-Ti oxide crystallisation

All of the crystallization modeling predicts the early and continued crystallization of olivine. It is therefore noteworthy that significant primary olivine is absent from the Panzhihua rocks, occurring only in small amounts (< 5 modal %) (Zhou et al. 2005; this study). Assuming a common parental magma for the Fe-Ti oxide-bearing members of the PANXI rift layered suite, which include Panzhihua, Baima, Hongge, and Taihe, many of which are olivine-rich, then it must be assumed that olivine did crystallise, but must have been lost through fractionation prior to emplacement at Panzhihua, in particular. The presence of olivine phenocrysts in the MGZ rocks further favours early crystallisation of olivine at depth.

The Fe-Ti oxide ores and gabbroic rocks of the Panzhihua intrusion are similar in mineralogy. They are comprised of primocrysts of plagioclase, clinopyroxene and Fe-Ti oxides (± olivine). Fe-Ti oxides within the gabbroic rocks are clearly interstitial, indicating late crystallisation after plagioclase and clinopyroxene. There is some debate on the timing of Fe-Ti oxide crystallisation within the ore rocks. Pang et al. (2008b) suggested that Fe-Ti oxides crystallise early based on the occurrence of Cr-rich Ti-magnetite as inclusions in olivine grains in the MGZ. The occurrence of similar Cr-rich Ti-magnetite at the Xinjie intrusion also implies early crystallisation of these Fe-Ti oxide phases (Wang et al. 2008). However the Ti-magnetite in the Fe-Ti oxide ore layers of the Panzhihua intrusion are characterised by very low Cr contents. This implies that Cr-rich Ti-magnetite may crystallise early but is likely related to an earlier stage of evolution at depth rather than indicating early crystallisation of Fe-Ti oxides within the Panzhihua intrusion. Pang et al. (2008a) suggested early crystallisation of Fe-Ti oxides based on the occurrence of euhedral inclusions of Fe-Ti oxides within clinopyroxene grains. This is compelling evidence to support this interpretation however I have not observed similar euhedral inclusions within any ore rocks observed in this study. This implies that this feature is particularly rare and may indicate some late crystallisation of interstitial clinopyroxene. Ganino et al. (2008) suggested early crystallisation of Fe-Ti oxides to form ore layers through an increase in fO_2

related to CO_2 degassing of the footwall carbonates. Zhou et al. (2005) suggested later crystallisation of Fe-Ti oxides from an immiscible Fe-rich liquid, which is also responsible for the consumption of silicate grains.

The plagioclase crystal habit is corroded and reacted, but is nonetheless fundamentally elongate & lath-like tabular (Figure 4.4). It may be suggested that some of the more anhedral grains are intercumulus material that have undergone late stage sub-solidus textural readjustment such as in the case of silicates at the Isle of Skye (O'Driscoll et al. 2008). We interpret the embayed/corroded margins of lath shaped plagioclase as more likely to reflect a secondary magmatic process (i.e., modification of previously-crystallised plagioclase) rather than the product of crystallization of interstitial trapped liquid. This is based on the clear lath shaped crystal habit, which on a macroscopic scale appears euhedral (Figure 2.11) and only on closer petrographic inspection are the distinct embayment's observed. In particular Figure 2.11 (e) shows the incorporation of plagioclase from the gabbroic rock beneath an ore layer. These plagioclase laths are typically embayed/resorbed and have distinct reaction rims, which are clearly not late stage interstitial minerals. A similar interpretation of early silicate crystallisation followed by later consumption is made by Zhou et al. (2005); Zhou et al. (2008) and Zhou et al. (2013). Fine-grained rounded grains are more difficult to interpret, in terms of their timing of crystallisation. These grains may represent either highly resorbed early crystallised silicate or later crystallising silicates from intercumulus liquids.

9.2.2 Modeling constraints on Fe-Ti oxide ore petrogenesis and the evaluation of current models

Pang et al. (2008a, 2008b, 2009, 2010) and Zhang et al. (2012) present a model for the formation of the Fe-Ti oxide ore layers through early crystallisation of Fe-Ti oxides from a parent magma with 1.5 wt % H_2O at fO_2 of FMQ at a depth equivalent to 5 kb. Ganino et al. (2008) presented a model for the formation of Fe-Ti oxides through an increase in fO_2 related to CO_2 degassing of the footwall rocks at a depth equivalent to 2 kb. Evidence for the variation in fO_2 conditions presented in this study is in agreement with the latter model. However, two major problems exist with this model: 1) several Fe-Ti oxide-bearing intrusions in the PANXI area do not have carbonate footwall and 2) an increase in the fO_2 conditions does not explain the silicate disequilibrium textures observed in this study.

The basic requirements of models discussed below include:

- ore layers are more oxidised than their host rocks
- disequilibrium textures exist between oxides and silicates
- discordant contact relationships of ore reefs with host rocks (i.e. varied stratigraphic height of main ore layer)
- mineral compositional constraints (modeling must correspond to observations)
- gradational lower contacts where plagioclase is being incorporated into the ore layer
- presence of gabbroic xenoliths within ore layers

The modeling results for a typical Emeishan high-Ti basalt magma suggest that variation in H_2O content is the most prominent influence on the crystallisation sequence of the magma. Ilmenite is not a cumulus phase in the lower parts of the intrusion indicating that the lower intrusion crystallised at higher fO_2. On the basis of previously proposed genetic models and our results, three main potential scenarios can therefore be outlined in order to account for oxide crystallisation: 1) a wet parent magma, 2) an evolved but dry parent magma, and 3) a dry parent magma which is later hydrated.

1. *Wet magma (> 1.5 wt % H_2O) sequence:* Pang et al. (2008a, 2008b, 2009, 2010) presented a model for the formation of the Fe-Ti oxide ore layers through early crystallisation of Fe-Ti oxides from a parent magma with 1.5 wt % H_2O at fO_2 represented by FMQ at a depth equivalent to 5 kb. Our modeling results also indicate that a wet magma will crystallise Ti-magnetite appropriately early in the sequence (Figure 9.6), and on first inspection may be a logical model to account for the presence of massive oxide ore layers at the base of the intrusion. However, we can identify three problems with a simple wet magma crystallisation model. First, a wet magma would be expected to crystallise plagioclase with ± An_{70}, whereas plagioclase analysed from the Panzhihua intrusion is typically ± $An_{55\text{-}60}$ and laths are never as calcic as An_{70}. Secondly, the silicates and coexisting oxides ought to have crystallized in equilibrium, and therefore magmatic disequilibrium textures (i.e. consumption of silicates) are not accounted for in this model. Thirdly, the plagioclase and clinopyroxene textures within the ore rocks suggest their crystallisation prior to that of the Ti-magnetite (Zhou et al. 2005; Zhou et al. 2008; this study). Finally, evidence presented by Ganino et al. (2008) based on H_2O/Ce ratios (Dixon et al. 2002) suggests that H_2O content of the Panzhihua parent magma was low (0.2-0.7 wt %). A similar estimate of H_2O (0.3-0.5 wt %) content is made in

this study; section 9.1.4. It seems therefore unlikely that the Panzhihua magma forming the gabbroic rocks was wet (> 1.5 wt % H_2O) at the time of emplacement.

2. *Dry magma (< 0.5 wt % H_2O) sequence:* Fe-Ti oxides typically crystallise late in normal gabbroic sequences as a result of progressive Fe-enrichment in the residual liquid. This would also occur from a dry Panzhihua parent magma (Figure 9.6) having undergone significant crystallisation of silicate (i.e., 50% crystallization over ± 150^{o}C of cooling) wherein Fe-enrichment would induce crystallisation of Ti-magnetite. This is not obviously consistent with the occurrence of massive ore layers at or near the base of the intrusion. The most obvious solution to this problem involves emplacing a more evolved initial melt, which could be derived by either a) invoking a more evolved, Fe-rich parent magma than has previously been proposed, or b) assuming some silicate (i.e., olivine + plagioclase) crystallization (hence also driving evolution of the liquid) of the high-Ti basaltic magma parent prior to emplacement. This could allow for "early" crystallization of Fe-Ti-oxides. This would then be consistent with the observed "dry melt" plagioclase compositions (< An_{60}).

   It then remains to be asked whether fractional crystallization is an appropriate process to produce a magnetite-rich assemblage consistent with the ore layers (as distinct from a merely magnetiferous assemblage, secondary physical enrichment processes notwithstanding). Predicted cotectic proportions for ol:plag:cpx:mt-uv for this magma at FMQ are 8:32:28:32. A significant amount of secondary enrichment by a process of gravity-driven settling of the dense magnetite would be required to get from the cotectic proportions to the observed modal proportions in the ore zone (i.e., 68-96 vol. % oxide).

   This suggests that it may not be possible to concentrate the required amount of Ti-magnetite in order to account for ore layer formation. The fact that the main massive ore layer cross-cuts previously crystallised gabbroic rocks requires that a portion of the intrusion was already in place and semi-solid prior to the emplacement of the Ti-magnetite. In addition, the silicates are not in textural equilibrium with the Ti-magnetite, which is not obviously consistent with the formation of the massive ore layers through simple dry equilibrium crystallisation.

3. *Initially dry magma with subsequent hydration or oxidation:* Ganino et al. (2008) presented a model for the formation of Fe-Ti oxides through a post-emplacement increase in magma fO_2 related to CO_2-degassing of the footwall rocks at a depth equivalent to 2 kb. An alternative model which exploits the sensitivity of silicate stability to water content would involve post-

emplacement hydration (where possible water sources are discussed below in 9.2.5). Initial crystallisation of a dry magma will produce ol. + sodic plagioclase (with the same composition of the plagioclase at the Panzhihua intrusion; "dry" plagioclase with < An_{60}). Later addition of H_2O would induce Mt-Uv saturation at the expense of plagioclase. Alternatively, later oxidation of the magma would result in an increase in the magnetite to ilmenite ratio of the crystallising oxides.

9.2.3 Liquid immiscibility

The variation in the stratigraphy of the main ore layer can be explained by allochthonous emplacement of an extremely dense liquid, such as in the case of the Jianshan section where the ore layer is seen in contact with footwall rocks, interpreted by Zhou et al. (2005) as evidence of an immiscible Fe-rich liquid. Immiscible Fe- and Si-rich liquids forming from tholeiitic magmas have been documented in numerous experimental and natural studies. Phillpots (1982) analysed late stage Fe- and Si-rich glasses within tholeiitic rocks from numerous localities around the world, which were interpreted to result from immiscible Fe-and Si-rich liquids separating late in the crystallisation sequence. Furthermore, recent studies on the Skaergaard intrusion have shown that late stage Fe-enrichment trends may be due to the formation of Fe-rich immiscible liquids (e.g. Jakobsen et al. 2011). However, in both of these cases the Fe-rich immiscible liquids contained significant SiO_2 content (35-45 wt %) and relatively low Fe_2O_3 (30-40 wt %). In the case of the Panzhihua intrusion the silicates are in disequilibrium with the Fe-Ti oxides and are most likely not related. This would indicate that an immiscible liquid forming the Fe-Ti oxides ore layers would have to have been very Si-poor and very Fe- and Ti-rich (> 85 vol. % combined). The Panzhihua ore layers are extremely rich in TiO_2 (± 16 wt % TiO_2) and poor in P_2O_5 (< 0.05 wt %). Fe-rich immiscible liquids with up to 94 wt % Fe_2O_3 forming massive oxide deposits have been proposed for several occurrences such as the Chupaderos caldera, Mexico (Lyons, 1988) and Marcona Magnetite deposit, Peru (Chen et al. 2010). However, in each of these cases, the proposed Fe-rich immiscible liquids are TiO_2-poor and P_2O_5-enriched. Furthermore, typical immiscible liquids are in equilibrium with each other, which suggests that the currently entrained silicates did not originate from the coexisting silicate liquid, but must have been acquired after the formation of the proposed immiscible Fe-Ti liquid, perhaps during emplacement. While the formation of Fe-immiscible liquids can account for many of the observations made from ore layers, the complete absence of apatite (i.e. low P_2O_5 content of ore layers) suggests that Fe-immiscible liquids are likely not an important mechanism for ore rock formation of the Panzhihua intrusion.

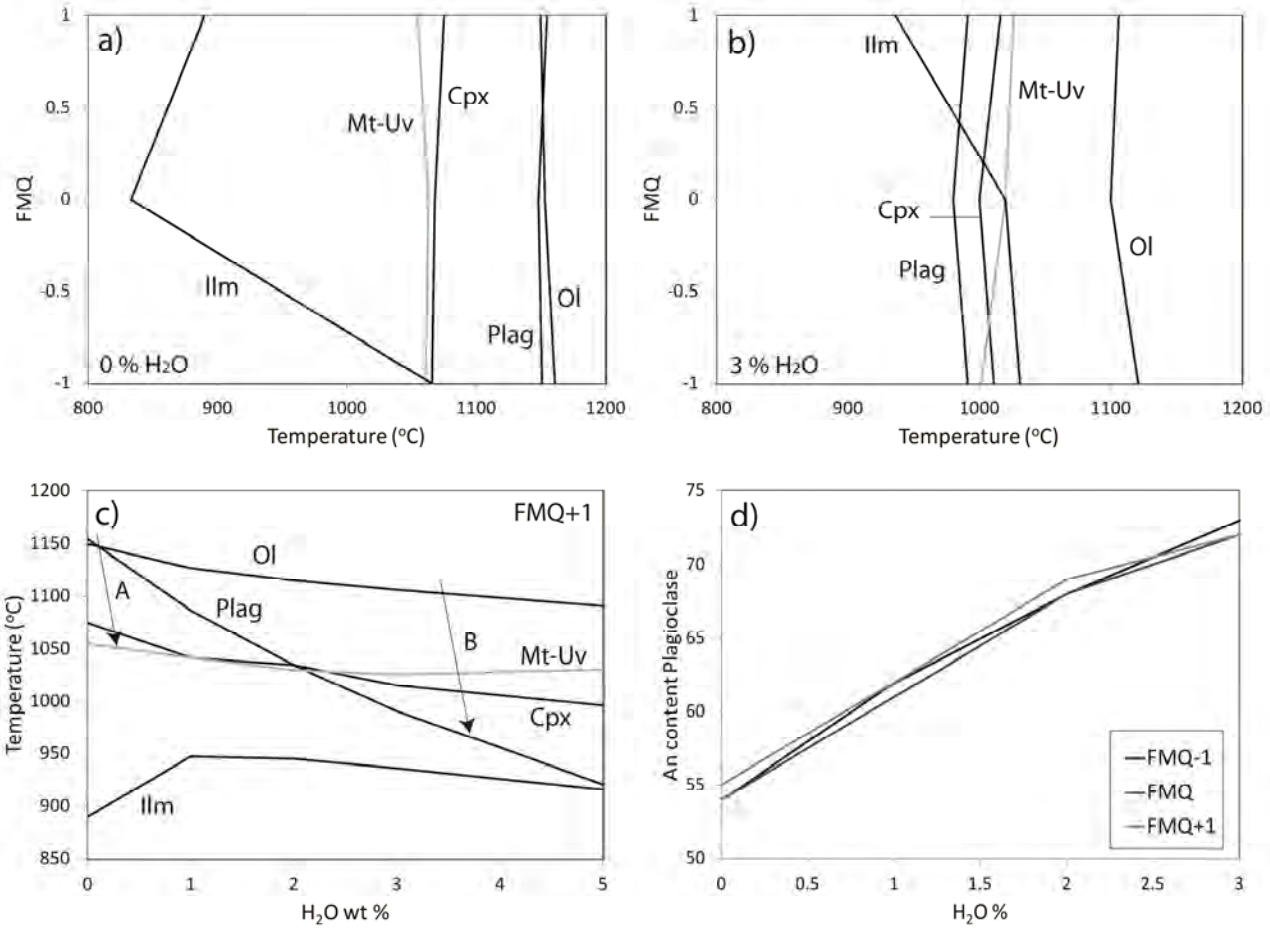

Figure 9.6 PELE modeling results for an average high-Ti Emeishan basalt composition. a) and b) Phase equilibria as a function of FMQ with temperature at 0 % H_2O (a) and 3 % H_2O (b). c) Phase equilibria as a function of H_2O with temperature at FMQ+1 showing the stability of silicates with increasing H_2O content of the parent magma. Plagioclase crystallisation temperature, in particular, is significantly reduced by increasing the H_2O content of the parent magma. d) Plagioclase composition as a function of increasing H_2O content. Note that at low H_2O plagioclase is more sodic and progressively becomes more calcic with increasing H_2O content.

9.2.4 Silicate consumption in Fe-Ti oxide ore layers and development of reaction rims

The importance of the bulk H_2O content on the crystallisation of Emeishan basaltic magmas has been shown in section 7.10 and above in section 9.2.2. H_2O significantly depresses the crystallisation temperature of plagioclase to a point where Fe-Ti oxides crystallise early prior to plagioclase and

clinopyroxene. The overriding characteristic of the Fe-Ti oxide ores at the Panzhihua intrusion is the highly embayed plagioclase grains and to a lesser extent clinopyroxene. In section 7.10 and 9.2.2 I suggested that Fe-Ti oxide ores form by an influx of an H_2O-rich fluid or liquid, which is based on the highly consumed silicate phases.

Temperature constraints for reaction product assemblage formation can be estimated using the TiO_2 and Al_2O_3 content of calcic amphiboles by using the semi-quantitative thermobarometer developed by Ernst and Liu (1998). The TiO_2 content of amphiboles analysed in this study contain slightly higher values (5 wt %) relative to the upper limit of the thermobarometer (4 wt %) but still provide a useful estimation of temperature and pressure based on using both TiO_2 and Al_2O_3 contents. Application of this thermobarometer suggests high temperatures (1000-1050^oC) at relatively low pressures (< 6 kb). Therefore consumption of silicate grains within ore layers at the Panzhihua intrusion likely occurred at relatively high temperatures (> 1000-1050^oC) with later formation of reaction product assemblages from late stage reactions involving Ti-magnetite and silicates at ± 1000^oC.

Typical formation temperatures for the development of coronas in gabbroic rocks have been estimated in numerous studies; e.g. 580-880 ^oC (Acquafredda et al. 1992); 800 (± 30) ^oC (Cleason, 1998), layered intrusions; e.g. 560-800 ^oC (Fornoni Candia et al. (1988) and from experimental work 670-700 ^oC (Larikova and Zaraisky, 2009). These estimates are significantly lower than the estimate of ± 1000 ^oC for the formation of the reaction assemblages observed at the Panzhihua intrusion. Therefore reaction assemblages at Panzhihua formed at significantly higher temperatures than typical late stage sub-solidus reactions and corona development at low temperatures.

Zhou et al. (2005; 2013) suggest that the Fe-Ti oxide ore layers form through the separation of a Fe-immiscible liquid, which effectively consumes pre-existing silicate phases. Holness et al. (2011) present a detailed study of late stage reaction product assemblages in gabbroic rocks of the Skaergaard intrusion, which have been interpreted to result from the reaction of silicate primocrysts with late stage Fe-immiscible liquids. Microtextures described from Skaergaard are somewhat similar to that observed in this study (in particular the development of olivine rims and An-rich plagioclase) except that amphibole is not a common feature of the reaction product assemblage and reaction product plagioclase typically has high Fe contents (1.4 wt %), which is not the case for the Panzhihua intrusion (Table 5.1). Furthermore Fe-immiscible liquids typical concentrate P, the

complete absence of apatite in the Fe-Ti oxide ores at Panzhihua does not favour the formation of a Fe-immiscible liquid.

A recent series of experimental studies on hydrous partial melting of gabbroic rocks at relatively low pressure (e.g. Koepke et al. 2003; 2004; 2005; France et al. 2010) provides further constraints on a hydration model invoking an influx of H_2O-rich liquid. In particular Koepke et al. (2003) present an experimental study on hydrous partial melting of ferrogabbroic rocks, similar in composition to the high-Ti Emeishan basalt (interpreted to be the parent magma composition for the Panzhihua intrusion; Zhou et al. 2005; Pang et al. 2008b; this study: section 7) apart from slightly higher TiO_2 content (1 wt % higher) and FeO_T content (2 wt % higher). The results of the study (Koepke et al. 2003) are summarised here:

- First melts produced at 930^oC – very rich in normative plagioclase (72%)
- Plagioclase is initially the major phase consumed
- Reaction product assemblage of: plag+cpx+amphibole+ rare Fe-Ti oxide
- Plagioclase composition as reaction product increases in An content with increasing temperature
    - 930-970^oC – An_{60}-An_{63}
    - 970-1030^oC – An_{63}-An_{81}
    - 1030-1060^oC – An_{81}-An_{83}
- Amphibole is stable up to 1030^oC and has a composition of titanian magnesiohastingsite (after Leake et al. 1997)
- Ti-magnetite crystallises at temperatures > 1100^oC
- Olivine is not observed as a reaction product

It must be noted here that ongoing experimental work has shown that a similar effect has been observed by percolation of a ferrobasaltic melt through a gabbro (Koepke pers comm.). The reaction product assemblage observed in this study is in decreasing abundance: amphibole+Fo-enriched olivine+An-enriched plagioclase (± Fe-Ti oxides+hercynitic spinel+clinopyroxene). This is consistent with the experimental results with the exception of the abundance of olivine as a reaction product in this study. Further features observed in this study which are consistent with the study of Koepke et al. (2003) are: 1) amphibole composition (Ti-rich), 2) An-enrichment in plagioclase reaction product and 3) large scale consumption of silicates, in particular plagioclase. The presence of plagioclase-rich

segregations within the Fe-Ti oxide ore layers (Figure 2.11 e and f) at Panzhihua as well as late stage anorthosite veins cross-cutting magmatic layering in the MZa may provide evidence for plagioclase normative melts generated during partial melting of the gabbroic rocks. This may be somewhat speculative and it would be more likely that any consumed plagioclase melts would likely mix with the overlying magma within the chamber.

The one major discrepancy between the results of Koepke et al. (2003) and features of the Panzhihua Fe-Ti oxide ores is the abundance of olivine in the reaction product assemblage. Olivine as reaction products is observed in hydrous partial melting experiments at high temperatures (980^{o}C) for normal gabbroic protolith compositions (Koepke et al. 2004) and as late stage reaction textures at the Skaergaard intrusion (Holness et al. 2011). Koepke et al. (2005) suggest a reaction product assemblage of An-enriched plagioclase+orthopyroxene+paragasitic amphibole as indicative of hydrous partial melting for oceanic gabbroic rocks at temperatures below 980^{o}C. Olivine becomes the stable phase at higher temperatures rather than orthopyroxene. Koepke et al. (2004) shows that olivine is typically enriched in Fo with increasing H_2O for a given temperature, which is consistent with olivine compositions in this study (i.e. olivine as reaction products have higher Fo content relative to olivine grains in the same sample; Table 5.3). Therefore the presence of abundant olivine as a reaction product at the Panzhihua intrusion may be interpreted to indicate high temperature (similar to temperatures estimated previously) consumption of gabbroic protolith composition intermediate between ferrogabbro and gabbro. This is also consistent with the slightly higher TiO_2 and FeO_T contents of the starting composition used by Koepke et al. (2003) relative to the composition of the Emeishan high-Ti basaltic magma, interpreted to be parental to the Panzhihua intrusion (Zhou et al. 2005, Pang et al. 2008b, this study).

Temperature constraints based on comparison of experimental observations and the compositions of reaction product assemblages observed in this study suggest: Firstly, the abundance of amphibole, which is only stable up to 1030^{o}C (Koepke et al. 2003), suggests temperatures below 1030^{o}C. The composition of plagioclase occurring as reaction products at the Panzhihua intrusion shows some variation but is commonly observed > An_{80}, suggesting a maximum temperature of 1000-1060^{o}C according to results given in Koepke et al. (2003) and summarised above. This is consistent with temperature estimates discussed earlier using the thermobarometer of Ernst and Liu (1998).

Hydrous partial melting experiments of Koepke et al. (2003); Koepke et al. (2005) were used to explain microtextures associated with gabbroic rocks in oceanic settings. In these cases the influx of a H_2O-rich fluid phase (thought to occur through shear zones: Koepke et al. 2005) results in the large scale consumption of plagioclase and the generation of up to 30 % partial melting (Koepke et al. 2003). In section 9.2.2 I presented a scenario (scenario 3) where an influx of H_2O can result in the instability of silicate phases, in particular plagioclase, crystallised from an essentially anhydrous ferrobasaltic magma. This is consistent with comparison of reaction product assemblages observed at the Panzhihua intrusion and those of hydrous partial melting experimental work. However while an influx of H_2O into a partially crystallised gabbroic cumulate pile can account for the observed reaction product assemblages it cannot account for the association with massive Fe-Ti oxide ore layers.

Therefore a source of Fe for large scale precipitation of Mt-Uv is required along with the hydrous partial melting or consumption of a gabbroic protolith. Again it is emphasised that ongoing experiments based on the percolation of ferrobasaltic magmas through a gabbro produce a similar effect of consumption of silicate phases Koepke per comm.).

9.2.5 Sources of H_2O-rich fluid or liquid responsible for silicate consumption

Potential sources for the addition of H_2O include: a) Assimilation of wet footwall rocks (such as carbonates), as has been proposed by Ganino et al. (2008) on the basis of evidence for magma oxidation. If this was the case the magma might reasonably be expected to continue to crystallise silicate minerals with a "wet" composition i.e. calcic plagioclase (An_{75}; Figure 9.6 d). No plagioclase of such a composition has been found at the Panzhihua intrusion, with the exception of rare plagioclase as part of reaction product assemblages. If either of these processes (hydration and/or oxidation) occurred as a consequence of in situ footwall assimilation, it might reasonably be expected to produce magnetite precipitation at the immediate base of the intrusion, at the magma-footwall contact. This is not, in general, observed to be the case. If, conversely, progressive degassing of the footwall results in a cumulative enrichment in the volatile content of the basal magma which only induces oxide precipitation at a certain critical gas concentration, then this could account for the observation that the main oxide ore layer varies locally in stratigraphic position from the actual footwall contact to tens to hundreds of meters above it, locally. Magnetite saturation would then depend on local heterogeneities in footwall composition, permeability, etc.

Furthermore, while the footwall rocks at the Panzhihua intrusion may contain significant water and CO_2 for assimilation, this is not necessarily the case for the PANXI region in general; for example, the Baima Fe-Ti oxide ore-bearing intrusion has a syenite footwall and Xinjie intrusion has a basaltic footwall (Figure 2.6).

b) The magma could have become hydrated by mixing of a hypothetical hydrous roof rock through a process of magma fountaining (e.g. Campbell & Turner 1989) and roof interaction, with the resultant formation, separation and lateral emplacement of a gravity-driven oxide-slurry, such as has been proposed by Kinnaird et al. (2002) for chromitite formation in the Bushveld Complex. This model effectively allows for the massive ores being intrusive into lower lithologies within the intrusion. However, as with the previous model it requires a suitable country rock contaminant. The top contact of the Panzhihua intrusion is fault-bounded, which makes the composition of the roof rock uncertain. However, the comparably-mineralised Hongge, Xinjie and Baima intrusions have basaltic and syenitic roof rocks (Figure 2.6), which are unlikely to contain significant H_2O. Moreover, one would still expect to find "wet" (i.e., calcic) plagioclase compositions at some level in the intrusion, although given that the upper part of the intrusion has been removed, this could also suggest that "wet" plagioclase has been removed as it could have remained near the roof of the intrusion.

c) Late magmatic fluids, evolved by crystallisation of anhydrous assemblages and subsequently ascending through the compacting crystal-magma pile, have been proposed as mechanisms to facilitate sulphide (e.g. Boudreau and Meurer 1999) and chromite (e.g. Nicholson & Mathez, 1991) redistribution. However, magmatic fluids are unlikely to represent a significant source of fluids for triggering magnetite crystallization at the Panzhihua intrusion given that the major Fe-Ti oxide layer is at the base of the Panzhihua intrusion, providing very little underlying cumulate rock as a source for H_2O-rich intercumulus liquid.

d) Magma hydration elsewhere (i.e. prior to final emplacement), which results in Mt-Uv saturation with subsequent emplacement (prior to "wet" plagioclase crystallisation) into the current Panzhihua level. This can account for intrusive relationships of the ore bodies, possible magmatic alignment of the silicates within the oxide ores, and the silicate-disequilibrium textures. This is similar to that described above for roof interaction but occurs at depth rather than within the current emplacement site. Ganino et al. (2008) suggested that the Panzhihua intrusion crystallised at a

depth equivalent to 2 kb based on the preservation of shallow water textures in the carbonate footwall rocks. Pang et al. (2008a) interpreted an intrusion depth of 5 kb based on the composition of the Ti-magnetite in the Fe-Ti oxide ore layers of the Panzhihua intrusion. These interpretations can be reconciled with a model where Ti-magnetite crystallised at depth (5 kb) elsewhere in the plumbing system and was subsequently intruded into the Panzhihua chamber at 2 kb. This model would still require a trigger for magnetite crystallisation, such as assimilation of country rock, which is then more difficult to constrain in terms of its availability at depth. The Ti-magnetite layer would then have been emplaced as a crystal slurry sill with entrained "dry" ol.+ plag. Entrained silicate phases would become consumed with resultant late stage reaction product assemblage formation at high temperature. This model can account for the composition and silicate consumption textures of entrained plagioclase within the massive ore layers. Similar crystal slurry models for the emplacement of chromitite layers in the Bushveld Complex have been invoked by Eales (2000); Mondal and Mathez (2007) and Eales and Costin (2012). Furthermore, emplacement of a massive layer (or layers) as a dense sill can also account for the current position of the ore layers and the variation in stratigraphic height of the main ore layer.

e) The Panzhihua intrusion has been shown to be an open system with multiple pulses of magma forming the intrusion (Pang et al. 2009, this study; section 9.1.2 and 9.1.5). Studies on chromitite seams in layered intrusions often report cross-cutting relationships with the cumulate stratigraphy (e.g. O'Driscoll et al. 2010). In these cases a new more primitive magma pulse thermo-chemically erodes the floor of the chamber, which results in silicate instability and crystallisation of chromite. Evolving magma at depth below the Panzhihua chamber will result in an increase in H_2O content of residual liquid. A new pulse of magma with high H_2O content, due to evolution at depth, intruding the Panzhihua intrusion will have a similar effect to that described in d) above. Thermo-chemical erosion of the floor of the chamber will assimilate previously crystallised silicates, where the high H_2O content and higher temperature will result in the incorporation and consumption of silicate grains (e.g. Figure 2.11 g). Footwall cumulate erosion is also indicated by the presence of gabbroic xenoliths within the ore layers (Figure 2.11 b) and microgabbro xenoliths within the gradational lower contact of the MZa ore layer (Figure 2.12). The resultant crystallisation path will be similar to that of B in Figure 9.6 c implying early crystallisation of extensive Mt-Uv. Recent work of Xing et al. (2012) showed that Ti-magnetite within the ore layers of PANXI layered intrusions has higher primary magmatic H_2O than the co-existing silicates. This can be explained in this model by assimilation of silicate floor rocks by a H_2O-rich later pulse of magma. Silicates would crystallise from

an earlier low-H_2O magma whereas Ti-magnetite would crystallise from the new H_2O-rich pulse of magma.

The major difference between scenarios d and e are: 1) in scenario d the intruding magma is oxide crystal-rich whereas in e the magma is not and 2) in model d the new magma intrudes a crystal pile and would have a footwall and hanging-wall of previously crystallised gabbroic rocks whereas in e the new magma intrudes into a mostly liquid chamber with cumulate rocks at the base. In both cases thermo-chemical erosion of the footwall gabbro occurs, which results in the incorporation of silicate minerals that are subsequently consumed due to the H_2O-rich nature of the intruding magma. I favour a model where Fe-Ti oxide ore layers form in an open system through multiple replenishments of magma with variable H_2O contents similar to scenarios (d) and (e) which can account for the high temperature formation of reaction product assemblages as well. A petrogenetic model for Fe-Ti oxide ore formation is outlined below.

9.3 Petrogenetic model for Fe-Ti oxide ore formation

The Panzhihua intrusion varies along strike from the northern Zujiabaobao block to the southern Nalaqing block. The northern section is characterised by the thickest cumulate sequence as well as the most extensive ore layers. The cumulate sequence and the ore layers become less extensive to the south. This may suggest that the northern Zujiabaobao block formed in a vent proximal setting where magma essentially intrudes from north to south, rather than from the middle outwards. This is highlighted by extensive mining operations in the northern block and absence of any mining in the central and southern regions. The model presented below is based on this assumption of magma intrusion in the north and spreading southward, although this is not critical for ore forming processes.

Several key observations from this study and previous studies need to be taken into account in any model proposed for the formation of Fe-Ti oxide ore layers at the Panzhihua intrusion. These include:

1. Formation in an open system chamber
2. Highly consumed silicate primocrysts, which crystallised prior to extensive Fe-Ti oxide crystallisation

3. Gradational lower and upper contacts
4. Occurrence of gabbroic xenoliths within ore layers; including microgabbro xenoliths incorporated in the MZa ore layer lower contact.
5. Variation in stratigraphic height of main ore layer and cross-cutting nature of smaller ore layers, which traverse the cumulate stratigraphy
6. Development of reaction assemblages surrounding consumed silicates at high temperatures; ± 1000^{o}C
7. The complete gradational variation in whole-rock Fe_2O_3 contents from gabbro-oxide gabbro-Fe-Ti oxide ore
8. Higher primary magmatic H_2O content of Ti-magnetite relative to co-existing silicates (Xing et al. (2012)
9. Intrusion depth of ± 2 kb indicated by footwall carbonate preservation but crystallisation of Ti-magnetite at 5 kb (Pang et al. 2008a)

I outline here four stages in the development of the main ore layer, which also applies to the smaller ore layers. 1) Firstly the MGZ develops as described in section 9.1.2, by multiple replenishments of olivine phenocryst-bearing magmas becoming less contaminated with time. This results in the initial opening of the Panzhihua chamber by successive low volume pulses of magma.

2) The formation of the MGZ is terminated by a large volume pulse of new basaltic magma, which is the parent magma to the LZ gabbroic rocks. The magma forming the LZ gabbro has low H_2O content (< 0.5 wt %), which is indicated by the plagioclase composition of the gabbroic rocks (± An_{55-60}) (Figure 9.5 b - A). A cumulate pile develops at the base of the chamber with a silicate population dominated by plagioclase and clinopyroxene with lesser olivine (i.e. LZ massive gabbro) as well as late Fe-Ti oxides as predicted by modeling. This “dry” magma crystallisation path is indicated in Figure 9.6 c - Path A.

3) Magma evolving at depth in the plumbing system subsequently becomes H_2O enriched, likely due to typical incompatible enrichment in residual liquid as a result of anhydrous mineral crystallisation. A new pulse of basaltic magma now enters the chamber, which is characterised by high H_2O content (> 2 wt %) and by the presence of Ti-magnetite microphenocrysts. The presence of Ti-magnetite microphenocrysts is based on the interpretation of Pang et al. (2008a) indicating crystallisation at 5

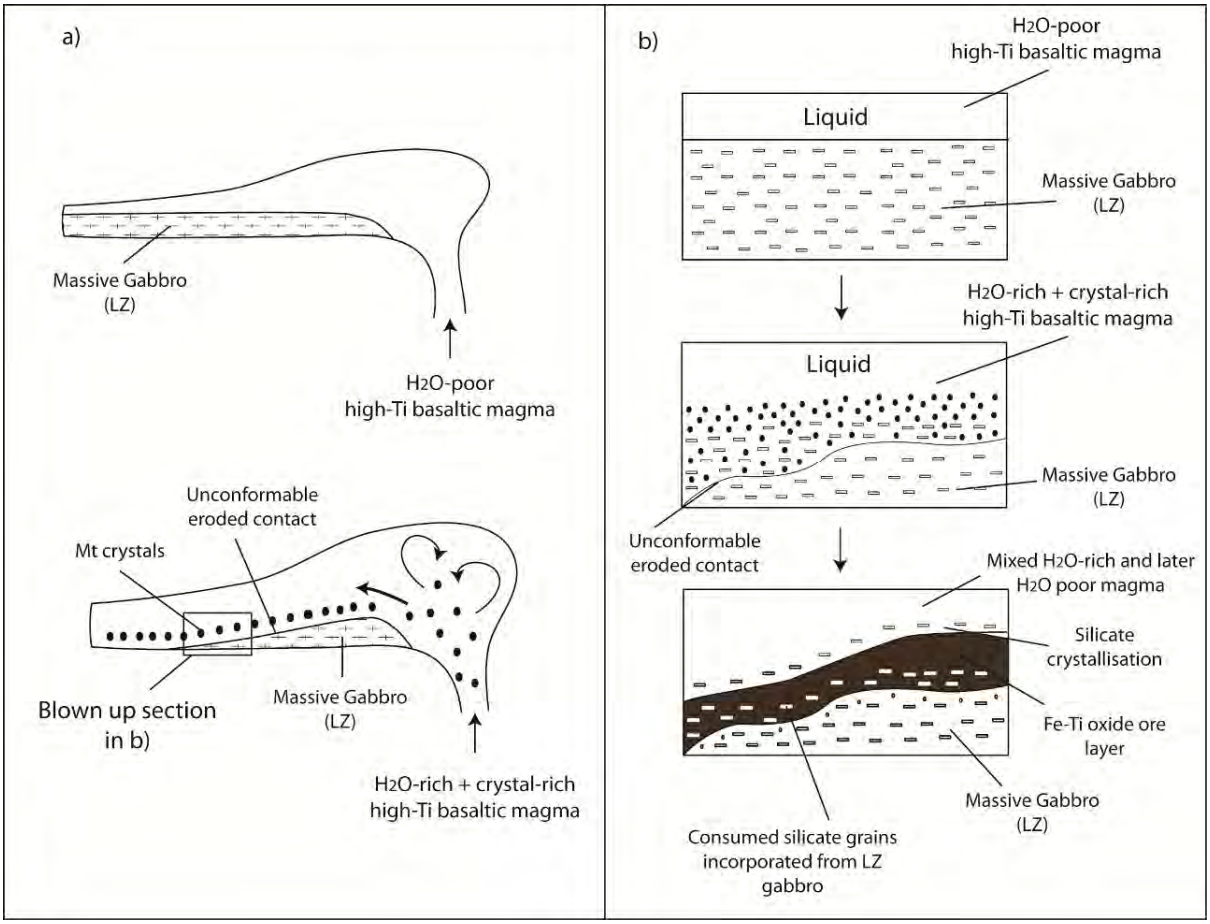

Figure 9.7. Simplified schematic illustration of the proposed model for ore formation at the Panzhihua intrusion. This stage would be preceded by the formation of the MGZ/LZ as shown in Figure 9.4.

kb relative to an intrusion depth of 2 kb for the Panzhihua chamber (Ganino et al. 2008). Xing et al. (2012) showed that Ti-magnetite has highly primary magmatic H_2O within its crystal structure relative to the co-existing silicates. This supports the interpretation of an H_2O-rich magma intruding at this stage. Eales (2000) showed that the amount of chromite added to the parental liquid for the critical zone of the Bushveld Complex is only 3 %. This accounts for all the chromitite layers within this zone, which has a cumulative thickness of ± 20 m (Eales, 2000). Furthermore chromite present as microphenocrysts within the magmas were very fine-grained (< 0.1 mm) making transportation of these dense minerals possible. This implies that the presence of only a small proportion of Ti-magnetite microphenocrysts can account for the extensive ore layers observed at the Panzhihua intrusion. The crystallisation of Ti-magnetite microphenocrysts occurred either at depth within a staging chamber or en route to the current chamber from a H_2O-rich magma. The new influx of magma thermo-chemically erodes the footwall cumulate pile incorporating “dry composition” plagioclase and clinopyroxene, which becomes significantly consumed in the magma. The potential

for partial melting of the cumulate pile also exist, however the melts would likely be mixed with the intruded liquid. Any partial melts that may segregate from partial melting of gabbroic rocks would be rich in normative plagioclase (e.g. Koepke et al. 2003). The presence of late stage quartz-rich leucocratic veins cross-cutting the cumulate stratigraphy in the MZa may form in this way but further geochemical work on these veins is required to constrain their formation. In the case of the Jianshan section the LZ cumulate pile is completely eroded away and incorporated into the new H_2O-rich magma. A ± 30 m thick sequence of LZ gabbros is present below the main ore layer in the northern vent proximal Zujiabaobao block suggesting at least this volume of cumulates must be eroded/incorporated into the main ore layer or else partially melted and mixed with the liquid. The high H_2O content of the magma results in further crystallisation of Ti-magnetite (Figure 9.6 – path B), which quickly settles to the floor of the chamber; LZ gabbroic cumulates in the Zujiabaobao block and the MGZ rocks in the Jianshan section. The presence of plagioclase included in olivine grains (with similar composition consumed plagioclase laths; Table 5.1) of the ore layers indicates that olivine is crystallising from the H_2O-rich magma, as predicted by thermodynamic modeling (Figure 9.6 – B). Percolation of the dense crystal-rich magma into the underlying eroded cumulate footwall will result in gradational lower contacts, such as observed for the MZa ore layer and smaller ore layers in the MZa. This magma percolating downward through the cumulate pile will react with earlier formed silicates producing the distinct mineral assemblages observed as reaction rims (e.g. lower contact of ore layer in Figure 2.11 g).

4) Accumulation of abundant Ti-magnetite grains at the floor of the chamber results in the formation of an extremely dense layer, which is unstable and collapses/slumps through the MGZ rocks to the base of the chamber along the country rock contact. This is strongly suggested by the distinct break in Sr-Nd isotopic ratios between the main ore layer at the base of the intrusion and the overlying MGZ/LZ. This interpretation suggests that the MZa ore layer is either part of the main ore layer, which did not slump through the MGZ of forms from a later pulse of magma. This can only be resolved by further observations of the main ore layer relationships in the field. 5) Compaction of the Ti-magnetite and entrained silicate grains results in the alignment of plagioclase laths parallel to the footwall contact. Furthermore at this stage distinct reaction rim assemblage will form as a result of silicate-Ti-magnetite interaction at high temperatures. The top contacts will also be gradational as silicates begin to crystallise at temperatures < 1025^{o}C (Figure 9.6 c – path B) from a hybrid magma of mixed characteristics of earlier H_2O poor and later H_2O rich magmas.

For this model to stand it must account for the formation of gabbroic rocks and the oxide-rich gabbros. As described above gabbroic rocks are interpreted to crystallise from H_2O-poor pulses of magma whereas the Fe-Ti oxide ores form as a result of H_2O-rich magma pulses. Oxide-rich gabbroic rocks form as either gradational contacts between ore layers and gabbroic rocks or potentially as a result of an intermediate composition in terms of H_2O and microphenocryst abundance.

10. Conclusions

10.1 Parent magma evolution

Recent work on the layered intrusions from the PANXI region of the ELIP has shown that parent magmas for layered intrusions likely evolved from picritic magma at depth prior to intrusion at their current levels (e.g. Zhang et al. 2009; Bai et al. 2012; Wang et al. 2012). The significant depletion in PGEs of the Panzhihua intrusion relative to typical undepleted high-Ti basalt and picrite allows for detailed modeling of the extent of fractionation at depth in the plumbing system. Modeling presented in this study suggests PGE depletion occurred in both S-saturated and S-undersaturated stages of depletion, which is indicated by high Cu/Pd (sulphide control) and high Pd/Pt (oxide and Pt-alloy control). Two potential scenarios are proposed in order to account for the large scale depletion of PGEs through fractionation and removal of a sulphide liquid at depth beneath the Panzhihua intrusion. This further implies that there may be a PGE sulphide ore deposit at depth related to the plumbing system of the Panzhihua intrusion.

10.2 Formation of the marginal zone (MGZ)

Ganino et al. (2013) recently suggested that carbonate footwall contamination has little effect on Sr-Nd isotopic ratios due to the low concentrations of Sr and Nd of the footwall carbonates. However O-isotopes show that the gabbroic and ore rocks have undergone 8-14 % contamination by footwall carbonates. Sr-Nd isotopic ratios of gabbroic and ore rocks show no evidence of contamination, which is consistent with interpretations of Ganino et al. (2013). However the MGZ microgabbro clearly show enriched Sr-Nd isotope ratios indicating some either minor degree of contamination (5-8 %) at some stage during the evolution of the parent magma or major footwall contamination in situ.

The MGZ of the Panzhihua intrusion is not a chilled margin. The lack of correlation between O-isotopes and Sr-Nd isotopes indicates that contamination has occurred prior to intrusion at the current level. Furthermore the gradational upward change in the Sr-Nd isotopes provides strong evidence for open system formation of the MGZ by prolonged magma emplacement. The MGZ is interpreted to form by multiple pulses of low volume basaltic magma. The upward depletion in incompatible elements is linked to continuous flow of magma along the base of the chamber, which effectively removes evolved interstitial liquid between in situ cumulates. The formation of the MGZ

is terminated by a large volume pulse of magma forming the LZ and later Fe-Ti oxide ore layers. Significant compaction of the MGZ by the sudden increase in volume resulting in significant compaction and recrystallisation of the MGZ cumulates. Recrystallisation significantly reduces the grain size of the earlier formed cumulates of the MGZ. The MGZ forms a thermal insulator to later pulses of magma; i.e. later large volume pulses of magma do not interact with cold country rock footwall. This suggest that models invoking footwall contamination as a mechanism for Fe-Ti oxide ore formation are likely not viable for the Panzhihua intrusion.

10.3 H_2O and fO_2 conditions of parent magma

The H_2O content of the parent magma has been estimated at 0.3-0.5 wt % based on the composition of plagioclase. The relatively low H_2O content is consistent with modeling showing a typical crystallisation sequence observed in the Panzhihua gabbros. This is also consistent with interpretations of Ganino et al. (2008) for low initial H_2O contents for the parent magma.

fO_2 conditions vary significantly within the Panzhihua intrusion. Firstly, clear variation in the Fe_2O_3/TiO_2 ratio, controlled by the occurrence of cumulus ilmenite, suggests that the lower ± 270 m of the intrusion crystallised at higher fO_2 conditions. The dominance of Ti-magnetite over ilmenite in indicates fO_2 conditions significantly greater than FMQ (e.g. Toplis and Carroll, 1995). Secondly, the distinct variation in Ti-magnetite microtextures indicates varying fO_2 between the ores and gabbros, e.g. Buddington and Lindsley (1969). This indicates that ores formed at higher fO_2 relative to the gabbroic rocks of the lower ± 270 m of the intrusion.

10.4 Timing of Fe-Ti oxide crystallisation and silicate consumption

Distinct highly consumed plagioclase and clinopyroxene grains within ore layers clearly indicate that Fe-Ti oxides crystallise after silicates. This key characteristic of the ore layers has been overlooked in numerous recent studies on the Fe-Ti oxide ores of the PANXI region. Silicates are in disequilibrium with a later liquid and become highly consumed as a result. The importance of H_2O has been highlighted several times in this study as it has a significant effect on the stability of plagioclase in a crystallising magma. Reaction products forming around consumed silicates are very similar to those observed in experimental hydrous partial melting studies, e.g. Koepke et al. 2003. Major silicate

consumption at the Panzhihua intrusion is related to intrusion of later stage H_2O-rich liquids incorporating silicates from a partly crystallised sequence of gabbroic cumulates.

10.5 Petrogenesis of Fe-Ti oxide ore layers

A new model is proposed here for the formation of Fe-Ti oxide ore layers at the Panzhihua intrusion by multiple pulses of magma in an open system magma chamber. Initial formation of the LZ gabbroic cumulates form from a parent magma with low H_2O. An influx of new H_2O-rich magma is parental to Fe-Ti oxide ore layers. It has been shown here and in the studies of Pang et al. (2008a) that Ti-magnetite crystallises early for hydrous magmas (> 2 wt %). An influx of H_2O-rich magma effectively erodes the gabbroic cumulate rocks now forming the footwall to the ore layers. Silicates become highly consumed in the H_2O-rich magma. Gradational lower contacts and the presence of gabbroic and microgabbroic xenoliths within ore layers is strong evidence for thermo-chemical erosion and incorporation of footwall gabbroic cumulates. Ti-magnetite likely crystallises at depth either within a staging chamber or en route to the current chamber. This is indicated by the crystallisation depth of 5 kb, indicated by Ti-magnetite composition (Pang et al. 2008a) whereas the footwall rocks of the Panzhihua intrusion have been interpreted to form at depth equivalent to 2 kb. Ti-magnetite crystallisation from a hydrous magma is further supported by analyses of Xing et al. (2012) who showed that Ti-magnetite has significantly higher amounts of primary magmatic H_2O locked in its crystal structure relative to co-existing silicates.

All observations made in this study indicate that Fe-Ti oxide ore layers form by a new pulse of magma into the chamber, which effectively incorporates previously crystallised gabbroic cumulates.

10.6 Applicability to other oxide deposits in the PANXI region

Fe-Ti oxide ores occur in numerous layered intrusion within the PANXI region including: Hongge, Baima, Taihe and Xinjie. Ore layers may be hosted within the lower or upper parts of the intrusions within gabbroic or ultramafic silicate host rocks (Pang et al. 2010). Their occurrence within ultramafic host rocks is not consistent with traditional fractional crystallisation models as Fe-enrichment is typically only achieved in the upper more gabbroic portions of a particular intrusion or as a result of crystallisation from evolved parent magmas (still crystallising gabbroic rocks).

The footwall varies significantly between the intrusions and the model of Ganino et al. (2008) may not be valid for intrusions which do not have footwall carbonate; e.g. Baima. The applicability of this model to the PANXI region as a whole is unlikely to hold up to scrutiny.

Formation of ore layers by either multiple replenishments of H_2O-rich magmas or Fe-immiscible liquids forming at depth and subsequently intruding partly crystallised chambers can account for varied footwall rocks and the variation in stratigraphic occurrence of ore layers. As discussed previously, Fe-immiscible liquids are not likely to have formed at the Panzhihua intrusion. However both the model proposed in this study and the Fe-immiscible model are applicable for the stratigraphic variation of all Fe-Ti oxide ore deposits within the PANXI region. The major concern with the immiscibility model is the complete absence of apatite within the ores, which is generally abundant in oxide ores interpreted to form by Fe-immiscible liquids.

References

Acquafredda, P., Caggianelli, A. and Piccarreta, G. 1992. Late magmatic to subsolidus coronas in gabbroic rocks from the Sila Massif (Calabria Italy). Mineralogy and Petrology, 46, 229-238.

Ali, J. R., Thompson, G. M., Zhou, M-F. and Song, X. 2005. Emeishan large igeous province, SW China. Lithos, 79, 475-489.

Bai, Z-J., Zhong, H., Naldrett, A. J., Zhu, W-G. and Xu, G-W. 2012. Whole-rock and mineral composition constraints on the genesis of the giant Hongge Fe-Ti-V oxide deposit in the Emeishan Large Igneous Province, Southwest China. Economic Geology, 107, 507-524.

Barnes, S-J. and Liu, W. 2012. Pt and Pd mobility in hydrothermal fluids: Evidence from komatiites and from thermodynamic modelling. Ore Geology Reviews. 44, 49-58.

Bateman, A. M. 1951. The formation of late magmatic oxide ores. Economic Geology, 46, 404-426.

Berndt, J., Koepke, J. and Holtz, F. 2005. An experimental investigation of the influence of water and oxygen fugacity on differentiation of MORB at 200 MPa. Journal of Petrology, 46, 135-167.

Barnes, S-J. and Picard, C. P. 1993. The behaviour of platinum-group elements during partial melting, fractional crystallisation, and sulphide segregation: an example from the Cape Smith Fold Belt, northern Quebec. Geochimica et Cosmochimica Acta, 57, 79-87.

Botcharnikov, R. E., Almeev, R. R., Koepke, J. and Holtz, F. 2008. Phase relations and liquid lines of descent in hydrous ferrobasalt- Implications for the Skaergaard intrusion and Columbia river flood basalts. Journal of Petrology, 29, 1687-1727.

Boudreau, A.E. 1999. PELE—a version of the MELTS software program for the PC platform. Computers & Geosciences, 25, 201-203.

Boudreau, A.E., and Meurer, W.P. 1999. Chromatographic separation of the platinum-group elements, gold, base metals and sulfur during degassing of a compacting and solidifying crystal pile. Contributions to Mineralogy and Petrology, 134, 174-185.

Buddington, A. F. And Lindsley, D. H. 1964. Iron-Titanium oxide minerals and synthetic equivalents. Journal of Petrology, 5, 310-357.

Cameron, E. N. 1980. Evolution of the lower critical zone, central sector, eastern Bushveld Complex, and its chromite deposits. Economic Geology, 75, 845-871.

Campbell, I.H. and Turner, J.S. 1989. Fountains in magma chambers. Journal of Petrology, 30, 885-923.

Cawthorn, R. G. and Ashwal, L. D. 2009. Origin of anorthosite and magnetitite layers in the Bushveld Complex, constrained by major element compositions of plagioclase. Journals of Petrology, 50, 1607-1637.

Cawthorn, R. G. and McCarthy, T. S. 1980. Variations in Cr content of magnetite from the upper zone of the Bushveld Complex – evidence for heterogeneity and convection currents in magma chambers. Earth and Planetary Science Letters, 46, 335-343.

Chen, H., Clark, A. H. and Kyser, T. K. 2010. The Marcona magnetite deposit, Ica, south-central Peru: a product of hydrous, iron oxide-rich melts? Economic Geology, 105, 1441-1456.

Chiba, H., Chacko, T., Clayton, R. N. and Goldsmith, J. R. 1989. Oxygen isotope fractionation involving diopside, forsterite, magnetite and calcite: Application to geothermometry. Geochimica et Cosmochimica acta, 53, 2985-2995.

Chung, S-L. and Jahn, B-M. 1995. Plume-lithosphere interaction in generation of the Emeishan flood basalt at the Permian-Triassic boundary. Geology, 23, 889-892.

Cleason, D. T. 1998. Coronas, reaction rims, symplectites and emplacement depth of the Rymmen gabbro, Transscandinavian igneous belt, southern Sweden. Mineralogical Magazine, 62, 743-757.

Delong, S. E. and Chatelain, C. 1990. Trace-element constraints on accessory-phase saturation in evolved MORB magma. Earth and Planetary Science Letters, 101, 206-215.

Dixon, J. E., Leist, L,. Langmuir, C. and Schilling, J. G. 2002. Recycled dehydrated lithosphere observed in plume-influenced mid-ocean-ridge basalt. Nature, 420, 385-389.

Dmitriev, Y. L. and Bogatikov, O. A. 1996. Emeishan flood basalts, Yangtze Platform: indicators of an aborted oceanic environment. Petrology, 4, 407-418.

Duchesne, J. C., Shumlyanskyy, L. and Charlier, B. 2006. The Fedorivka layered intrusion (Korosten Pluton, Ukraine): An example of highly differentiated ferrobasaltic evolution. Lithos, 89, 353-376.

Eales, H. V. and Costin, G. 2012. Crustally contaminated komatiite: Primary source of the chromitites and marginal, lower and critical zone magmas in a staging chamber beneath the Bushveld Complex. Economic Geology, 107, 645-665.

Eales, H. V. 2002. Caveats in defining the magmas parental to the mafic rocks of the Bushveld Complex, and the manner of their emplacement: review and commentary. Mineralogical Magazine, 66, 815-832.

Eales, H. V. 2000. Implications of the chromium budget of the Western limb of the Bushveld Complex. South African Journal of Geology, 103, 141-150.

Eiler, J. M. 2002. Oxygen isotope variations of basaltic lavas and upper mantle rocks. Reviews in Mineralogy and Geochemistry, 43, 319-364.

Egorova, V. and Latypov, R. 2012a. Prolonged magma emplacement as a mechanism for the origin of the marginal reversal of the Fongen-Hyllingen layered intrusion, Norway. Geological Magazine, 5, 909-926.

Egorova, V. and Latypov, R. 2012b. Processes operating during the initial stage of magma chamber evolution: Insights from the marginal reversal of the Imandra layered intrusion, Russia. Journal of Petrology, 53, 3-26.

Ernst, W. G. and Liu, J. 1998. Experimental phase-equilibrium study of Al- and Ti-contents of calcic amphibole in MORB - A semiquantitative thermobarometer. American mineralogist, 83, 952-969.

Ely, J. C. and Neal, C. R. 2003. Using platinum-group elements to investigate the origin of the Ontong Java Plateau, SW Pacific. Chemical Geology, 196, 235-257.

Fagereng, A., Harris, C., La Grange, M and Stevens, G. 2008. Stable isotope study of the Archaean rocks of the Vredefort impact structure, Central Kaapvaal Craton, South Africa. Contributions to Mineralogy and Petrology, 155, 63-78.

Fenner, C. N. 1929. The crystallisation of basalt. American Journal of Science, 18, 225-253.

Fleet, M. E., Crocket, J. H. and Stone, W. E. 1996. Partitioning of platinum-group elements (Os, Ir, Ru, Pt, Pd) and gold between sulphide liquid and basalt melt. Geochimica et Cosmochimica Acta, 60, 2397-2412.

Fleet, M. E. and Pan, Y. 1994. Fractional crystallisation of anhydrous sulphide liquid in the system Fe-Ni-Cu-S, with application to magmatic sulphide deposits. Geochimica et Cosmochimica Acta, 58, 3369-3377.

Fleet, M. E., Stone, W. E. and Crocket, J. H. 1991. Partitioning of palladium, iridium, and platinum between sulphide liquid and basaltic melt: effects of melt composition, concentration, and oxygen fugacity. Geochimica et Cosmochimica Acta, 55, 2545-2554.

Fornoni Candia, M. A., Mazzucchelli, M. and Siena, F. 1989. Sub-solidus reactions and corona structures in the Niquelandia layered complex (Central Goais, Brazil). Mineralogy and Petrology, 40, 17-37.

France, L., Koepke, J., Ildefonse, B., Cichy, S. B. and Deschamps, F. 2010. Hydrous partial melting in the sheeted dike complex at fast spreading ridges: experimental and natural observations. Contributions to Mineralogy and Petrology, 160, 683-704.

Gaillard, F., Pichavant, M. and Scaillet, B. 2003. Experimental determination of activities of FeO and Fe_2O_3 components in hydrous silicic melts under oxidizing conditions. Geochimica et Cosmichimica Acta, 67, 4389-4409.

Ganino, C., Harris, C., Arndt, N.T., Prevec, S.A. and Howarth, G.H. 2013. Assimilation of carbonate country rock by the parent magma of the Panzhihua Fe-Ti-V deposit (SW China): evidence from stable isotopes. Submitted to Geoscience Frontiers, Sept. 2012.

Ganino, C., Arndt, N. T., Zhou, M. –F., Gaillard, F. and Chauvel, C. 2008. Interaction of magma with sedimentary wall rock and magnetite ore genesis in the Panzhihua mafic intrusion, SW China. Mineralium Deposita, 43, 677-694.

Giletti, B. J. 1986. Diffusion effects on oxygen isotope temperatures of slowly cooled igneous and metamorphic rocks. Earth and Planetary Science Letter, 77, 218-228.

Grove, T. L., Elkins-Tanton, L. T., Parman, S. W., Chatterjee, N., Muntener, O. and Gaetani, G. A. 2003. Fractional crystallisation and mantle-melting controls on calc-alkaline differentiation trends. Contributions to Mineralogy and Petrology, 145, 515-533.

Guo, F., Fan, W. M., Wang, Y. and Li, C. 2004. When did the Emeishan mantle plume activity start? Geochronological and geochemical evidence from the ultramafic-mafic dikes in Southwestern China. International Geology Reviews, 46, 226-234.

Harris, C. and Ashwal, L. D. 2002. The origin of low dO18 granites and related rocks from the Seychelles. Contributions to Mineralogy and Petrology, 143, 366-376.

Hatton, C. J. 1984. The effect of pressure, temperature and composition on the distribution of Fe and Mg between olivine, orthopyroxene and liquid: An appraisal of the reversal in the normal fractionation trend in the Bushveld Complex. Contributions to Mineralogy and Petrology, 86, 45-53.

He, B., Xu, Y-G., Huang, X-L., Luo, Z-Y., Shi, Y-R., Tang, Q-J. and Yu, S-Y. 2007. Age duration of the Emeishan flood volcanism, SW China: Geochemistry and SHRIMP zircon U-Pb dating of silicic

ignimbrites, post-volcanic Xuanwei formation and clay tuff at the Chaotian section. Earth and Planetary Science Letter, 255, 306-323.

Hill, R. E. T., Barnes, S.J., Gole, M. J. and Dowling, S. E. 1995. The volcanology of komatiites as deduced from field relationships in the Norseman-Wiluna Greenstone belt, Western Australia. Lithos, 34, 159-188.

Holland, T. and Blundy, J. 1994. Non-deal interactions in calcic amphiboles and their bearing on amphibole-plagioclase thermometry. Contributions to Mineralogy and Petrology, 116, 433-447.

Holness, M. B., Stripp, G., Humphreys, M. C. S., Veksler, I. V., Nielson, T. F. D. And Tegner, C. 2011. Silicate liquid immiscibility within the crystal mush: Late-stage magmatic microstructures in the Skaergaard Intrusion, East Greenland. Journal of Petrology, 52, 175-222.

Hoover, J.D. 1989. The chilled marginal gabbro and other contact rocks of the Skaergaard Intrusion. Journal of Petrology, 30, 441-476.

Hou, T., Zhang, Z., Encarnicion, J. and Santosh, M. 2012. Petrogenesis and metallogenesis of the Taihe intrusion associated with Fe-Ti-oxide ores in the Panxi district, Emeishan Large Igneous Province, southwest China. Ore Geology Reviews, http://dx.doi.org/10.1016/j.oregeorev.2012.09.004

Hunter, R. H. and Sparks, R. S. J. 1987. The differentiation of the Skaergaard Intrusion. Contributions to Mineralogy and Petrology, 95, 451-461.

Iacono-Marziano, G., Gaillard, F. and Pichvant, M. Limestone assimilation by basaltic magmas: an experimental re-assessment and application to Italian volcanoes. Contributions to Mineralogy and Petrology, 155, 719-738.

Jakobsen, J. K. Veksler, I. V., Tegner, C. and Brooks, C. K. 2011. Crystallisation of Skaergaard intrusion from an emulsion of immiscible iron- and silica-rich liquids: evidence from melt inclusions in plagioclase. Journal of Petrology, 52, 345-373.

Keays, R. R. 1995. The role of komatiitic and picritic magmatism and S-saturation in the formation of ore deposits. Lithos, 34, 1-18.

Kirkland, C.L., Spaggiari, C.V., Pawley, M.J., Wingate, M.T.D., Smithies, R.H., Howard, H.M., Tyler, I.M., Belousova, E.A. and Poujol, M. 2011. On the edge: U-Pb, Lu-Hf, and Sm-Nd data suggests reworking of the Yilgarn craton margin during formation of the Albany-Fraser Orogen. Precambrian Research, 187, 223-247.

Kinnaird, J. A., Krugger, F. J., Nex, P. A. M. and Cawthorn, R. G. 2002. Chromitite formation-a key understanding processes of platinum enrichment. Transactions of the Institutions of Mining and Metallurgy, Section B: Applied Earth Science 111, 23-35.

Klemm, D. D., Henckel, J., Dehm, R. and von Gruenewaldt, G. 1985. The geochemistry of titanomagnetite in magnetite layers and their host rocks of the eastern Bushveld Complex. Economic Geology, 80, 1075-1088.

Koepke, J., Feig, S. T. and Snow, J. 2005. Hydrous partial melting within the lower oceanic crust. Terra nova, 17, 286-291.

Koepke, J., Feig, S. T., Snow, J. and Freise, M. 2004. Petrogenesis of oceanic plagiogranites by partial melting of gabbros: an experimental study. Contributions of Mineralogy and Petrology, 146, 414-432.

Koepke, J., Berndt, J. and Bussy, F. 2003. An experimental study on the shallow-level migmatization of ferrogabbros from the Fuerteventura Basal Complex, Canary Islands. Lithos, 69, 105-125.

Lange, R. A. 2002. Constraints on the preeruptive volatile concentrations in the Columbia River flood basalts. Geology, 30, 179-182.

Larikova, T. L and Zaraisky, G. P. 2009. Experimental modelling of corona textures. Journal of Metamorphic Geology, 27, 139-151.

Latypov, R., Hanski, E., Lavrenchuk, A., Huhma, H. and Havela, T. 2011. A 'three-increase model' for the origin of the marginal reversal of the Koitelainen layered intrusion, Finland. Journal of Petrology, 52, 733-764.

Latypov, R., Chistyakova, S. and Alapieti, T. 2007. Revisiting problem of chilled margins associated with marginal reversals in mafic-ultramafic intrusive bodies. Lithos, 99, 178-206.

Latypov, R. 2003. The origin of marginal compositional reversals in basic-ultrabasic sills and layered intrusions by Soret Fractionation. Journal of Petrology, 44, 1579-1618.

Leake, B. E., Woolley, A. R., Arps, C. E. S., Birch, W. D., Gilbert, M. C., Grice, J. D., Hawthorne, F. C., Kato, A., Kisch, H. J., Krivovichev, V. G., Linthout, K., Laird, Jo., Mandarino, J. A., Maresch, W. V., Nickel, E. H., Rocks, N. M. S., Schumacher, J. C., Smith, D. C.,Stephenson, N. C. N., Ungaretti, L., Whittaker, E. J. W. and Youzhi, G. 1998. Nomenclature of amphiboles: report of the subcommittee on amphiboles of the International mineralogical association, commission on new minerals and mineral names. The Canadian mineralogist, 25, 219-246.

Li, C., Tao, Y., Qi, L. And Ripley, E. M. 2012. Controls on PGE fractionation in the Emeishan picrites and basalts: Constraints from integrated lithophile-siderophile elements and Sr-Nd isotopes. Geochimica et Cosmochimica Acta, 90, 12-32.

Li, J., Xu, J-F., Suzuki, K., He, B., Xu, Y-G. and Ren, Z-Y. 2010. Os, Nd and Sr isotope and trace element geochemistry of the Muli picrites: Insights into the mantle source of the Emeishan Large Igneous Province. Lithos, 119, 108-122.

Li, C., Maier, W. D. and de Waal, S. A. 2001. Magmatic Ni-Cu versus PGE deposits: constraining genetic controls and exploration implications. South African Journal of Geology, 104, 205-214.

Lindsley, D. H. 1962. Investigations in the system FeO-Fe_2O_3-TiO_2. Carnige Institute. Washington Yearbook, 61, 100-106.

Lyons, J. L. 1988. Volcanogenic iron oxide deposits, Cerro de Mercado and vicinity, Durango, Mexico. Economic Geology, 83, 1886-1906.

Ma, Y. X., Ji, X. T., Li, J. C., Huang, M. and Min, Z. Z. 2003. Mineral resources of Panzhihua, Sichuan Province, SW China: Chengdu, Chengdu University of Technology (in Chinese).

Maier, W. D., Barnes, S-J.,Gartz, V. and Andrews, G. 2003. Pt-Pd reefs in magnetitites of the Stella layered intrusion, South Africa: A world of new exploration opportunities for platinum group elements. South African Journal of Geology, 31, 885-888.

Maier, W. D. and Barnes, S-J. 1999. Platinum-group elements in silicate rocks of the lower, critical and main zones at the Union Section, western Bushveld Complex. South African Journal of Geology, 102, 286-292.

Mavrogenes, J. A. and O'Neill, H. C. 1999. The relative effects of pressure, temperature and oxygen fugacity on the solubility of sulphide in mafic magmas. Geochimica et Cosmochimica Acta, 63, 1173-1180.

McBirney, A. R. 1996. The Skaergaard Intrusion. In: Cawthorn, R. G. (ed.) Layered Intrusions. Developments in Petrology, 15, 147-180.

McDonough, W.F. and Sun, S. S. 1995. The composition of the earth. Chemical Geology. 120, 223-253.

Mondel, S. K. and Mathez, E. A. 2007. Origin of the UG2 chromitite layer, Bushveld Complex. Journal of Petrology. 48, 495-510.

Morimoto, N., Fabries, J., Ferguson, A. K., Ginzburg, I. V., Ross, M., Seifert, F. A., Zussman, J., Aoki, K. and Gottardi, G. 1988. Nomenclature of pyroxenes. American Mineralogist, 73, 1123-1133.

Naldrett, A. J. 2010. Secular variation of magmatic sulphide deposits and their source magmas. Economic Geology, 105, 669-688.

Namur, O., Charlier, B., Toplis, M. J., Higgins, M.D., Liegeois, J-P. and vander Auwera, J. 2010. Crystallisation sequence and magma chamber processes in the ferrobasaltic Sept Iles layered intrusion, Canada. Journal of Petrology, 51, 1203-1236.

Nicholson, D. M. and Mathez, E. A. 1991. Petrogenesis of the Merensky Reef in the Rustenburg section of the Bushveld Complex. Contributions to Mineralogy and Petrology, 107, 293-309.

O'Driscoll, B., Emeleus, C. H., Donaldson, C. H. and Daly, J. S. 2010. Cr-spinel seam Petrogenesis in the Rum Layered Suite, NW Scotland: cumulate assimilation and in situ crystallisation in a deforming crystal mush. Journal of Petrology, 51, 1171-1201.

O'Driscoll, B., Stevenson, C. T. E. and Troll, V. R. 2008. Mineral lamination development in layered gabbros of the British Palaeogene Igneous Province: A combined anisotropy of magnetic susceptibility, quantitative textural and mineral chemistry study. Journal of Petrology, 49, 1187-1221.

Pang, K.-N, Zhou, M. –F., Liang, Q., Shellnutt, G., Wang, C. Y. and Zhao, D. 2010. Flood basalt-related Fe-Ti oxide deposits in the Emeishan large igneous province, SW China. Lithos, 119, 123-136.

Pang, K. –N., Li, C., Zhou, M. –F. and Ripley, E. M. 2009. Mineral compositional constraints on petrogenesis and oxide ore genesis of the late Permian Panzhihua layered gabbroic intrusion, SW China. Lithos, 110, 199-214.

Pang, K. –W., Zhou, M. F-., Lindsley, D., Zhao, D. and Malpas, J. 2008a. Origin of Fe-Ti oxide ores in mafic intrusions: Evidence from the Panzhihua intrusion, SW China. Journal of Petrology, 49, 295-313.

Pang, K. –N., Li, C., Zhou, M. –F. and Ripley, E. M. 2008b. Abundant Fe-Ti oxide inclusions in olivine from the Panzhihua and Hongge layered intrusions, SW China: evidence for early saturation of Fe-Ti oxides in ferrobasaltic magma. Contributions to Mineralogy and Petrology, 156, 307-321.

Pang, K-N. 2008. Origin of the Permian Panzhihua layered gabbroic intrusion and the hosted Fe-Ti-V oxide deposit, Sichuan Province, SW China. PhD thesis, University of Hong Kong. 303pp.

Philpotts, A. R. 1982. Compositions of immiscible liquids in volcanic rocks. Contributions to mineralogy and petrology, 80, 201-218.

Philpotts, A. R. 1967. The origin of certain iron-titanium oxide and apatite rocks. Economic Geology, 62, 303-315.

Putchel, I. S. and Humayun, M. 2001. Platinum group element fractionation in a komatiitic basalt lava lake. Geochimica et Cosmochimica Acta, 65, 2979-2993.

Reynolds, I. M. 1985a. The nature and origin of titaniferous magnetite-rich layers in the upper zone of the Bushveld Complex: a review and synthesis. Economic Geology, 80, 1089-1108.

Reynolds, I. M. 1985b. Contrasted mineralogy and textural relationships in the uppermost titaniferous magnetite layers of the Bushveld Complex in the Bierkraal area north of Rustenberg. Economic Geology, 80, 1027-1048.

Righter, K., Campbell, A. J., Hunayun, M. and Hervig, R. L. 2004. Partitioning of Ru, Rh, Pd, Re, Ir, and Au between Cr-bearing spinel, Ol, pyroxene and silicate melts. Geochimica et Cosmochimica Acta, 68, 867-880.

Savard, D., Barnes, S.-J. and Meisel, T. 2010. Comparison between nickel-sulfur fire assay Te-co-precipitation and isotope dilution with high-pressure asher acid digestion for the determination of platinum-group elements, rhenium and gold. Geostandards and Geoanalytical Research, 34, 281-291.

Sharp, Z. D. 1991. Determination of oxygen diffusion rates in magnetite from natural isotopic variations. Geology. 19, 653-656.

Shellnutt, J. G. and Pang, K-N. 2012. Petrogenetic implications of mineral chemical data for the Permian Baima igneous complex, SW China. Mineralogy and Petrology, 106, 75-88.

Shellnutt, J. G. and Jahn, B-M. 2010. Formation of the late Permian Panzhihua plutonic-volcanic igneous complex: Implications for the genesis of Fe-Ti oxide deposits and A-type granites of SW China. Earth and Planetary Science Letters, 289, 509-519.

Sisson, T. W. and Grove, T. L. 1993. Experimental investigations of the role of H_2O in calc-alkaline differentiation and sub-duction zone magmatism. Contributions to Mineralogy and Petrology, 113, 73-86.

Song, X-Y., Keays, R. R., Xiao, L. Qi, H-W. and Ihlenfeld, C. 2009. Platinum-group element geochemistry of the continental flood basalts in the central Emeishan Large Igneous Province, SW China. Chemical Geology, 262, 246-261.

Sorensen, H. S. and Wilson, J.R. 1995. A strontium and neodymium isotopic investigation of the Fongen-Hyllingen layered intrusion, Norway. Journal of Petrology, 36, 161-187.

Sparks, R. S. J., Meyer, P. And Sigurdsson, H. 1980. Density variation amongst Mid-Ocean Ridge Basalts-Implications for magma mixing and the scarcity of primitive lavas. Earth and Planetary Science Letters, 46, 419-430.

Synder, D., Carmichael, I. S. E and Wiebe, R. A. 1993. Experimental study of liquid evolution in an Fe-rich, layered mafic intrusion-Constraints on Fe-Ti oxide precipitation on the T-fO2 and T-P paths of tholeiitic magmas. Contributions to Mineralogy and Petrology, 113, 73-86.

Tait, S. and Jaupart, C. 1996. The producing of chemically stratified and adcumulate plutonic igneous rocks. Mineralogical Magazine, 60, 99-114.

Tang, D., Qin, K., Li, C., Qi, L., Su, B. and Qu, W. 2011. Zircon dating, Hf-Sr-Nd-Os isotopes and PGE geochemistry of the Tianyu sulfide-bearing mafic-ultramafic intrusion in the Central Asian Orogenic Belt, NW China. Lithos, 126, 84-98.

Tao, Y. Li, C., Song, X-Y. and Ripley, E. M. 2008. Mineralogical, petrological, and geochemical studies of the Limahe mafic-ultramafic intrusion and associated Ni-Cu sulphide ores, SW China. Mineralium Deposita, 43, 849-872.

Taylor, S. R., McLennan, S. M. 1985. The Continental Crust: its Composition and Evolution. Blackwell Scientific, London.

Toplis, M. J. and Carroll, M. R. 1995. An experimental study of the influence of oxygen fugacity on Fe-Ti oxide stability, phase relations, and mineral-melt equilibria in ferro-basaltic systems. Journal of Petrology, 36, 1137-1170.

Toplis, M. J. and Corgne, A. 2002. An experimental study of element partitioning between magnetite, clinopyroxene and iron-bearing silicate liquids with particular emphasis on vanadium. Contributions to Mineralogy and Petrology, 144, 22-37.

Van Lamoen, H. 1979. Coronas in olivine gabbros and iron ores from Susimaki and Riuttamaa, Finland. Contributions to Mineralogy and Petrology, 68, 259-268.

Von Gruenewaldt, G., Klemm, D. D., Henckel, J. and Dehm, R. M. 1985. Exsolution features in titanomagnetites from massive magnetitite layers and their host rocks of the upper zone, eastern Bushveld Complex. Economic Geology, 80, 1049-1061.

Wager, L. R. and Brown, G. M. 1968. Layered Igneous Rocks. Oliver andBoyd, Edinburgh London, 588pp.

Wang, C. Y., Zhou, M-F., Sun, Y and Arndt, N. T. 2012. Differentiation, crustal contamination and emplacement of the magmas in the formation of the Nantianwan mafic intrusion of the 260 Ma Emeishan large igneous province, SW China. Contributions to Mineralogy and Petrology. DOI 10.1007/s00410-012-0738-4.

Wang, C.Y., Zhou, M-F. and Qi, L. 2010. Origin of extremely PGE-rich mafic magma system: An example from the Jinbaoshan ultramafic sill, Emeishan large igneous province, SW China. Lithos, 119, 147-161.

Wang, C. Y., Zhou, M-F. and Zhao, D. 2008. Fe-Ti-Cr oxides from the Permian Xinjie mafic-ultramafic layered intrusion in the Emeishan large igneous province, SW China: Crystallisation from Fe- and Ti-rich basaltic magmas. Lithos, 102, 198-217.

Wang, C. Y., Zhou, M-F. and Qi, L. 2007. Permian flood basalts and mafic intrusions in the Jinping (SW China) – Song Da (northern Vietnam) district: Mantle sources, crustal contamination and sulphide segregation. Chemical Geology, 243, 317-343.

Wang, C. Y., Zhou, M-F. and Keays, R. R. 2006. Geochemical constraints on the origin of the Permian Baimazhai mafic-ultramafic intrusion, SW China. Contributions to Mineralogy and Petrology, 152, 309-321.

Wignall, P. B. 2001. Large igneous provinces and mass extinctions. Earth-Science Reviews, 53, 1-33.

Willis, J. P. 1999. Instrumental parameters and data quality for routine major and trace element determinations by WDXRFS. University of Cape Town, Cape Town, 11pp.

Xiao, L., Xu, Y. G., Mei, H. J., Zheng, Y. F. He, B. and Pirajno, F. 2004. Distinct mantle sources for low-Ti and high-Ti basalts from the western Emeishan large igneous province, SW China: implications for plume-lithosphere interaction. Earth and Planetary Science Letters, 228, 525-546.

Xiao, L., Xu, Y-G., Chung, S-L., He, B. and Mei, H. 2003 Chemostratigraphic correlation of the upper Permian lavas from Yunnan province, China: Extent of the Emeishan Large Igneous Province. International Geology Review, 45, 756-766.

Xing, C.M., Wang, C.Y., Zhang, M., 2012. Volatile and C-H-O isotopic compositions of giant Fe-Ti-V oxide deposits in the Panxi region and their implications for the source of volatiles and the origin of Fe-Ti oxide ores. Science China Earth Sciences, doi: 10.1007/s11430-012-4468-2.

Xu, Y-G. He, B., Chung, S-L., Menzies, M. A. and Frey, F. A. 2004. Geologic, geochemical, and geophysical consequences of plume involvement in the Emeishan flood-basalt province. Geology, 32, 917-920.

Xu, Y-G., Mei, H.J., Xu, J.F. Huang, X. L. Wang, Y. J. and Chung, S-L. 2003. Origin of two differentiation trends in the Emeishan flood basalts. Chinese Science Bulletin, 48, 390-394.

Xu, Y., Chung, S-L., Jahn, B-M. and Wu, G. 2001. Petrologic and geochemical constraints on the petrogenesis of Permian-Triassic Emeishan flood basalts in southwestern China. Lithos, 58, 145-168.

Zhang, X-Q., Dong, X-Y., Chen, L-M., Xie, W., Yu, S-Y., Zheng, W-Q., Deng, Y-F., Zhang, J-F. and Gui, S-G. 2012. Fractional crystallisation and the formation of thick Fe-Ti-V oxide layers in the Baima

layered intrusion, SW China. Ore Geology Reviews, http://dx.doi.org/10.1016/j.oregeorev.2012.09.003

Zhang, Z., Mao, J., Saunders, A. D., Ai, Y., Li, Y. and Zhao, L. 2009. Petrogenetic modelling of three mafic-ultramafic layered intrusions in the Emeishan large igneous province, SW China, based on isotopic and bulk chemical constraints. Lithos, 113, 369-392.

Zhang, Z., Mahoney, J. J., Mao, J. and Wang, F. 2006. Geochemistry of Picritic and Associated Basalt Flows of the Western Emeishan Flood Basalt Province, China. Journal of Petrology, 47, 1997-2019.

Zhao, Z-F. and Zheng, Y-F. 2002. Calculation of oxygen isotope fractionation in magmatic rocks. Chemical Geology, 193, 59-80.

Zhou, M-F., Chen, W. T., Wang, C. Y., Prevec, S. A. and Howarth, G. H. 2013. Reviews and an integrated model of magmatic Fe-Ti-V oxide deposits in the Emeishan Large Igneous Province, SW China and Northern Vietnam. Geoscience Frontiers.

Zhou, M-F., Arndt, N. T., Malpas, J., Wang, C. Y. and Kennedy, A. K. 2008. Two magma series and associated ore deposit types in the Permian Emeishan large igneous province, SW China. Lithos, 103, 352-368.

Zhou, M. –F., Robinson, P. T., Lesher, C. M., Keays, R. R., Zhang, C. –J. and Malpas, J. 2005. Geochemistry, Petrogenesis and Metallogenesis of the Panzhihua gabbroic layered intrusion and associated Fe-Ti-V oxide deposits, Sichuan Province, SW China. Journal of Petrology, 46, 2253-2280.

Zhou, M-F., Malpas, J., Song, X-Y., Robinson, P. T., Sun, M., Kennedy, A. K., Lesher, C. M. and Keays, R. R. 2002. A temporal link between the Emeishan large igneous province (SW China) and the end-Giadalupian mass extinction. Earth and Planetary Science Letters, 196, 113-122.

Zhong, H. and Zhu, W-G. 2006. Geochronology of layered mafic intrusions from the Pan-Xi area in the Emeishan large igneous province, SW China. Mineralium Deposita, 41, 599-606.

Zhong, H., Yao, Y., Prevec, S. A., Wilson, A. H., Viljoen, M. J., Viljoen, R. P., Liu, B-G. and Luo, T-N. 2004. Trace-element and Sr-Nd isotopic geochemistry of the PGE-bearing Xinjie layered intrusion in SW China. Chemical Geology, 203, 237-252.

Appendix A. GPS data for sample sites from the Jianshan Block and Nalaqing Block

Location	GPS Co-ordinate
Bench transect start (PH-BT-01)	N 26°36’56.1’’ E 101°43’22.9’’
Gravel Site (PH-BT-55)	N 26°37’07.1’’ E 101°43’37.3’’
Look-out road transect end (PH-BT-62)	N 26°36’10.7’’ E 101°43’31.7’’
Road Cut Site 1	N 26°38’20.3’’ E 101°43’23.7’’
Road Cut Site 2	N 26°38’03.0’’ E 101°43’24.4’’
Road Cut Site 3	N 26°37’45.1’’ E 101°43’27.9’’
Road Cut Site 4	N 26°37’43.2’’ E 101°43’28.8’’
Road Cut Site 5	N 26°37’39.3’’ E 101°43’29.5’’
Road Cut Site 6	N 26°37’33.3’’ E 101°43’27.7’’
Road Cut Site 7	N 26°37’31.8’’ E 101°43’26.9’’
Road Cut Site 8	N 26°37’28.8’’ E 101°43’26.1’’
PH-RC Samples	N 26°37’30.5’’ E 101°43’35.8’’
RC end	N 26°37’26.3’’ E 101°43’30.8’’
Nalaqing Block Sample Site	N 26°33’01.5’’ E 101°40’49.1’’

Appendix B. Whole-rock major and trace element geochemical data

	Main Ore	Main Ore	Main Ore	Main Ore	Main Ore	Main Ore	Main Ore	Main Ore	Main Ore	Main Ore
Height (m)	8	10	16	23	35	41	44	50	54	60
Sample	05_1	05_2	05_3	05_4	05_6	05_7	05_7/8	05_8	05_9	05_10
SiO_2	38.523	16.059	14.692	4.473	5.686	10.854	6.850	9.964	43.491	18.337
TiO_2	4.601	11.076	12.430	15.268	14.907	13.352	14.657	13.313	3.303	11.235
Al_2O_3	12.419	6.532	6.469	5.033	5.486	6.247	5.615	6.323	14.483	7.469
Fe_2O_3	22.958	54.473	55.412	69.569	68.688	60.703	66.713	61.324	15.889	49.602
MnO	0.189	0.335	0.343	0.376	0.364	0.347	0.369	0.336	0.156	0.331
MgO	6.162	5.250	5.680	5.276	4.932	5.662	4.959	5.509	5.731	6.035
CaO	12.233	5.479	4.893	1.068	1.714	3.282	2.124	2.992	12.602	6.029
Na_2O	2.032	0.589	0.689	0.358	0.256	0.687	0.420	0.634	2.615	0.964
K_2O	0.246	0.038	0.040	0.006	0.009	0.058	0.004	0.028	0.407	0.086
P_2O_5	0.069	0.056	0.033	0.030	0.016	0.038	0.014	0.028	0.104	0.028
SO_3	0.201	0.240	0.002	0.094	0.001	0.077	0.052	0.033	0.323	0.055
Cr_2O_3	0.003	0.025	0.023	0.020	0.020	0.017	0.023	0.017	0.003	0.013
NiO	0.013	0.062	0.091	0.021	0.023	0.025	0.025	0.022	0.008	0.018
H_2O-	0.096	0.069	0.067	0.075	0.072	0.027	0.030	0.087	0.044	0.036
LOI	-0.072	-1.234	-1.427	-1.739	-2.400	-1.530	-1.980	-0.886	0.331	-1.154
Total	99.671	99.048	99.438	99.931	99.775	99.846	99.877	99.725	99.492	99.084
Mg#	34.27	15.77	16.61	12.84	12.24	15.34	12.62	14.86	41.21	19.12
Li	3.59	1.28	1.74	0.77	0.64	1.25	0.97	1.19	3.89	2.06
Sc	32.5	22.2	22.5	16.6	15.3	18.4	17.7	17.4	28.8	23.7
V	745	2062	2126	2823	2762	2442	2625	2515	485	2001
Cr	3.52	3.63	3.82	18.1	34.8	7.77	14.1	8.90	6.08	7.06
Co	74.7	181	179	223	216	196	216	205	61.3	173
Ni	82.8	276	240	164	149	179	142	173	45.3	140
Cu	107	414	184	0.7	0.7	0.7	0.7	0.7	40.6	0.7
Zn	160	320	372	450	434	393	446	405	113	332
Rb	3.90	0.88	0.78	0.87	1.20	1.44	1.16	1.91	6.34	1.09
Sr	488	151	142	30.6	54.3	126	96.1	128	607	204
Y	8.39	4.00	3.60	1.89	1.31	2.68	1.58	2.30	10.9	4.07
Zr	35.7	21.7	26.2	21.7	19.4	23.1	19.7	21.1	48.0	22.0
Nb	4.88	6.52	4.36	4.06	3.80	3.87	3.60	3.93	5.61	3.70
Ba	140	24.7	26.2	14.8	13.5	28.3	15.6	28.0	230	41.8
La	4.81	2.45	1.24	1.25	0.64	1.29	0.65	1.26	1.40	14.5
Ce	11.7	5.29	3.48	2.91	1.63	3.20	1.69	3.12	3.89	35.9
Pr	1.64	0.73	0.57	0.42	0.25	0.48	0.26	0.46	0.64	5.04
Nd	7.97	3.69	3.02	2.01	1.23	2.40	1.36	2.26	3.47	23.4
Sm	2.18	1.02	0.91	0.51	0.34	0.67	0.38	0.62	1.06	5.84
Eu	1.10	0.46	0.43	0.20	0.17	0.33	0.20	0.29	0.51	1.98
Tb	0.35	0.16	0.15	0.08	0.05	0.11	0.07	0.10	0.17	0.92
Gd	2.51	1.16	1.06	0.56	0.39	0.77	0.48	0.68	1.22	6.12
Dy	2.00	0.95	0.87	0.45	0.32	0.62	0.39	0.54	0.97	5.21
Ho	0.36	0.17	0.15	0.08	0.06	0.11	0.07	0.10	0.17	0.97
Er	0.91	0.44	0.38	0.20	0.15	0.30	0.17	0.25	0.42	2.49
Tm	0.11	0.06	0.05	0.03	0.02	0.04	0.02	0.03	0.05	0.34
Yb	0.65	0.32	0.29	0.15	0.11	0.23	0.14	0.18	0.31	1.97
Lu	0.09	0.05	0.04	0.02	0.02	0.03	0.02	0.03	0.04	0.31
Hf	1.10	0.77	0.87	0.72	0.70	0.79	0.68	0.74	1.43	0.74
Ta	0.18	0.24	0.28	0.26	0.26	0.26	0.27	0.26	0.28	0.25
Pb	1.78	3.00	1.06	0.75	0.61	0.38	0.27	0.73	2.82	0.39
Th	0.92	0.36	0.08	0.10	0.05	0.10	0.05	0.09	1.19	0.08
U	0.55	0.28	0.04	0.03	0.02	0.03	0.02	0.02	0.46	0.56

	MGZ/LZ	MGZ/LZ	MGZ/LZ	MGZ/LZ	MGZ/LZ	MGZ/LZ	MGZ/LZ	MGZ/LZ	MGZ/LZ
Height (m)	100	115	137	138	139	140	141	142	143.8
Sample	BT-01	BT-02	BT03 A	BT-03 B	BT-03 C	BT-03 X	BT-03 D	BT-03 E	BT-03 f
SiO_2	42.598	40.82	46.750	44.779	42.792	43.182	4.634	35.038	22.665
TiO_2	2.556	4.35	2.407	2.774	1.600	1.802	15.819	6.071	10.105
Al_2O_3	13.153	11.20	20.025	11.620	6.623	7.337	4.697	11.317	8.516
Fe_2O_3	14.463	20.66	10.522	15.777	17.259	16.382	71.038	27.806	44.650
MnO	0.192	0.21	0.101	0.186	0.236	0.227	0.404	0.234	0.302
MgO	7.776	6.95	2.988	8.375	18.981	17.742	3.736	6.704	5.876
CaO	15.717	12.39	10.652	13.091	11.460	11.775	1.524	9.747	6.746
Na_2O	1.853	1.81	3.884	2.144	0.850	1.196	0.251	1.579	0.875
K_2O	0.277	0.69	0.557	0.317	0.020	0.043	0.013	0.740	0.383
P_2O_5	0.180	0.33	0.139	0.094	0.017	0.020	0.008	0.068	0.027
SO_3	0.127	0.07	0.280	0.267	0.016	0.082	0.001	0.100	0.225
Cr_2O_3	0.029	0.01	0.002	0.045	0.258	0.250	0.022	0.006	0.011
NiO	0.013	0.01	0.003	0.019	0.099	0.085	0.025	0.013	0.014
H_2O-	0.051	0.11	0.069	0.058	0.032	0.047	0.007	0.058	0.049
LOI	0.951	0.47	1.047	0.261	-0.602	-0.329	-2.425	0.212	-0.686
Total	99.937	100.07	99.425	99.808	99.641	99.841	99.754	99.691	99.759
Mg#	51.09	39.54	35.56	50.77	68.12	67.79	9.27	31.90	20.36
Li	7.22	4.32	3.83	2.25	2.04	2.55	0.76	3.04	2.37
Sc	36.8	34.6	15.8	39.4	28.0	26.9	15.6	35.2	27.2
V	334	642	283	435	310	296	2886	931	1674
Cr	184	8.97	4.38	291	1835	1624	37.2	10.3	13.7
Co	44.1	62.6	33.7	55.4	91.3	81.5	210	92	135
Ni	85.7	56.9	19.6	145	769	628	194	88.3	110
Cu									
Zn	128	141	82.4	119	119	114	471	214	317
Rb	4.87	16.4	9.6	5.78	0.46	1	0.66	17	8.17
Sr	674	616	996	524	192	230	41.8	688	323
Y	19.5	13.9	7.59	12.1	8.51	9.71	1.04	9.44	5.38
Zr	65.9	52.1	42.0	44.4	17.2	30.1	29.8	39.6	35.1
Nb	7.75	6.63	4.71	3.86	0.42	0.70	5.63	4.20	4.52
Ba	184	372	268	183	28.0	33.5	11.5	429	206
La	9.77	9.96	7.74	6.51	1.47	1.48	0.44	3.94	1.70
Ce	27.6	23.6	16.6	15.8	4.99	5.00	1.07	10.5	4.61
Pr	4.10	3.18	2.05	2.21	0.94	0.95	0.16	1.58	0.75
Nd	19.7	14.8	8.77	10.5	5.76	5.52	0.91	7.88	4.32
Sm	4.81	3.57	1.93	2.70	1.93	1.85	0.26	2.12	1.28
Eu	1.70	1.48	1.24	1.24	0.77	0.84	0.12	1.03	0.62
Tb	0.69	0.54	0.28	0.44	0.31	0.35	0.04	0.36	0.20
Gd	4.85	3.90	2.03	3.10	2.20	2.33	0.30	2.56	1.45
Dy	4.09	3.01	1.59	2.55	1.90	2.09	0.24	2.10	1.21
Ho	0.74	0.53	0.29	0.47	0.33	0.39	0.04	0.37	0.21
Er	2.00	1.35	0.75	1.20	0.85	1.00	0.11	0.95	0.54
Tm	0.26	0.17	0.10	0.15	0.10	0.13	0.01	0.12	0.07
Yb	1.63	1.01	0.62	0.96	0.62	0.82	0.10	0.71	0.40
Lu	0.23	0.14	0.09	0.14	0.08	0.12	0.02	0.10	0.06
Hf	2.21	1.51	1.22	1.35	0.78	1.12	0.85	1.20	0.98
Ta	0.49	0.39	0.29	0.20	0.03	0.05	0.39	0.28	0.31
Pb	1.50	2.07	2.79	1.91	0.59	0.67	0.55	1.23	1.00
Th	1.62	0.77	0.86	0.49	0.06	0.06	0.05	0.33	0.15
U	0.41	0.29	0.20	0.13	0.02	0.02	0.05	0.11	0.09

	MZa 146.9	MZa 150	MZa 160.8	MZa 160	MZa 170.24	MZa 180.37	MZa 190.49	MZa 200.61	MZa 210.73	MZa 220.85	MZa 230.98	MZa 241.1
Height (m)	BT-04	BT-05	BT-06A	BT-06B	BT-07	BT-08	BT-09	BT-10	BT-11	BT-12	BT-13	BT-14
Sample	2.921	11.699	31.64	4.05	44.94	31.124	11.91	35.55	45.08	42.589	40.03	36.679
SiO_2	15.765	12.768	7.20	15.97	3.29	7.021	13.09	5.06	2.37	2.923	3.95	4.604
TiO_2	4.757	6.440	15.67	4.86	15.19	8.616	7.88	13.96	19.56	19.318	14.16	12.924
Al_2O_3												
Fe_2O_3	72.156	61.759	32.25	72.08	14.52	33.447	58.66	26.49	11.94	14.660	20.69	23.613
MnO	0.385	0.343	0.21	0.43	0.17	0.257	0.36	0.18	0.13	0.112	0.17	0.174
MgO	5.049	4.844	3.67	4.25	5.48	7.784	4.50	5.41	3.86	4.277	6.16	7.223
CaO	0.846	3.509	8.16	0.83	12.93	10.859	3.92	10.86	13.53	12.760	12.89	12.280
Na_2O	0.230	0.532	2.04	0.43	2.18	1.171	0.81	1.70	2.42	2.646	1.66	1.608
K_2O	-0.004	0.016	0.17	0.04	0.25	0.062	0.09	0.15	0.26	0.153	0.14	0.104
P_2O_5	0.016	0.016	0.06	0.04	0.11	0.040	0.02	0.03	0.09	0.068	0.04	0.024
SO_3	0.049	0.073	0.03	0.05	0.06	0.098	0.07	0.06	0.06	0.102	0.06	0.039
Cr_2O_3	0.025	0.027	0.02	0.05	0.02	0.010	0.04	0.02	0.02	0.005	0.02	0.054
NiO	0.026	0.041	0.01	0.03	0.01	0.010	0.01	0.01	0.02	0.006	0.01	0.019
H_2O-	0.015	0.021	0.06	0.01	0.06	0.041	0.04	0.05	0.05	0.035	0.07	0.037
LOI	-2.534	-2.104	-1.22	-3.57	0.17	-0.636	-1.71	0.06	0.78	0.037	0.07	0.023
Total	99.703	99.984	99.97	99.55	99.37	99.904	99.67	99.59	100.16	99.691	100.09	99.404
Mg#	11.97	13.22	18.13	10.28	42.31	31.14	12.96	28.41	38.59	36.18	36.64	37.28
Li	0.67	0.84		0.38	2.16	1.29	0.61	1.92	3.07	1.53	0.89	3.07
Sc	17.4	21.3		14.5	32.7	26.6	19.9	30.0	23.5	26.1	39.4	41.5
V	2859	2341		2945	408	1181	2255	947	364	494	681	951
Cr	18.1	20.6		16.4	4.56	12.5	10.7	7.38	24.4	15.1	9.54	320
Co	226	212		231	54.3	134	182	114	43.9	55.6	87.7	85.6
Ni	175	165		114	16.8	70.7	67.9	61.8	58.2	22.8	40.3	128
Cu												
Zn	465	376		482	90.1	228	371	157	78.1	97.0	120	140
Rb	0.4	0.32		0.3	3.14	1	0.75	1.61	3.59	2.31	1.32	2.07
Sr	23.70	142		22.50	673	261.0	205	576	711	679	503	437
Y	1.26	2.31		1.28	8.59	8.01	2.06	5.10	5.90	5.94	6.84	6.20
Zr	23.8	20.1		39.4	26.0	25.6	20.2	17.0	24.2	21.5	20.1	17.5
Nb	4.05	3.85		4.90	3.50	2.69	3.32	1.80	2.75	2.43	1.68	1.27
Ba	10.8	21.9		9.08	121	46.4	33.1	74.4	97.7	92.8	66.1	61.2
La	0.66	0.77		0.50	3.76	2.05	0.71	1.72	3.53	3.20	2.06	1.67
Ce	1.58	2.10		1.20	9.90	6.18	1.90	4.59	8.55	7.78	5.70	4.60
Pr	0.22	0.34		0.17	1.51	1.06	0.30	0.73	1.20	1.11	0.93	0.80
Nd	1.04	1.85		0.83	7.84	6.00	1.63	4.02	5.80	5.53	5.07	4.54
Sm	0.26	0.54		0.21	2.15	1.85	0.48	1.18	1.48	1.45	1.51	1.43
Eu	0.12	0.29		0.10	1.18	0.87	0.28	0.72	0.91	0.89	0.87	0.73
Tb	0.04	0.09		0.04	0.33	0.32	0.08	0.20	0.23	0.23	0.27	0.24
Gd	0.29	0.64		0.25	2.43	2.24	0.57	1.43	1.65	1.68	1.91	1.75
Dy	0.26	0.53		0.23	1.91	1.84	0.47	1.17	1.31	1.34	1.55	1.43
Ho	0.05	0.10		0.05	0.34	0.32	0.08	0.20	0.23	0.24	0.27	0.25
Er	0.13	0.24		0.15	0.84	0.80	0.21	0.51	0.58	0.58	0.68	0.62
Tm	0.02	0.03		0.02	0.10	0.10	0.03	0.06	0.07	0.07	0.08	0.08
Yb	0.14	0.17		0.18	0.60	0.58	0.15	0.36	0.41	0.42	0.47	0.44
Lu	0.02	0.03		0.03	0.08	0.08	0.02	0.05	0.06	0.06	0.07	0.06
Hf	0.75	0.70		1.03	0.88	0.97	0.65	0.64	0.73	0.73	0.75	0.72
Ta	0.30	0.30		0.36	0.24	0.20	0.24	0.13	0.18	0.17	0.12	0.09
Pb	0.77	0.93		0.11	0.43	0.58	0.21	0.53	1.22	0.97	0.82	0.56
Th	0.07	0.05		0.09	0.22	0.10	0.05	0.07	0.23	0.22	0.11	0.08
U	0.02	0.02		0.03	0.05	0.02	0.02	0.02	0.06	0.05	0.03	0.02

	MZa	MZa	MZa	MZa	MZa	MZa	MZa	MZa	MZa	MZa	MZa	MZa
Height (m)	251.22	261.34	265	271.46	271.6	281.585	311.95	322.07	322.3	332.2	336	342.32
Sample	BT-15	BT-16	BT-17	BT-19A	BT-19B	BT-20	BT-23	BT-24	BT-25	BT-26	BT-27	BT-29
SiO_2	47.74	42.587	10.15	41.90	13.26	42.699	28.23	57.858	33.77	40.918	14.60	41.60
TiO_2	1.15	2.312	11.47	2.53	11.29	3.056	8.33	0.507	6.41	4.020	12.84	4.14
Al_2O_3	20.45	24.122	9.93	22.05	7.79	17.555	10.69	19.257	10.91	12.939	6.86	17.40
Fe_2O_3	6.84	11.852	59.47	15.55	57.09	15.923	36.69	4.587	29.59	18.042	52.26	17.09
MnO	0.10	0.066	0.29	0.09	0.31	0.121	0.26	0.044	0.25	0.180	0.38	0.16
MgO	4.46	2.097	4.94	2.01	6.21	4.672	5.77	1.774	6.96	7.090	6.52	4.16
CaO	14.80	12.219	3.45	10.82	4.59	12.044	8.75	6.387	10.99	13.062	6.13	11.54
Na_2O	2.48	3.522	0.85	2.25	0.66	2.773	1.20	7.433	1.37	2.075	0.74	2.58
K_2O	0.44	0.234	0.07	0.19	0.06	0.208	0.11	0.061	0.13	0.101	0.06	0.19
P_2O_5	0.11	0.154	0.04	0.06	0.03	0.033	0.02	0.170	0.04	0.058	0.03	0.05
SO_3	0.09	0.052	0.06	0.15	0.05	0.314	0.07	0.002	0.06	0.174	0.06	0.08
Cr_2O_3	0.01	0.005	0.07	0.04	0.09	0.001	0.02	0.006	0.03	0.003	0.04	0.02
NiO	0.01	0.006	0.06	0.10	0.04	0.001	0.01	0.002	0.01	0.002	0.03	0.01
H_2O-	0.09	0.040	0.03	0.06	0.01	0.030	0.03	0.096	0.04	0.054	0.02	0.02
LOI	1.27	0.659	-1.58	1.79	-1.21	0.230	-0.18	1.802	-0.42	0.662	-0.99	0.72
Total	100.03	99.926	99.29	99.59	100.28	99.659	99.99	99.987	100.13	99.380	99.56	99.74
Mg#	55.92	25.59	13.88	20.10	17.44	36.31	23.39	42.90	31.37	43.30	19.51	32.09
Li	2.20	3.56	0.62		0.65	4.11	1.19	0.26	0.96	1.66	0.68	1.66
Sc	27.1	9.91	15.8		23.7	26.1	27.4	13.0	33.7	37.9	28.9	21.6
V	179	437	2597		2242	468	1299	73.9	1000	585	1879	525
Cr	10.8	26.6	238		331	4.68	34.6	41.4	41.1	10.9	35.1	29.7
Co	27.8	40.0	215		233	57.1	131	11.7	108	63.0	182	58.8
Ni	34.3	29.0	291		220	< 75 ppb	37.0	3.98	24.7	< 40 ppb	42.8	< 75 ppb
Cu												
Zn	31.3	77.4	310		302	120	254	50.5	184	121	319	122
Rb	4.86	3.19	0.44		0.63	3	0.94	1.86	1.42	1.56	0.42	1.98
Sr	725	830	204		148	660	374	350	378	439	161	683
Y	7.22	5.12	0.91		2.30	5.71	4.79	27.5	7.02	9.30	3.82	5.46
Zr	23.1	21.1	12.3		13.4	21.9	17.6	13.9	23.2	25.3	19.8	19.9
Nb	1.83	2.34	1.90		1.64	1.72	1.91	7.23	2.36	2.21	2.83	2.31
Ba	121	120	23.3		19.6	143	40.1	71.1	56.4	64.6	18.1	109
La	4.21	4.91	0.73		0.65	2.97	1.23	41.9	2.06	2.93	0.70	2.62
Ce	10.2	11.4	1.61		1.85	7.25	3.54	84.8	5.75	8.22	2.18	6.07
Pr	1.49	1.53	0.22		0.31	1.03	0.60	8.55	0.97	1.37	0.40	0.90
Nd	7.31	6.97	1.04		1.76	5.12	3.41	32.2	5.44	7.56	2.40	4.69
Sm	1.87	1.51	0.25		0.54	1.36	1.07	5.84	1.68	2.24	0.79	1.28
Eu	0.92	0.82	0.17		0.26	0.84	0.60	1.36	0.80	1.06	0.41	0.87
Tb	0.28	0.19	0.04		0.09	0.23	0.19	0.80	0.27	0.36	0.15	0.22
Gd	2.01	1.49	0.26		0.63	1.60	1.35	5.35	1.94	2.60	1.05	1.56
Dy	1.61	1.11	0.21		0.52	1.30	1.09	4.87	1.59	2.13	0.88	1.23
Ho	0.28	0.20	0.04		0.09	0.23	0.20	0.95	0.28	0.37	0.16	0.22
Er	0.70	0.49	0.09		0.23	0.57	0.48	2.72	0.69	0.92	0.39	0.54
Tm	0.09	0.06	0.01		0.03	0.07	0.06	0.37	0.08	0.11	0.05	0.06
Yb	0.51	0.36	0.08		0.17	0.43	0.34	2.42	0.50	0.65	0.29	0.40
Lu	0.07	0.05	0.01		0.02	0.06	0.05	0.34	0.07	0.09	0.04	0.06
Hf	0.75	0.59	0.42		0.51	0.71	0.66	0.60	0.85	0.94	0.73	0.65
Ta	0.12	0.15	0.15		0.13	0.11	0.15	0.41	0.17	0.16	0.24	0.17
Pb	3.91	1.50	0.96		2.06	6.15	0.94	11.6	1.07	1.18	0.61	1.27
Th	0.31	0.38	0.06		0.04	0.29	0.06	8.79	0.12	0.16	0.03	0.15
U	0.07	0.10	0.02		0.01	0.06	0.01	1.54	0.03	0.04	0.01	0.03

	MZa	MZa	MZa	MZa	MZa	MZa	MZa	MZa	MZa	MZa	MZa	MZa
Height (m)	352.44	362.56	372.68	382.8	392.93	403.05	423.29	433.41	494.15	500	544.9	565
Sample	BT-30	BT-31	BT-32	BT-33	BT-34	BT-35	BT-37	BT-38	BT-45	BT-48	BT-53	BT-55
SiO_2	24.80	38.25	36.31	34.47	37.14	36.89	38.24	39.79	39.28	24.96	37.33	42.88
TiO_2	11.95	7.36	7.06	9.38	7.72	7.78	7.39	5.77	6.64	9.49	7.33	5.00
Al_2O_3	10.31	11.48	13.75	11.11	11.80	11.63	12.08	13.17	11.79	4.48	10.54	15.15
Fe_2O_3	36.16	20.91	24.54	25.43	22.87	23.74	21.95	17.82	19.91	32.65	22.44	15.63
MnO	0.30	0.21	0.21	0.23	0.22	0.24	0.23	0.20	0.23	0.37	0.26	0.17
MgO	6.26	7.58	5.59	6.75	6.45	6.49	6.62	6.22	7.00	10.26	7.57	5.66
CaO	8.95	12.29	10.89	11.27	11.71	11.73	12.08	12.24	12.97	12.74	12.44	12.82
Na_2O	1.35	1.52	1.83	1.49	1.88	1.59	1.65	2.28	1.77	0.68	1.58	2.22
K_2O	0.11	0.10	0.13	0.10	0.13	0.11	0.10	0.12	0.12	0.04	0.11	0.14
P_2O_5	0.04	0.04	0.03	0.03	0.03	0.05	0.03	0.03	0.02	4.84	0.04	0.03
SO_3	0.07	0.06	0.06	0.06	0.11	0.06	0.05	0.31	0.08	0.22	0.08	0.08
Cr_2O_3	0.04	0.02	0.02	0.02	0.02	0.01	0.02	0.02	0.02	0.02	0.02	0.01
NiO	0.01	0.00	0.01	0.01	0.00	0.01	0.00	0.00	0.00	0.04	0.00	0.00
H_2O-	0.02	0.02	0.01	0.03	0.08	0.06	0.09	0.05	0.01	0.00	0.00	0.03
LOI	-0.86	-0.46	-0.61	-0.78	-0.24	-0.57	-0.45	1.78	-0.26	-1.13	-0.24	0.29
Total	99.50	99.38	99.82	99.60	99.91	99.81	100.07	99.79	99.58	99.66	99.51	100.12
Mg#	25.17	41.31	30.68	34.02	35.41	34.69	36.93	40.40	40.61	37.90	39.60	41.30
Li	0.98				1.54			1.81				
Sc	31.5	33.7	26.5	33.7	32.0	30.2	29.9	30.3	32.4	28.3	33.2	26.9
V	1167	610.9	838.4	830.7	638	706.3	627.1	481	556.7	440.6	626	444.8
Cr	17.7	19.7	26	29.1	4.34	16.2	16.8	2.18	16.6	27.8	17	27.7
Co	136	86.4	101.3	103.3	77.9	86.5	79.4	55.4	71	80.9	85.9	61.6
Ni	17.1				40			40				
Cu												
Zn	227				151			118				
Rb	0.84	1	1.5	1	0.97	1	0.9	1.74	0.6	0.3	1.3	1
Sr	370	528.6	673.7	526.4	470	585.6	595.8	523	600.6	424.3	499.1	756.6
Y	4.74	8.3	6.5	8	6.98	7.4	9.1	7.03	9.7	53.5	8.6	6.7
Zr	25.7	27.3	22.7	29.5	23.1	22.7	23.5	20.4	24.9	23.1	26.4	19.4
Nb	5.70	7.6	5.1	8.6	6.47	5.9	6.7	4.04	4.3	8.7	5.6	4.3
Ba	42.0	71	89.9	72.6	55.3	75.6	71.1	63.2	78.5	31.4	64.1	95.8
La	1.06				1.92			1.59				
Ce	3.12	9.2	9.8	8.6	4.43	10.1	4.3	4.65	11.5	116.1	9.5	6.9
Pr	0.56				0.82			0.85				
Nd	3.29	9.1	7.3	7.2	4.97	7.1	5.2	5.09	9.6	100.1	7.2	6.6
Sm	1.07				1.65			1.66				
Eu	0.59				0.90			0.96				
Tb	0.18				0.28			0.28				
Gd	1.30				1.98			1.99				
Dy	1.08				1.63			1.62				
Ho	0.19				0.28			0.28				
Er	0.48				0.70			0.70				
Tm	0.06				0.08			0.08				
Yb	0.35				0.48			0.48				
Lu	0.05				0.07			0.07				
Hf	0.91				0.88			0.76				
Ta	0.53				0.50			0.34				
Pb	0.43	0.9	0.6	-0.8	0.53	1	-1.6	0.52	1.5	-2.5	1.1	3.4
Th	0.05	3.6	0.5	3.4	0.04	3.3	0.3	0.03	0.1	-2.7	3.2	0.1
U	0.01	-2.1	0.4	2.2	0.01	0.6	0.5	0.01	-0.6	2.8	0.3	-1

	MZb	MZb	MZb	MZb	MZb	MZb	MZb	MZb	MZb
Height (m)	1090	1051.6	999.2	946.8	789.6	737.2	684.8	632.4	580
Sample	BT-63	BT-64	BT-65	BT-66	BT-69	BT-70	BT-71	BT-72	BT-73
SiO_2	44.72	40.54	47.62	42.36	27.32	43.91	52.72	48.68	48.09
TiO_2	3.78	4.52	2.78	4.22	8.80	3.53	0.82	1.95	1.93
Al_2O_3	13.62	8.66	20.26	15.43	5.16	17.54	24.85	21.40	21.32
Fe_2O_3	18.74	26.17	8.65	14.37	31.98	10.95	3.51	6.54	5.99
MnO	0.35	0.75	0.12	0.22	0.37	0.15	0.06	0.10	0.09
MgO	4.19	4.85	3.24	5.35	11.18	3.78	1.65	2.41	2.14
CaO	9.39	10.30	11.13	11.86	11.49	12.26	7.18	10.65	12.00
Na_2O	3.54	2.70	3.81	3.13	0.86	3.30	4.33	4.26	3.73
K_2O	0.17	0.22	0.18	0.18	0.05	0.26	2.27	0.13	0.60
P_2O_5	1.87	2.41	1.50	2.38	3.96	1.99	0.28	1.03	0.95
SO_3	0.07	0.08	0.11	0.14	0.15	0.16	0.07	0.07	0.13
Cr_2O_3	0.01	0.01	0.01	0.01	0.02	0.01	0.01	0.01	0.01
NiO	0.00	0.01	0.00	0.01	0.01	0.00	0.00	0.00	0.00
H_2O-	0.03	0.01	0.01	0.01	0.02	0.09	0.01	0.05	0.03
LOI	-0.36	-1.27	0.51	0.05	-1.20	1.80	1.46	1.95	2.33
Total	100.12	99.96	99.94	99.71	100.16	99.73	99.22	99.24	99.35
Mg#	30.30	26.49	42.14	41.96	40.44	40.16	47.71	41.70	40.98
Li									
Sc	41.6	61.1	8.1	18.1	25.9	10.9	3	5.3	4
V	45.4	52.9	78.6	139.5	412.6	119.2	27.8	53.2	51.1
Cr	19	21.1	11.7	14.9	23.9	11.1	11.7	7.8	8.7
Co	7.5	13.3	16.8	25.1	74.5	23	9.6	17.1	15.4
Ni									
Cu									
Zn									
Rb	0.9	0.1	1	2.9	0.4	1.4	20.3	1	5.7
Sr	1074	492.4	1479.5	1211.7	461.8	1201.3	2294.8	1419	1453
Y	20.1	26	16	27.8	48	21.8	3.7	12.8	9.9
Zr	5.5	4.5	9.1	13.7	23.9	11.3	7.1	11	11.4
Nb	1.7	2.4	3.2	4.1	9.1	3.1	0.4	3.1	2.3
Ba	178.8	589.9	167.5	156.6	40.6	120.3	743.4	113.1	164
La									
Ce	43.8	58.9	41	56.1	109.9	45.6	16.2	28.7	25.6
Pr									
Nd	38.4	55.6	29.2	47.6	88.7	35.3	8.6	21.2	19.2
Sm									
Eu									
Tb									
Gd									
Dy									
Ho									
Er									
Tm									
Yb									
Lu									
Hf									
Ta									
Pb	-2.3	-0.5	-1.7	1.2	-4	0.1	-2.5	-1.3	2.2
Th	0.1	-0.4	-0.9	0.3	-1	-1	-0.3	-0.6	0.2
U	1	-0.8	0	0.7	-1.5	1.6	0.1	-0.5	0.6

	UZ	UZ	UZ	UZ	UZ
Height (m)	1131.0	1130.0	1129.2	1127.0	1120.0
Sample	RC-01	RC-02	RC-04	RC-05	RC-A6
SiO_2	44.88	45.19	45.99	45.01	43.63
TiO_2	2.45	3.00	2.15	2.79	2.87
Al_2O_3	17.38	15.66	18.77	16.81	16.65
Fe_2O_3	12.21	14.78	10.82	14.15	14.87
MnO	0.14	0.17	0.13	0.17	0.17
MgO	4.12	4.92	3.71	4.60	5.26
CaO	12.52	11.78	11.37	11.98	11.39
Na_2O	2.69	2.56	3.15	2.81	2.61
K_2O	0.15	0.24	0.38	0.26	0.25
P_2O_5	0.05	0.06	0.07	0.08	0.09
SO_3	0.31	0.31	0.25	0.32	0.26
Cr_2O_3	0.02	0.02	0.02	0.02	0.02
NiO	0.02	0.02	0.03	0.01	0.02
H_2O-	0.03	0.04	0.10	0.03	0.12
LOI	2.76	1.08	2.78	0.84	1.50
Total	99.73	99.82	99.72	99.88	99.71
Mg#	39.61	39.27	39.98	38.71	40.73
Li					
Sc	30.6	36.4	26.3	35	27.6
V	405.2	501.7	348.4	452.1	459.6
Cr	34	84.7	43.8	69.7	55.9
Co	45.1	55.3	45	46.2	55.8
Ni					
Cu					
Zn					
Rb	1.2	2.5	3.2	2.8	2.3
Sr	664.5	770.4	957.9	806.8	843.2
Y	4.7	5.1	3.1	4.7	3.8
Zr	8.3	10.4	7.3	11	7.3
Nb	1.3	1.4	0.5	0.8	0.4
Ba	128.6	242.1	310.1	206.3	261.2
La					
Ce	10.3	9.3	8.9	11.8	9.3
Pr					
Nd	7.7	7.6	6.2	7.1	8.1
Sm					
Eu					
Tb					
Gd					
Dy					
Ho					
Er					
Tm					
Yb					
Lu					
Hf					
Ta					
Pb	3.5	1.9	3.5	5.5	1.6
Th	1.7	1.7	0.2	0.1	2.9
U	0.2	0.5	-0.6	2.3	-1.7

Height (m)	Nalaqing 2	Nalaqing 7	Nalaqing 12	Nalaqing 18	Nalaqing 21	Nalaqing 26.5	Nalaqing 36	Nalaqing 51	Nalaqing 75
Sample	S-02	S-03	S-X	S-04	S-05	S-01 (A)	S-07	S-08	S-09
SiO2	40.70	5.54	32.94	39.71	15.99	0.00	32.07	39.45	46.95
TiO2	1.35	15.62	6.72	3.36	9.17	14.40	6.59	6.64	2.25
Al2O3	5.09	4.93	10.90	14.78	12.61	5.28	11.76	11.52	19.71
Fe2O3	19.24	67.45	30.38	19.74	49.86	73.44	30.99	20.75	10.40
MnO	0.27	0.42	0.25	0.16	0.26	0.38	0.23	0.23	0.13
MgO	21.25	4.52	6.27	5.59	4.22	4.44	7.55	7.03	3.60
CaO	10.09	1.62	10.81	12.68	5.64	0.51	9.18	12.68	12.02
Na2O	0.50	0.42	1.32	1.84	1.08	0.38	1.37	1.75	3.08
K2O	0.06	0.03	0.19	0.18	0.12	0.02	0.16	0.12	0.19
P2O5	0.03	0.04	0.07	0.08	0.06	0.03	0.05	0.03	0.36
SO3	0.06	0.19	0.11	0.15	0.20	0.20	0.12	0.08	0.07
Cr2O3	0.29	0.03	0.02	0.01	0.09	0.09	0.03	0.02	0.02
NiO	0.14	0.02	0.01	0.04	0.07	0.07	0.01	0.01	0.00
H2O-	0.13	0.21	0.05	0.10	0.07	0.22	0.07	0.05	0.06
LOI	0.63	-0.92	0.02	0.98	0.03	-0.24	0.07	-0.08	0.67
Total	99.82	100.12	100.08	99.41	99.46	99.23	100.25	100.28	99.50
Li	2.04	0.39	2.71	1.72	0.76	0.15	2.02	1.65	1.34
Sc	32.6	16.2	20.3	30.1	11.9	14.1	23.5	19.6	14.1
V	244	2582	1074	615	2056	3038	1099	554	225
Cr	1714	14.4	10.9	6.20	378	295	77.3	7.02	7.63
Co	110	225	102	105	212	280	119	63.2	26.6
Ni	975	153	65.6	246	458	371	43.3	0.75	0.75
Cu	17.4	0.7		885	780		0.7		
Zn	111	476	218	111	270	407	191	153	77.8
Rb	2.09	2.48	2.68	5.23	3.82	0.14	5.67	480	1002
Sr	135	37.8	413	556	338	8.31	440	1.53	1.21
Y	5.68	1.49	6.92	7.10	1.34	0.46	4.93	8.34	6.88
Zr	11.9	22.7	23.5	26.8	15.7	14.2	17.8	34.4	11.8
Nb	0.30	5.01	3.16	2.97	2.03	2.31	1.87	5.74	1.07
Ba	12.8	6.96	70.5	95.6	35.5	3.78	57.3	61.6	114
La	0.97	0.43	2.65	3.51	1.14	0.28	1.86	2.26	4.18
Ce	3.42	1.24	6.99	9.16	2.44	0.63	5.03	6.34	10.5
Pr	0.65	0.21	1.09	1.37	0.33	0.09	0.81	1.05	1.57
Nd	3.92	1.15	6.06	6.98	1.52	0.47	4.31	5.88	8.20
Sm	1.31	0.34	1.75	1.87	0.36	0.12	1.27	1.83	2.04
Eu	0.58	0.18	0.83	0.91	0.28	0.05	0.66	1.02	1.35
Tb	0.23	0.06	0.26	0.29	0.05	0.02	0.21	0.34	0.30
Gd	1.63	0.44	1.93	2.12	0.39	0.13	1.51	2.35	2.35
Dy	1.35	0.36	1.54	1.68	0.30	0.10	1.21	1.90	1.58
Ho	0.24	0.06	0.27	0.30	0.06	0.02	0.21	0.33	0.26
Er	0.59	0.16	0.68	0.75	0.14	0.05	0.54	0.84	0.62
Tm	0.07	0.02	0.08	0.09	0.02	0.01	0.07	0.10	0.07
Yb	0.42	0.14	0.48	0.54	0.16	0.04	0.38	0.66	0.40
Lu	0.06	0.02	0.07	0.08	0.02	0.01	0.05	0.09	0.06
Hf	0.55	0.78	0.88	0.90	0.49	0.50	0.69	1.12	0.40
Ta	0.00	0.37	0.26	0.16	0.13	0.18	0.11	0.41	0.09
Pb	0.51	0.47	0.47	2.45	2.60	1.70	0.93	0.66	0.47
Th	0.03	0.04	0.18	0.18	0.07	0.02	0.12	0.14	0.06
U	0.01	0.01	0.03	0.06	0.02	0.01	0.03	0.03	0.02

Appendix C. Clinopyroxene composition for the Jianshan section, Panzhihua intrusion.

Height (m)	8	10	16	23	41	44	50	54	60	100	115	144.0	146.9
Sample	05_1	05_2	05_3	05_4	05_7	05_78	05_8	05_9	05_10	BT_01	BT-02	BT-03F	BT-04
No.	n=8	n=3	n=8	n=7	n=9	n=7	n=7	n=8	n=15	n=11	n=12	n=8	n=9
SiO_2	50.86	50.05	51.51	51.03	51.44	50.28	51.37	51.34	50.16	52.01	51.19	51.45	51.06
Al_2O_3	3.21	3.26	3.64	3.63	3.15	3.37	3.67	3.29	3.69	2.39	3.21	2.99	3.73
TiO_2	1.05	0.97	1.17	1.41	1.07	1.37	0.56	1.07	1.30	0.66	0.98	0.95	1.41
FeO	7.05	6.06	6.32	6.48	6.73	6.78	6.84	7.68	7.08	6.36	7.64	7.34	6.14
MnO	0.24	0.17	0.22	0.07	0.06	0.07	0.07	0.26	0.19	0.31	0.27	0.24	0.16
MgO	14.33	16.01	14.46	12.47	12.39	12.62	12.57	14.43	15.16	15.52	14.58	14.75	14.04
CaO	21.71	22.33	21.93	25.01	25.11	24.09	24.90	21.02	21.23	21.86	21.16	21.53	23.57
Na_2O	0.43	0.51	0.59	0.68	0.61	0.58	0.62	0.54	0.57	0.45	0.62	0.45	0.02
K_2O	0.02	0.01	0.03	0.01	0.02	0.02	0.02	0.03	0.00	0.03	0.12	0.03	0.02
Cr_2O_3	0.00	0.00	0.00	0.00	0.00	0.00	0.00	0.00	0.01	0.00	0.01	0.00	0.01
Total	98.91	99.37	99.87	100.79	100.58	99.19	100.62	99.66	99.39	99.59	99.79	99.73	100.16
Si	1.90	1.84	1.90	1.88	1.90	1.88	1.89	1.91	1.86	1.92	1.89	1.91	1.89
Al	0.14	0.14	0.16	0.16	0.14	0.15	0.16	0.14	0.16	0.10	0.14	0.13	0.16
Ti	0.03	0.03	0.03	0.04	0.03	0.04	0.02	0.03	0.04	0.02	0.03	0.03	0.04
Fe	0.22	0.19	0.20	0.20	0.21	0.21	0.21	0.24	0.22	0.20	0.24	0.23	0.19
Mn	0.01	0.01	0.01	0.00	0.00	0.00	0.00	0.01	0.01	0.01	0.01	0.01	0.01
Mg	0.80	0.88	0.80	0.69	0.68	0.70	0.69	0.80	0.84	0.85	0.80	0.81	0.77
Ca	0.87	0.88	0.87	0.99	0.99	0.97	0.98	0.84	0.84	0.86	0.84	0.85	0.93
Na	0.03	0.04	0.04	0.05	0.04	0.04	0.04	0.04	0.04	0.03	0.04	0.03	0.00
K	0.00	0.00	0.00	0.00	0.00	0.00	0.00	0.00	0.00	0.00	0.01	0.00	0.00
Cr	0.00	0.00	0.00	0.00	0.00	0.00	0.00	0.00	0.00	0.00	0.00	0.00	0.00
Total	4.00	4.00	4.00	4.00	4.00	4.00	4.00	4.00	4.00	4.00	4.00	4.00	4.00
Mg#	78	82	80	77	77	77	77	77	79	81	77	78	80
Wo	46	45	47	53	53	51	52	45	44	45	45	45	49
En	42	45	43	37	36	37	37	43	44	45	43	43	41
Fs	12	10	11	11	11	11	11	13	12	10	13	12	10

Appendix C. Continued

Height (m)	150.0	160.2	180.4	200	265.0	271.0	336.0	352.0	382.0	423.0	453.0	494.0	504.0	545.0
Sample	BT-05	BT-06	BT-08	BT-10	BT-17	BT-19	BT-27	BT-30	BT-33	BT-37	BT-41	BT-45	BT-48	BT-53
No.	n=8	n=6	n=9	n=3	n=3	n=8	n=9	n=7	n=10	n=10	n=9	n=9	n=4	n=5
SiO_2	51.02	51.01	51.48	51.80	49.36	50.01	51.14	51.24	51.04	51.02	51.07	51.30	52.36	50.94
Al_2O_3	3.59	3.67	3.25	3.10	4.51	4.27	3.65	3.25	3.40	3.07	3.05	3.10	2.36	3.08
TiO_2	1.38	1.44	1.19	0.99	1.56	1.68	1.41	1.26	1.36	1.16	1.11	1.16	0.88	1.12
FeO	7.53	7.28	8.41	7.30	6.19	7.00	6.81	7.08	7.75	7.51	7.56	7.66	7.84	7.89
MnO	0.25	0.24	0.28	0.24	0.13	0.19	0.22	0.21	0.26	0.26	0.26	0.26	0.35	0.31
MgO	14.15	14.21	14.69	14.92	15.24	14.05	14.56	14.77	14.46	14.44	14.45	14.56	14.85	14.31
CaO	22.26	22.81	21.05	21.65	22.76	22.31	21.75	21.60	21.47	21.37	21.39	21.46	21.78	21.60
Na_2O	0.01	0.01	0.42	0.45	0.02	0.02	0.57	0.52	0.50	0.50	0.46	0.51	0.47	0.45
K_2O	0.02	0.02	0.00	0.01	0.02	0.01	0.02	0.02	0.02	0.03	0.02	0.03	0.02	0.02
Cr_2O_3	0.01	0.00	0.01	0.00	0.00	0.01	0.01	0.00	0.00	0.01	0.00	0.01	0.00	0.00
Total	100.22	100.68	100.79	100.47	99.82	99.54	100.14	99.95	100.26	99.36	99.38	100.06	100.93	99.70
Si	1.89	1.88	1.89	1.90	1.82	1.87	1.88	1.89	1.88	1.90	1.90	1.90	1.92	1.89
Al	0.16	0.16	0.14	0.13	0.20	0.19	0.16	0.14	0.15	0.13	0.13	0.14	0.10	0.13
Ti	0.04	0.04	0.03	0.03	0.04	0.05	0.04	0.04	0.04	0.03	0.03	0.03	0.02	0.03
Fe	0.23	0.22	0.26	0.22	0.19	0.22	0.21	0.22	0.24	0.23	0.24	0.24	0.24	0.25
Mn	0.01	0.01	0.01	0.01	0.00	0.01	0.01	0.01	0.01	0.01	0.01	0.01	0.01	0.01
Mg	0.78	0.78	0.81	0.82	0.84	0.78	0.80	0.81	0.80	0.80	0.80	0.80	0.81	0.79
Ca	0.89	0.90	0.83	0.85	0.90	0.89	0.86	0.85	0.85	0.85	0.85	0.85	0.86	0.86
Na	0.00	0.00	0.03	0.03	0.00	0.00	0.04	0.04	0.04	0.04	0.03	0.04	0.03	0.03
K	0.00	0.00	0.00	0.00	0.00	0.00	0.00	0.00	0.00	0.00	0.00	0.00	0.00	0.00
Cr	0.00	0.00	0.00	0.00	0.00	0.00	0.00	0.00	0.00	0.00	0.00	0.00	0.00	0.00
Total	4.00	4.00	4.00	4.00	4.00	4.00	4.00	4.00	4.00	4.00	4.00	4.00	4.00	4.00
Mg#	77	78	76	78	81	78	79	79	77	77	77	77	77	76
Wo	47	47	44	45	47	47	46	45	45	45	45	45	45	45
En	41	41	43	43	43	41	43	43	42	42	42	42	43	42
Fs	12	12	14	12	10	12	11	12	13	12	12	13	13	13

Appendix D. Composition of Ti-magnetite for the Jianshan section, Panzhihua intrusion.

Sample	05_1	05_2	05_3	05_4	05_6	05_7	05_78	05_8	05_9	05_10
Height	8	10	16	23	35	41	44	50	54	60
No.	n=13	n=6	n=8	n=9	n=5	n=10	n=8	n=8	n=12	n=7
MgO	1.12	2.12	1.76	3.23	3.00	3.09	3.69	2.93	0.74	1.55
Al_2O_3	3.82	4.58	3.35	3.71	3.04	4.79	4.27	3.88	3.10	2.71
FeO	40.93	40.06	39.97	36.28	36.57	35.74	35.46	36.50	41.38	38.16
Fe_2O_3	47.07	46.07	45.96	41.36	41.69	40.75	40.43	41.61	48.83	44.08
MnO	0.25	0.26	0.26	0.45	0.25	0.52	0.43	0.43	0.20	0.32
V_2O_3	0.00	0.50	0.00	0.00	1.86	0.00	0.00	0.00	0.00	1.64
TiO_2	6.63	6.45	8.36	15.30	13.38	14.89	15.04	14.97	5.69	11.58
Cr_2O_3	0.03	0.07	0.04	0.00	0.13	0.00	0.00	0.00	0.03	0.07
Total	99.85	100.10	99.70	100.33	99.93	99.78	99.31	100.33	99.98	100.11
Mg	0.06	0.12	0.10	0.18	0.16	0.17	0.20	0.16	0.04	0.09
Al	0.17	0.20	0.15	0.16	0.13	0.21	0.18	0.17	0.14	0.12
Fe2+	1.27	1.22	1.24	1.10	1.12	1.09	1.08	1.11	1.29	1.18
Fe3+	1.31	1.26	1.28	1.13	1.15	1.12	1.11	1.14	1.37	1.23
Mn	0.01	0.01	0.01	0.01	0.01	0.02	0.01	0.01	0.01	0.01
V	0.00	0.00	0.00	0.00	0.05	0.00	0.00	0.00	0.00	0.00
Ti	0.18	0.18	0.23	0.42	0.37	0.41	0.41	0.41	0.16	0.32
Cr	0.00	0.01	0.00	0.00	0.00	0.00	0.00	0.00	0.00	0.05
Total	3.00	3.00	3.00	3.00	3.00	3.00	3.00	3.00	3.00	3.00

Appendix D. Continued

Sample	BT-01	BT-02	BT-03 F	BT-04	BT-05	BT-06	BT-08	BT-10	BT-17
Height	100	115	144.0	146.9	150.0	160.2	180.4	200	265.0
No.	n=11	n=9	n=13	n=7	n=6	n=3	n=6	n=9	n=7
MgO	0.39	0.50	1.70	3.77	2.85	2.45	1.50	0.98	3.29
Al_2O_3	2.79	1.61	3.27	0.07	0.07	0.07	5.59	2.85	5.16
FeO	41.04	42.78	37.96	36.31	37.21	37.15	38.37	39.19	36.32
Fe_2O_3	49.66	50.48	45.18	42.84	43.91	43.84	44.13	47.03	41.76
MnO	0.16	0.12	0.30	0.47	0.41	0.54	0.35	0.28	0.33
V_2O_3	0.00	0.00	0.00	0.00	0.00	0.00	0.00	0.00	0.00
TiO_2	5.54	3.63	11.66	16.09	15.38	15.92	9.80	9.85	12.91
Cr_2O_3	0.24	0.05	0.04	0.04	0.05	0.04	0.06	0.06	0.11
Total	99.82	99.17	100.09	99.58	99.87	100.01	99.81	100.24	99.87
Mg	0.02	0.03	0.09	0.21	0.16	0.14	0.08	0.05	0.18
Al	0.12	0.07	0.14	0.00	0.00	0.00	0.24	0.12	0.22
Fe2+	1.29	1.35	1.17	1.13	1.16	1.16	1.18	1.22	1.10
Fe3+	1.40	1.44	1.26	1.20	1.23	1.23	1.22	1.32	1.14
Mn	0.01	0.00	0.01	0.01	0.01	0.02	0.01	0.01	0.01
V	0.00	0.00	0.00	0.00	0.00	0.00	0.00	0.00	0.00
Ti	0.16	0.10	0.32	0.45	0.43	0.45	0.27	0.28	0.35
Cr	0.01	0.00	0.00	0.00	0.00	0.00	0.00	0.00	0.00
Total	3.00	3.00	3.00	3.00	3.00	3.00	3.00	3.00	3.00

Appendix D. Continued

Sample	BT-19	BT-27	BT-30	BT-33	BT-37	BT-41	BT-45	BT-48	BT-53
Height	271.0	336.0	352.0	382.0	423.0	453.0	494.0	504.0	545.0
	n=4	n=6	n=5	n=7	n=6	n=5	n=5	n=6	n=5
MgO	1.97	2.84	1.55	1.19	1.09	0.27	0.76	0.88	0.60
Al_2O_3	0.04	4.92	2.87	2.99	3.77	2.58	5.14	4.04	2.79
FeO	39.64	36.18	40.21	40.63	40.36	40.21	40.29	39.64	41.30
Fe_2O_3	46.77	41.61	46.24	46.72	47.63	47.44	46.74	45.59	47.90
MnO	0.25	0.45	0.29	0.37	0.25	0.18	0.19	0.45	0.20
V_2O_3	0.00	0.00	0.00	0.00	0.00	0.00	0.00	0.00	0.00
TiO_2	11.29	13.55	8.29	7.63	6.30	8.50	6.33	9.64	6.41
Cr_2O_3	0.12	0.06	0.06	0.07	0.05	0.05	0.06	0.04	0.07
Total	100.07	99.60	99.51	99.60	99.45	99.23	99.50	100.27	99.25
Mg	0.11	0.15	0.09	0.07	0.06	0.02	0.04	0.05	0.03
Al	0.00	0.21	0.13	0.13	0.17	0.12	0.22	0.18	0.12
Fe2+	1.24	1.10	1.25	1.27	1.26	1.27	1.25	1.23	1.30
Fe3+	1.32	1.14	1.29	1.31	1.33	1.35	1.30	1.27	1.36
Mn	0.01	0.01	0.01	0.01	0.01	0.01	0.01	0.01	0.01
V	0.00	0.00	0.00	0.00	0.00	0.00	0.00	0.00	0.00
Ti	0.32	0.37	0.23	0.21	0.18	0.24	0.18	0.27	0.18
Cr	0.00	0.00	0.00	0.00	0.00	0.00	0.00	0.00	0.00
Total	3.00	3.00	3.00	3.00	3.00	3.00	3.00	3.00	3.00

Appendix E. Ilmenite composition from the Jianshan section, Panzhihua intrusion.

Sample No.	05_1 n=5	05_2 n=8	05_3 n=8	05_4 n=5	05_6 n=6	05_7 n=4	05_78 n=3	05_8 n=4	05_9 n=7	BT-01 n=11	BT-02 n=9	BT-03F n=4	BT-04 n=3
MgO	2.78	4.35	4.15	6.93	7.05	5.71	6.67	6.20	2.72	0.59	1.14	3.63	7.45
TiO_2	51.46	52.14	52.43	55.51	54.88	53.50	54.84	53.73	50.71	51.16	50.38	52.33	56.83
Al_2O_3	0.00	0.00	0.01	0.00	0.01	0.01	0.02	0.01	0.67	0.01	0.01	0.01	0.01
FeO	44.34	41.51	42.37	36.83	36.10	39.87	38.07	39.28	44.82	46.28	47.65	43.14	34.65
MnO	0.62	0.63	0.53	0.57	0.44	0.06	0.50	0.06	0.60	1.33	0.62	0.48	0.47
Cr_2O_3	0.01	0.00	0.01	0.00	0.01	0.01	0.00	0.02	0.01	0.01	0.01	0.01	0.00
Total	99.20	98.63	99.50	99.84	98.47	99.15	100.11	99.30	99.54	99.37	99.82	99.59	99.42
Mg	0.10	0.16	0.15	0.25	0.26	0.21	0.24	0.22	0.10	0.02	0.04	0.13	0.27
Ti	0.96	0.97	0.97	1.00	1.00	0.98	0.99	0.98	0.94	0.97	0.95	0.97	1.03
Al	0.00	0.00	0.00	0.00	0.00	0.00	0.00	0.00	0.02	0.00	0.00	0.00	0.00
Fe	0.92	0.86	0.87	0.74	0.73	0.81	0.76	0.80	0.93	0.98	1.00	0.89	0.70
Mn	0.01	0.01	0.01	0.01	0.01	0.00	0.01	0.00	0.01	0.03	0.01	0.01	0.01
Cr	0.00	0.00	0.00	0.00	0.00	0.00	0.00	0.00	0.00	0.00	0.00	0.00	0.00

Appendix E. Continued

Sample No.	BT-05 n=4	BT-08 n=8	BT-10 n=7	BT-17 n=8	BT-19 n=4	BT-27 n=10	BT-30 n=8	BT-33 n=9	BT-37 n=9	BT-41 n=7	BT-45 n=7	BT-48 n=5	BT-53 n=5
MgO	6.73	3.02	3.21	6.36	6.91	5.26	4.56	3.86	3.32	1.48	1.57	2.84	3.36
TiO_2	57.11	52.57	52.37	54.45	56.44	54.00	53.04	52.28	52.16	51.25	51.38	52.66	51.76
Al_2O_3	0.01	0.00	0.01	0.01	0.02	0.01	0.02	0.01	0.01	0.01	0.01	0.01	0.03
FeO	36.54	43.58	43.18	38.75	35.98	40.51	41.83	43.48	43.39	46.03	45.72	44.45	43.87
MnO	0.53	0.53	0.46	0.35	0.46	0.42	0.46	0.43	0.46	0.57	0.56	0.57	0.45
Cr_2O_3	0.00	0.01	0.01	0.01	0.00	0.01	0.00	0.01	0.00	0.01	0.00	0.01	0.01
Total	100.91	99.71	99.24	99.93	99.82	100.22	99.91	100.06	99.35	99.36	99.24	100.53	99.48
Mg	0.24	0.11	0.12	0.23	0.25	0.19	0.17	0.14	0.12	0.06	0.06	0.10	0.12
Ti	1.02	0.98	0.98	0.99	1.02	0.98	0.97	0.96	0.97	0.97	0.97	0.97	0.96
Al	0.00	0.00	0.00	0.00	0.00	0.00	0.00	0.00	0.00	0.00	0.00	0.00	0.00
Fe	0.73	0.90	0.89	0.78	0.72	0.82	0.85	0.89	0.90	0.97	0.96	0.91	0.91
Mn	0.01	0.01	0.01	0.01	0.01	0.01	0.01	0.01	0.01	0.01	0.01	0.01	0.01
Cr	0.00	0.00	0.00	0.00	0.00	0.00	0.00	0.00	0.00	0.00	0.00	0.00	0.00

Appendix F. Analytical standards for PGE analysis.

	99 Ru		103 Rh		105 Pd		189 Os		193 Ir		195 Pt		197 Au	
Sample No.	Conc. [ppb]	+/- (ppb)	Conc. [ppb]	+/- (ppb)	Conc. [ppb]	+/- (ppb)	Conc. [ppb]	+/- (ppb)	Conc. [ppb]	+/- (ppb)	Conc. [ppb]	+/- (ppb)	Conc. [ppb]	+/- (ppb)
DP-7	2.18	0.08	0.40	0.01	13.61	0.21	1.11	0.06	0.41	0.02	2.72	0.09	8.25	0.04
DP-8	1.61	0.07	1.43	0.04	14.69	0.30	0.46	0.03	0.58	0.02	11.06	0.22	1.51	0.08
RV-1	11.06	0.17	129.48	1.50	4 716.46	53.83	3.90	0.11	26.19	0.40	1 258.38	26.35	214.37	3.75
RV-2	19.56	0.16	220.77	1.65	7 613.39	84.67	7.12	0.18	45.37	0.96	2 160.91	27.23	304.76	4.42
RV-5	0.69	0.06	8.69	0.24	203.37	6.34	0.27	0.03	1.64	0.04	49.64	1.05	17.38	0.14
RV-6	1.76	0.09	16.72	0.29	335.61	6.03	0.63	0.05	3.17	0.09	100.62	3.79	52.00	0.74
RV-9	1.21	0.07	18.96	0.72	629.11	27.21	0.40	0.03	3.93	0.15	200.96	3.63	23.06	0.29